ABSTRACT

Title of dissertation: DEVELOPMENT OF A MAGNETORHEOLOGICAL FLUID BASED HYBRID ACTUATOR

Shaju John, Doctor of Philosophy, 2007

Dissertation directed by: Professor Norman M. Wereley
Department of Aerospace Engineering

A hybrid hydraulic actuation system is proposed as an active pitch link for rotorcraft applications. Such an active pitch link can be used to implement Individual Blade Control (IBC) techniques for vibration and noise reduction, in addition to providing primary control for the helicopter. Conventional technologies like electric motors and hydraulic actuators have major disadvantages when it come to applications on a rotating environment. Centralized hydraulic system require the use of mechanically complex hydraulic slip rings and electric motors have high precision mechanical moving parts that make them unattractive in application with high centrifugal load. The high energy density of smart materials can be used to design hydraulic actuators in a compact package. MagnetoRheological (MR) fluids can be used as the working fluid in such a hybrid hydraulic actuation system to implement a valving system with no moving parts. Thus, such an actuation system can be theoretically well-suited for application in a rotating environment.

To develop an actuation system based on an active material stack and MR fluidic valves, a fundamental understanding of the hydraulic circuit is essential. In

order to address this issue, a theoretical model was developed to understand the effect of pumping chamber geometry on the pressure losses in the pumping chamber. Three dimensional analytical models were developed for steady and unsteady flow and the results were correlated to results obtained from Computation Fluid Dynamic simulation of fluid flow inside the pumping chamber. Fundamental understanding regarding the pressure losses in a pumping chamber are obtained from the modeling process. Vortices that form in the pumping chamber (during intake) and the discharge tube (during discharge) are identified as a major cause of pressure loss in the chamber. The role of vortices during dynamic operation is also captured through a frequency domain model.

Extensive experimental studies were conducted on a hybrid hydraulic system driven by a pump (actuated by a 2” long and 1/4” diameter Terfenol-D rod) and a Wheatstone bridge network of MR fluidic valves. The Wheatstone bridge network is used to provide bi-directionality to the load. Through a variety of experimental studies, the main performance metrics of the actuation system, like output power, blocked force, maximum no-load velocity and efficiency, are obtained. The actuation system exhibits a blocked force of 30 N and a maximum no-load velocity of 50 mm/s. Extensive bi-directional tests were also done for cases of no-load, inertial load and spring load to establish the frequency bandwidth of the actuator. The actuation system can output a stroke of 9 mm at an output actuator frequency of 4 Hz. An analytical model was developed to predict the performance of the hybrid hydraulic actuation system. A state space representation of the system was derived using equations derived from the control volume considerations. The results of the analytical model show that the model predicts the frequency peak of the system to within 20 Hz of the actual resonance frequency.

In the third part of this dissertation, the effectiveness of the hybrid hydraulic actuation system is evaluated in a rotating environment. A piezoelectric stack that is driven by three PI-804.10 stacks was attached at the end of a spin bar. After balancing the spin bar using a counterweight, the spin bar is spun to an RPM of 300. This simulates a centrifugal loading of 400 g, which is slightly higher than the full-scale centrifugal loads experienced by a pitch link on a UH-60. The performance of the actuator was measured in terms of velocity of an output cylinder shaft. Since some deterioration of performance was expected at 300 RPM, the output cylinder was redesigned to include roller bearings to support the excess force. Through no load and load tests, the effectiveness of the current hybrid actuation system design was shown as the performance of the system did not deteriorate in performance with greater centrifugal acceleration.

DEVELOPMENT OF A MAGNETO-RHEOLOGICAL FLUID BASED HYBRID ACTUATION SYSTEM

by

Shaju John

Dissertation submitted to the Faculty of the Graduate School of the
University of Maryland, College Park in partial fulfillment
of the requirements for the degree of
Doctor of Philosophy
2007

Advisory Commmittee:

Professor Norman M. Wereley, Chair/Advisor
Professor Amr Baz (Dean's Representative)
Professor Christopher Cadou (Co-advisor)
Professor Inderjit Chopra
Professor Alison B. Flatau

Dedication

To Kesi, the love of my life,

and,

To my parents.

Acknowledgements

I would like to sincerily and wholeheartedly thank my advisor, Dr. Norman M. Wereley for all the guidance and support through the my graduate school years. I am extremely grateful for the oppurtunities offered to me to develop and hone my skills and for his patience and trust that he extended to me. I would also like to thank Dr. Christopher Cadou, my co-advisor, for his guidance and advice and my graduate committee, Dr. Inderjit Chopra, Dr. Alison Flatau and Dr. Amr Baz for agreeing to serve on my committee and for their insighful critique of my work. I have taken several classes with these professors and have greatly benefited from their teaching.

This work would not have been possible without the help of several colleagues. Foremost, I would like to thank Dr. Jayant Sirohi for his intellectual and selfless contributions and for his mentorship. I would like to thank Dr. Jin-Hyeong Yoo, Dr. Gang Wang and Dr. Young-Tai Choi for their support and guidance during my 'formative years' in the lab. I also want to thank Dr. Peter Chen for our discussions and for the oppurtunity that he extended to me. I want to thank Anirban Chaudhuri for his help during the completion of this dissertation and for our discussion regarding the papers we have authored together and Dr. Wei Hu, Dr. Anubhav Datta, Dr. Ronald Couch, Dr. Filipe Bohorquez and Dr. Atulasimha *Babyblue* Jayasimha for their inputs and critiques. Cubicle life can be boring without interesting office-mates. Peter Copp, Jaye Falls and Nick Rosenfeld made my life very interesting with our animated discussions and arguments. I thank Peter Copp also for the fellowship we have had during our busy graduate lives.

I also want to thank my house-mates from my bachelor days - Sudarshana Koushik, Rahul Ratan, Vikas Malla and Subramanium Rajgopal- for our good times together. I want to especially thank Sudarshana Koushik for his friendship and help during all these years and looking forward to many more years of friendship.

This dissertation is dedicated to my wife, Kesi, who has stood by me during this entire endeavor. She has encouraged and strengthened me throughout my graduate school years. She is God's gift to me, a true help-meet, and I could not have done it so well without her. This work is also dedicated to my parents who have longed to see a successful completion of my student life. They cared for my well-being while going through financial hardships. This dissertation is a fruit of their labours.

TABLE OF CONTENTS

LIST OF TABLES

LIST OF FIGURES

Chapter 1

Introduction

1.1 Background

Helicopters are uniquely designed to hover, take-off and land vertically, perform low speed maneuvers and to cruise forward at high speeds. All these different types of operations are performed using the rotor system. The rotor system generates the lift to hover, the propulsive force to move forwards at high speeds and the control forces necessary to perform different maneuvers. In forward flight, the rotor blades encounter different flow regions in the advancing and retreating sides. The angle of attack of the rotor blade has to be changed in a continuous manner throughout the rotation of the blade. At higher forward speeds, the blades encounter transonic flow regimes that gives rise to unsteady rotor forces. In addition, individual blades also have to encounter the vortex wake fields of other blades and other random occurrences like gusts. Maneuvers like high acceleration ascend or descent also present additional difficulties due to the high disk loadings involved. Due to the need to perform the functions of lift generation, propulsion and control, the design of the swashplate becomes very complex and the rotor system is forced to operate in a complex aerodynamic environment. The forces generated by the rotor blades are transmitted to the fuselage through the rotor head in the form of vibrations. The different sources of helicopter vibration can be seen in Figure 1.1. For example, 90% of the vibrations in a fuselage of a UH-60 helicopter arise due to the rotor system (Bousmann, 1999). Fuselage vibration affects the life of the various critical structural systems of the helicopter, reduces crew awareness, reliability and comfort, and increases crew fatigue. Thus, the need to reduce vibration levels is an important area of research in the field of rotorcraft.

Vibrations are also caused by dissimilarities in rotor blades. These dissimilarities are caused by differences in rotor blade inertias or differences in rotor blade aerodynamics. Inertial dissimilarities arise when the center of inertia of the blade does not coincide with the rotational axis of the rotor. Aerodynamic dissimilarities are caused by differences in blade twist, blade airfoil shape or blade drag characteristics. In an ideal rotor system with identical blades, the rotor hub acts as a filter and only kN_b/rev (N_b is the number of blades and k is any integer) harmonic loads are transmitted to the fuselage. Due to dissimilarities in the rotor blades, other harmonic loads are also transmitted to the fuselage.

Several vibration reductions techniques have been proposed, that can broadly be classified as passive and active techniques.

- Traditional passive techniques have relied on pendulum absorbers (Ellis and Jones, 1963; Schuett, 1969; Amer and Neff, 1974) or modal placement methods (Taylor, 1982; Leconte and Geoffroy, 1994). Passive techniques have limited effectiveness over a narrow range of operating conditions. Vibration suppressors have also been installed at specific points inside the fuselage or directly on the rotor hub. But such systems incur weight and parasitic drag penalties. Other passive methods include aeroelastic optimization (Lim, 1988) and composite couplings in the rotor blades (Bao et al., 2002). Although such methods add little or no significant additional weight to the helicopter, their effectiveness is low.

- Active methods involve placing actuators with high control authority at critical positions in the fuselage. Two examples of helicopters where active methods have been used are EH101 (Staple, 1990; Staple and Wells, 1990) of Westland helicopters and S-76 (Welsh et al., 1990) and S-92 (Welsh and Millott, 1999) of Sikorsky helicopters. These schemes implement the control in the fixed frame of the fuselage. Schemes which implement the control in the rotating frame, like Higher Harmonic Control (HHC) or Individual Blade Control (IBC) have greater effectiveness as they reduce the vibration at the source.

Higher Harmonic Control (HHC) uses the non-rotating swash-plate to provide control inputs to the rotor blades. The swash-plate is actuated at a frequency of N_b/rev in both collective and cyclic modes. An N_b/rev collective input results in an N_b/rev response in the blade pitch angle. A similar input in the cyclic mode results in $(N_b - 1)/rev$ and $(N_b + 1)/rev$ response in the rotor blade pitch angles. Thus, blade pitch inputs in the fixed frame results in a $(N_b - 1)/rev$, N_b and $(N_b + 1)/rev$ harmonic response in the rotating frame. Since these are the major harmonics that contribute to helicopter vibrations, an appropriate N_b/rev control input would be sufficient for vibration reduction. HHC has been demonstrated to be a viable option during full-scale tests (Wood et al., 1985; Miao et al., 1986; Achache and Polychroniadis, 1986). The major disadvantages of HHC are the high actuation power required to provide the required control inputs to the blades and the large weight penalty of the associated systems. Other control objectives like noise reduction and stall alleviation require control input at other frequencies. It is well known that other harmonics are important to minimize blade stresses and to improve rotor performance (Chopra, 2000).

Individual Blade Control (IBC) uses actuators (Guinn, 1982) to individually control rotor blades. IBC systems attempt to avoid the limitation posed by HHC by imparting control input at any desired frequency (Ham, 1987). This allows for the control of each blade at frequencies other than just integral multiples of $1/rev$, thus simultaneously tackling the issues of vibration reduction, stall alleviation and noise reduction.

There has been considerable interest in achieving primary flight control through IBC techniques, thus eliminating the use of the mechanically complex swashplate. Such techniques require actuators that can provide the necessary force and stroke. Also, the actuator must have sufficient frequency bandwidth to tackle issues like vibration and noise reduction. One of the complicating factors that arises when choosing an actuator for a rotating environment is the high centrifugal forces involved. These loads can be significant enough to cause locking of mechanical moving parts. IBC techniques look for reducing rotor vibratory loads by giving appropriate force feedback input to the rotors at particular frequencies. For an N bladed rotor, the bulk of the vibratory loads in the rotating frame are in the frequencies of $(N-1)/rev$, N/rev and $(N+1)/rev$. For a full scale UH-60 helicopter, this translates to an operational bandwidth of at least 23Hz. Thus, an actuator being considered as a potential active pitch must have a bandwidth of at least 23Hz and be able to withstand a centrifugal loading of 350g in addition to providing the required force and stroke necessary.

Summarizing, any actuator considered for rotorcraft IBC applications must satisfy the following criteria:

- The actuator should be able to provide the force and stroke required to move the rotor blade and should have adequate bandwidth necessary for vibration and noise reduction.

- The actuator should have a low number of moving parts, if any. The presence of moving parts makes an actuator very unfavorable in applications with high centrifugal loading.

- The actuator should have power-off stiffness. In the event of loss of power, the actuator should have inherent locking capability.

- The actuator should be compact and should not add significant weight or drag penalty.

Conventional actuation methods like hydraulics or electromechanical actuators can be used in these applications. However, they have certain disadvantages. Using conventional hydraulic system to change the profile of the entire blade or parts of the blade requires the transmission of pressurized fluid from the fuselage to the rotating environment of a rotor blade. This requires complex hydraulic slip rings that adds weight and drag penalties to the helicopter. Electric motors have high energy density and are a very mature technology. However, associated moving parts like rotors and ball-screws make them unattractive in applications in a rotating environment.

Actuation systems based on active materials have emerged as a viable alternative to conventional actuators in these rotorcraft applications because they are compact, light-weight, possess high energy densities and high bandwidth. Additionally, hybrid actuators can be designed to have a very low number of moving parts, thus improving their reliability. Other than the field of rotorcraft, actuation systems based on active materials also find applications in automobile (Lam and Liao, 2003) and biomedical (Shoji and Esashi, 1994) engineering. Despite their high energy density and actuation bandwidth, the factor that limits the use of such actuators is their low induced strain.

1.1.1 Smart material based on-blade actuators

Active materials are materials that undergo an induced strain due to the application of an electric (piezoelectrics and electrostrictives), magnetic (magnetostrictives, magnetic shape memory alloys) or thermal (shape memory alloys) field. Smart material based actuators have been considered for a wide range of rotorcraft applications (Chopra, 2000).

The most commonly researched application for an active material driven actuator is to actuate a trailing edge flap. Early studies researched the use to piezoelectric bimorph benders on a Froude scale bearingless rotor (Samak and Chopra, 1996; Koratkar and Chopra, 1997). In these studies, the bender was connected to the flap through hinges and mechanical links were used to amplify the stroke produced by the bender. Similar bimorph based bender actuated wing sections were also made by Spangler and Hall (1990) and Hall and Prechtl (1996). It was shown that the efficiency of the bimorph actuator can be improved by altering the thickness of the piezoelectric sheets and that the frictional loss in hinges and backlash can be minimized by using flexural amplification mechanism. Fulton and Ormiston (2001) demonstrated that such piezo-bimorph driven on-blade flaps can be used effectively to control vibratory loads.

Since the force capability of piezoelectric bimorphs are limited, piezoceramic stack actuators emerged as a possible alternative. Piezoceramic stacks are high force low stroke devices. Mechanical amplification devices were explored to trade the high force for high stroke in such actuators. Spencer *et al*. (1995) demonstrated a trailing edge flap driven by two piezoelectric stacks and an L-arm amplification method. This model was later improved by Chandra and Chopra (1997) through the use of high performance piezoelectric stack actuators with flexures. Lee *et al*. (1999; 1990; 1999) compared different commercially available piezostack actuators to evaluate their actuation properties. The stack actuators were then used to manufacture a double-L (L-L) stroke amplification device for a full-scale trailing edge flap. Straub *et al*. (2001) also developed a stack-actuated trailing edge flap for the full-scale MD-900 Explorer rotor system. This device was designed to actively control vibration, noise and aerodynamic performance of the rotor system. Prechtl and Hall (1999; 2000) developed an piezoelectric stack based actuator for a full-scale rotor application. This device performed stroke amplification using a criss-crossing frame, and was called the X-frame actuator. Designs of trailing edge flaps based on magnetostrictive actuators have also been developed (Bothwell et al., 1995; Fenn et al., 1996). Bothwell *et al*. developed a extension-torsion coupled composite tube that is wrapped around a magnetostrictive stack actuator. One end of the tube was fixed at the root of the blade and the other end of the tube is attached to a flap. As the actuator length changed depending on the provided excitation, the free end of the tube rotates to provide the necessary motion to the flap.

Berhard *et al*. (1999; 2000) developed a novel method of varying the ply layup of the beam such that the phasing of surface mounted piezoceramic actuators is used to convert the bending-torsion coupled structure into a pure twist structure. Embedded piezoceramic actuators have been used to actively control the twist of the rotor blade. There have also been other studies done on coupling piezoelectric actuators with tailored composite blades (Chen and Chopra, 1996; Rodgers et al., 1997).

The major challenge of these approaches is the integration of the actuators within the blade cross-section, while achieving the required power output, and meeting weight and aeroelastic constraints of the rotor blade. In addition, as the trailing-edge flaps are typically located at around 75% blade span (Fulton and Ormiston, 2001; Milgram et al., 1998; Straub et al., 2001), the actuators must operate under large centrifugal loads. Also, most of the above mentioned schemes use mechanical levers and hinges to amplify the stroke of the active material. Such methods of mechanical amplification leads to 60-80% reduction in the overall energy density of the device, as compared to the base active material (Paine and Chaudhry, 1996). Schemes that involve coupling of the actuator and the composite blade appear feasible, however, they may not be cost effective to extend their application to vibration and noise reduction (Chopra, 2000). Frequency rectification methods have been used as an alternate scheme to overcome the low strain of the active materials by trading high frequency low stroke motion of the active material for a low frequency, high stroke motion of the load through the use of active or passive means. Examples of such frequency rectified devices are ultrasonic motors (Sashida and Kenjo, 1993; Uchino, 1997), rotary piezoelectric motors (Duong and Garcia, 1996; Frank et al., 2003) and inch-worm motors (Hemsel and Wallaschek, 2000; Galante et al., 2000). These devices use friction for rectification, they are highly prone to rapid wear and tear and are not suitable for use in application with high centrifugal loading.

1.1.2 Active pitch links

An alternate approach to the above mentioned techniques of on-blade actuators or coupled blade schemes, is to incorporate active pitch links (APL) in the rotating frame that change the blade pitch by varying their length. This approach has three major advantages. Firstly, the rotor blade is unchanged and does not require any redesign, modification or change in production method. Secondly, as the pitch links are located close to the rotor shaft, they experience a significantly lower centrifugal force than trailing edge flap actuators, and do not face as stringent volumetric constraints as trailing edge flaps. For example, the centrifugal acceleration experienced by a pitch link of a UH-60 helicopter is of the order of 350g. Thirdly, as the rotor blade does not employ a discrete control surface, the APLs do not create an additional profile drag penalty. The actuators, placed directly in the rotating frame, can also achieve vibration reduction via Individual Blade Control (IBC) over a wide band of excitation frequencies, in addition to primary control. Active pitch link concepts have been investigated for IBC applications on rotorcraft, both on model scale (Lorber et al., 2001) and on full-scale rotors (Arnold and Strecker, 2002). Such a hydraulic actuator can be seen in Figure 1.2. These concepts involve hydraulic actuators mounted on the main rotor hub in the rotating frame, and consequently require a hydraulic slip-ring. As a result, these systems are complicated, difficult to maintain and result in a large weight penalty. For example, on a system tested on the CH-53G helicopter, the pitch link actuators weighed approximately 10kg, while the overall hydraulic system including the pump, tubing and slip-ring weighed 600kg (Arnold and Strecker, 2002).

Hybrid hydraulic devices are another class of smart material based devices that use the frequency rectification technique to provide actuation to the load. In these devices, an active material stack, such as piezoelectric, magnetostrictives or electrostrictive, is used to pressurize a hydraulic fluid in an enclosed pumping chamber. The bi-directional motion of the active stack is then rectified using one-way valves. These valves, which act in a similar manner to electric diodes, allow flow in only one direction depending on the pressure difference across them. This results in a uni-directional fluid flow exiting the pumping chamber and thus, a uni-directional motion of the output load. To obtain bi-directional motion of the output load, an additional valving system (active or passive) must be introduced. Such devices takes advantage of the high energy density of smart materials to produce actuation systems that are compact and have a low number of moving parts.

1.2 Proposed Actuation System

This dissertation proposes the use of a hybrid hydraulic actuation system as an active pitch link for rotorcraft applications. The proposed system is composed of three main parts - a hybrid pump, an MR fluid based valve system and an output cylinder that is connected to the load. The schematic of the proposed system is given in Figure 1.3.

- A hybrid pump, actuated by a Terfenol-D stack, acts as a pressure source. Like most other hybrid actuator technologies, the frequency rectification is performed using passive reed valves. MR fluid is used as the hydraulic fluid in the hybrid pump.

- The use of MR fluid as the main working fluid in the actuation system enables the implementation of MR fluid based valves. A Wheatstone bridge network of four MR fluidic valves is used as the valving system to enable the bi-directional motion of the load.

- The load is attached to the output cylinder shaft. The pressurized fluid flow generated by the hybrid pump is channeled into the appropriate region of the output cylinder through the MR valve network.

The proposed actuation system has several advantages over conventional technologies. A design of the hybrid hydraulic pump is compact owing to its use of the high energy density of Terfenol-D through high frequency operation. A compact pressure source for each active pitch link eliminates the need for a centralized pressure source and heavy hydraulic slip rings to transmit the fluid pressure to the individual pitch link. Since the hybrid hydraulic actuation concept works on the frequency rectification scheme, there are no mechanical stroke magnification devices to impede the frequency response of the actuation system.

Since flow emanating from the hybrid pump is uni-directional, bi-directional motion can be produced in the load through an appropriate valving system. Among studies into hybrid hydraulic actuation, bi-directional motion has been reported by Tan *et al*. (2005) and Ellison *et al* (2004) through the use of active solenoid valves. Solenoid valves have a spring loaded plunger that physically opens closes and opens a particular fluid flow path depending on the magnetic field that is applied to an attached solenoid. Owing to the inertia of the plunger, the frequency response of solenoid valves is limited to less than 50Hz. Additionally, the dynamics of the plunger will be different when the solenoid works under centrifugal loading. Valves based on MR fluids work on the basis of induced magnetic field and are limited only by the magnetic field induction response times of the ferromagnetic particles in the MR fluid and the response time of the magnetic circuit. One of the key aspects is the time taken by the ferromagnetic particles to form the chains in the viscous medium. Jolly *et al.* (2000) used a magnetic induction technique to detect the formation of chains on time scales on the order of milliseconds. This response time has a large dependence on the viscosity of the medium. Typical response times of commercially available MR fluids is of the order of 10 milliseconds, which translates to a frequency bandwidth of 100Hz. MR fluid based devices can be designed for a faster response time of under 5 milliseconds (Takesue et al., 2004) through better design of the magnetic circuit and by reduction of eddy current effects. Hence, in theory, an MR fluid based valve system can be designed to have a frequency bandwidth of over 100Hz, thus providing adequate bandwidth for primary and secondary control as an active pitch link. Also, the use of MR based fluidic valves enables an actuation system design with no moving parts.

Another advantage of the proposed actuation system is the fact that the system can function in a semi-active mode in the form of a damping system and can be used to augment the stability of the rotor blade. Figure 1.4(a) shows the schematic of operation of the proposed actuation system in an active mode where the system provides the necessary forces at the required frequency for primary and secondary control of the helicopter. In this mode, the hybrid hydraulic pump is producing a flow rate and the MR valves are regulating the direction of flow into the output cylinder in order to produce the necessary actuation. Figure 1.4(b) shows the case where the hybrid pump is switched off and is not producing a net flow rate and thus is , effectively, cut off from the rest of the system. In this case, the network of MR valve can act as a semi-active damping system that can be used for stability augmentation through the control signal that is given to the four valves.

The prototype of the proposed actuation system can be seen in Figure 1.5. The proposed system encompasses two main research areas - hybrid hydraulic actuation and MR fluids. A considerable amount of work has gone into the these two broad areas of research. A review of the state-of-the-art is given in the following sections.

1.3 Literature Review

1.3.1 Hybrid Hydraulic Actuation

One of the first reported hybrid hydraulic actuator was the piezoelectric stack based actuator developed by Konishi *et al*. (1993b), which was a piezoelectric stack based actuator capable of a power output of 34W and had a peak pumping frequency of around 300Hz. A magnetostrictive stack based hybrid pump was developed by Gerver *et al*. (1998) that employed hydraulic stroke amplification techniques and showed a power output of less than 1 W for a consumed power of around 25-30 W. Mauck and Lynch (2000) developed a piezoelectric stack based device that had an output power of around 4W and a blocked force of 271N (61lbs). However, it operated at relatively low pumping frequencies of less than 100Hz and performed frequency rectification using passive valves. Nasser and Leo (2000; 2000) developed a piezo based actuator which was capable of an output power of 4.5W and operated at slightly higher pumping frequencies of around 200Hz. This design has since been improved upon by the addition of active valves for rectification (Tan et al., 2005). A compact hybrid hydraulic actuation device was developed by Sirohi and Chopra (2003; 2004) that can be driven by piezoelectric, magnetostrictive or electrostrictive stacks. This device has an output power of 2.5W, a blocked force of around 138N (31lbs) and operates at relatively high pumping frequencies of around 600-700Hz. This device along with solenoid valves can be seen in Figure 1.6. The design was further improved and modified for a dedicated magnetostrictive actuator (Chaudhuri et al., 2006b). When tested with a 0.5" thick Terfenol-D rod, this device showed a no-load velocity of 89mm/s (3.5in/s), blocked force of approximately 178N (40lbs) and a peak power output of 3.6W. Greg Carmen *et al*. (2004) developed a piezoelectric hydraulic pump with active unimorph disc valves for frequency rectification. They report an output flow rate of 3.4cc/s, a pump specific energy density of 12W/kg and a stall pressure of 8.3MPa. Ullmann developed a valve-less piezoelectric pump which uses appropriately shaped and directed nozzles to rectify the flow. Since there are no reed valves in this actuator, there is no power-off stiffness. This actuator is in a much smaller scale than the other actuators presented above and has flow rate of 0.2cc/s and a pressure of around 13psi (90kPa). There have been hybrid hydraulic actuator development among commercial establishments also. A high pressure magnetostrictive pump was developed by Bridger *et al.*(2004b) that achieved an operating pressure of 3000psi (20.7MPa) and 60% electro-mechanical coupling. CSA Engineering have reported the development of a piezoelectric hydraulic actuator with a power output of more than 100W (Sneed et al., 2006). Over the years, there have also been several patents dealing with hybrid hydraulic actuation (Beckman and Blickstein, 1984, 1985; Culp and Nuys, 1993; Sager and Matice, 1998; Ogawa et al., 1999; Bishop et al., 2000; Bridger et al., 2004a). A table showing the major hybrid actuator developments are shown in Table 1.1. In this table, the performance of the different actuators have been converted into output flow rate, blocking force, frequency bandwidth of operation and output power.

1.3.2 Actuator Modeling

Modeling of hybrid hydraulic actuators have been attempted using several techniques. One of the earliest models was the quasi-static model developed by Mauck and Lynch (2001). The active material was modeled as a linear material with a blocked force and free displacement. Since the model did not account for fluid compressibility or inertia, it was able to model the behavior only at very low frequencies. Zhang and Cadou (2003) also developed a quasi-static model that accounted for fluid compressibility in the pumping chamber. This model accounted for the pressure drop associated with impulsively accelerating the fluid in the fluid lines of the system. The model was compared with experimental data and showed good correlating at low frequencies, but under-predicted the resonant frequency of the hydraulic system. Nasser *et al*. (2000) developed a lumped parameter model that used the force-voltage analogy to derive the fluid elements of resistance, capacitance and inductance. A lumped parameter model was also developed by Oates and Lynch (2002) using mechanical analogies. A frequency domain model based on the assumption of lossless fluid lines within the system was developed by Sirohi and Chopra (2003). This model captured the performance of the actuator at high pumping frequencies. Since the model did not account for all the losses within the system, the prediction of the resonant frequency was not accurate. Regelbrugge *et al*. (2003) used the method of direct integration of time domain equations of the system that were derived from the principle of mass conservation. A comprehensive model was developed by Chaudhuri *et al*. (2006b) that accounted for the minor and major losses within the pumping chamber and the fluid lines. This model also takes into account the inertial losses in the fluid as the pump is operated at high pumping frequencies. This model analyzes the performance of the actuator over the entire frequency range more accurately than prior models.

All of these approaches treat the flow in an essentially one dimensional manner in which pressure losses through the discharge and inlet ports of the pumping chamber are related to the volume flow rate using a loss coefficient. These coefficients are usually derived from standard fluid handbooks but Oates and Lynch (2001) used the results of axi-symmetric CFD analyzes to estimate the loss coefficient in their device. While computational fluid dynamics (CFD) has been used as a tool to design fluidic components like pumps (Hamkins and Bross, 2002; Goto et al., 2002), valves (Kiris et al., 1997; Fiore et al., 2002), and diffusers (Sano et al., 2002; Goto and Zangeneh, 2002), the role that CFD can play in design is limited by the large costs of developing computer codes, running them until they converge, and subsequently extracting the relevant performance parameters from the large multi-dimensional data sets. As a result, CFD cannot be used effectively to explore large parameter spaces in design. On the other hand, the extremely high level of detail makes it an excellent tool for understanding and improving the performance of existing designs where the parameter space is much more restricted.

Since the hybrid hydraulic configuration explored in this research involves fluid flow through a discharge tube, insights can be drawn from work that has been done on fluid flow undergoing rapid expansions and constrictions. A considerable amount of work has been devoted to experimentation, modeling and predicting fluid flow through an orifice (Smith et al., 2005; Thurston et al., 1957; Thurston and Martin, 1953; Washio et al., 1982b,a). These efforts show that the relationship between pressure and volume flow rate is highly non-linear. They also show that the inertia of the fluid and the nonlinear relationship between pressure and volume flow rate becomes important when the pumping frequency is greater than 100Hz and the driving pressure gradient becomes unsteady. The impact of orifice parameters like diameter and length also have been explored (Thurston and Martin, 1953). These studies offer valuable insights into the frequency content of pressure signals in flows that encounter rapid contractions or expansions and the formation of vortices in the pumping chamber due to the oscillatory fluid flow in the pumping chamber.

The performance of hybrid hydraulic actuation systems depends on several factors like pump head design, hydraulic circuit dynamics and electric drive circuit design. The properties of the active driving material are also highly critical to the performance of a hybrid hydraulic actuator. Therefore, investigation into the impact of different active material stacks on the performance of hybrid hydraulic actuator systems becomes important. There have been several studies that compared the bulk material properties - mechanical and electrical - of different active materials (Pan et al., 2000; Zhao and Zhang, 1996; Pomirleanu and Giurgiutiu, 2004). Studies into a comprehensive comparison of these active materials from an application point of view have been few (Janocha et al., 1994; Ellison, 2004; Damjanovic and Newnham, 1992). A direct comparison between the different active materials (piezoelectric, electrostrictive and magnetostrictive) was conducted by John *et al.*(2007). The active material stacks used in this study were of the same length and all the stacks were tested using the same actuator. Thus, all the geometrical parameters of the active material and the actuator was held constant. Since most aerospace applications impose geometric constraints on the proposed actuator, this allowed for a direct comparison between the active materials. This study is given in Appendix A.

1.3.3 MR Fluids and Rheological Models

Magnetorheological (MR) fluids are suspensions of ferromagnetic particles in a carrier fluid. Upon the application of an external magnetic field, the ferromagnetic particles form chains among themselves due to the induced magnetization in these particles. The force of attraction between the particles in the chains manifests as a resistance to shear deformation and consequently, fluid flow. In an idealized MR fluid, the fluid does not start flowing till a particular value of shear stress, called the yield stress, has been reached. Thus, the viscosity of these fluids can be changed using an external magnetic field. This unique property of MR fluids has been used in various commercial applications. MR fluids have been used in optical polishing (Kordonski and Golini, 1999), fluid clutches (Lee et al., 2000; Takesue et al., 2001), vibration isolation systems and a variety of aerospace (Kamath et al., 1999; Marathe et al., 1998), civil (Sodeyama et al., 2001; Ribakov and Gluck, 2002) and automotive (Lam and Liao, 2003; Lindler et al., 2003) damping applications The important rheological characteristics of an MR fluid are its yield force, viscosity and settling rate (Kordonski et al., 1998; Phule and Ginder, 1998; Rosenfeld et al., 2002). The yield force and viscosity of an MR fluid can be continuously varied using appropriate magnetic fields. Using this property, control schemes can be implemented in devices using MR fluids.

The rheological behavior of MR fluids is typically treated as Bingham plastic in steady fully developed flow (Stanway et al., 1996; Wereley and Pang, 1998). For a Bingham plastic fluid, no shearing motion occurs in the pre-yield condition where the applied shear stress is less than the yield stress of the dynamic fluid. In the post-yield region, where the applied shear stress exceeds the dynamic yield stress, shearing motion, or flow, can occur. Dynamic viscosity is the ratio of the shear stress to the shear rate. A Bingham plastic fluid models the MR fluid as having infinite viscosity in the pre-yield region and a constant viscosity in the post yield region. The Bingham plastic model has been extensively used to describe MR due to its simplicity (Stanway et al., 1996; Wereley and Pang, 1998; Gavin et al., 1996a; Peel and Bullough, 1996; Hong et al., 2005a). In the case of a real MR fluid, a small amount of fluid flow occurs in the pre-yield region. Thus, the pre-yield viscosity is not infinite, but is several orders higher than the post-yield value. The yield stress is then defined as the high shear rate asymptote of the flow curve.

The Bingham plastic model is not sufficient for many applications involving MR fluids. To mitigate the drawbacks of the Bingham plastic model, a bi-viscous model was developed (Stanway et al., 1996; Williams et al., 1993; Wereley et al., 2004). In this model, there there is a high viscosity pre-yield behavior over a low shear rate range below the yield stress. This model also does not predict a smooth transition from pre-yield to post-yield behavior, as is practically observed. Lionel *et al* (2005) developed an Eyring-Plastic model to incorporate a smooth transition between the pre-yield and post-yield behavior, thus improving upon the Bingham plastic and bi-viscous models. In this model, an arc hyperbolic sine function is used to model both the pre-yield and post-yield region. However, both bi-viscous and Eyring models, are inadequate in describing pre-yield stiffness effects and the force-velocity hysteresis behavior of MR fluids. Typically, MR fluids also exhibit shear thickening or shear thinning effects at high shear rates. None of the above described models account for the changing viscosity in the post-yield region. Herschel-Bulkley model (Wolf-Jesse and Fees, 1998; Wang and Gordaninejad, 2000; Lee and Wereley, 2000; Wereley, 2003) assumes a power law behavior between shear rate and shear stress for values of shear stress above the yield stress, that is, variable viscosity in the post-yield region. This will account for post-yield shear thinning or shear thickening behavior. However, the Herschel-Bulkley model does not account for pre-yield viscosity captured by the earlier described models. Comprehensive models have been developed that take into account the pre-yield viscosity and the post-yield shear thickening or thinning effects (Hong et al., 2005b). The three main rheological models can be seen in Figure 1.7

In dynamic operation, MR fluids demonstrate hysteresis behavior which enable them to be used in damping applications. Various phenomenological models have been developed to describe the hysteresis behavior of MR fluids. The hysteretic Bi-viscous model uses a combination of several piecewise continuous models (Wereley et al., 1999). The nonlinear hysteretic Bingham model is simple in form and was proposed to describe the low speed hysteresis characteristics of an MR fluid based isolator (Choi et al., 2005). Kamath and Wereley (Kamath et al., 1999; Kamath and Wereley, 1997) developed a nonlinear, piecewise smooth viscoelastic-plastic model using a nonlinear shape function.

In an ideal MR fluid (Bingham Plastic fluid), no flow can occur when the shear stress is less than the yield stress. Thus, if a high enough magnetic field is applied across a particular flow channel, the fluid flow can be completely prevented. This *blocking* property of MR fluids can be exploited to implement fluidic valves that have no moving mechanical parts and that can be controlled through an externally applied magnetic field. Valves using Electrorheological (ER) fluids (which are similar to MR fluids and are activated by an electric field instead of a magnetic field) have been research by Choi *et al*. (2000; 2002) and used for position control of a hydraulic cylinder and to implement control schemes like neural networks. However, in a real MR fluid, there is a leakage flow that occurs at all values of shear stress. Hence, in reality, the pre-yield viscosity of a real MR fluid is very high when compared to the viscosity in the post-yield region. MR valves have been used together with a piezoelectric stack driven pump for producing bi-directional motion in an output cylinder (Yoo et al., 2005). In both the above mentioned studies, a Wheatstone bridge network of four fluidic valves is used to control the motion of the output cylinder. In such a system, MR fluids are used as the working fluid and a Wheatstone bridge network of MR (or ER) valves enables bi-directional actuation of the output cylinder through activation of magnetic fields across the flow path of MR fluids. The need for such systems arise where there is a necessity to provide highly reliable, accurate and compact actuation systems in a constrained volume. Fluidic valves also have the advantage of not having any moving parts and thus being attractive to application with high centrifugal loading.

1.3.4 Prior research at the University of Maryland

Research into hybrid actuation systems was done at the University of Maryland under the Compact Hybrid Actuator Program (CHAP). Sirohi and Chopra (2002) developed the first generation piezoelectric stack driven pump that used passive reed valves to rectify the oscillatory motion of the stacks and achieved a maximum no load velocity of 28mm/s (1.1in/s) and a blocked force of around 133N (30lbs). This design used two piezoelectric stacks (PI804.10). The peak output power obtained was 0.9W at a pumping frequency of 300Hz. This design was improved upon to develop the second generation hybrid hydraulic pump that could be driven by a magnetostrictive (Ellison, 2004), electrostrictive (John et al., 2007) or piezoelectric stack (Sirohi and Chopra, 2003). This design was more compact and was sized to fit inside a rotor blade of a UH-60 helicopter. The first and second generation pumps had similar pumping chamber dimensions (1" chamber diameter and 0.030" chamber height). Experience gained from these designs was used to design a magnetostrictive pump (Chaudhuri et al., 2006a) that can be driven by a Terfenol-D or Galfenol stack. This pump has a pumping chamber diameter of 2" and chamber height of 0.03" and was used in the studies reported in Chapters 4 and 5.

An MR valving system was developed by Yoo and Wereley (2005). The performance of the MR valve system was analyzed analytically using a quasi-steady method (Yoo and Wereley, 2004) and measured experimentally using a gear pump as the pressure source (Yoo et al., 2004). A Wheatstone bridge network of MR valves was coupled with the second generation piezoelectric pump and uni-directional motion of the output cylinder was demonstrated (Yoo et al., 2005).

1.4 Objectives of the present research

As mentioned earlier, preliminary studies into a hybrid hydraulic actuation system were done at the University of Maryland in which a hybrid pump was coupled with a network of MR fluid based valves. However, only uni-directional motion of this actuation system was performed. This study advances the state-of-the-art of this actuation system. There are three main objectives of this present research.

1. Identify the major sources of pressure loss within the pumping chamber of a hybrid hydraulic actuator and the issues the come into prominence during high frequency operation. Also, what are the major design parameters that affect the fluid pressure loss in a pumping chamber.

2. To evaluate the performance of a self-contained bi-directional hybrid actuator and to model its performance using an analytical model.

3. To ascertain the effectiveness of the hybrid actuator under centrifugal loading.

This work also lists two ancillary studies that were done towards obtaining a better understanding of the working of the actuation system. The questions tackled in these ancillary studies were:

- Evaluate the effect of different active materials like magnetostrictives, piezoelectrics and electrostrictives on the performance of a hybrid hydraulic actuator.

- Construction of a comprehensive rheological model for MR fluids that takes into account pre-yield viscosity and post-yield shear thinning or shear thickening. The model is a modification of the conventional Herschel Bulkley model to include a pre-yield viscosity.

1.5 Outline of the dissertation

The dissertation is organized as seven chapters. Chapters 2 and 3 deal with modeling of the fluid in the pumping chamber of a hybrid actuator. Chapters 4 and 5 deal with the bi-directional MR fluid based actuator and its modeling. Chapter 7 lists the results of spin testing of a piezoelectric hydraulic actuator in the uni-directional mode. Chapter 8 sums up the major contributions of this work. A brief description of the chapter is given below:

1. **Chapter 1: Introduction.** A brief introduction is given to the swashplateless concept in rotorcraft. The issues associated with the swashplateless concept and the commonly proposed alternatives have been presented. This chapter motivates the exploration of the hybrid hydraulic actuation concept for an active pitch link application. A detailed survey of the state-of-the-art of hybrid hydraulic actuation, actuator modeling and MR fluids is presented. The stated goals of this dissertation is also outlined.

2. **Chapter 2: Application of CFD in the Design and Analysis of a Hybrid Hydraulic Actuators.** This chapter discusses the use of CFD as a tool to understand the fluid behavior in the pumping chamber of a hybrid actuator. An analytical 3D model for fluid flow in a pumping chamber and discharge tube is derived for the case of steady flow. A comparison is made between 3D and 2D models to justify the time-consuming and complex 3D calculations necessary to adequately model a hybrid actuator. The model is verified using the CFD results. On the basis of information derived from CFD simulations, loss coefficients which describe the pressure loss in the pumping chamber are derived.

   CFD is also used to perform parametric studies into three main design variables in a pumping chamber design - pumping chamber height, location of ports and port chamfer. Vortices that form in the pumping chamber as a result of high accelerations experienced by the flow is identified as a major contributor to the pressure loss.

3. **Chapter 3: Unsteady Fluid Flow in Hybrid Hydraulic Actuators.** This chapter discusses the use of CFD to analyze the fluid dynamics involved with high frequency operation of a hybrid actuator. An analytical 3D model for pressure loss in a pumping chamber is derived for the case of oscillatory flow. This chapter discusses the various modes of pressure loss that occurs in the pumping chamber of a hybrid pump during high frequency operation. This is very important since hybrid hydraulic actuators are usually operated at

high pumping frequencies to utilize the high energy density of active material stacks that drive them. Parallels are drawn between flow in the pumping chamber and classical research into oscillatory flow through an orifice. The analytical 3D model is expanded into the frequency domain to highlight the rich frequency domain behavior of flow during the dynamic operation. The model is verified using CFD simulations. The 3D model is also extended to account for vortex behavior during dynamic operation.

4. **Chapter 4: A Hybrid Hydraulic Actuation System - Development and Testing.** The magnetorheological fluid based hybrid actuation system is discussed. A hybrid pump driven by Terfenol-D serves as the pressure source. Fluidic valves that exploit the blocking properties of MR fluids are used for bi-directional motion of the output cylinder shaft. Thus, the fluidic valves can be controlled by an appropriate current provided to the magnetizing coils. A wide range of experimental data is presented. Uni-directional testing establishes the maximum no load velocity, block force, power output and electromechanical efficiency of the actuation system. Bi-directional no-load testing establishes the frequency bandwidth of the system. Bi-directional tests were also conduced under both inertial and stiffness load to demonstrate the performance of the actuator in a real-life application.

5. **Chapter 5: A Hybrid Hydraulic Actuation System - Actuator Modeling.** A model that describes the operation of a hybrid hydraulic MR fluid based bidirectional actuator is presented in this chapter. The results are compared to the experimental data presented in the earlier chapter. Insight derived through the CFD models presented in chapters 2 and 3 have also been used in this model. The model is used to predict the uni-directional and bi-directional performance of the actuator.

6. **Chapter 6: Spin Testing of a Hybrid Hydraulic Actuator.** The goal of this chapter is to evaluate the performance of a hybrid hydraulic actuator in a rotating environment. A piezoelectric stack driven actuator was operated

in uni-directional mode in a rotating frame. Issues that hamper the performance were identified and the necessary design changes were made. Further testing of the improved design proved that the present design of the hybrid hydraulic actuator is able to withstand the centrifugal forces experienced by a full scale UH-60 helicopter pitch link. Also, the performance of the actuator was evaluated for the case when the actuator works against a stiffness load.

7. **Chapter 7: Conclusions and Future Work** This chapter lists the discusses major contributions in this work and highlights a few suggestions for future work in hybrid hydraulic actuation systems.

Table 1.1: State of the art in hybrid hydraulic actuator

Device	$Q_{out}(cc/s)$	$F_{block}(N)$	$BW(Hz)$	$P_{out}(W)$
Piezoelectric				
Konishi *et al.* (1997)	-	-	<300	34
Mauck *et al.* (2000)	-	271	<100	4
Nasser *et al.* (2000)	-	-	<200	4.5
Carmen *et al.* (2004)	3.4	-	-	-
Sirohi *et al.*(2003)	15.04	53	<700	2
Magnetostrictive				
Gerver *et al.* (1998)	-	-	-	1
CSA *et al.* (2006)	7.57	-	-	100
Chaudhuri *et al.* (2006b)	22.5	178	<300	3.6
Electrostrictive				
John *et al.* (2007)	21.37	57.8	<500	2.5

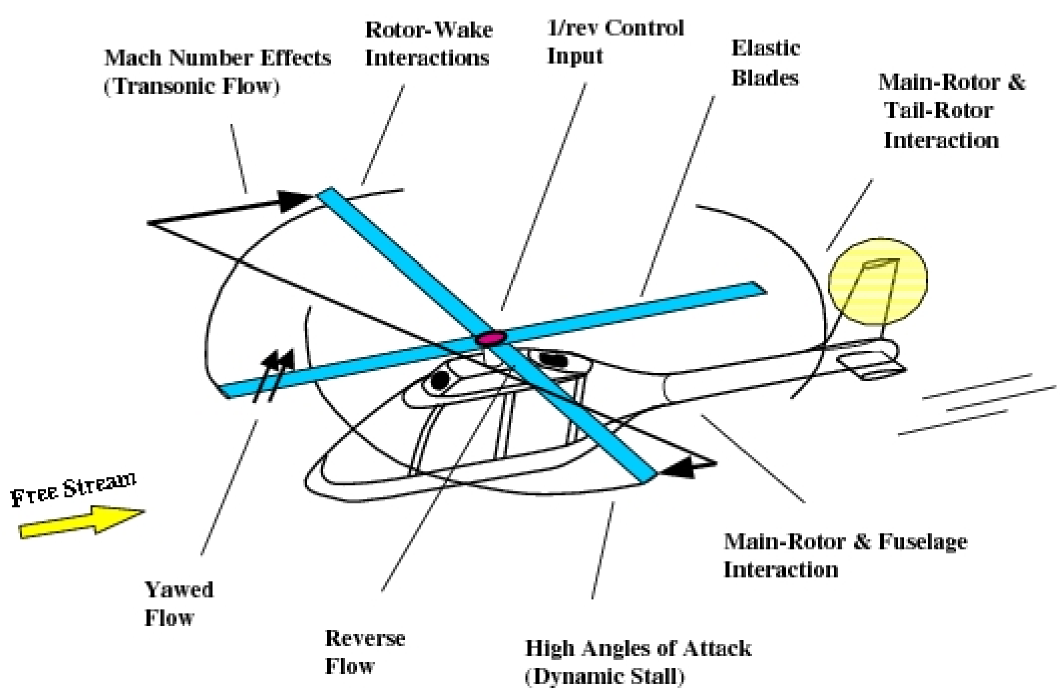

Figure 1.1: Sources of helicopter vibration

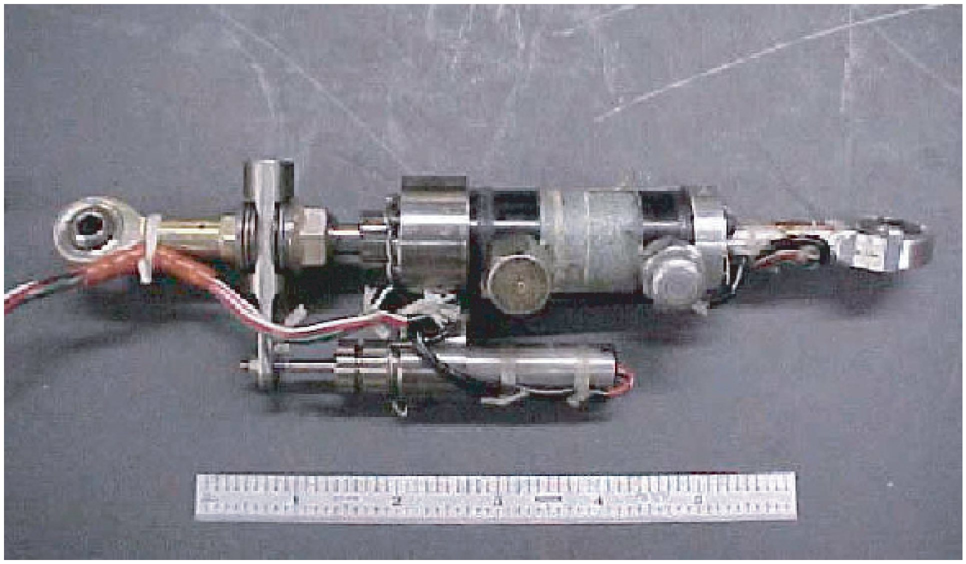

Figure 1.2: A hydraulic pitch link used for IBC application (Lorber et al., 2001)

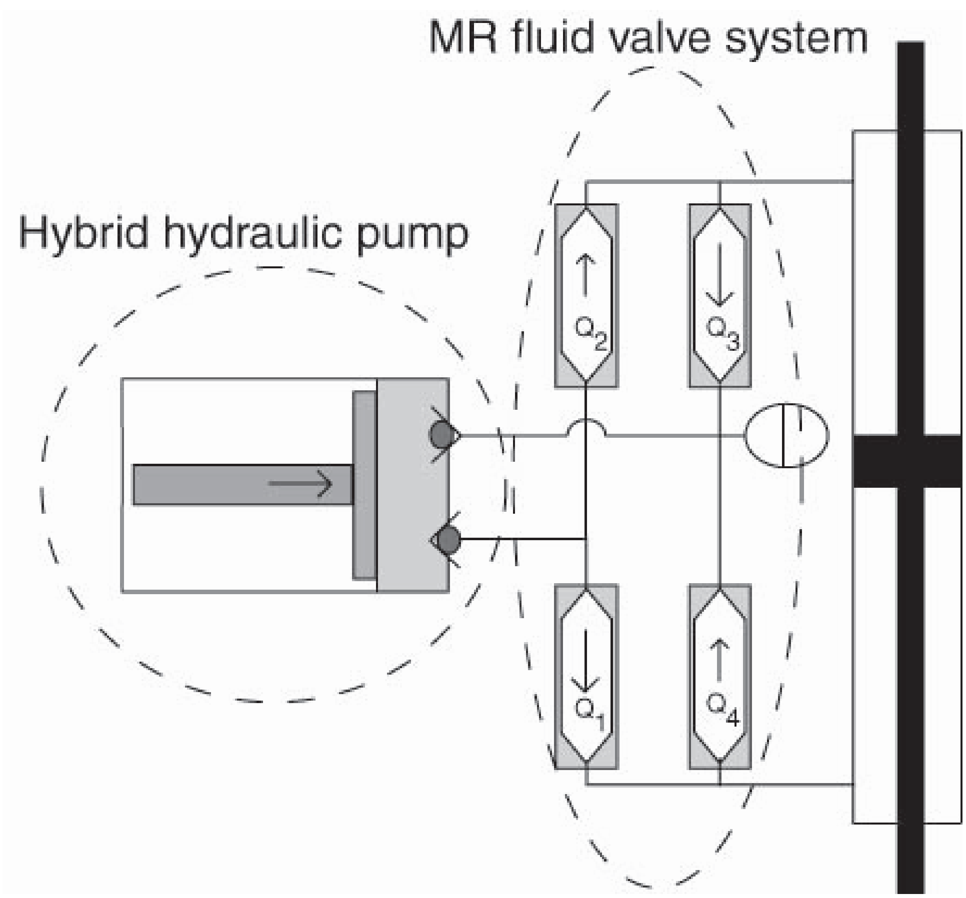

Figure 1.3: Schematic of the proposed hybrid hydraulic actuation system

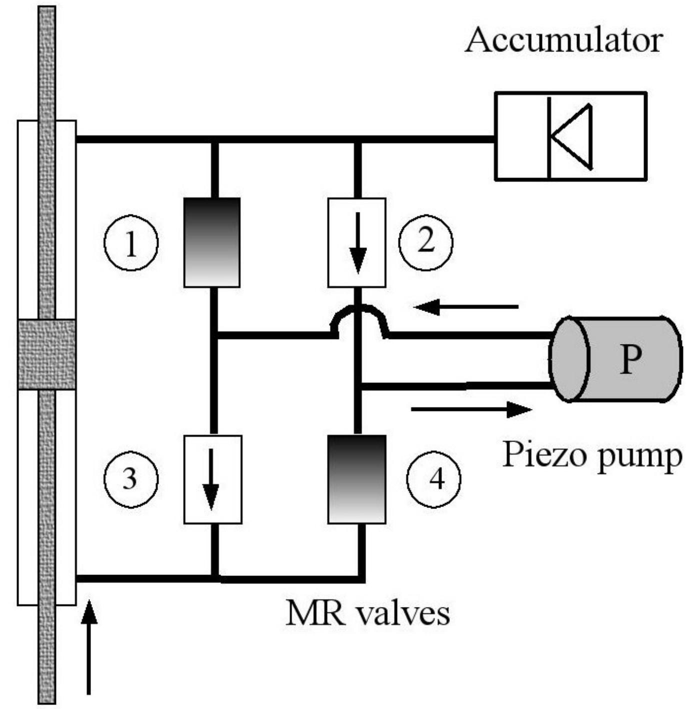

(a) Active mode

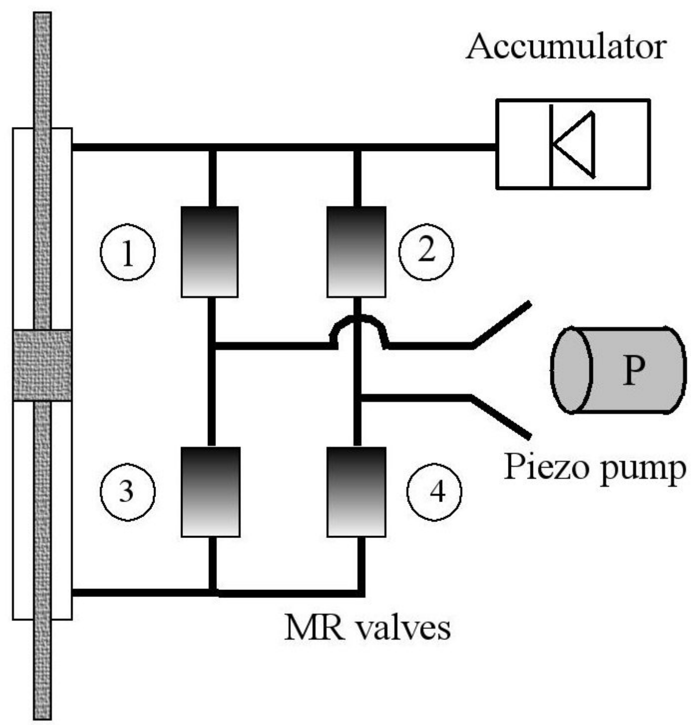

(b) Semi-active mode

Figure 1.4: Two modes of operation of the proposed actuation system

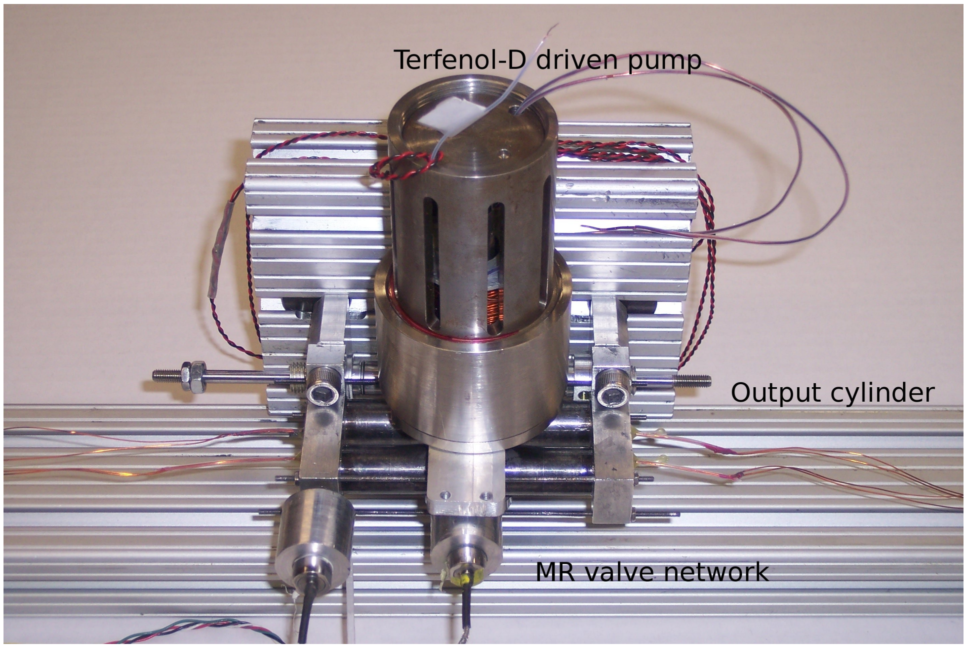

Figure 1.5: Picture of the proposed hybrid hydraulic actuator with MR fluid based valves

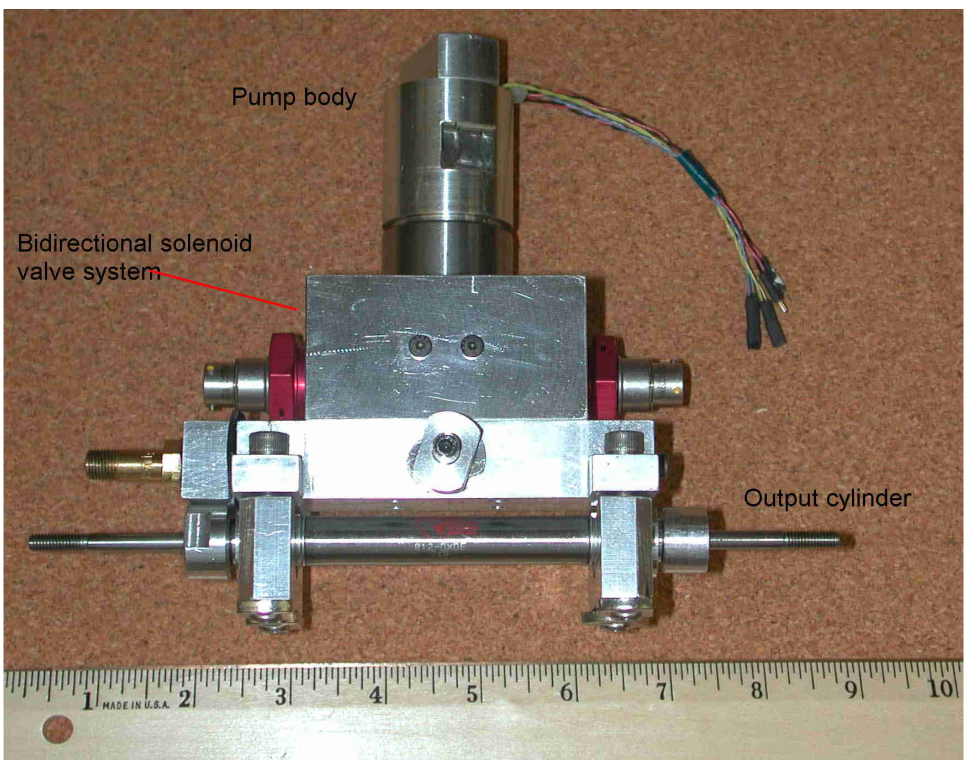

Figure 1.6: Picture of a hybrid hydraulic actuator with solenoid valves

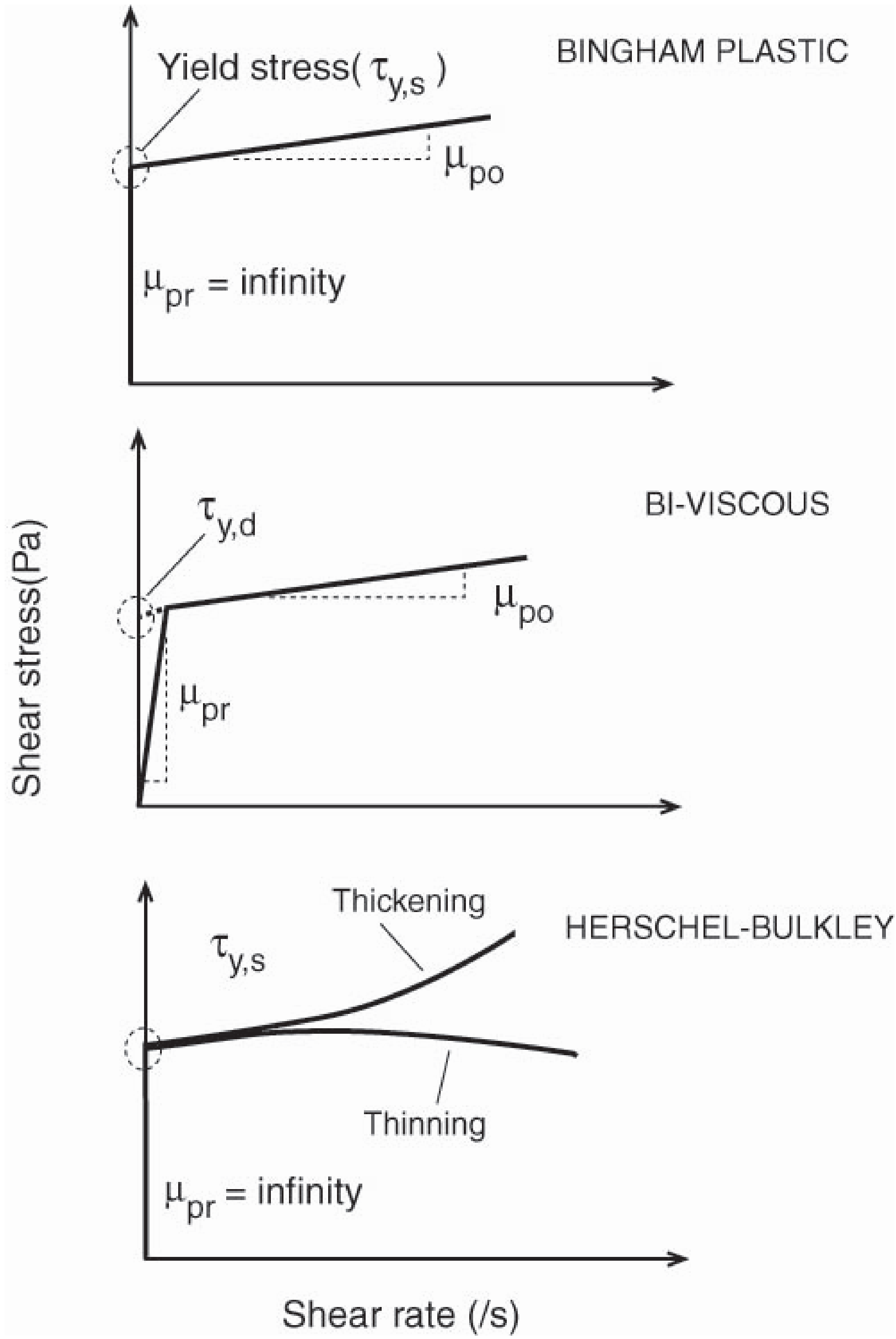

Figure 1.7: Flow curves of the three rheological models typically used to describe the behavior of MR fluids

Chapter 2

Application of CFD in the Design and Analysis of Hybrid Hydraulic Actuators

The maturity of hybrid actuator technologies depends on an accurate understanding of the underlying fundamental issues. One of the fundamental issues that directly affects the performance of the hybrid hydraulic actuator is the fluid dynamics of the hydraulic fluid used. Much research has undertaken the development of a comprehensive model of the actuation system in order to better understand these issues and their impact on actuator performance. Such a comprehensive model has to take into account the complex fluid dynamic phenomenon that occurs in the hydraulic circuit during high frequency pumping operation of the actuator. Computational fluid dynamics (CFD) has been used to design devices like pumps, valves, and diffusers. However, the importance of CFD as a design tool is limited by the large costs of developing computer codes, ensuring that the codes converge, and subsequently extracting the relevant performance parameters from the large multi-dimensional data sets that are generated by the calculations. As a result, CFD can be used to explore large parameter spaces in design only at great cost. On the other hand, the extremely high level of detail in computational results makes CFD an excellent tool for understanding and improving the performance of existing designs where the design parameter space is constrained.

As mentioned earlier, the existing state-of-the-art has used CFD to analyze pumping chamber fluid dynamic issues to a very limited extent. These previous analyses dealt with steady flows and the computational domain was approximated as two dimensional (2D) and axisymmetric. This study advances the state-of-the-art into a three dimensional (3D) CFD analysis and examines geometries that are not axisymmetric. A detailed 3D CFD analysis with fluid structure coupling (arising from the stress boundary condition between the fluid in the pumping chamber and the active material) will be shown in a subsequent chapter.

A schematic of the pump design is shown in Figure 2.1. The pump consists of a piston driven by a piezo-stack that is used to pressurize fluid in a round chamber of diameter d_p and height h. Fluid enters and exits the pumping chamber through intake and discharge tubes of diameter d_o that are located eccentrically at a distance R from the axis of symmetry of the pumping chamber. A set of fast acting, out-of-phase valves ensures that the fluid motion is uni-directional in each tube so that the oscillatory motion of the piston alternately draws fluid into the pumping chamber through the intake tube and discharges it through the discharge tube. The quasi-static performance of this system has been explained and modeled in previous work (Cadou and Zhang, 2003). The dimensions of the pump are presented in Table 2.1 and the properties of the working fluid are summarized in Table 2.2.

The present work is primarily concerned with understanding the unsteady fluid dynamic processes occurring in the pumping chamber itself and the force coupling between the piezo and the fluid element. Therefore, to ensure computational tractability, the fluid flow due to the unsteady behavior of the check valves is not included. As a result, the intake tube illustrated in Figure 2.1 is not included in the computational domain and the intake and discharge processes are simulated by allowing fluid to enter and leave the pumping chamber through a single intake/discharge port.

2.1 Preliminary Analysis

A preliminary analysis is performed to estimate how fluid losses would be expected to scale with operating frequency in this device and to provide some basic insight into the fluid environment that needs to be simulated. In particular, we are interested in determining whether or not the simulations need to include fluid compressibility, turbulence, fluid-elastic coupling of the fluid with the piezo element, and 3D effects.

The volume flow rate of the fluid exiting the pumping chamber is approximated as the product of the cross-sectional area of the pumping chamber, the free displacement of the piezo element δ_f, and the driving frequency f:

$$Q = \delta_f \frac{\pi D^2}{4} f \tag{2.1}$$

Three processes are expected to account for most of the forces experienced by the fluid (and, hence, the piezo stack) during pump operation: viscous shear across the piston face as the fluid moves from the outer edges of the pumping chamber to the discharge tube, the acceleration of the fluid associated with the flow area change as it moves radially inward across the piston face, and viscous shear in the discharge tube.

The pressure loss in the discharge tube is given by:

$$\Delta P_{tube} = 128 \frac{\mu l}{\pi d_o^4} Q \tag{2.2}$$

assuming fully developed pipe flow(Fox and McDonald, 1992). In this expression, d_o is the diameter of the discharge tube/orifice, l is the length of the discharge tube and μ is the viscosity of the fluid. Estimates of the pressure change across the piston face depend on whether a 2D or 3D approach is used. In 3D, mass conservation for steady incompressible flow in a cylindrical coordinate system is given by

$$\frac{1}{r}\frac{\partial}{\partial r}(r u_r) + \frac{1}{r}\frac{\partial u_\theta}{\partial \theta} + \frac{\partial u_z}{\partial z} \quad = \quad 0 \tag{2.3}$$

where, u_r, u_θ and u_z are the components of velocity in the pumping chamber in the r, θ and z directions respectively. Neglecting the axial($i.e$ non-radial) term gives

$$\frac{u_r}{r} + \frac{\partial u_r}{\partial r} \quad = \quad 0 \tag{2.4}$$

The expression for momentum conservation in the radial direction for steady, incompressible flow can be written as

$$(u \cdot \nabla) u_r - \frac{u_\theta}{r} = -\frac{1}{\rho}\frac{\partial p}{\partial r} + \nu \left(\nabla^2 u_r - \frac{u_r}{r^2} - \frac{2}{r^2}\frac{u_\theta}{\partial \theta} \right) \tag{2.5}$$

Neglecting non-radial terms and derivatives gives

$$\rho u_r \frac{\partial u_r}{\partial r} \quad = \quad -\frac{\partial p}{\partial r} + \mu \frac{\partial^2 u_r}{\partial z^2} \tag{2.6}$$

Assuming that the steady radial flow has a parabolic velocity profile in the axial(z) direction, the form of the radial velocity that satisfies mass conservation is

$$u_r = \frac{C_1 z (h - z)}{r} \tag{2.7}$$

Substituting equation 2.7 into equation 2.6 and denoting the average flow rate across the pumping chamber height (represented by the z coordinate) as Q gives the following expression for the radial pressure gradient in the pumping chamber:

$$\frac{\partial p}{\partial r} = \frac{9\rho Q^2}{\pi^2 h^6 r^3} z^2 (h - z)^2 - \frac{6Q\mu}{\pi h^3 r} \tag{2.8}$$

Integrating equation 2.8 gives the following expression for the pressure differential required to drive the fluid flow across the piston face:

$$p_2 - p_1 = \frac{6\mu Q}{\pi h^3} ln \left(\frac{d_1}{d_2}\right) + \frac{\rho}{60} \left(\frac{6Q}{\pi h d_1}\right)^2 \left[\left(\frac{d_1}{d_2}\right)^2 - 1\right] \tag{2.9}$$

In equation 2.9, $Q > 0$ represents discharge (radial flow from d_p to d_o), the first term represents the pressure loss due to viscous effects, and the second term represents the pressure loss due to fluid acceleration associated with the change in flow area as one moves radially inward along the piston face.

A similar analysis of the same flow condition in 2D (where the radial area change is neglected and the flow passage is assumed to be a rectangular channel) gives the well known expression for Poiseuille flow.

$$\Delta P_{chamber,2D} = \frac{3\mu l}{2h^3} q \tag{2.10}$$

In this expression, q is the volume flow rate per unit depth which can be written as

$$q = \frac{Q}{\frac{1}{2}\pi (d_p + d_o)} \tag{2.11}$$

Substituting Equation 2.11 into 2.10 and noting that $l = d_p - d_o$ gives:

$$P_2 - P_1 - = \frac{3\mu Q}{\pi h^3} \left(\frac{d_p - d_o}{d_p + d_o}\right) \tag{2.12}$$

In summary, the expressions for pressure loss in the pumping chamber for discharge in the 2D and 3D cases are

$$\Delta P_{chamb,2D} = \frac{3\mu Q}{\pi h^3}\left(\frac{d_p - d_o}{d_p + d_o}\right) \tag{2.13}$$

$$\Delta P_{chamb,3D} = \frac{6\mu Q}{\pi h^3} ln\left(\frac{d_p}{d_o}\right) + \frac{\rho}{60}\left(\frac{6Q}{\pi h d_p}\right)^2\left[\left(\frac{d_p}{d_o}\right)^2 - 1\right] \tag{2.14}$$

In these expressions, d_p is the diameter of the pumping chamber, h is the pumping chamber height and ρ is the fluid density. In the 2D case, viscous shear is the only contributor to the pressure loss, whereas, in the 3D case, an additional inertial term arises that is associated with the change in flow cross-sectional area with radial position

While both equations 2.13 and 2.14 have been derived assuming steady, fully developed flows - conditions that certainly will not hold in the real device - they can be used to provide zeroth order estimates for how pressure losses in the hybrid actuator scale with the operating frequency of the prototype actuator specified in Tables 2.1 and 2.2. The results are presented in Figure 2.2 where the pressure loss is non-dimensionalized by the maximum pressure that the stack is able to generate ($F_{blocked}/A_{piston}$). Figure 2.2 shows that pressure losses associated with 3D effects are substantially greater than those associated with 2D ones and become even larger at high frequencies. The change in the slope of the 3D curve marks the point where inertial effects associated with the area change in the pumping chamber (and which scale with f^2) become stronger than viscous ones. This occurs at frequencies around 100 Hz. At low frequencies, the difference between the 2D and 3D representations results from differences between the viscous terms. At high frequencies, the difference between the 2D and 3D representations arises because the 2D model does not include the effects of the flow area change across the piston face. This shortcoming can be corrected by adding the following additional term to Equation (2.13) to account for 3D effects in the pumping chamber.

$$\Delta P_{chamber,correction} = \frac{\rho}{2}\left(\frac{Q}{\pi h d_p}\right)^2\left[\left(\frac{d_p}{d_o}\right)^2 - 1\right] \tag{2.15}$$

This gives the light dashed curve in Figure 2.2. The fact that it merges with the 3D curve at high frequencies indicates that this correction term captures the relevant aspects of the physics. The figure also shows that the pressure forces approach the blocked force of the piezo stack in the operating range of interest and can exceed the blocked force at frequencies greater than about 2 kHz. Based on the results of this simple modeling, we conclude that any realistic simulation of the performance of the pump must include 3D fluid effects and fluid-elastic coupling between the piezo stack and the fluid.

While it is has just been shown that a relatively complex 3D calculation with fluid-elastic coupling will be required, there are also some simplifying factors: First, mechanical resonances associated with the piezo stack and the fluid in the pumping chamber and the discharge tube will probably not be issues as their characteristic frequencies (indicated by the markers on the horizontal axis of Figure 2.2) are greater than the piezoelectric excitation or pumping frequency. Second, acoustic and turbulent effects do not need to be included as plots of Reynolds number and Mach number as a function of frequency (Figure 2.3) show that Mach numbers are less than 0.3 and Reynolds numbers are less than 2500 in the frequency range of interest. The equations used to calculate Reynolds and Mach numbers are given below.

$$Re = \frac{\rho U l_{char}}{\mu} \tag{2.16}$$

$$M = \frac{U}{a} \tag{2.17}$$

In these equations, ρ is the fluid density, U is the fluid velocity, l_{char} is the characteristic length, μ is the dynamic viscosity of the fluid and a is the velocity of sound in the fluid.

2.2 Approach

Since the only unusual complicating factor in the problem is the fluid-elastic coupling between the fluid and the piezo stack, we decided to address the problem using CFD-ACE, a commercial Navier-Stokes solver with multi-physics capabilities produced by ESI-CFD(Bachtold, 1997; Newmark, 1959). The software solves the viscous, incompressible, steady Navier-Stokes equations(Munson et al., 1990), given by equations 2.3 and 2.5, on a grid using a finite-volume discretization. Body forces on the fluid are neglected. Various interpolation schemes with various levels of numerical accuracy and stability are available. This work uses a first-order upwind scheme for the velocity while the velocity and stress fields are determined using a Conjugate Gradient Squared (CGS) method with preconditioning(Hirsch, 1990). The pressure field is determined using an Algebraic Multigrid solver (AMG). Suitable relaxation parameters are chosen to constrain the change in variables from iteration to iteration. This is necessary to ensure stability and convergence. The CFD model of the pump is created using CFD-GEOM, which is a comprehensive interactive geometry and grid generation system for CFD analysis. CFD-GEOM has a fully integrated NURBS geometry engine (Yu, Soni and Shih, 1995) with multi-block structured, multi-domain unstructured and multi-element hybrid grid system capability. The computational volume was discretized using a structured mesh of quadrilateral elements(Vinokur, 1983).

While the software is capable of solving the fully coupled unsteady 3D problem, such calculations are extremely time consuming and are impractical for optimizing pump design. As a result, a stepwise approach is taken in which more tractable steady 2D and 3D simulations are used to develop understanding of the flow and the effects of changing various design parameters. These results are reported here. Future work will investigate the fully coupled unsteady problem for a single pump geometry.

Figure 2.4 shows the computational domain used to perform the 2D calculations and illustrates two of the important design parameters: the pumping chamber height h and the discharge tube radial location R. The other important design parameter that is not illustrated in the figure is the discharge tube chamfer ratio, which is the radius of curvature of the chamfer divided by the discharge tube radius. The boundary conditions are a steady, uniform velocity field at the piston face (to simulate the motion of the piston) and zero pressure at the discharge tube outlet. While the pressure at the discharge tube will certainly not be zero in a *real* device, the choice of discharge pressure in these calculations is arbitrary because the flow is only influenced by the pressure difference. As a result, zero pressure at the discharge tube is chosen for convenience.

The CFD solutions are used in several ways. Vector plots of the velocity field and contour plots of the pressure field provide qualitative visualizations of the flow field and the driving pressure gradient field. Since the pressure at the pump exit is taken to be zero, the pressure difference is simply the average pressure at the grid points on the piston face. The volume flow rate is determined by integrating the velocity profile over the discharge tube outlet. Figure 2.5 shows the computational domain for the 3D calculations.

2.2.1 Grid Convergence and Stability Studies

In order to ensure that the solutions to the Navier-Stokes equations obtained by the CFD package are physically meaningful, it needs to be established that solutions are converged and that they do not depend on either the number of grid points or the grid configuration. The convergence criteria recommended by ESI is to continue iteration until the residual has decreased by four orders of magnitude. In this work we are more conservative and continue iteration until the residual has decreased by at least six orders of magnitude. A grid convergence test was performed to establish the number of data points required to make the solutions grid-independent. Figure 2.6 indicates that 400,000 points provide adequate resolution. Another important consideration is the effect of the configuration of the grid itself. Calculations were performed using three different grids with 400,000 elements and the results were all the same. These results are shown in Figure 2.7 and the grids themselves are shown in Figure 2.8 (a), (b) and (c). As a result, we are confident that the solutions presented are converged and independent of the computational grid.

2.3 Results

2.3.1 Steady CFD

Figure 2.9 shows pressure drop as a function of piston velocity for different values of the pumping chamber height. Note that discharge corresponds to a rightward motion of the piston in Figure 2.1 while intake corresponds to leftward motion. The outer plot in Figure 2.9 (a) presents 3D results while the inset shows corresponding results in the 2D situation. Taken together, the figures show that pressure losses increase non-linearly with driving frequency and pumping chamber height, and are much greater in 3D than in 2D. These results are also consistent with the predictions of the simple model. Finally, the results show that the pressure losses associated with the 3D flow approach those associated with the blocked force of the piezo actuator ($\sim$59MPa) as the height of the pumping chamber decreases. This suggests that there will be a tradeoff between pressure loss and pumping effectiveness since previous work (Cadou and Zhang, 2003) has shown that a stiff fluid column (*i.e* small h) is required to get good pumping performance.

Figure 2.10 shows the effect of the radial location of the discharge tube on pressure losses through the pumping chamber. The outer plot in Figure 2.10(a) shows the 3D results while the inset shows the 2D results. $R = 0$ corresponds to a discharge tube centered on the axis of symmetry while $R = 8.89$ mm corresponds to a port centered 8.89 mm radially outward from the axis of symmetry. As before, the results show that the 2D model greatly under-predicts the pressure losses. Changes in pressure drop associated with moving the discharge tube radially outward are of similar magnitude in both the 2D and 3D cases. However, since the baseline pressure losses are so much larger in the 3D case, the discharge tube location has a relatively unimportant effect on the performance of the 3D device.

Figure 2.11 shows pressure loss as a function of inlet velocity for a range of discharge tube chamfers. The outer plot in Figure 2.11(a) shows the 3D results while the inset shows the 2D results. It is clear from the figure that chamfering the discharge tube can substantially reduce the pressure losses through the pumping chamber. The results also show that the effect of chamfer is more important in the 3D case.

The reasons for this latter observation, as well as the effects of the pumping chamber height and discharge tube location can be deduced from an examination of the velocity field in the pumping chamber. Figure 2.12 shows that during discharge a vortex ring (which appears as a vortex pair in the transverse slice presented in the figure) is formed at the edges of the entrance to the discharge tube as the flow turns 90 degrees to enter the discharge tube. The vortex ring is much larger and more asymmetric (*i.e.* distorted) when the pumping chamber height is small because the flow has less space to negotiate the turn. This large vortex impedes flow into the discharge tube and increases the pressure loss. This, in turn, explains why the pressure loss increases as the pumping chamber height decreases. Figure 2.13 shows the effect of pumping chamber height on these vortices. When the height is increased, the fluid has more space to negotiate the turn and so the discharge vortices are smaller and obstruct less of the flow. This also indicates that shifting the discharge tube outward will have a proportionally smaller impact on the pressure loss when the pumping chamber height is relatively large.

Figure 2.14 shows that centering the discharge tube on the axis of the pumping chamber removes the asymmetry in the vortex rings completely. However, the overall size of the vortex pair remains proportionally large because the pumping chamber height is still small compared to the discharge tube diameter. As a result, when $R = 0$, the overall pressure loss is not affected much by relocating the discharge tube. Figure 2.15 shows that chamfering the discharge tube entrance gives the flow more room to negotiate the 90 degree turn. This reduces the size of the trapped vortex, the flow blockage, and hence the pressure loss.

Figure 2.16 shows radial pressure profiles at three axial locations in the pumping chamber. In the figure, $x = 0$ corresponds to the piston face and $x = h$ corresponds to the pumping chamber wall. The computational domain is 2D and the inlet velocity is 20.32 mm/s. The pressure is minimum at the discharge tube because the fluid velocity is high as it leaves the pumping chamber. The radial pressure distribution is non-uniform because more pressure is required to move fluid from points in the chamber that are farther away from the discharge tube. The variation in pressure with axial location is negligible except in the immediate vicinity of the discharge tube entrance. The inset provides a magnified view of this region. The axial uniformity of the pressure field indicates that one ought to be able to reduce the resolution of the grid in the axial direction with little loss of simulation fidelity.

Figure 2.17 shows the corresponding radial pressure distribution in the 3D situation. While qualitatively similar to the 2D case, the pressure gradients are much steeper and there appear to be two pressure peaks as opposed to the single peak in the 2D case. As in the 2D case, the pressure profile also seems to be relatively insensitive to axial position indicating that it may be possible to reduce the resolution of the grid in places without loss of accuracy.

2.4 Loss Coefficients

While the results of the previous section are very useful for understanding the effects of design changes on pressure losses in the pumping chamber, they are too complex to be useful for developing models of entire hybrid actuator systems. What is required are relatively simple analytical expressions deduced from the CFD calculations that relate pressure loss in the pumping chamber to volume flow rate Q.

Equation (2.14) suggests that a simple analytical expression for the pressure loss should have the following functional form:

$$\Delta P = AQ + BQ^2 \tag{2.18}$$

The coefficients A and B are functions of d_o, d_p, h, l, and μ as follows:

$$A = \frac{6\mu}{\pi h^3} \ln\left(\frac{d_p}{d_o}\right) + 128\frac{\mu l}{\pi d_o^4} \tag{2.19}$$

$$B = \frac{\rho}{60}\left(\frac{6}{\pi h d_p}\right)^2 \left[\left(\frac{d_p}{d_o}\right)^2 - 1\right] \tag{2.20}$$

The results of the previous section demonstrate that a major source of pressure loss in the pumping chamber is the change in effective flow area caused by vortex rings that form in either the discharge tube or the pumping chamber. During discharge, a vortex ring forms in the entrance of the discharge tube that reduces the effective area of the tube. Similarly during intake, a vortex ring forms in the pumping chamber that reduces the effective height of the pumping chamber. This suggests that it may be possible to modify the simple analytical model to account for the flow area reductions that occur during discharge and intake. Therefore for discharge, the orifice diameter (d_o) in equations 2.19 and 2.20 is replaced by:

$$d_o = \left(\frac{k_{dis}}{k_{dis} + Q} \right) d_{o,nom} \tag{2.21}$$

This allows the effective diameter to range from its nominal value $d_{0,nom}$ at zero flow rate, to zero (*i.e.* complete blockage) at infinite Q. Applying similar reasoning for intake, the pumping chamber height (h) in Equations (2.19) and (2.20) is replaced by:

$$h = \left(\frac{k_{in}}{k_{in} + Q} \right) h_{nom} \tag{2.22}$$

This allows the effective pumping chamber height to range from its nominal value h_{nom} to zero (corresponding to complete blockage) at infinite Q.

Figure 2.18 shows the comparison of the normalized pressure between the CFD results and the modified analytical model developed above. The pressure is normalized by P_{block}, which is defined as the blocking force of the piezoelectric stack divided by the piston area. We can see from the figure that choosing $k_{dis} = 0.001$ and $k_{in} = 0.0005$ fits the CFD results for discharge and intake reasonably well. However, it should be noted that the logarithmic scale magnifies the apparent differences between intake and discharge at low frequencies while reducing them at high frequencies. The figure also shows that the relative importance of pressure losses during discharge vs. intake depends on the operating frequency. At frequencies below 100 Hz, the pressure losses associated with discharge and intake are virtually indistinguishable to the piezo stack. At frequencies above 100Hz, however, the pressure losses associated with intake become larger than those associated with discharge and force coupling with the piezo stack becomes more important during intake than during discharge. This effect coupled with cavitation effects (which have not been simulated here) may explain the abrupt reduction in mass flow that has been observed experimentally at frequencies above 400 Hz.

Finally, we check the initial assumption that the flow in the pump is laminar and incompressible. Figure 2.19 shows contours of Reynolds number based on the pumping chamber height at the maximum flow rate investigated here ($1.6 \times 10^{-4} m^3/s$) for a nominal pumping chamber configuration. The figure shows that the flow is laminar ($Re < 2400$) everywhere and that the omission of a turbulence model in the simulations is justified. Similarly, Figure 2.20 shows that the Mach number never exceeds 0.3 ($M_{max} = 0.17$) in the flow field indicating that the incompressible assumption also appears to be valid for this work.

However, the true role of compressibility in this device is less clear-cut than is suggested by Figure 2.20. The present work has shown that pressure differences associated with pumping at high frequency are very large (59MPa). Therefore, unless the system is charged with a correspondingly large pre-load pressure (which is not realistic for a practical device), compressibility effects arising from two-phase flow conditions (*i.e* cavitation) will probably be important in a '*real*' device. On the other hand, however, the model used to relate the flow rate to the operating frequency in this work certainly over-estimates the flow rate because it does not account for the reduction in piezo stroke caused by force feedback between the stack and the fluid. Therefore, in order to determine the true role of compressibility in these devices and to make realistic predictions of the device's performance with frequency, one really needs to solve the fully-coupled unsteady problem where the fluid in the pumping chamber is driven by a piezo stack and the force feedback between the fluid and the piezo stack is included. Preliminary work by the authors in this area is reported in (John and Cadou, 2005).

2.5 Summary

Computational fluid dynamics is used to investigate fluid flows in the pumping chamber of a piezo-hydraulic pump being developed as part of a compact piezohydraulic hybrid actuation system. The results show that the flow is 3D and that 2D approaches are not appropriate because they can underestimate losses by a factor of up to 40. A large fraction of the fluid losses during intake and discharge can be attributed to the formation of vortex rings in the discharge tube entrance and in the pumping chamber during the pump operation. Modifying simple physical models for the flow in the discharge tube and pumping chamber to incorporate the reduction in effective flow area with increasing flow rate leads to relationships between pressure loss and flow rate that are in good agreement with simulation results. Finally, the fact that the pressure forces approach the blocked pressure of the piezo stack indicate that incorporating the fluid-elastic coupling between the piezo stack and the fluid is very important in order to provide realistic performance estimates. The reason is that fluid-elastic coupling reduces the net motion of the piezo stack in a way that will ultimately lead to stalling at high frequencies.

Table 2.1: Pump Geometry

Parameter	**Symbol**	**Value**
Pumping chamber diameter	d_p	31.75 mm
Discharge tube diameter	d_o	1.5875 mm
Pumping chamber height	h	0.254 mm
Discharge tube offset	R	8.89 mm
Discharge tube length	l	15.75 mm

Table 2.2: Fluid Properties

Parameter	**Symbol**	**Value**
Density	ρ	850 kg/m^3
Kinematic viscosity	ν	3.61×10^{-5} m^2/s

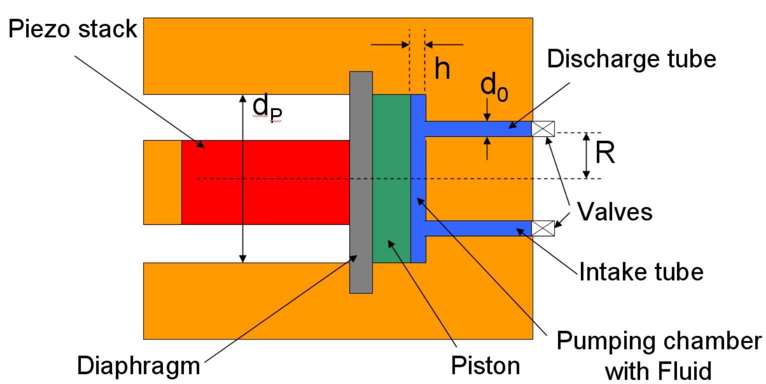

Figure 2.1: Schematic diagram of the pump illustrating the important design parameters like the pumping chamber height (h), the discharge tube location (R), the pumping chamber diameter (d_p) and the discharge tube diameter (d_p).

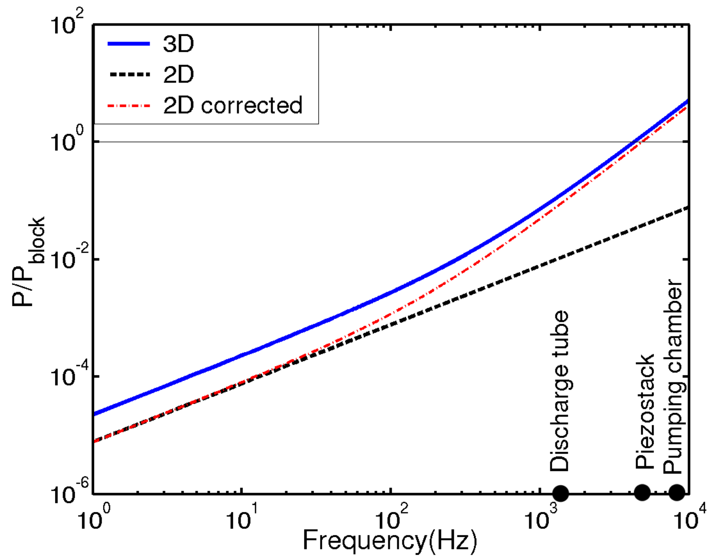

Figure 2.2: Comparison of the predictions of 2D and 3D analytical models for the variation of non-dimensional pressure drop in the pumping chamber with driving frequency. The pressure drop is non-dimensionalized using P_{block}, which is the blocked force of the actuator divided by the piston area. The solid circles on the horizontal axis denote the resonant frequencies of various pump components.

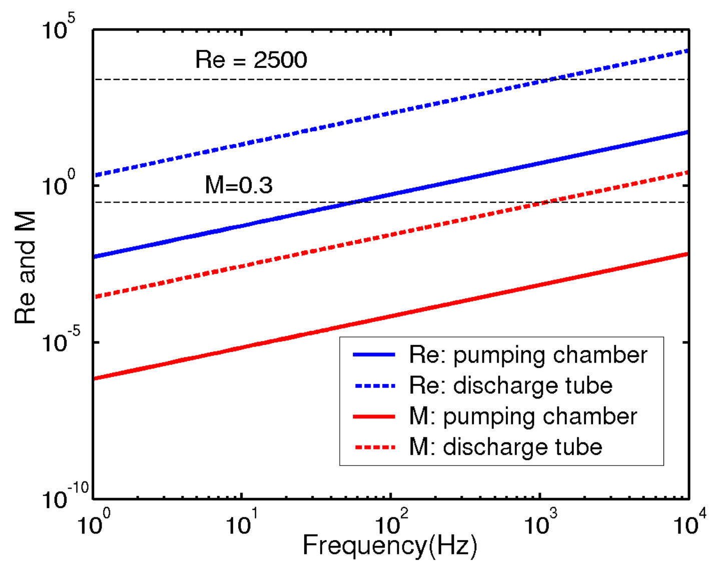

Figure 2.3: Variation of Reynolds and Mach numbers at two locations in the pumping chamber with driving frequency. The upper and lower horizontal lines respectively denote the boundaries of turbulent and compressible flow.

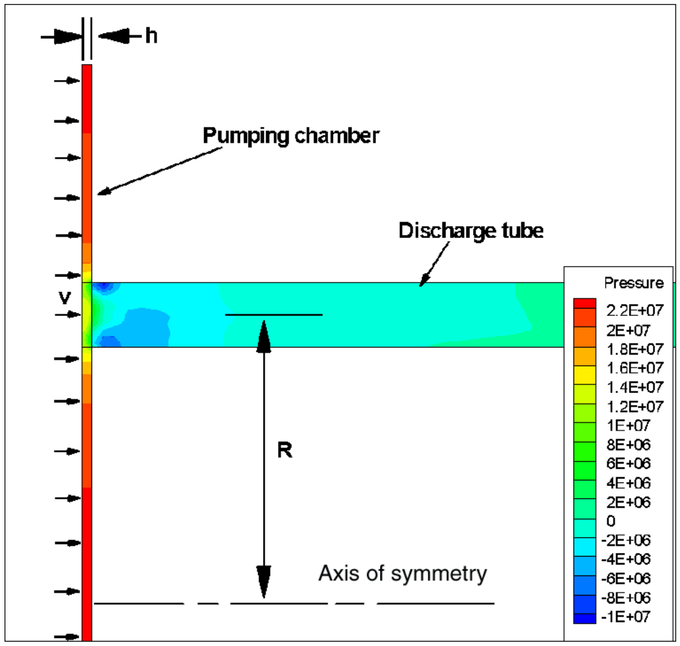

Figure 2.4: Computational domain for the 2D problem illustrating the boundary conditions and a sample pressure distribution

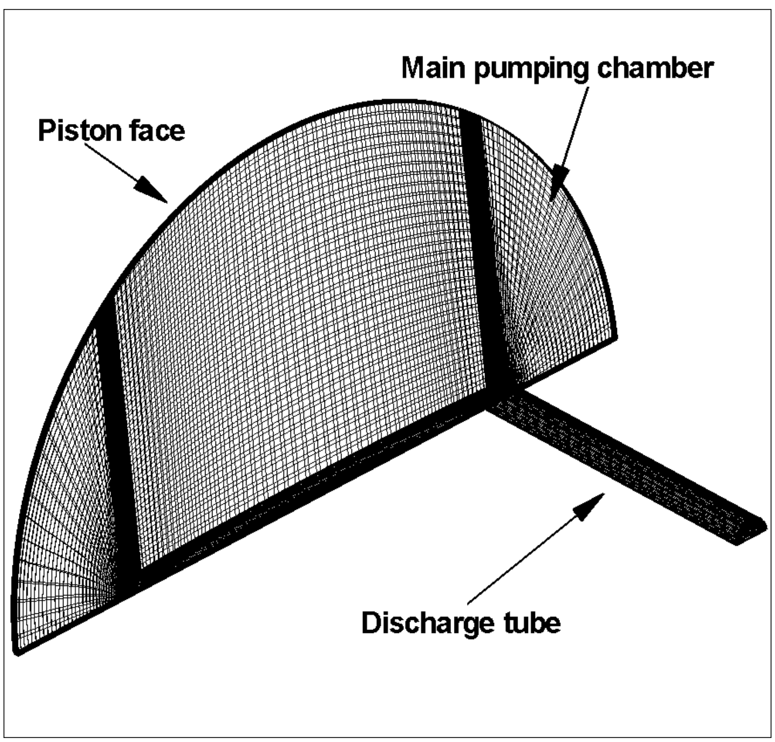

Figure 2.5: Computational grid for the 3D problem showing the discharge tube, pumping chamber and piston face.

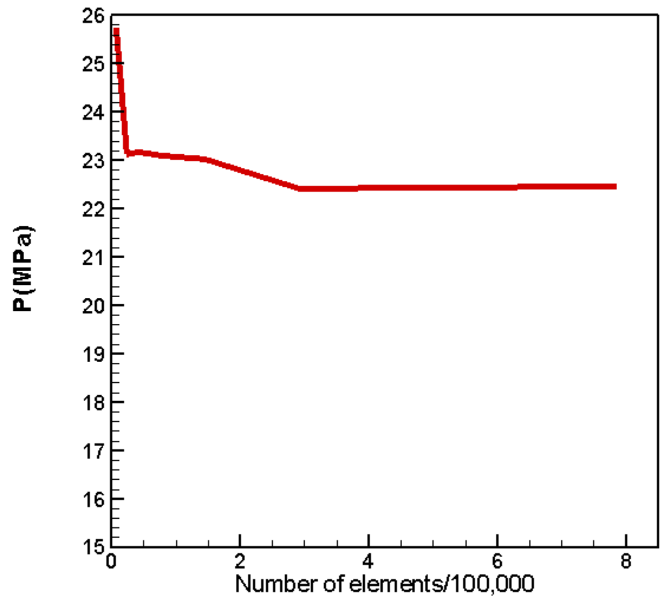

Figure 2.6: Results of grid convergence test showing that 400,000 elements are adequate. The vertical axis represents the pressure drop across the pumping chamber and the horizontal axis represents the number of computational elements used to model the device.

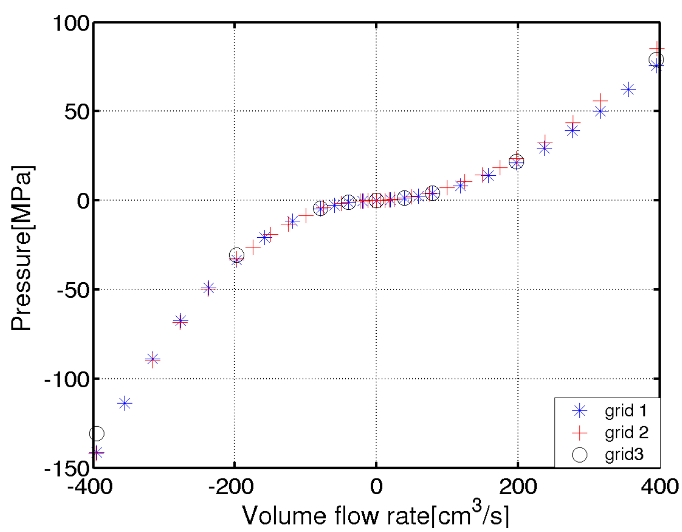

Figure 2.7: Comparison of pressure change across pumping chamber computed using three geometrically different grids, each having 400,000 elements.

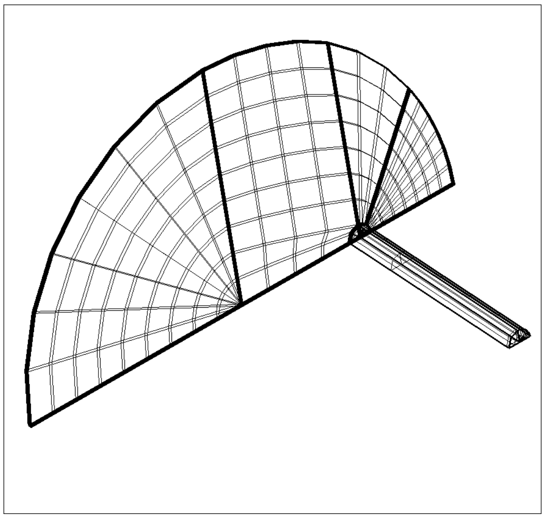

(a) Grid 1

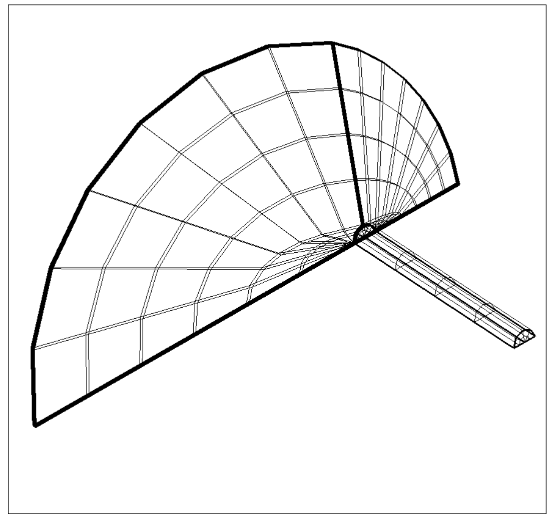

(b) Grid 2

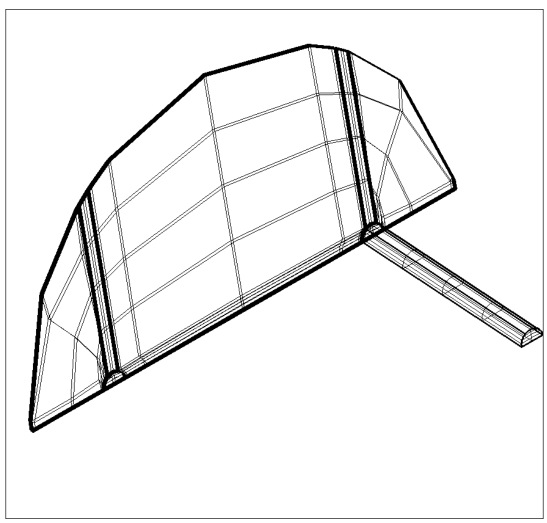

(c) Grid 3

Figure 2.8: Schematic illustrations of the three different grids used to establish grid convergence

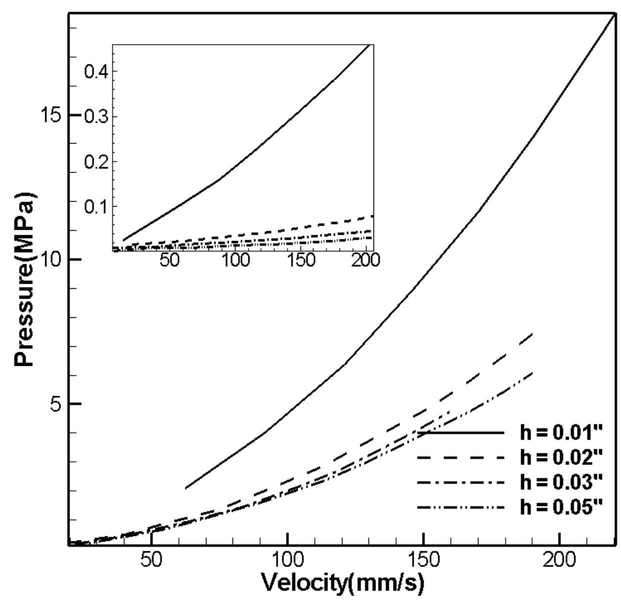

(a) Discharge

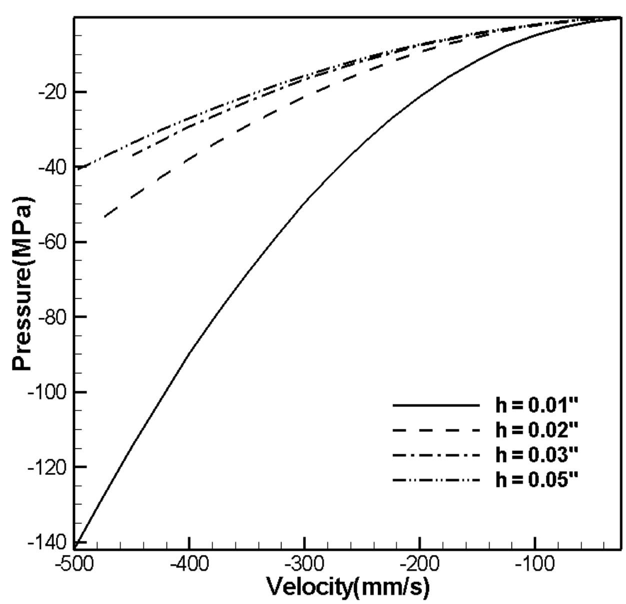

(b) Intake

Figure 2.9: Pressure loss as a function of piston velocity for various pumping chamber heights h. The inset on figure (a) shows results from 2D simulations.

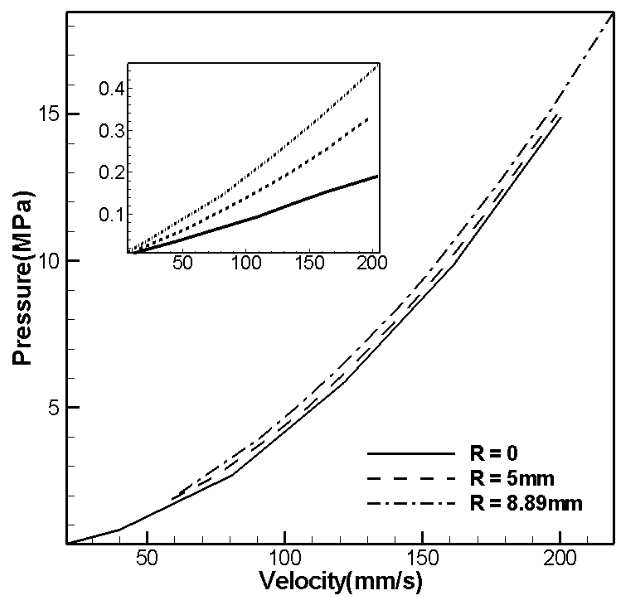

(a) Discharge

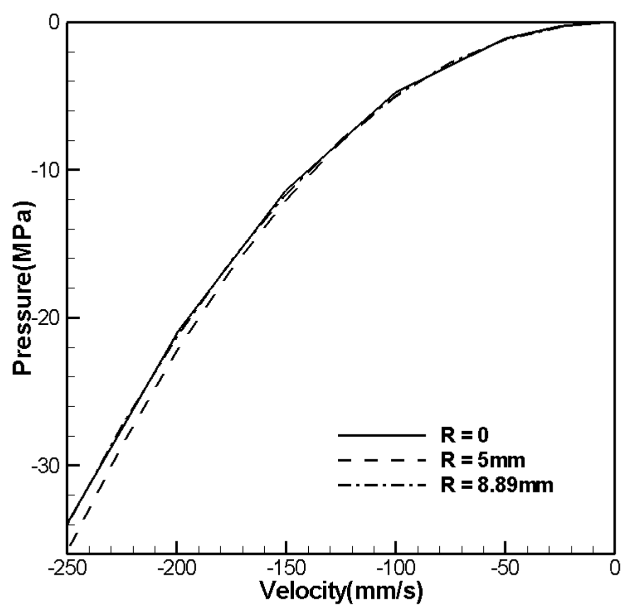

(b) Intake

Figure 2.10: Pressure loss as a function of piston velocity for various discharge tube locations R. The inset on figure (a) shows results from 2D simulations.

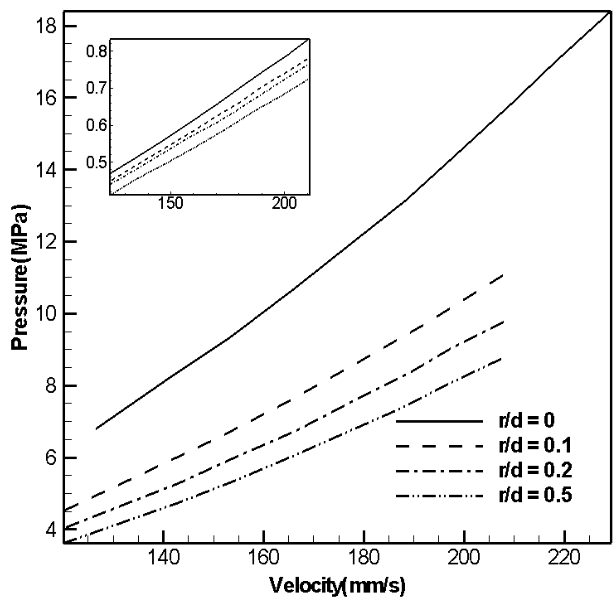

(a) Discharge

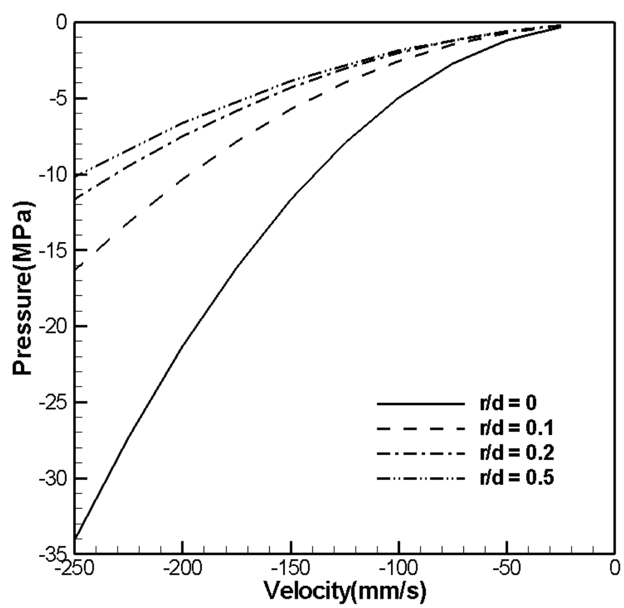

(b) Intake

Figure 2.11: Pressure loss as a function of piston velocity for various discharge tube chamfers r/d. The inset on figure (a) shows results from 2D simulations.

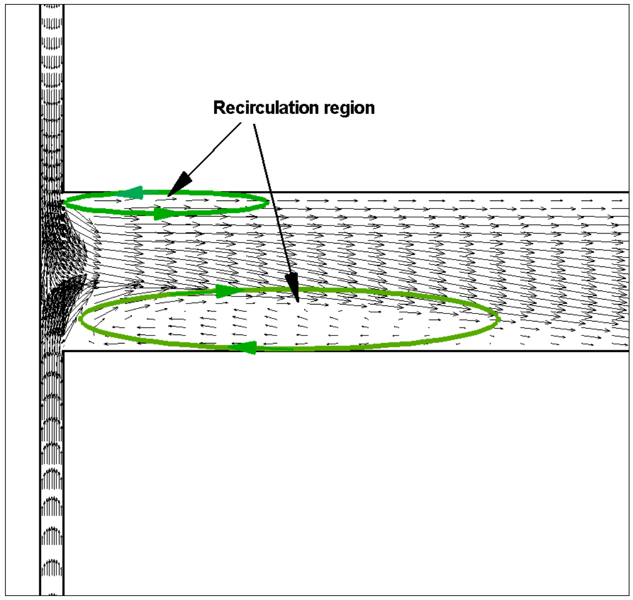

(a) Discharge

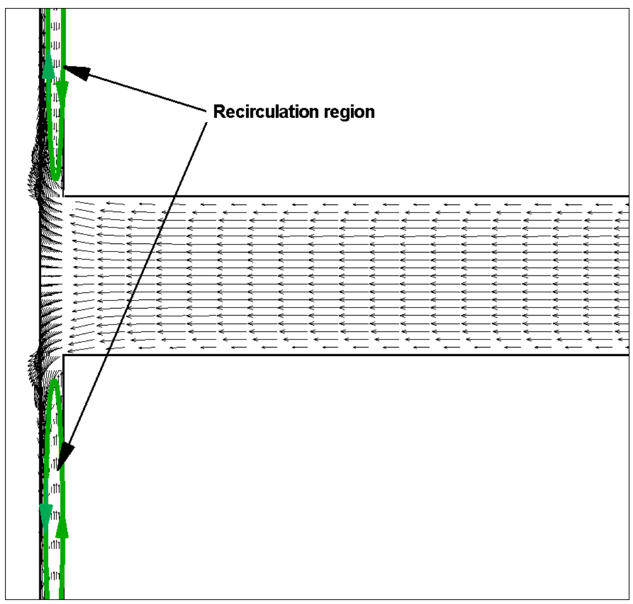

(b) Intake

Figure 2.12: Velocity vectors in the vicinity of the discharge tube showing the recirculation regions associated with the vortex rings that form in the discharge tube during discharge and in the pumping chamber during intake. The ring is very distorted because R=8.89mm and the pumping chamber height is relatively small ($h = 0.01in, r/d = 0, R = 8.89mm, V_p = 200mm/s$).

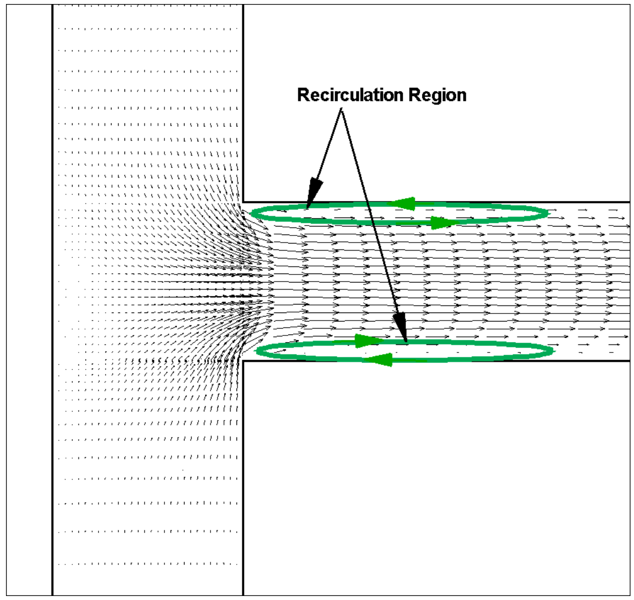

(a) Discharge

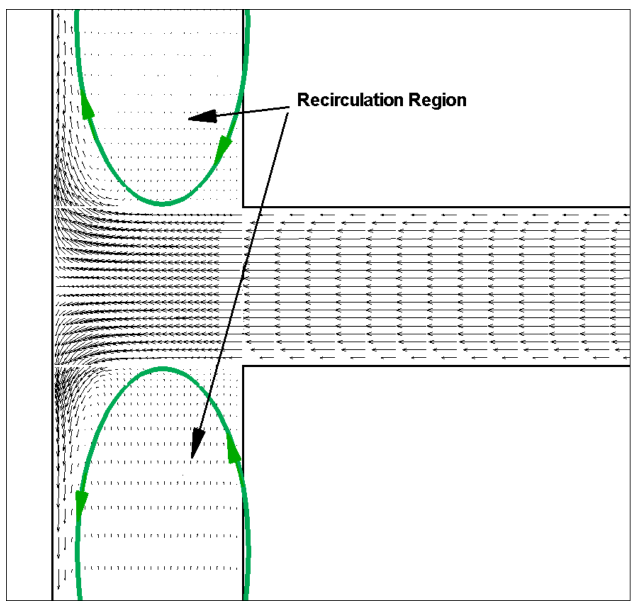

(b) Intake

Figure 2.13: Velocity vectors in the vicinity of the discharge tube showing the recirculation regions associated with the vortex rings that form in the discharge tube during discharge and in the pumping chamber during intake. The ring is less distorted because the pumping chamber height is of the same order of magnitude as the discharge tube diameter ($h = 0.08in, r/d = 0, R = 8.89mm, V_p = 200mm/s$).

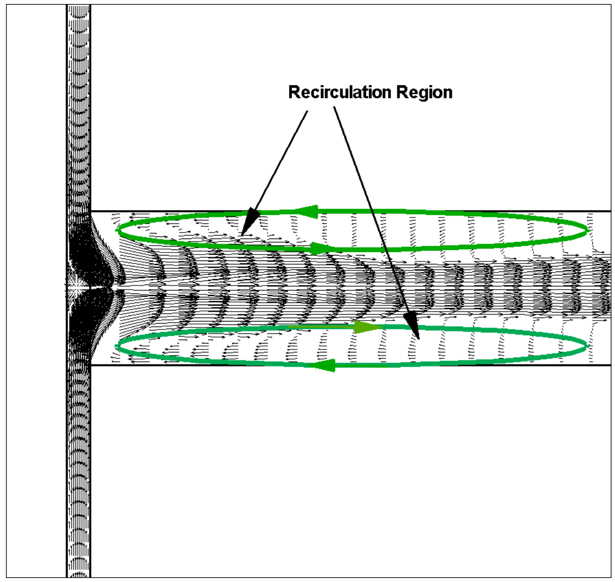

(a) Discharge

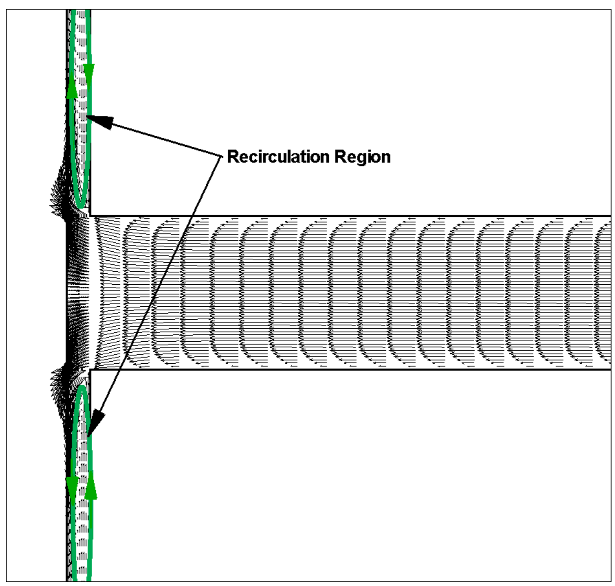

(b) Intake

Figure 2.14: Velocity vectors in the vicinity of the discharge tube showing the recirculation regions associated with the vortex rings that form in the discharge tube during discharge and in the pumping chamber during intake. The ring is symmetric because R=0mm ($h = 0.01in, r/d = 0, V_p = 200mm/s$).

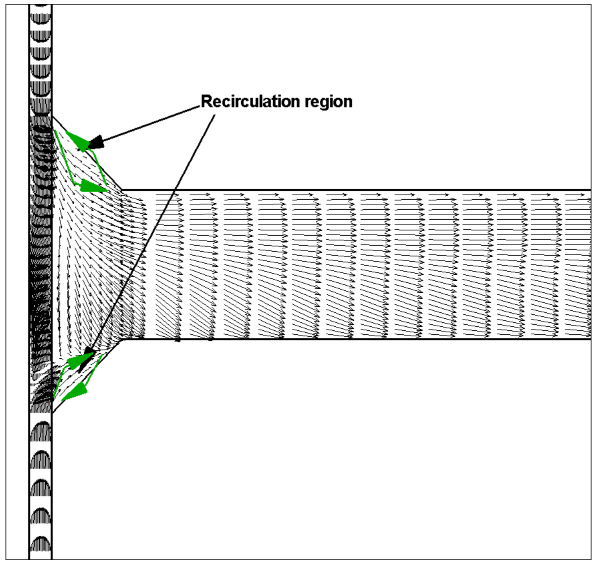

(a) Discharge

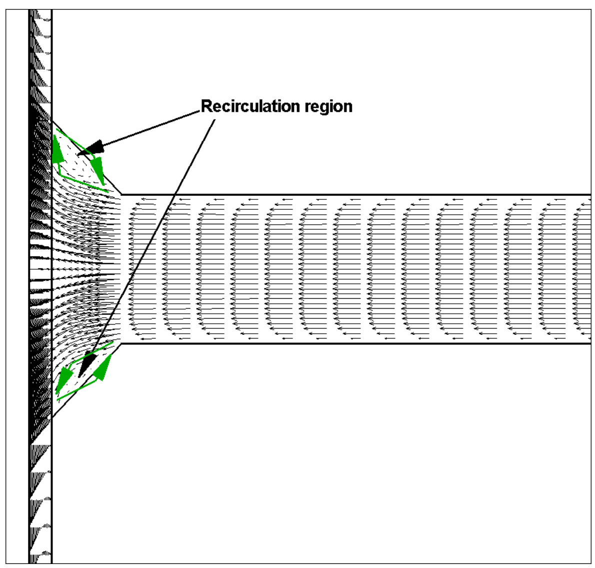

(b) Intake

Figure 2.15: Velocity vectors in the vicinity of the discharge tube ($h = 0.01in, r/d = 0.5, R = 8.89mm, V_p = 200mm/s$).

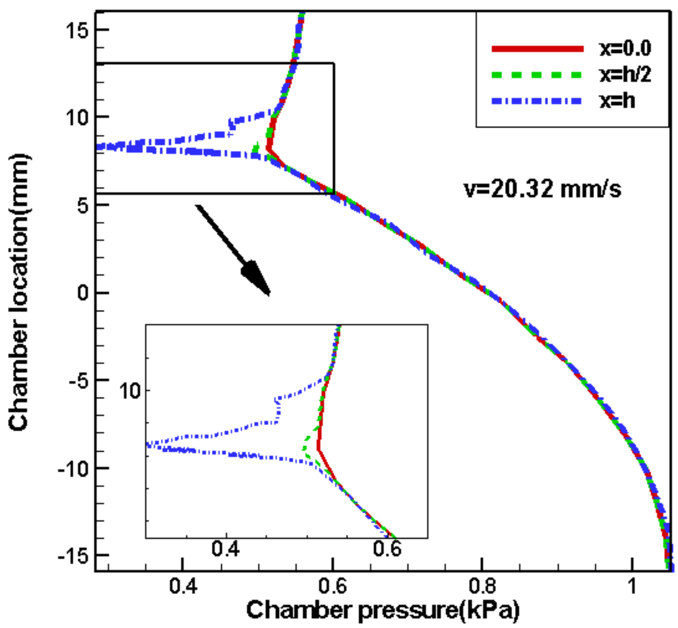

Figure 2.16: Radial pressure distributions at various axial locations in the pumping chamber during discharge. Results are from 2D simulations where the imposed piston velocity is 20.32 mm/s.

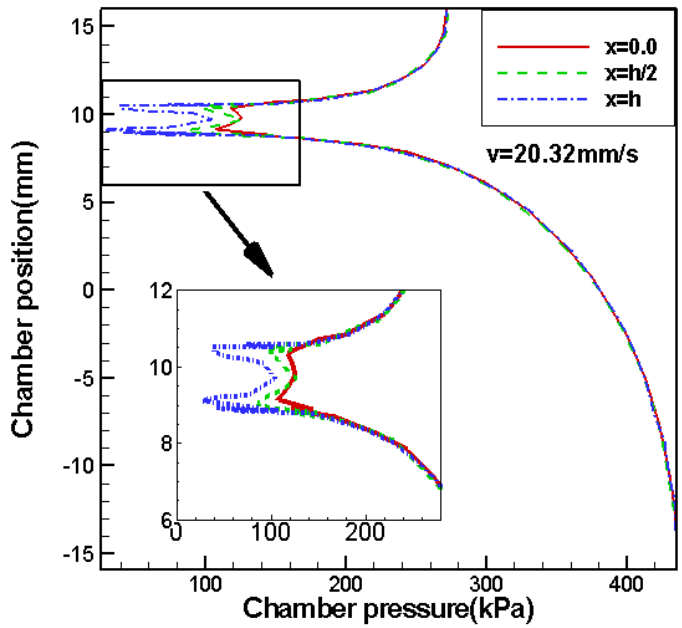

Figure 2.17: Radial pressure distributions at various axial locations in the pumping chamber during discharge. Results are from 3D simulations where the imposed piston velocity is 20.32 mm/s.

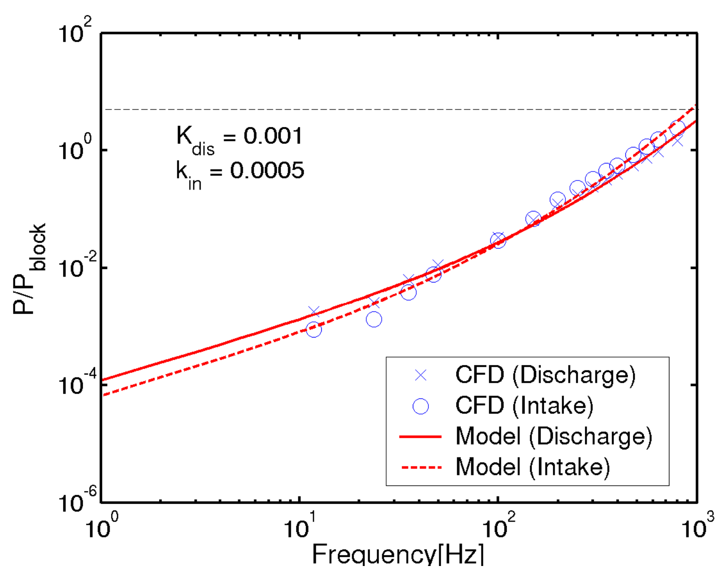

Figure 2.18: Comparison of CFD results to the predictions of the modified analytical models for intake and discharge

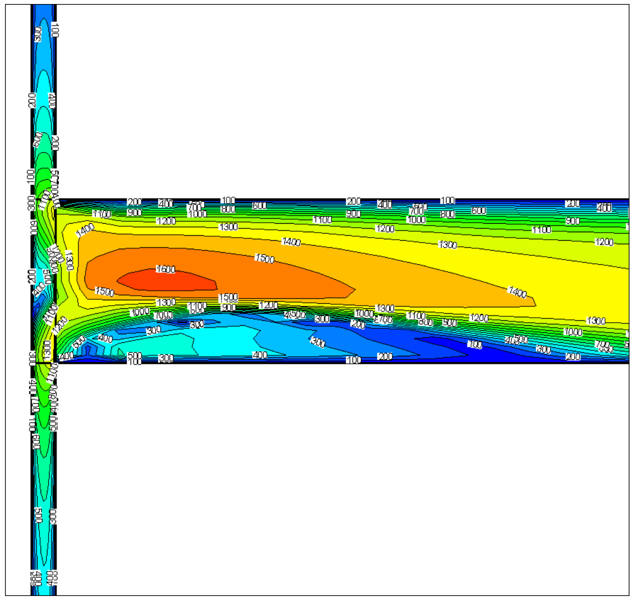

(a) Discharge

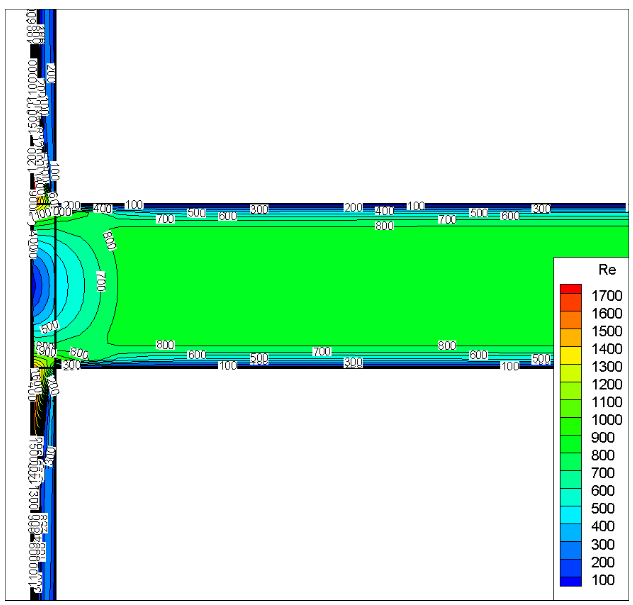

(b) Intake

Figure 2.19: Reynolds number distribution during discharge and intake at the maximum volume flow rate of $1.6 \times 10^{-4} m^3/s$.

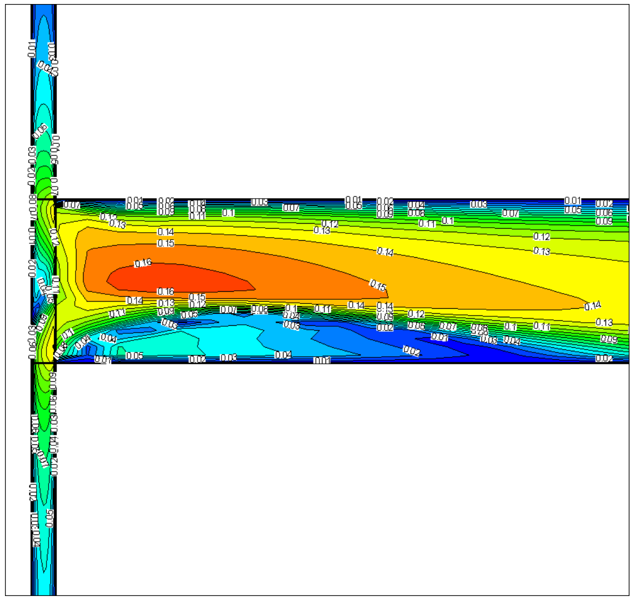

(a) Discharge

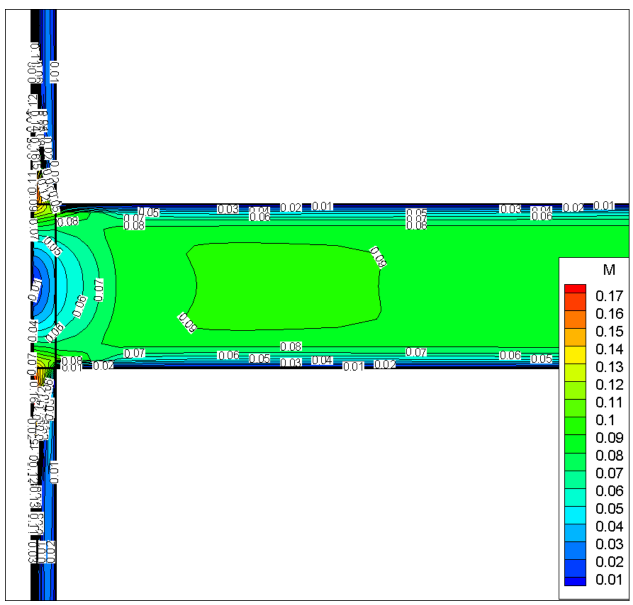

(b) Intake

Figure 2.20: Mach number distribution during discharge and intake at the maximum volume flow rate of $1.6 \times 10^{-4} m^3/s$.

Chapter 3

Unsteady Fluid Flow in Hybrid Hydraulic Actuators

The overall success of the hybrid actuation concept depends on the effectiveness of the coupling between the smart material and the fluid. A variety of models for this coupling have been developed based on quasi-static approaches (Mauck and Lynch, 2000; Cadou and Zhang, 2003), lumped parameter approaches using electrical (Nasser and Leo, 2000) and mechanical analogies (Oates, Mauck and Lynch, 2002), lossless-line (Sirohi, Cadou and Chopra, 2003) approaches, and integration of the mass conservation equations (Regelbrugge, Lindler and Anderson, 2003; Tan, Hurst and Leo, 2005; Chaudhuri, Yoo and Wereley, 2006b). All of these approaches treat the flow in an essentially one dimensional manner in which pressure losses through orifices are related to the volume flow rate using a loss coefficient. These coefficients are usually derived from standard fluid handbooks or from steady, axisymmetric CFD analysis (Oates and Lynch, 2001) While most of these models work reasonably well at low frequencies ($\leq$ 200Hz), they do not predict behavior well at the higher frequencies ($\sim$1kHz) where hybrid actuators are intended to operate.

The work presented in this chapter investigates fluid losses associated with high frequency operation (up to 1000 Hz) of a particular piezo-hydraulic actuator intended for use on the UCAV (Anderson et al., 2003). A schematic diagram of the system is given in Figure 2.1. The dimensions of the pump are presented in Table 2.1, the properties of the working fluid and the piezo stack are summarized in Table 3.1.

Work in the previous chapter investigated steady flow fields in the pumping chamber of this actuator (John et al., 2006). It was shown that the mechanical resonances associated with the piezo stack and the fluid in the pumping chamber and discharge tube can be neglected because their characteristic frequencies are above the pumping frequencies investigated here (0-1000 Hz) and because acoustic and turbulent effects are negligible. In contrast, three-dimensional and viscous effects were shown to have a large impact on pump performance. This chapter focuses on the unsteady flow in the pumping chamber that results when the piezostack is driven by a sinusoidal signal. Solutions of the unsteady Navier-Stokes equations in the pumping chamber with force feedback coupling between the fluid and the piezoelectric stack are presented and discussed. An analytical model is also derived to gain further understanding into the physics behind such fluid flows.

The objectives of this study are to:

- Develop an unsteady theoretical model for fluid dynamic behavior in the pumping chamber of a hybrid actuator.
- Quantify the effect of vortex formation on pressure losses during the pumping process.
- Perform CFD simulations of oscillating fluid flow in the pumping chamber and compare the pressure versus time behavior with the prediction of a theoretical model.

3.1 Problem Definition

The geometry studied is shown in Figure 3.1. An analytical model is first developed to find out closed form expressions for the pressure losses involved in oscillatory flow of fluid in a pumping chamber. The oscillatory flow is imposed at the location of the pump piston. CFD simulations are then performed on this geometry by incorporates a piezoelectric element as the active driving force. An oscillatory electric field signal is provided to the piezoelectric element to simulate the dynamic operation of the pump and the volume flow rate and pressure losses of the fluid are measured and correlated with the model.

3.2 Three Dimensional Analytical Model

The theoretical model proposed for the dynamic operation of the hydraulic hybrid actuator is an extension of the steady model presented in Chapter 2 (John et al., 2006). The flow is assumed to be incompressible, fully developed and laminar at all times. It is also assumed that the pumping chamber and the discharge tube are concentric, that is, there is no radial offset of the discharge tube entrance with respect to the axis of the pumping chamber. This assumption leads from the conclusions of the earlier work by the authors on the characteristics of steady flows. As will be evident in the modeling process, the integrals involve summation along streamlines starting at the edge of the chamber to the location of the discharge tube. For an eccentrically located discharge tube, these calculations are difficult. Thus, the assumption of concentricity simplifies the calculation of areas and the integrals involved. The The computational domain is divided into two sub-domains - the pumping chamber (cylindrical region with a diameter of 31.75 mm and height of 0.254 mm) and the discharge tube (cylindrical region with a diameter of 1.5875 mm and height of 15.875 mm). These two regions can be seen in Figure 3.1.

3.2.1 Pumping chamber

The flow is assumed to be purely radial in the pumping chamber, so that the components of the velocities and their derivatives in the θ and z direction are taken to be zero. The continuity equation is given by:

$$\begin{aligned} \frac{1}{r}\frac{\partial}{\partial r}(ru_r) + \frac{1}{r}\frac{\partial u_\theta}{\partial \theta} + \frac{\partial u_z}{\partial z} &= 0 \\ \frac{1}{r}\frac{\partial}{\partial r}(ru_r) &= 0 \end{aligned} \tag{3.1}$$

The simplified form of the momentum equation can be written as:

$$\rho\left(\frac{\partial u_r}{\partial t} + u_r\frac{\partial u_r}{\partial r}\right) = \mu\left[\frac{\partial}{\partial r}\left(\frac{1}{r}\frac{\partial}{\partial r}(ru_r)\right) + \frac{\partial^2 u_r}{\partial z^2}\right] - \frac{\partial P}{\partial r} \tag{3.2}$$

Putting equation 3.1 in equation 3.2, we get:

$$\rho\left(\frac{\partial u_r}{\partial t} + u_r\frac{\partial u_r}{\partial r}\right) = \mu\frac{\partial^2 u_r}{\partial z^2} - \frac{\partial P}{\partial r} \tag{3.3}$$

The solution process is similar to that used in Chapter 2 that considered steady flows through the pump (John et al., 2006), except that the radial velocity is assumed to be a function of time t, in addition to r and z. It is also assumed that the spatial and temporal components of the velocity are separable.

$$u_r = u_r\left(r,z\right)\alpha\left(t\right) \quad (3.4)$$

$$= \frac{C_1 z(h-z)}{r}\alpha\left(t\right) \quad (3.5)$$

The flow rate can be measured as by integrating the velocity in the z direction at a fixed radial location in the chamber, as in the following equation. This allows us to represent the parameter C_1 in terms of the flow rate, Q.

$$Q = 2\pi r\int_0^h u_r dz label eq: flowrate_basic \quad (3.6)$$

Replacing u_r in the above equation using equation 3.5, we get:

$$\begin{aligned} Q(t) &= 2\pi r\int_0^h \frac{C_1 z(h-z)\alpha(t)}{r}dz \\ &= 2\pi C_1\alpha(t)\int_0^h (hz-z^2)dz \\ &= 2\pi C_1\alpha(t)|\frac{hz^2}{2}-\frac{z^3}{3}|_0^h \\ &= \frac{1}{3}C_1\pi\alpha(t)h^3 \end{aligned} \quad (3.7)$$

Putting equations 3.7 and 3.5 into equation 3.3, we get:

$$\frac{\partial P}{\partial z} = -\frac{6\mu}{2\pi r h^3}Q + \frac{9\rho z^2\left(h-z\right)^2}{\pi^2 r^3 h^6}Q^2 - \frac{3\rho z\left(h-z\right)}{\pi r h^3}\dot{Q} \quad (3.8)$$

Averaging the above equation in the z direction (by integrating perpendicular to the flow direction) and then integrating in the radial direction from the outer radius (R_p) to the inner radius (R_o), leads to the following expression for the relationship between pressure drop and volume flow rate in the pumping chamber:

$$\begin{aligned} P\left(t\right)_{chamber} &= \frac{6\mu}{\pi h^3}ln\left(\frac{R_p}{R_o}\right)Q\left(t\right) + \frac{3\rho}{20\pi^2 h^2}\left(\frac{1}{R_o^2}-\frac{1}{R_p^2}\right)Q\left(t\right)\left|Q(t)\right| \\ &\quad + \frac{\rho}{2\pi h}ln\left(\frac{R_p}{R_o}\right)\dot{Q}\left(t\right) \end{aligned} \quad (3.9)$$

In this expression, R_o is the radius of the discharge orifice, R_p is the radius of the pumping chamber, μ is the dynamic viscosity of the fluid, h is the height of the pumping chamber, ρ is the density of the fluid, $Q(t)$ is the time varying flow rate and $\dot{Q}(t)$ is the time rate of change of the flow rate.

3.2.2 Discharge tube

A similar procedure is followed to develop an expression for the pressure difference across the discharge tube. In the case of the discharge tube, the flow is assumed to be purely in the z direction (axial and down the discharge tube) and the velocity components and derivatives in the r and θ direction are neglected. Assuming that the z component of the fluid flow velocity is $u_z = u_z(r,z)\,\alpha(t)$ and integrating perpendicular to the streamline (along the radius of the discharge tube) to relate u_z to Q gives the following expression for the pressure-volume flow rate relationship in the discharge tube:

$$P_{tube} = \frac{8\mu l}{\pi R_o^4} Q(t) + \frac{\rho l}{\pi R_o^2} \dot{Q}(t) \tag{3.10}$$

The first term in equation 3.10 is the steady Poiseuille flow component and the second term is the unsteady pressure loss component due to oscillatory flow. The total pressure difference across the pump is obtained by adding equations 3.9 and 3.10, which leads to:

$$P = AQ + BQ|Q| + C\dot{Q} \tag{3.11}$$

$$A = \left[\frac{6\mu}{\pi h^3} ln\left(\frac{R_p}{R_o}\right) + \frac{8\mu l}{\pi R_o^4}\right] \tag{3.12}$$

$$B = \frac{3\rho}{20\pi^2 h^2}\left(\frac{1}{R_o^2} - \frac{1}{R_p^2}\right) \tag{3.13}$$

$$C = \left[\frac{\rho}{2\pi h} ln\left(\frac{R_p}{R_o}\right) + \frac{\rho l}{\pi R_o^2}\right] \tag{3.14}$$

where, A, B and C are constants that depend on the geometrical parameters of the pump like R_o, R_p and h. Equation 3.11 shows that viscous losses vary linearly with flow rate (first term) whereas inertial losses associated with area change (second term) vary non-linearly with flow rate. The third term accounts for the inertial losses associated with the time rate of change of the flow rate.

3.2.3 Effect of Vortices

As described in Chapter 2, the pressure difference in a hybrid actuator pumping chamber is affected to a great extent by the vortices that form in the discharge tube and the pumping chamber. During discharge, the fluid negotiates a sharp turn from the pumping chamber into the discharge tube. As a result, the fluid experiences a large acceleration due to its high velocity and the sharpness of the turn, thus causing a recirculation region to form inside the discharge tube. The discharge tube vortex decreases the effective cross-sectional area of the discharge tube that is available for the fluid flow. Similarly, during intake, a vortex forms inside the pumping chamber thus reducing the effective pumping chamber height.

Since the vortices form and subsequently dissipate during every period of oscillation, their contribution to the total pressure loss is not easily modeled. Research into the oscillatory flow of oil past orifices (Washio et al., 1982a) has shown that the pressure losses associated with vortex formation and dissipation is non-linear with Q and can be expressed as follows:

$$P_v(t) = K^{\pm} Q(t - t_0) \left| Q(t - t_0) \right| \tag{3.15}$$

In this expression, P_v is the pressure loss contribution arising from these vortices, coefficient K^+ determines the magnitude of the pressure loss during discharge, and K^- determines the magnitude of the pressure loss during intake. There is a necessity for different coefficients for discharge and intake due to the different boundary conditions associated with intake and discharge. During intake, the vortex is formed in the pumping chamber, which is a cylindrical region of height 0.254 mm and diameter 31.75 mm. During discharge, the vortex occurs in the discharge tube with a diameter of 1.5875 mm. Thus, the geometrical boundary conditions under which the vortices are allowed to grow is different for intake and discharge. Also, the vortex dependent pressure loss contribution lags behind the flow rate variation by t_0. This is due to vortex inertia which tends to resist a sudden change of state. The lag time t_0 depends on the geometry of the orifice and the frequency of the oscillatory flow. We also note that since the lag time depends on the geometry, one should also expect the lag time to be different for intake and discharge. However, in this work, we assume them to be the same inorder to simplify the problem. Since there are no analytical formulations for K^+, K^- or t_0, their values will be determined empirically.

We can incorporate the pressure loss contribution due to vortices in the total pressure loss equation by adding equation 3.15 to 3.11. Thus, the modified total pressure loss equation becomes:

$$P(t) = AQ(t) + BQ(t)|Q(t)| + K^{\pm}Q(t-t_0)|Q(t-t_0)| + C\dot{Q}(t) \quad (3.16)$$

3.2.4 Fourier Series Representation

Results from the CFD simulations show that the pressure signal is not a pure sinusoid like the volume flow rate, but contains additional frequency content. To better understand the frequency domain behavior of equation 3.16, we perform a Fourier series expansion where periodic functions are expressed as a weighted sum of sinusoids. Since the forcing is purely sinusoidal, we assume that the volume flow rate is also a pure sinusoid, as given by equation 3.17. The pressure, however, is not a pure sinusoid and is written as the summation given by equation 3.18.

$$Q = Q_{1s}\sin(\omega t) \quad (3.17)$$

$$P = P_0 + \Sigma_{n=1}^{\infty}\left[P_{ns}\sin(n\omega t) + P_{nc}\cos(n\omega t)\right] \quad (3.18)$$

Since the sign of the quadratic term in equation 3.16 depends on whether the flow is in discharge or intake, and since the value of the coefficient K is different depending on whether the flow is in discharge or intake, equation 3.16 is discontinuous. The presence of discontinuities suggest that higher harmonics ought to be present in the expansion. Substituting equations 3.17 and 3.18 into 3.16 leads to the following expressions for the coefficients of the Fourier expansion:

$$\begin{aligned}
P_0 &= \frac{1}{\pi}\bigg[\int_0^{\pi} BQ_{1s}^2 \sin^2(\omega t) d(\omega t) - \int_{-\pi}^{0} BQ_{1s}^2 \sin^2(\omega t) d(\omega t) \\
&\quad + \int_0^{\pi} K^+ Q_{1s}^2 \sin^2(\omega t)\, d(\omega t) - \int_{-\pi}^{0} K^- Q_{1s}^2 \sin^2(\omega t)\, d(\omega t)\bigg] && (3.19) \\
P_{1s} &= AQ_{1s} \sin(\omega t) + \frac{1}{\pi}\bigg[\int_0^{\pi} BQ_{1s}^2 \sin^2(\omega t) \sin(\omega t)\, (\omega t) \\
&\quad - \int_{-\pi}^{0} BQ_{1s}^2 \sin^2(\omega t) \sin(\omega t)\, d(\omega t) + \int_0^{\pi} K^+ Q_{1s}^2 \sin^2(\omega t) \sin(\omega t)\, d(\omega t) \\
&\qquad - \int_{-\pi}^{0} K^- Q_{1s}^2 \sin^2(\omega t) \sin(\omega t)\, d(\omega t)\bigg] && (3.20) \\
P_{1c} &= CQ_{1s}\omega \cos(\omega t) + \frac{1}{\pi}\bigg[\int_0^{\pi} BQ_{1s}^2 \sin^2(\omega t) \cos(\omega t)\, (\omega t) \\
&\quad - \int_{-\pi}^{0} BQ_{1s}^2 \sin^2(\omega t) \cos(\omega t)\, d(\omega t) + \int_0^{\pi} K^+ Q_{1s}^2 \sin^2(\omega t) \cos(\omega t)\, d(\omega t) \\
&\quad - \int_{-\pi}^{0} K^- Q_{1s}^2 \sin^2(\omega t) \cos(\omega t)\, d(\omega t)\bigg] && (3.21) \\
P_{ns}|_{n>1} &= \frac{1}{\pi}\bigg[\int_0^{\pi} BQ_{1s}^2 \sin^2(\omega t) \sin(n\omega t)\, (\omega t) \\
&\quad - \int_{-\pi}^{0} BQ_{1s}^2 \sin^2(\omega t) \sin(n\omega t)\, d(\omega t) + \int_0^{\pi} K^+ Q_{1s}^2 \sin^2(\omega t) \sin(n\omega t)\, d(\omega t) \\
&\quad - \int_{-\pi}^{0} K^- Q_{1s}^2 \sin^2(\omega t) \sin(n\omega t)\, d(\omega t)\bigg] && (3.22) \\
P_{nc}|_{n>1} &= \frac{1}{\pi}\bigg[\int_0^{\pi} BQ_{1s}^2 \sin^2(\omega t) \cos(n\omega t)\, (\omega t) \\
&\quad - \int_{-\pi}^{0} BQ_{1s}^2 \sin^2(\omega t) \cos(n\omega t)\, d(\omega t) + \int_0^{\pi} K^+ Q_{1s}^2 \sin^2(\omega t) \cos(n\omega t)\, d(\omega t) \\
&\quad - \int_{-\pi}^{0} K^- Q_{1s}^2 \sin^2(\omega t) \cos(n\omega t)\, d(\omega t)\bigg] && (3.23)
\end{aligned}$$

Evaluating these integrals lead to the following values for the coefficients:

$$P_0 = \frac{K^+ - K^-}{4} Q_{1s}^2 \tag{3.24}$$

$$P_{1s} = AQ_{1s} + \frac{8BQ_{1s}^2}{3\pi} + \frac{K^+ + K^-}{\pi}\left(\frac{1}{3}\cos(2\phi) + 1\right) Q_{1s}^2 \tag{3.25}$$

$$P_{1c} = CQ_{1s}\omega - \frac{2}{3\pi}\left(K^+ + K^-\right)\sin(2\phi) Q_{1s}^2 \tag{3.26}$$

$$P_{2s} = -\frac{K^+ - K^-}{4}\sin(2\phi) Q_{1s}^2 \tag{3.27}$$

$$P_{2c} = -\frac{K^+ - K^-}{4}\cos(2\phi) Q_{1s}^2 \tag{3.28}$$

$$P_{ns}|_{n=3,5,7..} = -\frac{8BQ_{1s}^2}{\pi n (n^2 - 4)} + \frac{2(K^+ + K^-)}{\pi (n^2 - 4)}\left(n^2 \sin^2\phi - 2\right) Q_{1s}^2 \tag{3.29}$$

$$P_{nc}|_{n=3,5,7...} = \frac{2(K^+ - K^-)}{\pi (n^2 - 4)}\sin(2\phi) Q_{1s}^2 \tag{3.30}$$

$$P_{ns}|_{n=4,6,8..} = 0 \tag{3.31}$$

$$P_{nc}|_{n=4,6,8...} = 0 \tag{3.32}$$

where, ϕ is defined as:

$$\phi = \omega t_0 \tag{3.33}$$

As mentioned earlier, this phase difference has a different value for intake and discharge. This is because the vortices encounter different boundary conditions during the two different strokes. The implications of this difference will be examined in the next section, where its value will be deduced empirically from unsteady CFD results.

3.3 CFD Simulations

3.3.1 Approach

Figure 3.1 shows the computational domain for the 3D calculations and illustrates the high aspect ratio of the simulated region (ratio of pumping chamber height to the pumping chamber diameter). The piston-piezo combination is represented using a piezoelectric element having the same diameter as the pumping chamber. The piezoelectric element is driven by a sinusoidally varying voltage of a particular driving frequency. The properties of the piezo element are chosen so that the simulated stack has the same blocked force, free displacement, and stiffness as a stack used in a typical device. Table 3.1 shows the values of the parameters used to characterize the piezo stack in the CFD-ACE software. The pressure at the pump exit is taken to be zero to facilitate the numerical solution.

A commercial Navier-Stokes solver (CFD-ACE by ESI-CFD) is used since the only unusual aspects of this problem are the force coupling between the fluid and the piezo stack and the extremely high aspect ratio of the pumping chamber. The equations governing the flow of fluid in the device are the mass and momentum conservation equations. These are given in equations 3.34 and 3.35.

$$\frac{\partial \rho}{\partial t} + \overrightarrow{\nabla} \cdot \left(\rho \overrightarrow{\mathbf{u}}\right) = 0 \tag{3.34}$$

$$\rho \left(\frac{\partial u}{\partial t} + \overrightarrow{u} \cdot \nabla \overrightarrow{u} \right) = -\nabla P + \mu \nabla^2 \overrightarrow{u} \tag{3.35}$$

CFD-ACE was selected because its multi-physics capabilities enable it to model the fluid, the piezo stack element, and the coupling between the piezo stack element and the fluid. The software solves the unsteady Navier-Stokes equations on a grid using a finite-volume discretization and allows the user to select various interpolation schemes with various levels of numerical accuracy and stability. In this work, a first-order upwind scheme is used for the velocity while the velocity and stress fields are determined using a Conjugate Gradient Squared (CGS) method with preconditioning (Hirsch, 1990). The pressure field is solved using an Algebraic Multi-grid solver (AMG). Suitable relaxation parameters are also chosen to constrain the change in variables from iteration to iteration. This is necessary to ensure stability and convergence. The computations were performed on a dual-processor (Intel Xeon Processor with a clock speed of 3.06GHz and 533MHz front side bus) computer with 2GB RAM running the LINUX operating system. Only one half of the pumping chamber is simulated in order to reduce computational time. Typical computational times ranged from 48-96 hours

The CFD solutions are used in several ways. Vector plots of the velocity field and contour plots of the pressure field inside the pumping chamber enable visualization of the pressure gradient and the resulting flow field. Since the pressure at the pump exit is taken to be zero, the average pressure difference across the pump is determined by computing the average pressure across the piston face.

$$P_{av} = \frac{\int PdA}{A_p} \tag{3.36}$$

The volume flow rate of the pump at a particular point in time is determined by integrating the velocity profile at that time over the discharge tube cross-sectional area of the entrance, as shown in equation 3.37

$$Q = \int_{A_o} vdA \tag{3.37}$$

The overall volume flow rate is determined by integrating the instantaneous volume flow rate over the discharge portion of the piezo stroke (given by equation 3.38) to obtain the total volume of fluid displaced during the discharge stroke. Here, t_1 is the time at which the flow begins to exit the pumping chamber and t_2 is the time at which the discharge ends and the flow reverses its direction. Q_{net}, multiplied by the driving frequency, gives the flow rate that would be produced by the pump if it were coupled to a set of lossless, instantaneously acting, flow rectifying valves.

$$Q_{net} = f \int_{t_1}^{t_2} Q_{inst} dt \tag{3.38}$$

3.3.2 Grid Convergence and Stability Studies

Two characteristics of CFD solutions must be established in order to ensure that the numerical solutions to the Navier-Stokes equations are physically meaningful: the solutions must be converged and they must not depend on either the number of grid points or the particular grid configuration. The convergence criteria adopted in this study was to continue iterations until residuals diminished by at least four orders of magnitude. The results of a grid convergence test are presented in Figure 3.2. They show the peak pressure in the pumping chamber as a function of the number of elements used to represent the fluid domain. The driving signal provided to the piezoelectric stack has a frequency of 500Hz. The results indicate that 400,000 elements provide adequate spatial resolution. Simulations were also performed using three geometrically different grids each having 400,000 elements to ensure that the solutions are also independent of the grid geometry.

3.3.3 Pressure and Flow Rate Variations Through a Single Cycle

Figure 3.3 shows the variations of pressure drop, P, volume flow rate, Q, displacement of the piston face (or piezo), δ, and the drive voltage applied to the piezo stack as a function of the phase of the driving voltage. The driving frequency is 100Hz. The labels 1, 2, 3, and 4 on the figures correspond to the various critical positions in the piezo stack's cycle. Point 1 is the starting point corresponding to the equilibrium (zero) piezo position with the piezo stack moving back (intake). Point 2 corresponds to the minimum (fully contracted) piezo displacement, point 3 corresponds to the zero point as the piezo increases in length (discharge), and point 4 corresponds to the maximum (fully extended) piezo position. The labels A, B, C and D denote the various critical points in the volume flow rate cycle. Point A corresponds to the maximum intake volume flow rate. Point B corresponds to the zero flow rate point when the flow is transitioning from intake to discharge. This occurs when the piezo displacement reaches its minimum and the piston velocity is zero. Point C corresponds to maximum discharge flow rate, and point D corresponds to zero flow rate where the flow is transitioning from discharge to intake.

The shapes of the flow rate and piezo displacement traces are the same and the phase relationship between them is fixed - the flow rate lags the piezo displacement by 90 degrees everywhere - because of the assumption that the fluid is incompressible and the fact that mass must be conserved. The shape of the pressure variation, however, is different from the flow rate and displacement traces and varies throughout the cycle. This is due to the presence of additional harmonics in the pressure loss signal, as derived in the section on analytical modeling. The magnitude and phase of these additional harmonics depends on pumping frequency and the geometrical parameters of the pump.

Figures 3.4 to 3.11 show the time evolution of the flow patterns in the pumping chamber and the discharge tube. The volume flow rate responds to the velocity of motion of the active stack. Figures titled (a) show the snapshot of the region of the pump where the discharge tube and the chamber meet. The region enclosed by dotted lines is enlarged and shown in the corresponding Figures titled (b) show the flow structure in the zoomed in relevant region for clarification. Eight intermediate time instances during the span of one complete oscillation of the hybrid stack are shown in these figures and are explained below.

- t/T = 1/8: In Figure 3.4(a), the active stack is contracting, thus forcing fluid to flow into the chamber through the discharge tube. The figure also shows the presence of a vortex in the chamber. The rapid accleration encountered by the fluid at the turn from the discharge tube to the chamber causes a vortex to form in the chamber. This vortex decreases the effective pumping chamber height available for the fluid to flow. The vortical region can be clearly seen as the region where velocity vectors are pointing in the opposite direction to the net flow.

- t/T = 2/8: In Figure 3.5(a), the volume flow rate increases in intake and the size of the vortex in the chamber also increases. This can be seen from the increased length of the velocity vectors.

- t/T = 3/8: In Figure 3.6(a), the velocity of the active stack decreases as the stack contracts in length, reducing the intake flow rate. We can see that that size of the intake vortex also reduces in size. During intake stages, there is no vortex in the discharge tube.

- t/T = 4/8: In Figure 3.7(a), the active stack has started expanding and the fluid flow has started to flow out of the pumping chamber into the discharge tube. We can see that the vortex in the chamber has dissapeared and the fluid experiences an adverse pressure gradient in the discharge tube as it negotiates the sharp turn from the chamber into the discharge tube.

- t/T = 5/8: In Figure 3.8(a), the volume flow rate starts to increase in discharge and a vortex starts to form in the discharge tube. We can see that the vortex in the top part of the discharge tube is much smaller than the one in the bottom part of the discharge. This is due to the location of the discharge tube. Since the discharge tube is eccentrically located with respect to the chamber, the volume flow rate entering the discharge tube is asymmetric. This causes a difference in the size of the vortices formed. Also note that Figures 3.4-3.11 show two dimensional slices of a three dimensional geometry and in reality, the vortices are three dimensional. We can clearly see the effect of this discharge tube vortex as reducing the effective area of cross-section of the discharge tube thats available for the fluid to flow.

- t/T = 6/8: In Figure 3.9(a), the discharge flow rate increases as the velocity of the active stack increases in expansion. We also see that the reverse flow in the discharge tube vortex increses in magnitude.

- t/T = 7/8: In Figure 3.10(a), the reverse flow in the discharge tube vortex has strengthened further. We can also see a small vortex region in the top region of the discharge tube. As mentioned before, this vortex is much smaller than the one in the bottom half of the discharge tube.

- t/T = 8/8: In Figure 3.11(a), we can see that the vortex region has started to diminish in size and strength as the active stack starts to contract. The discharge tube vortex dissipates slowly as the inertia associated with the discharge tube vortex is large. The inertia of the vortex depends on the size of the relative size of the vortex and the fluid momentum associated with the vortex.

The above mentioned Figures 3.4-3.11 show the two main vortices in a hybrid pump. The vortices form due to the adverse pressure gradient experienced by the fluid in negotiating the corner between the chamber and the discharge tube. The size of the vortex depends on maximum instantaneous volume flow rate. However, due to the inertia associated with the vortex, there is a time lag between the maximum size of the vortex and the occurence of maximum instantneous volume flow rate. The size of the vortex decreases as the volume flow rate decreases. The evolution and dissipation of these two vortices occur during every oscilation of the hybird pump.

The three-dimensional illustration in Figure 3.12 shows the relationship between pressure, volume flow rate, and piezo stack displacement through a single pumping cycle at 100 Hz. The projections of this trace on the P-Q, Q-δ and P-δ planes are also illustrated. The labels A, B, C and D correspond to the labels described in an earlier section. During the operation of the pump, the pressure and volume flow rate move from A to D along the three-dimensional contour as the fluid moves into and out of the pumping chamber. The resistance of the fluid to acceleration (arising from viscous and inertial effects) leads to a time delay or phase difference between the applied pressure and the fluid response. This phase difference leads to the hysteresis loop shown in the $P - Q$ plane of the figure.

Figure 3.13 shows how the shape of the pressure versus the volume flow rate trace (the projection on the P-Q plane from Figure 3.12) changes with driving frequency. Figure 3.13(a) shows traces for frequencies ranging from 100Hz to 400Hz while 3.13(b) shows traces for frequencies in the 400Hz to 1000Hz range. The solid line with triangular symbols shows the pressure-flow rate relationship for steady flow and is provided as a reference. The distinctive feature of these curves are the hysteresis loops and the self crossings. The area enclosed by the pressure-volume flow rate curve shows the amount of energy spend in overcoming the different losses in the pump. The self crossings are seen only at low frequencies (100Hz - 550Hz) and vanish as the pumping frequency is increased. The gradual disappearance of these self-crossings as the pumping frequency is raised above 550 Hz is due to the dominance of unsteady inertial forces at higher frequencies. As the unsteady inertial forces gain prominence over the viscous and area change components, the self-crossings vanish. This phenomenon has also been observed in experimental investigation of oscillatory oil flows through orifices (Washio et al., 1982a).

3.3.4 Variation in Overall Pumping Performance with Frequency

Figure 3.14 shows how the peak volume flow rate (discharge) varies with operating frequency. At low frequencies, the volume flow rate increases approximately linearly with operating frequency as shown in Figure 3.14. This is consistent with the quasi-static model proposed by (Cadou and Zhang, 2003) for situations where the fluid forces are much smaller than the blocked force of the stack:

$$Q = \delta \pi R_p^2 f \tag{3.39}$$

Here, δ is the stack displacement, f is the piezo frequency and R_p is the radius of the pumping chamber. The straight line in figure 3.14 corresponds to Equation 3.39. Above, 200 Hz, however, the flow rate no longer increases linearly with frequency and the CFD simulations show that it reaches a limiting value at around 600 Hz. Increasing the driving frequency beyond 600 Hz does not change the volume flow rate appreciably until approximately 800 Hz where it begins to decrease as the device shows the first signs of stalling. Similar stalling has been observed experimentally (Sirohi et al., 2003) and in simpler quasi-static model (Cadou and Zhang, 2003).

The reason for the deviation from linear behavior and eventual stalling of the pump is explained by Figure 3.15 which shows non-dimensional pump pressure (pump pressure divided by the blocked pressure) and non-dimensional piston displacement (piston displacement divided by the free displacement) as a function of driving frequency. The figure shows that as the driving frequency increases, the forces felt by the stack as a result of fluid losses become an increasingly significant fraction of the blocked force or maximum force capacity of the stack. These increasing forces decrease the stack displacement δ thereby decreasing the amount of fluid moved during one pumping cycle. Eventually, the reduction in stack displacement with increasing frequency outstrips the increase in the number of pumping cycles per second and the pump begins to stall. Modifying δ in Eq. (3.39) to account for the reduction in stack displacement with frequency captures the actual behavior of the pump as indicated by the coincidence of the triangular symbols on Figure 3.14 with the dashed curve corresponding to the CFD results.

3.4 Modeling Results

The theoretical model developed in equations 3.11 - 3.32 can be used to develop an understanding of the scaling issues involved in an actuator. Figure 3.16 shows the variation of the total pressure loss and its three main components (losses due to fluid viscosity, area change and fluid inertia) with pumping frequency. The pressure in this figure has been non-dimensionalized using the blocking pressure of the actuating element (piezoelectric element). The figure shows that viscous losses dominate the total pressure loss at low pumping frequencies. This is because the velocity and acceleration of the fluid are low at lower pumping frequencies. However, as the pumping frequency is increased, the total pressure loss starts to be dominated by the losses due to area change and the pressure loss switches from a linear varition with frequency to a quadratic variation with frequency. The transition between viscous and area change dominance occurs at an approximate pumping frequency of 80 Hz and corresponds to the point in the CFD solution where the piezo stack displacement begins to decrease.

The theoretical model developed in the previous section has been derived using several simplifications. For instance, the discharge tube was assumed to be in the center of the pumping chamber. Moreover, the fluid flow is assumed to start at the circumferential part of the pumping chamber and move radially in towards the discharge tube. Both these assumptions were made to simplify the equations and the integrals involved. In equation 3.16, coefficients K^+, K^- and t_0 are parameters that determine the pressure loss caused by vortices in the discharge tube and pumping chamber and these coefficients must be determined empirically. Incorporating the non-linear vortex terms in equation 3.16 enables one to make similar comparisons between the model and CFD predictions for the unsteady case. The results are presented in Figure 3.17. The constrained optimization routine, $fmincon$, in MATLAB was used to obtain the values for K^+, K^- and t_0 that best fit the CFD results. The values of these three parameters are shown in the figure. The results show that the analytical model seems to match the CFD results better at high pumping frequencies like 700Hz, than at lower frequencies like 100Hz.

The most distinctive feature of the pressure-volume flow rate variation is the self-crossing behavior seen at lower frequencies (Figure 3.13) that vanishes as the pumping frequency is increased. The fact that the analytical model captures these self-crossing behavior of the fluid flow enables us to surmise that the self-crossings are generated by an interplay between the different harmonics of the pressure signal. As the frequency increases, the inertial component of the pressure loss in the model (primary harmonic, but with a phase difference of $\pi/2$) grows until it overwhelms the other harmonics leading to the dissapearance of these self crossings.

The poor agreement at low frequencies may be the results of deficiences in our representation of the vortex related losses. In order to determine how important vortex inertia is, we remove it from equation 3.18 and recompute the Fourier coefficients.

$$
\begin{aligned}
P_0 &= \frac{K^+ - K^-}{4} Q_{1s}^2 && (3.40)\\
P_{1s} &= AQ_{1s} + \frac{8BQ_{1s}^2}{3\pi} + \frac{K^+ + K^-}{\pi}\left(\frac{1}{3}\cos(2\phi) + 1\right) Q_{1s}^2 && (3.41)\\
P_{1c} &= CQ_{1s}\omega - \frac{2}{3\pi}\left(K^+ + K^-\right)\sin(2\phi)\, Q_{1s}^2 && (3.42)\\
P_{2s} &= 0 && (3.43)\\
P_{2c} &= -\frac{K^+ - K^-}{4} Q_{1s}^2 && (3.44)\\
P_{ns}|_{n=3,5,7..} &= -\frac{8BQ_{1s}^2}{\pi n\left(n^2-4\right)} - \frac{4\left(K^+ + K^-\right)}{\pi\left(n^2-4\right)} Q_{1s}^2 && (3.45)\\
P_{ns}|_{n=4,6,8..} &= 0 && (3.46)\\
P_{nc}|_{n=3,4,5...} &= 0 && (3.47)
\end{aligned}
$$

Comparing these fourier coefficients to equations 3.24-3.32, we see that the most dominant term in equations 3.24-3.32 that arises due to vortex inertia is the P_{2s} term. Thus the effect of the phase lag due to vortex inertia and its differing value during intake and discharge greatly affects the P_{2s} term. Therefore, a correction term is proposed to account for the frequency dependance of vortex inertia that retains the form of equation 3.28, $\chi P_{2s}\sin(2\omega t)$. The corrected pressure equation takes the following form:

$$P_{corrected} = P_{original} + \chi P_{2s} \sin(2\omega t) \quad (3.48)$$

where, χ is the correction factor and $P_{original}$ is the original value of pressure from equation 3.16. The effects of adding this is shown in Figure 3.18. The fit of the analytical model with the CFD results has been vastly improved at lower pumping frequencies like 100Hz by choosing χ of 3.4. At higher frequencies like 700Hz, the correction factor was not needed and its value was set to zero.

3.5 Summary

- A theoretical model was developed for the pressure variation in the pumping chamber during dynamic operation. It was derived from the mass and momentum conservation equations and show that there are three basic components of pressure loss. The first is viscous losses which depends on the flow rate. The second is an inertial component which results from area change encountered by the fluid as it moves from the chamber to the discharge tube. This component has a quadratic relationship with the volume flow rate. The third component is also an inertial component that arises from the unsteady flow produced by the oscillatory pressure gradient.

- The model did not take into account the pressure loss contribution from vortices. But past research show that vortices play a major role in the determining the pressure loss. Extrapolating from experimental studies performed by other researchers, we assume that the pressure drop associated with these trapped vortices also depends quadratically on the volume flow rate and that it has a phase lag with respect to the volume flow rate. This phase lag was determined by fitting the analytical model to the results of unsteady, 3-D CFD simulations.

  A Fourier expansion of the analytical pressure loss expression showed that the additional harmonics present in the pressure loss signal (2^{nd},3^{rd},5^{th} and so on) that arises due to the discontinuous nature of the pressure loss expression, governs the self-crossings of the $P - Q$ characteristics at low frequencies. Increasing the driving frequency causes more energy to be dissipated in the vortices which eventually eliminates the self-crossing behavior

- A computational mesh was generated for the pumping chamber geometry and a commercially available solver, CFD-ACE, was used to solve the Navier-Stokes equations on the grid. The earlier work by the authors had suggested the importance of three dimensional modeling and the fluid-elastic coupling between the fluid and the driving element. This was confirmed by the results obtained from the CFD simulations, which shows that the net volume flow rate reaches a maximum at a piezo excitation frequency of 800Hz. Such flow rate limits have also been observed in experimental studies. The CFD results show that this limit arises because of the pressure losses in the pumping chamber increases non-linearly as the pumping frequency is increased, causing the stack deflection to reduced. The results also show that vortex formation has a very important effect as the pressure losses. Vortices formed in the discharge tube and the chamber during discharge and intake respectively, decrease the effective flow area leading to increased inertial and viscous losses. The CFD results also show that the plot of pressure versus flow rate crosses on itself at lower values of pumping frequency.

- The fit between the analytical model and the CFD simulations was improved by adding, a correction factor to the term in the Fourier expansion that is generated solely by the vortex component. The addition of this correction factor improves the fit of the analytical model to the CFD simulation.

Table 3.1: Fluid and Piezo stack Properties

Fluid Properties	
Density(kg/m^3)	7600
Viscosity(m$^2/s$)	3.61×10^{-5}
Piezo Properties	
Length(in)	4.8
Diameter(in)	0.75
Block Force(N)	17100
Free displacement(mm)	0.1%
Youngs Modulus(GPa)	60
Density(kg/m^3)	7600
Relative Permittivity	3400
$\epsilon_1(F/m)$	3130
$\epsilon_2(F/m)$	3130
$\epsilon_3(F/m)$	3400
$d_{13}(C/m^2)$	-23.9
$d_{23}(C/m^2)$	-23.9
$d_{33}(C/m^2)$	-55.8

Table 3.2: Solver Parameters

Parameter	3-D coupled	3-D
Fluid elements	144100	144100
Piezo elements	28250	-
Time step	150 per period	50 per period
Stress-pressure coupling	5 iterations	-
Velocity-Spatial differencing	upwind	upwind
Velocity solver	CGS+Pre conditioning	CGS + Preconditioning
Pressure correction	AMG	AMG
Stress solver	CGS	Direct
Velocity relaxation	0.2	0.2
Pressure relaxation	0.2	0.2
Density relaxation	1	1
Viscosity relaxation	1	1
Grid motion relaxation	0.1-0.5	0.5
Computational time(approx)	40 hrs	7 hrs

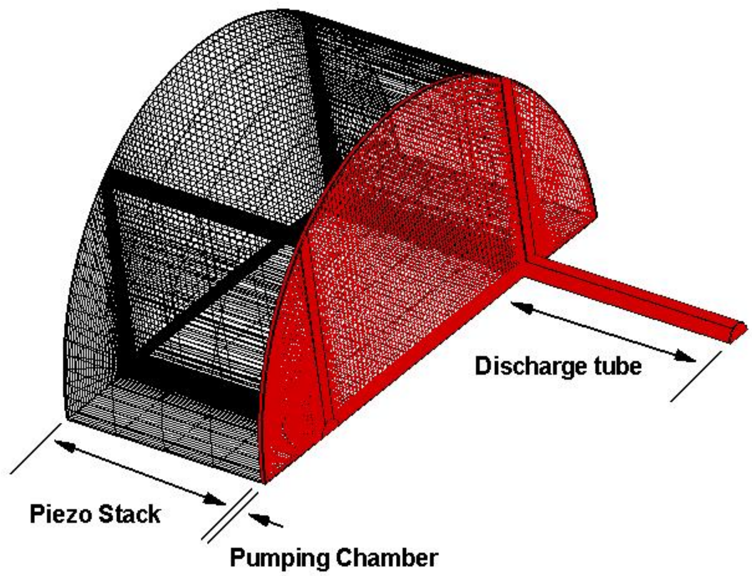

Figure 3.1: Computational domain for coupled problem illustrating the pumping chamber, discharge tube and the driving piezo stack

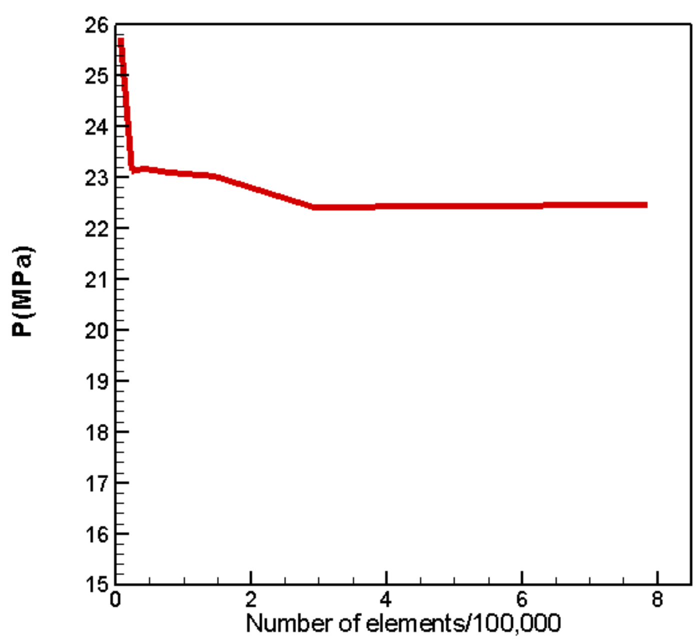

Figure 3.2: Comparison of pressure loss for different grid densities

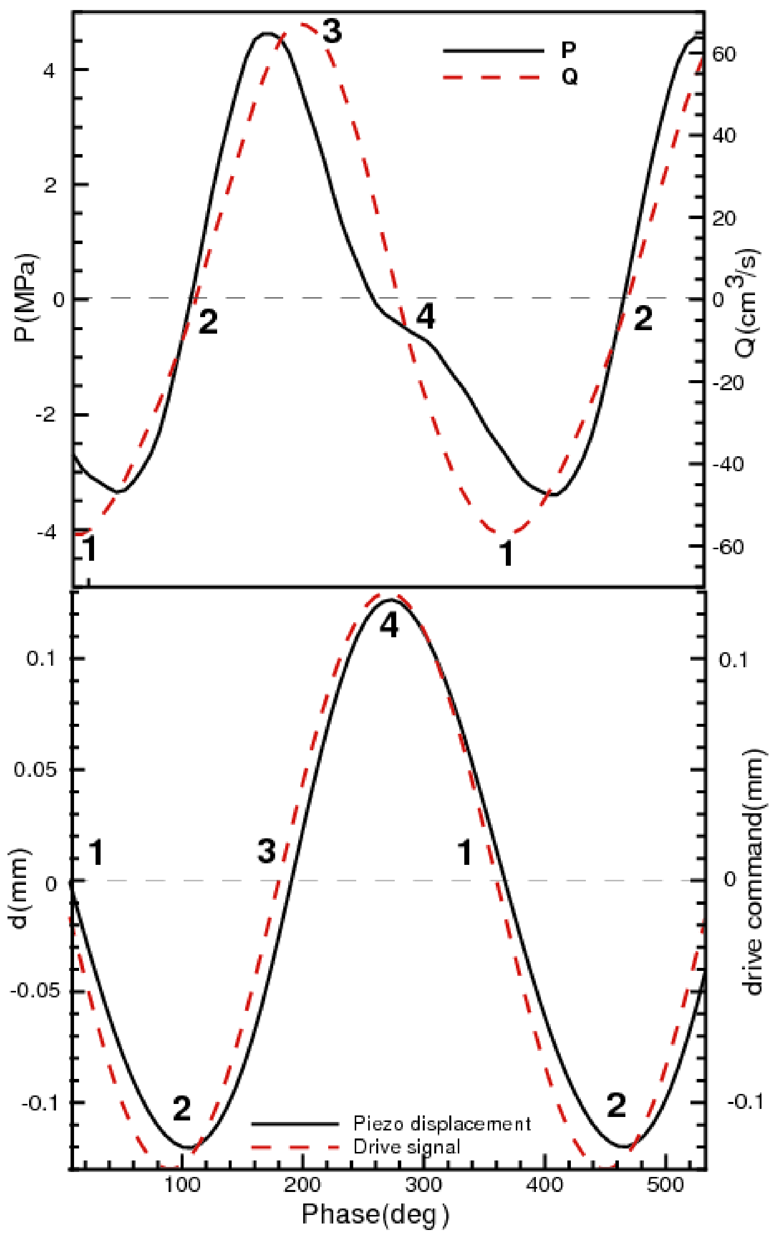

Figure 3.3: Variation of pressure and volume flow rate with phase for 100Hz excitation

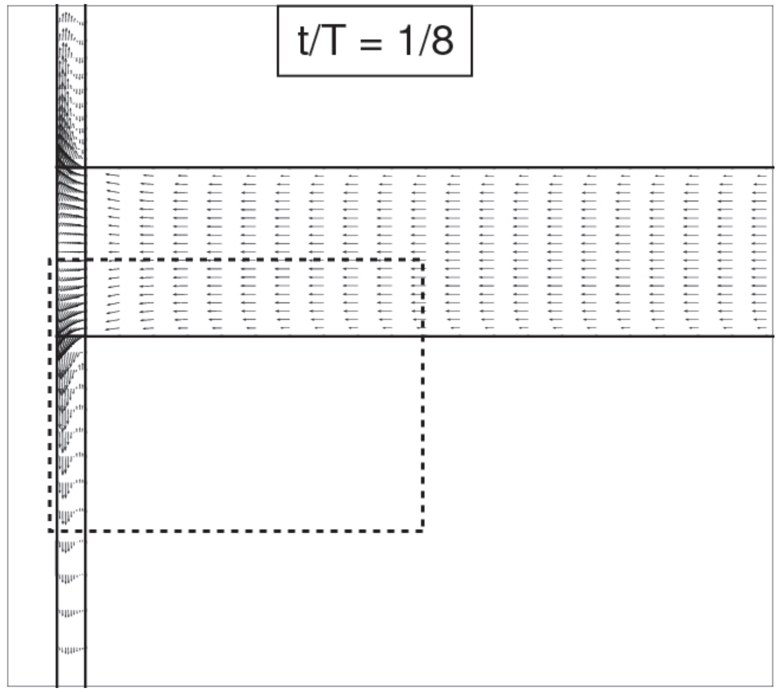

(a) Flow field

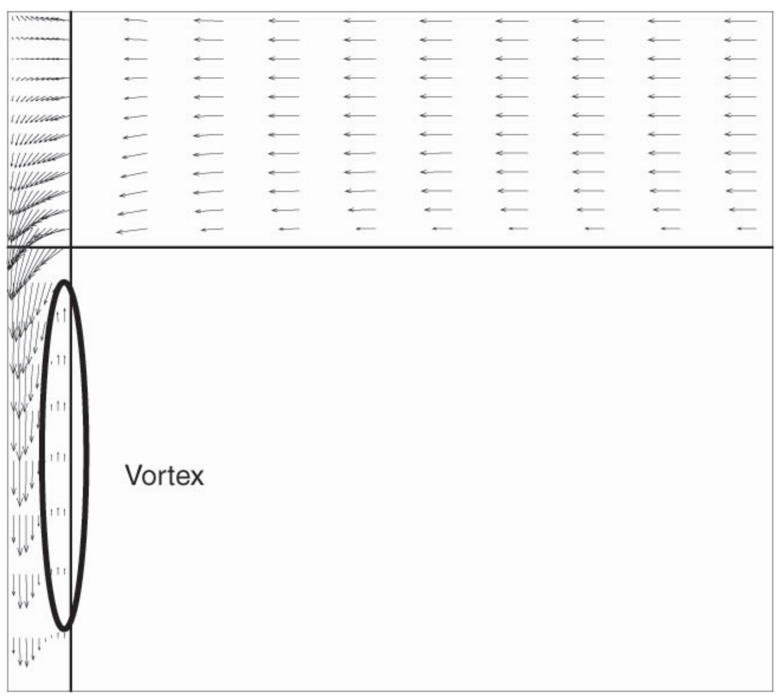

(b) Detailed section

Figure 3.4: Velocity vectors at one-eighth time period.

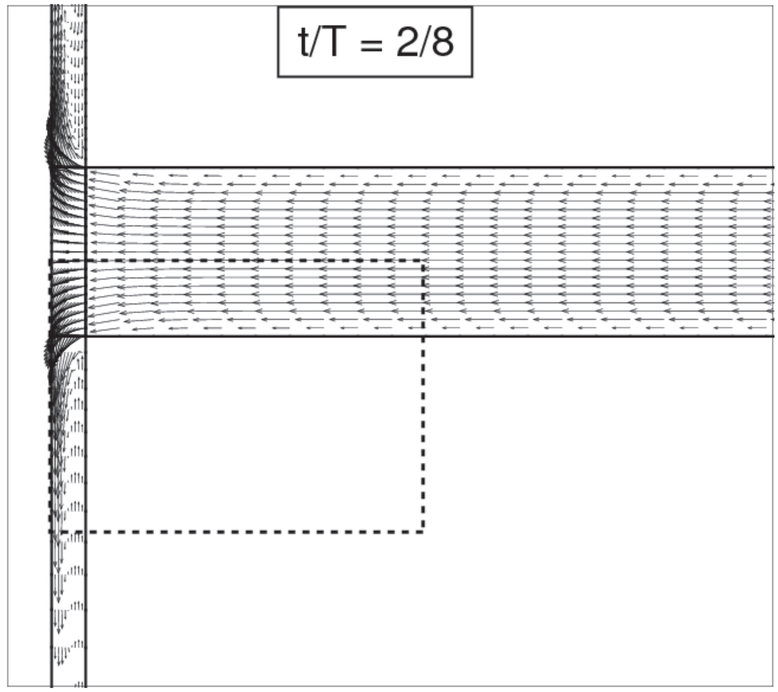

(a) Flow field

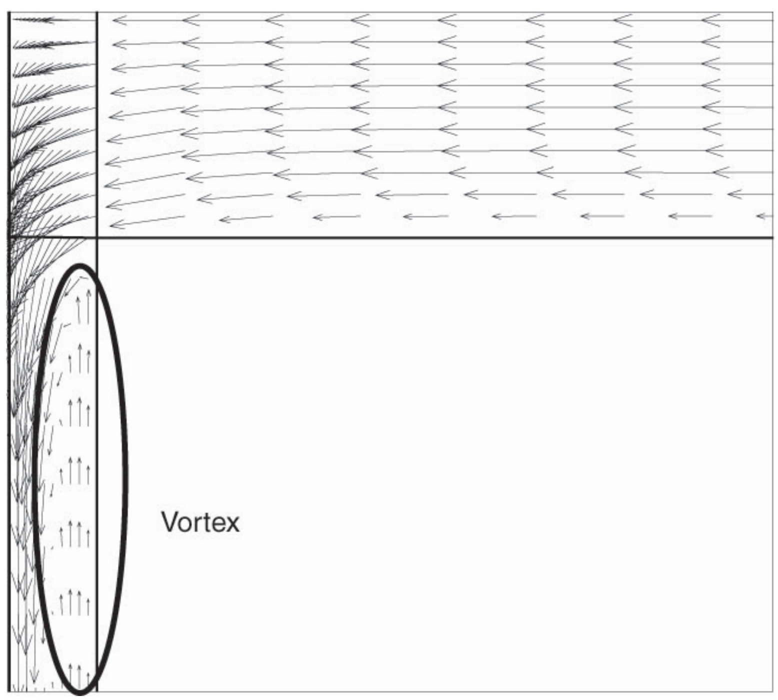

(b) Detailed section

Figure 3.5: Velocity vectors at quarter time period

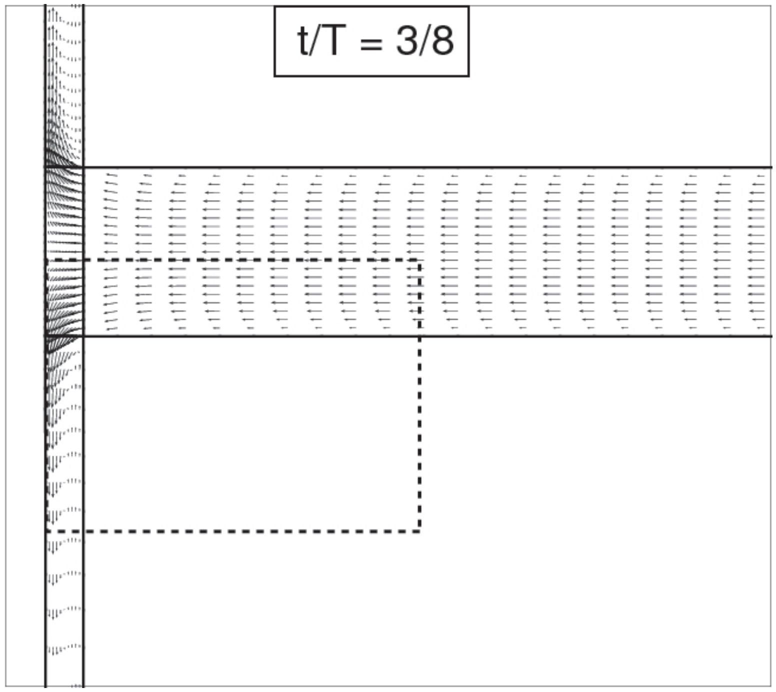

(a) Flow field

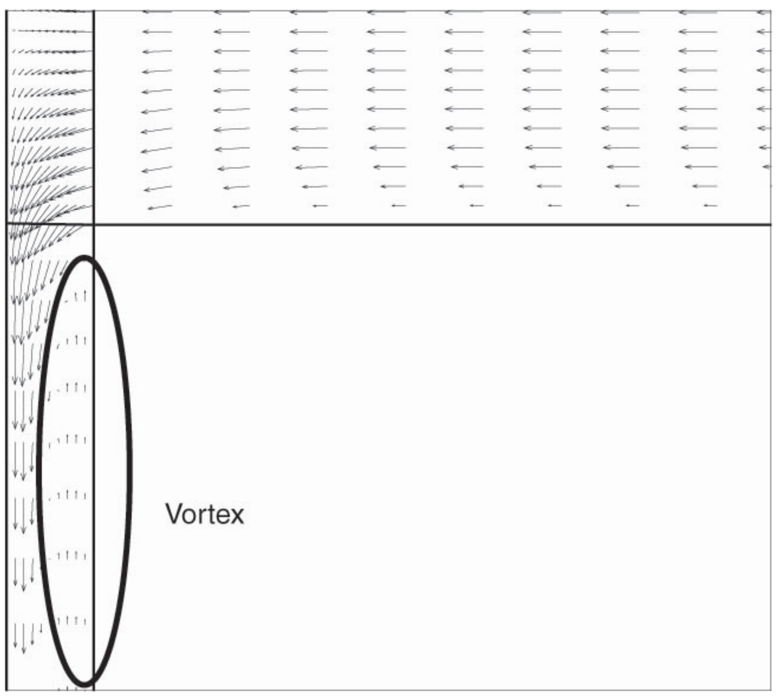

(b) Detailed section

Figure 3.6: Velocity vectors at three-eighth time period

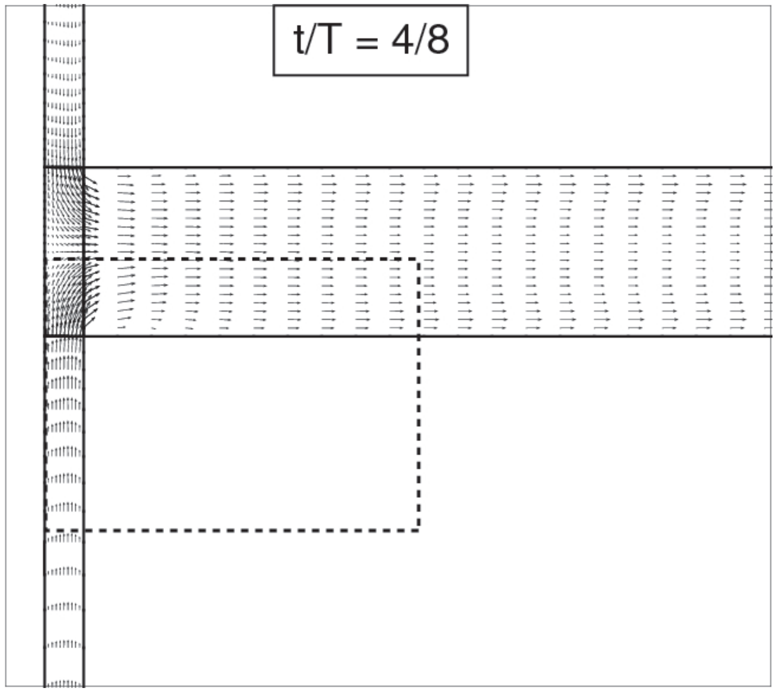

(a) Flow field

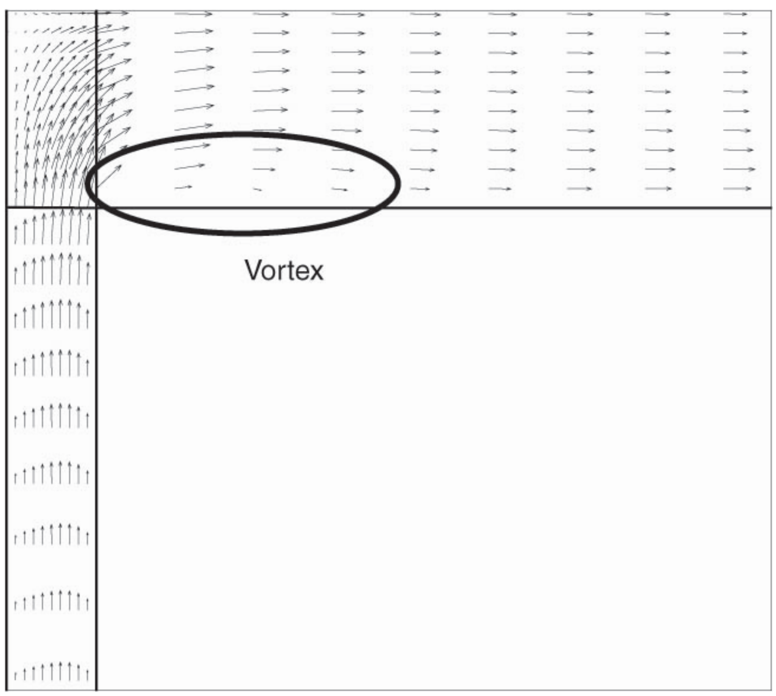

(b) Detailed section

Figure 3.7: Velocity vectors at half time period

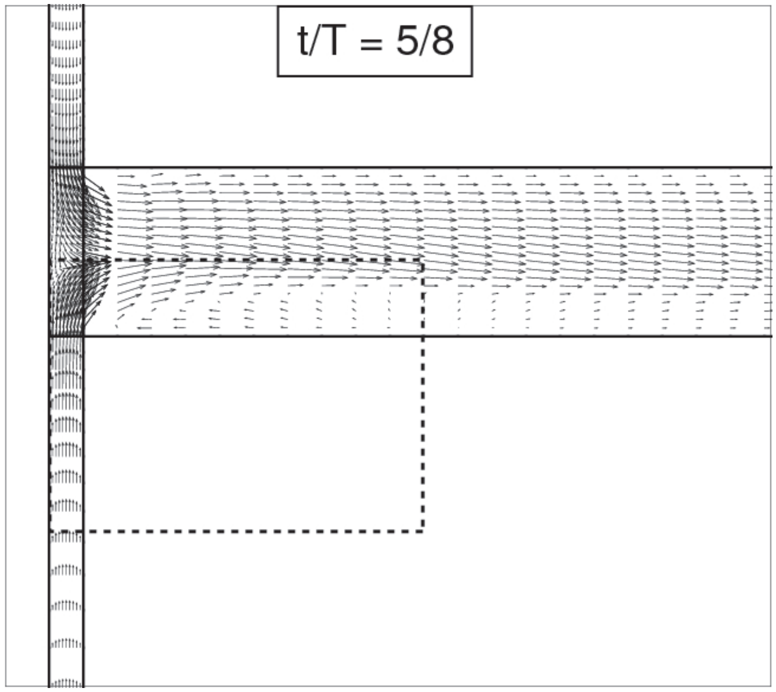

(a) Flow field

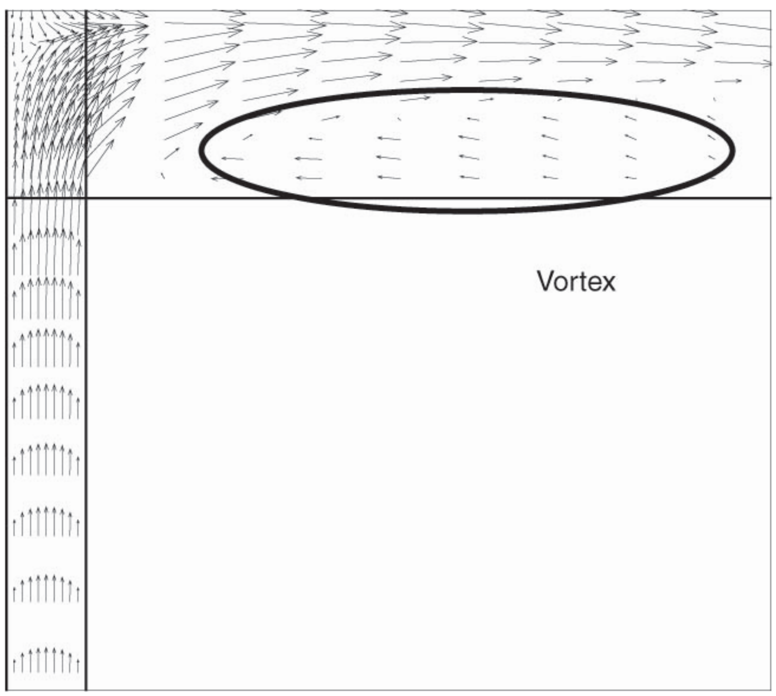

(b) Detailed section

Figure 3.8: Velocity vectors at five-eighth time period

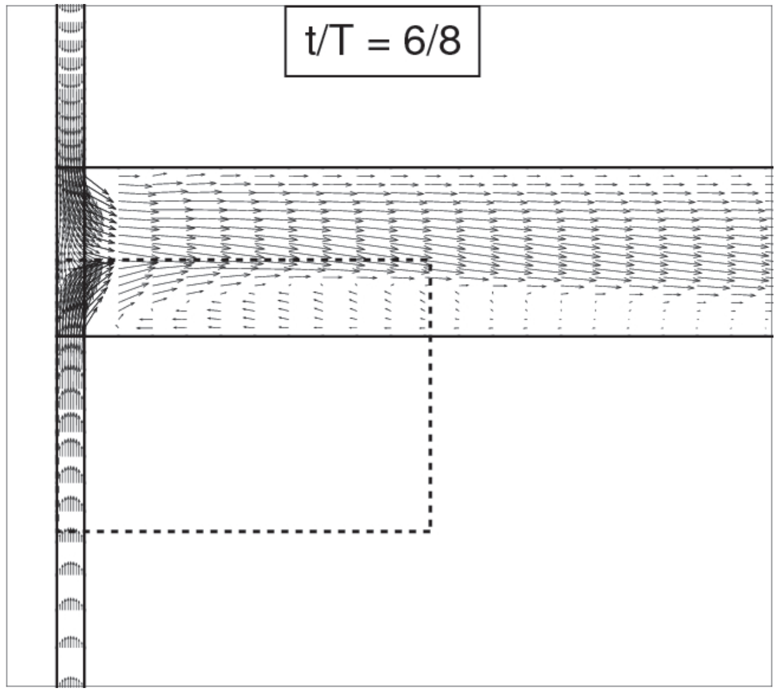

(a) Flow field

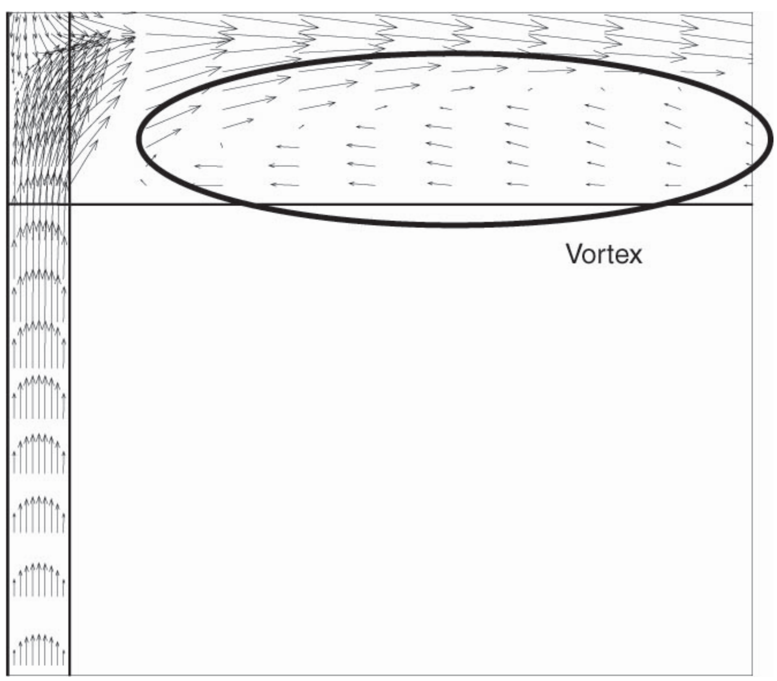

(b) Detailed section

Figure 3.9: Velocity vectors at three quarter time period

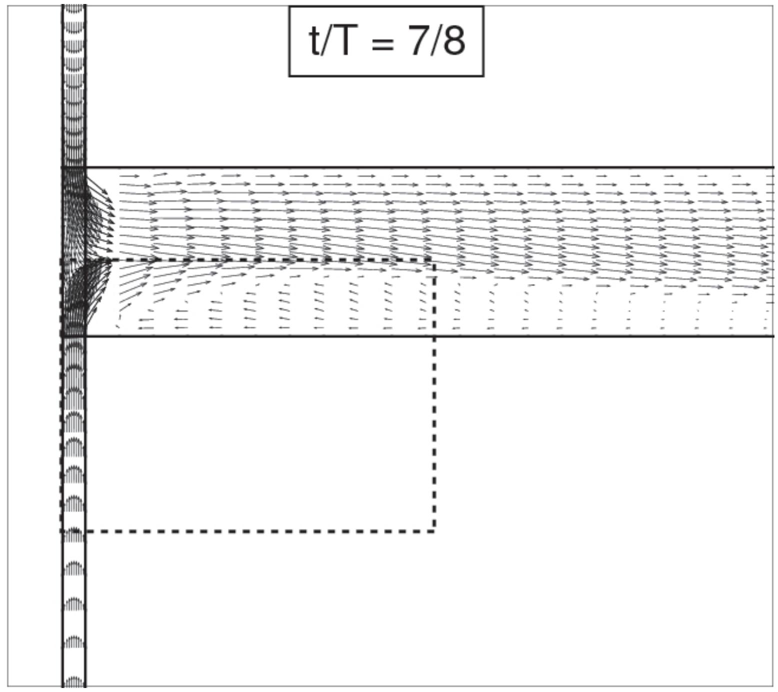

(a) Flow field

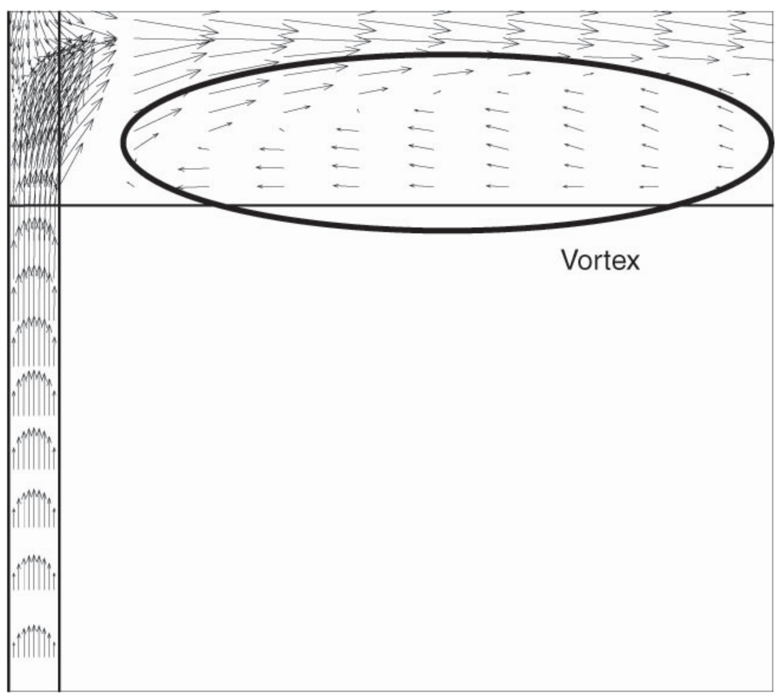

(b) Detailed section

Figure 3.10: Velocity vectors at seven eighth time period

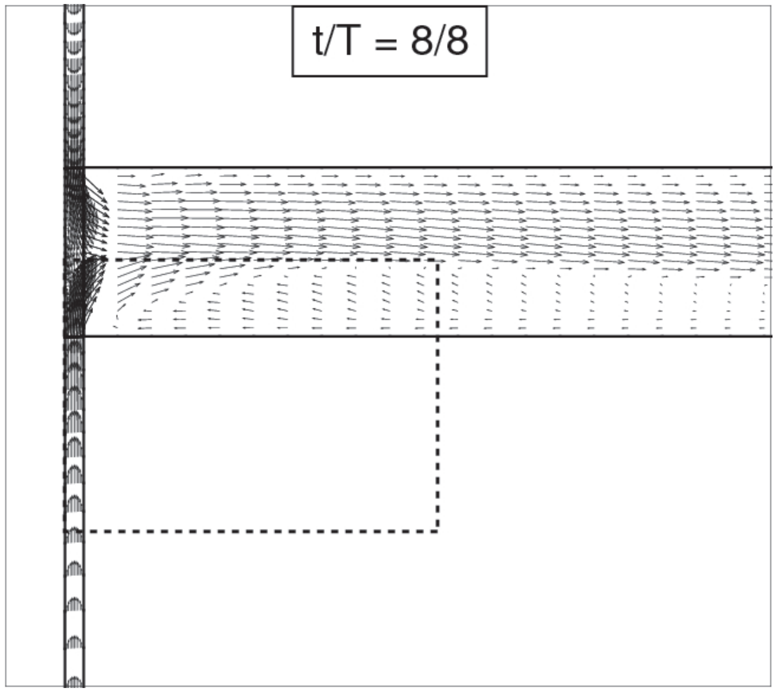

(a) Flow field

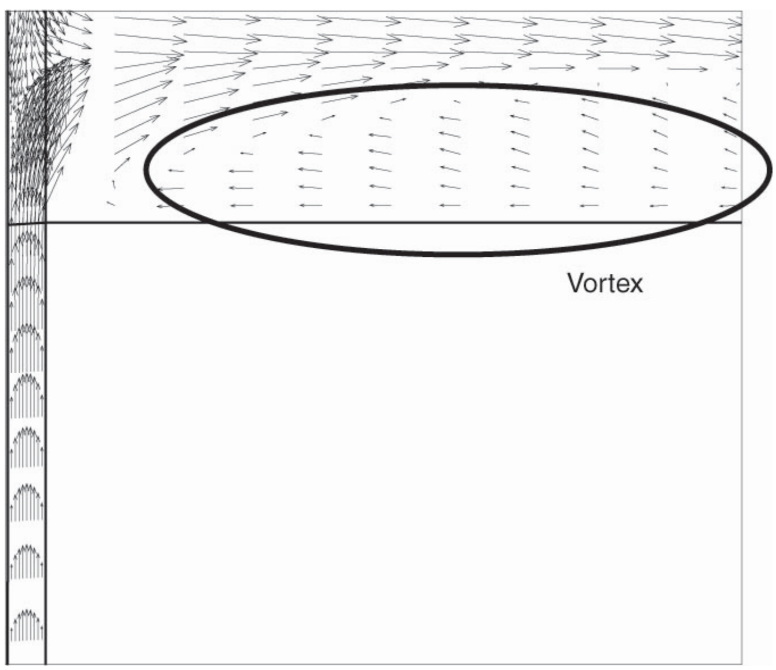

(b) Detailed section

Figure 3.11: Velocity vectors at one time period

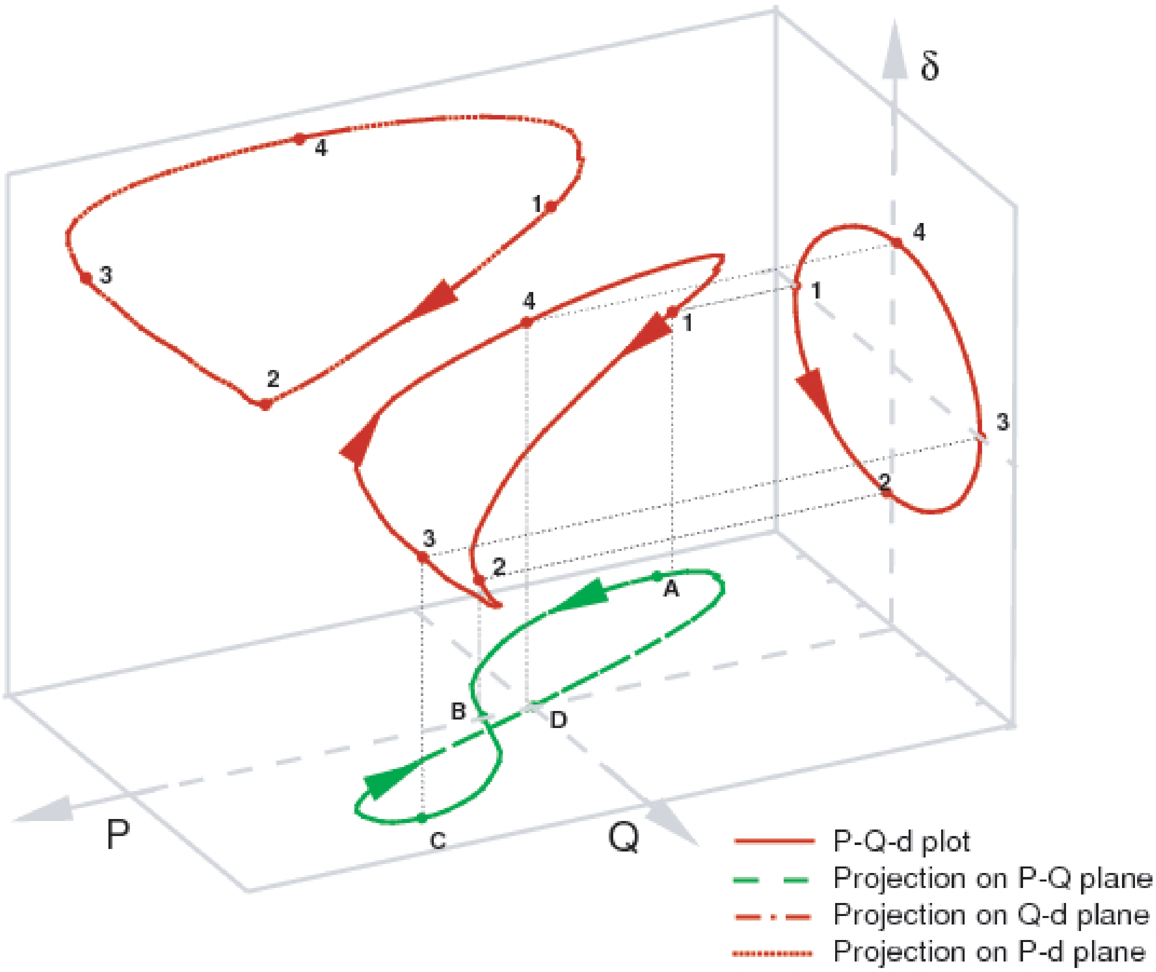

Figure 3.12: 3-d plot of pressure, flow rate and piston displacement for 100Hz excitation and its projection on P-d, Q-d and P-Q planes

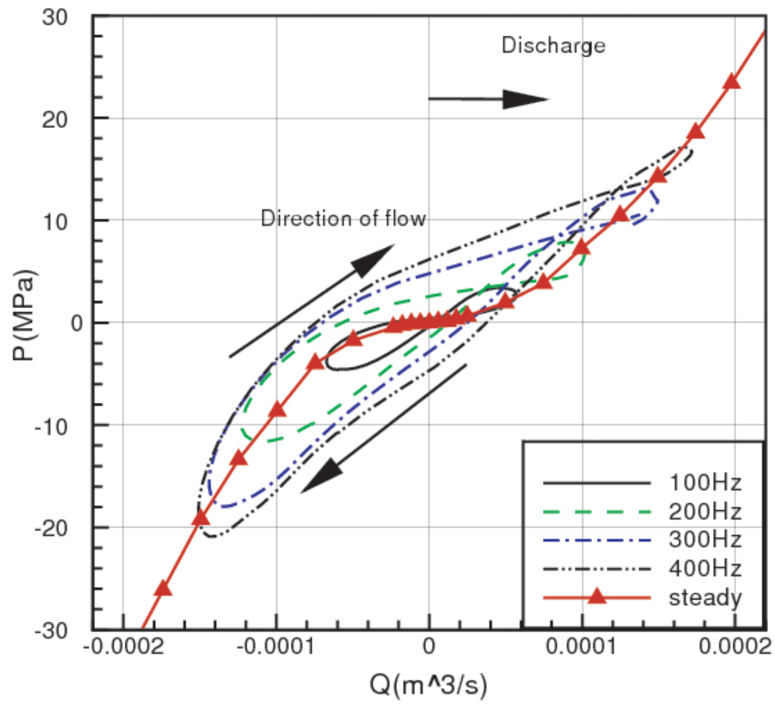

(a) 100Hz - 400Hz

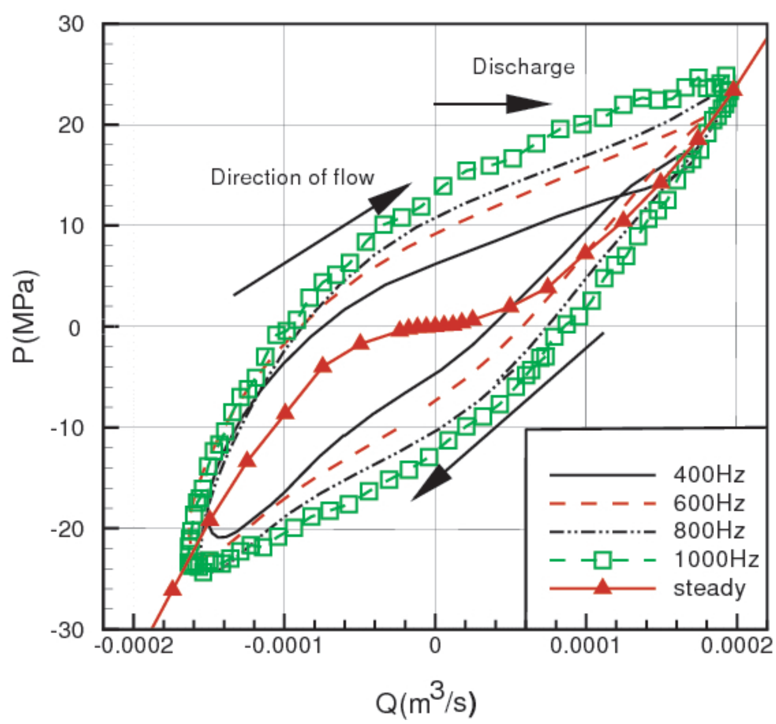

(b) 400Hz - 1000Hz

Figure 3.13: Variation of flow rate with pressure for pumping frequencies 100Hz - 1000Hz

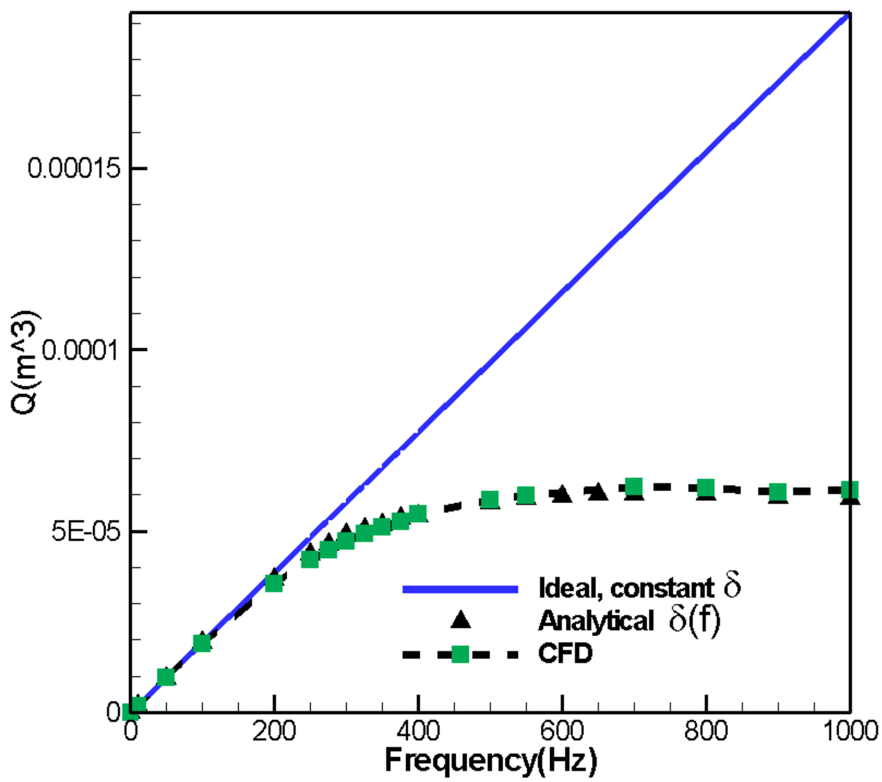

Figure 3.14: Variation of peak net flow rate, ideal flow rate and the flow rate from simplistic model prediction

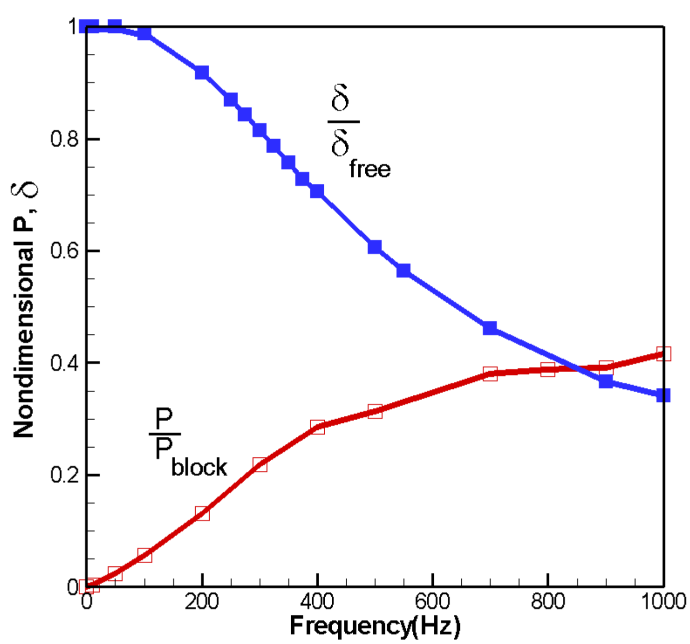

Figure 3.15: Variation of pressure and nondimensionalised piezo stack displacement with frequency

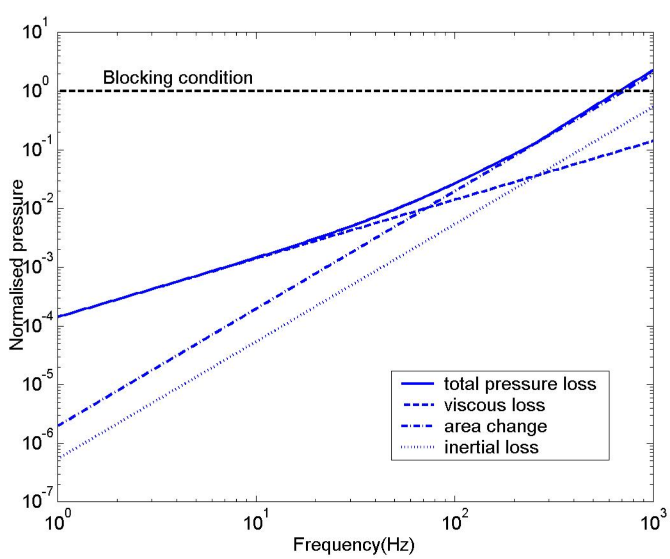

Figure 3.16: Scaling of total and component pressure losses with actuation frequency

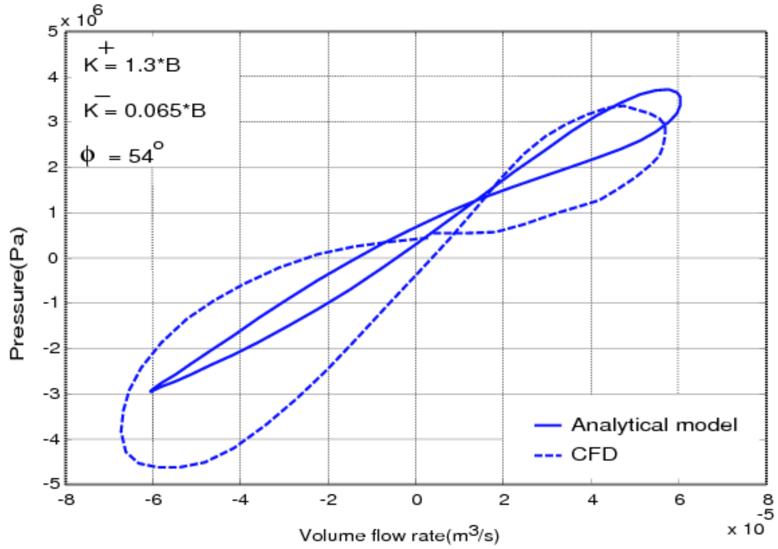

(a) 100Hz

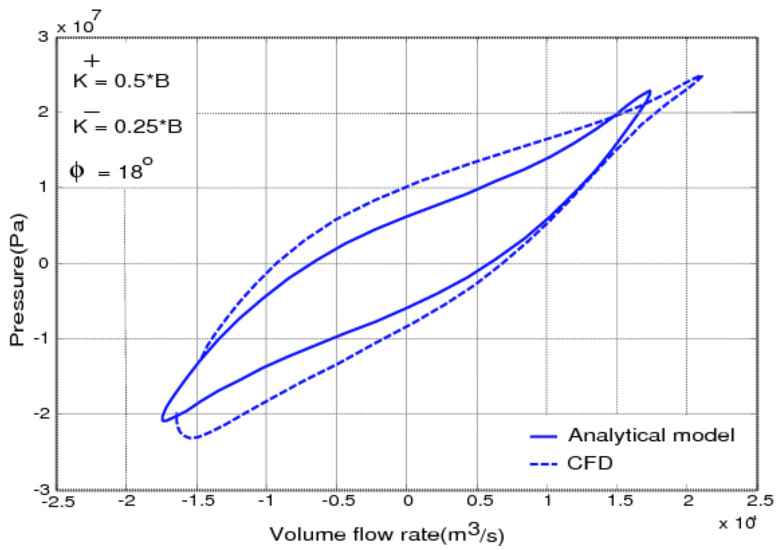

(b) 700Hz

Figure 3.17: Comparison of CFD results with the analytical model for pumping frequencies 100Hz and 700Hz.

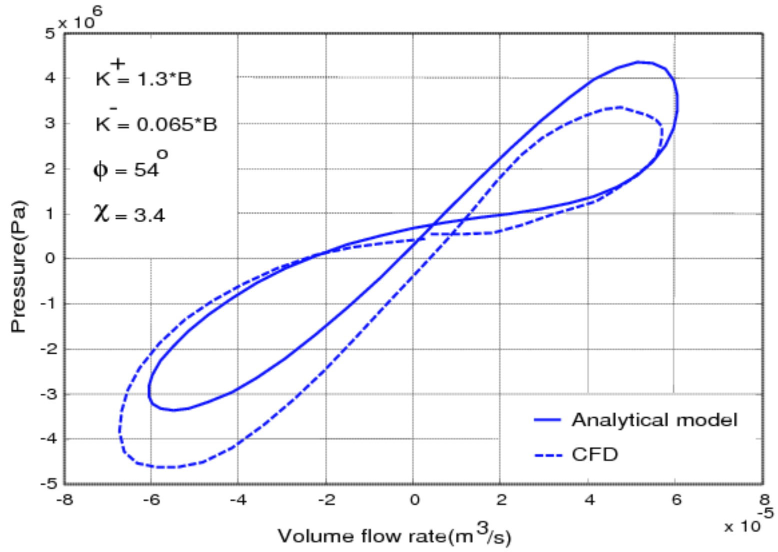

(a) 100Hz

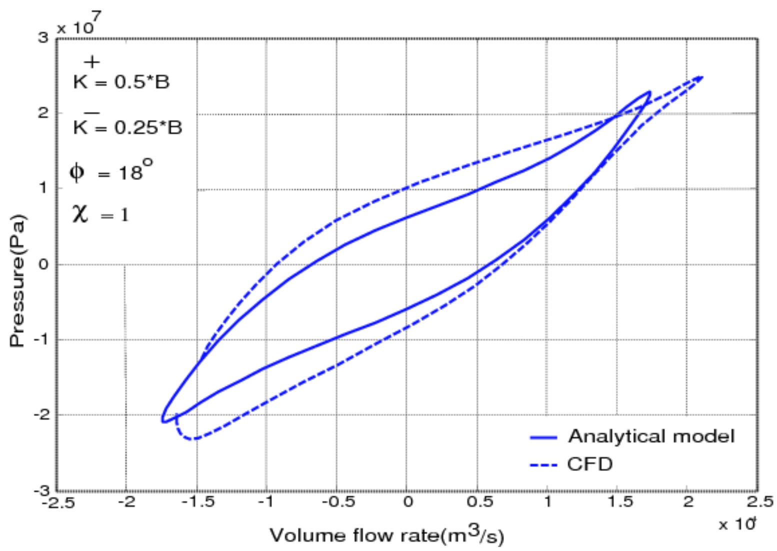

(b) 700 Hz

Figure 3.18: Comparison of CFD results with the modified analytical model for pumping frequencies 100Hz and 700Hz.

Chapter 4

A Hybrid Hydraulic Actuation System - Development and Testing

A hybrid hydraulic actuation system has distinct advantages over conventional hydraulic or electric actuators when it comes to applications like the active pitch link for a helicopter rotor. Apart from providing the adequate forces required to move the rotor blade, an active pitch link must also have a low number of mechanical moving parts. This is due to the high levels of centrifugal forces experienced by a pitch link of a helicopter that might cause moving parts to seize. For Individual Blade Control (IBC) techniques to tackle problems of vibration and noise reduction, the actuator must also be able to provide bi-directional actuation to the blade over a wide range of frequencies. Two of the most prominent design constraints for actuators considered for aerospace applications are the weight and the frontal area or volume of the actuator. The proposed solution should not cause an excessive weight or drag penalty. Three types of actuators can be considered as candidates for an active pitch link - hydraulic, electric and hybrid hydraulic systems.

- Traditionally, the actuators used in the aerospace industry are hydraulic actuators using a centralized pressure source and connecting fluid lines to convey the pressurized fluid to the location of the specific application. Hydraulic systems have the advantage of being able to deliver large forces. However, conventional hydraulic systems need complex redundancy systems and routine maintainance due to leakage issues. Also, conventional systems have servo-valves that are mechanically complex and have a high number of precision moving parts that reduce reliablity. A pitch link on a full scale UH-60 helicopter experiences a centrifugal load of 350 g. Such high levels of centrifugal acceleration causes increased stiction in high precision moving parts that are designed with low tolerances. Therefore, an actuator design with no moving mechancal parts will be especially suited for such applications involving high centrifugal loading. Conventional hydraulic systems with a centralized pressure source have been adapted for use as an active pitch link (Arnold and Strecker, 2002). The pressurized fluid has to be transmitted through fluid lines from the fuselage to a rotating environment like the rotor blades through a hydraulic slipring. Hydraulic sliprings are mechanically complex and also introduce a large weight penalty.

- Electric motors can be used as the actuator for the active pitch link. The basic advantage of using electric motors is that electric power can be transmitted to each rotor blade relatively easily through electrical slip rings. Also, electric motors offer higher power to weight ratio and reliability as compared to hydraulic systems. However, since electric motors have to be operated at very high rotational speeds, issues relating to bearing life become relevant. An electric motor based actuation system will also require gear systems to reduce the speed of the electric motor. Gear systems introduce additional penalties to the systems and also introduce reliability issues under centrifugal loading.

- Hybrid hydraulic systems are self-contained actuation systems containing an active material driven hydraulic pump or pressure source and a valving system. Such systems use the high energy density of active materials like piezoelectrics, electrostrictives or magnetostrives to produce a compact pressure source. Magnetorheological fluid is used as the hydraulic fluid in the pressure source and their rheological properties can be utilized to make fluidic valves. Such a valving system is activated using an appropriate electrical current provided to a coil (which generates a magnetic field).

A hybrid hydraulic actuation system scores favorably over conventional actuator technology in many of the requirements needed for an active pitch link. Magnetorheological fluids enable the design of a fluidic valving system without any moving parts. Active materials like Terfenol-D have high energy density. This enables the construction of compact actuation systems that do not involve a large drag penalty. Also, since the hybrid hydraulic actuation system is a self-contained unit, there is no necessity for hydraulic slip rings, thus greatly reducing the mechanical complexity and weight penalty. The only draw back of hybrid hydraulic systems is the fact that current hybrid actuator technology has demonstrated only a much smaller force capability. The Terfenol-D based pump was developed at the University of Maryland (Chaudhuri et al., 2006b) and is an improvement of an earlier designed developed as a part of the Compact Hybrid Actuator Program (CHAP) (Ellison, 2004). The valving system was also developed at the University of Maryland and preliminiary uni-directional tests were done using a gear pump (Yoo et al., 2005). A more detailed description of the construction and operation of the actuator and the valving system is given in subsequent sections.

4.1 Actuator Construction

An isometric layout view of the magnetostrictive pump assembly is shown in Figure 4.1. The hybrid magnetostrictive pump consists of three main parts.

- The pump body which houses the active material (Terfenol-D in this case), magnetizing coil and the preloading mechanism. One end of the pump body is the pump base which is fixed tightly to the pump body and the other end contains the pump piston.

- The pumping chamber containing the working fluid (magnetorheological fluid) that is pressurized by the motion of the piston. The two sides of the pumping chamber are the pump piston (being pushed by the Terfenol-D stack) and the reed valve assembly

- The pump head houses the reed valves that are used for frequency rectification.

The Terfenol-D stack used in this pump was 2" (50.8 mm) long and had a diameter of 0.5" (12.7 mm). Magnetic field is applied to the stack using a magnetizing coil which is also housed in the pump body. The magnetizing coil is made by winding 28-gage insulated copper wire on a plastic bobbin. The Terfenol-D rod forms the core of the coil. The pump body is made of magnetic steel to provide a flux return path to the magnetic field lines. The magnetostriction obtained from the stack increases when an optimum preload is applied (Calkins et al., 1997). The Terfenol-D rod can be preloaded by tightening the end cap using disc springs present within the housing. Another reason for preloading the stack is the fact that the Terfenol-D material should always operate in a state of compression. The pump piston is a precision machined component which has a running fit with the inside of the pump body with tolerances of less than 0.001". This ensures that the piston motion is purely linear and follows the motion of the Terfenol-D stack. Larger tolerances results in a wobbling rocking motion of the piston. Such a wobbling motion results in a less than optimum volume displacement and lower performance. The piston can be seen in Figure 4.2. The piston has a diameter of 1.5" (38.1 mm). The diaphragm is made of spring steel and has a thickness of 0.002" (0.05 mm).

The pump head assembly can be seen in Figure 4.3. The reed valves are housed in the pump head and are made of spring steel and serve as unidirectional ports for flow of fluid into and out of the pumping chamber. The effect of using reed valve thickness on the performance of the actuator has been tested before (Chaudhuri et al., 2006a). It was observed that the actuator configuration with a 4 mil thick reed valve resulted in maximum no-load output velocity. Hence, this particular reed valves was used for all further testing. The pump head assembly connects the fluid in the pumping chamber to the valve system and has two separate ports for fluid leaving and entering the chamber. The opening of each port is controlled (passively) by the deflection of the corresponding reed valve and the deflection of the reed is governed by the pressure difference across it. In Figure 4.3, we can clearly see the reed valve for the inlet port that opens into the pumping chamber, thus allowing fluid from the low pressure driven side to enter the pumping chamber.

4.1.1 Actuator operation

A typical hybrid hydraulic pump uses the principle of frequency rectification to produce a net flow rate from the pump. The frequency rectification is performed by passive uni-directional reed valves housed inside the pumping head of the actuator. The pump operates in four distinct stages, as seen in Figure 4.4.

- Compression stage: The first stage or *compression*, as shown in Figure 4.4(a), involves the expansion of the hybrid material stack. The stack pushes the piston and this action pressurizes the fluid in the chamber. The discharge reed valve is designed to only allow the flow of fluid out of the pumping chamber. In this stage, the pressure difference between the pumping chamber and the discharge tube is not large enough to open the discharge reed valve. Since there is no discharge fluid flow out of the chamber during this stage, the pressure in the chamber and the density of the fluid in the chamber increases. The intake reed valve is closed during this stage as the pressure in the chamber is greater than the pressure in the intake tube.

- Discharge stage: In the second stage or *discharge*, shown in Figure 4.4(b), the pressure difference between the chamber and the discharge tube becomes large enough to crack open the discharge reed valve and fluid starts to flow out of the chamber into the discharge tube. Fluid flows out of the pumping chamber as the stack continues to expand. The pressure and density of the fluid in the chamber changes only slightly as the fluid is free to flow out of the chamber in response to the piston motion. The intake reed valve remains closed during this stage also.

- Expansion stage: In the *expansion* stage, shown in Figure 4.4(c), the hybrid stack contracts, the piston retreats and the pressure in the pumping chamber starts to reduce. The intake reed valve is designed to only allow the flow of fluid into the pumping chamber. During this stage, there is no mass flow rate into the chamber as the pressure difference between the intake tube and the pumping chamber is not large enough to open the intake reed valve. The discharge reed valve is closed during this stage as the pressure in the chamber is less than the pressure in the discharge tube of the pump.

- Intake stage: In the *intake* stage, shown in Figure 4.4(d), the pumping chamber pressure drops further and the pressure difference between the chamber and the intake tube becomes large enough to crack open the intake reed valve and the fluid flows into the chamber as the hybrid stack and piston retreat further. The discharge reed valve remains closed during this stage as well.

These four stages are repeated every pumping cycle and result in a net mass flow rate out of the pump through the discharge tube and an equivalent mass flow rate into the pump through the intake tube.

The different stages of operation of the pump can also be described in terms of the force and displacement of the active stack. This allows us to understand the exact mechanism of work output from the actuator. We consider an ideal hydraulic fluid with infinite stiffness. Figure 4.5 shows the pumping cycle of a typical hybrid hydraulic actuator with an ideal working fluid. Here, AB shows the force displacement characteristics of the Terfenol-D stack, also called the load line. The compression stage, where the Terfenol-D stack expands and pressurizes the fluid in the pumping chamber, is shown as line OC. Since the hydraulic fluid is considered to be ideal, the pressure in the pumping chamber increases without the fluid undergoing any deformation. When the pressure of the fluid in the pumping chamber is large enough to overcome the load pressure, the pressurized fluid starts to flow out of the pumping chamber. This stage has been described as the discharge stage. This stage, where the fluid flows out of the chamber and the load undergoes displacement, is denoted by the line CD. Useful work is done during this stage. This stage continues till the displacement of the Terfenol-D stack reaches the maximum allowable value under the force considerations. After the maximum displacement, δ_0, is reached, the stack starts to contract (the expansion stage occurs). This stage, where the pressure in the pumping chamber drops is given by line DE. When the inlet reed valve opens, fluid flows back into the pumping chamber, thus restoring the stack back to its original displacement, that is, point O. The work done by the actuator during this pumping cycle is the area OCDE.

A real hydraulic fluid, however, has a finite value of bulk modulus. This results in the deformation of the fluid during the compression stage. The actuator will no longer work along the line OA, but OA', as seen in Figure 4.6. The slope of the line OA' is the stiffness of the fluid in the pumping chamber. When the pressure in the fluid equals the pressure required to crack open the reed valve and to move the load, the load starts to move and the actuator does useful work. Thus, for an actual working fluid with a less than infinite bulk modulus, the actuator operates in the polygon given by O'C'D'E'. The area O'C'D'E' is lower than the area OCDE due to the energy stored in the compressible fluid. This energy is returned to the stack at the end of the cycle and is not converted into useful work. Since the exact values of the force required to crack open the valves and the bulk modulus of the working fluid is difficult to ascertain, the ideal work output, or area OCDE, is usually used as the metric to measure the power output capability of the actuator.

4.2 MR Valve Network Concept and Construction

As a result of one typical pumping cycle, the flow emanating from the hybrid pump is uni-directional and, by itself, can only produce a uni-directional motion in the output cylinder shaft. All practical applications require the load to move in a bi-directional fashion. A valving system that will reverse the direction of the flow entering the output cylinder is necessary to move the cylinder shaft in both directions. The unique rheological properties of MR fluids can be used to make fluidic valves. One major disadvantage of this type of fluidic valves is the low blocked force. However, through previous studies at the University of Maryland, the MR valve performance has been optimized with the given volume (Yoo et al., 2005; Yoo and Wereley, 2002).

A schematic of the proposed hybrid actuation system is shown in Figure 4.7. The entire actuation system consists of four MR valves arranged in a Wheatstone bridge configuration, an accumulator, a Terfenol-D driven pump and an output cylinder. The accumulator is used to apply bias pressure to the hydraulic circuit. Applying bias pressure to the hydraulic circuit serves two functions:

- Bias pressure increases the stiffness of the fluid by increasing the bulk modulus of the fluid. Entrained air renders the hydraulic fluid compressible and reduces the amount of energy that can be transfered from the Terfenol-D stack to the load. This effect of entrained air is reduced by application of a bias pressure. Also, a vacuum is applied on the hydraulic fluid in the system before the start of operation to eliminate the entrained air as much as possible.

- Application of bias pressure reduces the possibility of cavitation in the fluid. Cavitation occurs when the absolute pressure of the fluid dips below the vapor pressure of the fluid. This causes the fluid to evaporate and form a two-phase system. Cavitation severely affects the performance of the actuator.

4.2.1 MR valve network operation

In the active mode, the pump functions as the pressure source to the system and the output displacement of the output cylinder shaft is controlled by activating the MR valve network.

In Figure 4.7(a), the Terfenol-D pump forces the fluid through the MR valve Wheatstone bridge network. Applying current to valves 2 and 4 prevents the MR fluid from flowing in these valves, thus forcing the fluid to flow through valves 1 and 3. Thus the fluid flows from the high pressure side of the pump through valve 1 into the lower chamber of the output cylinder, thus forcing the cylinder shaft to move upwards, as shown by the arrow in the figure. As the cylinder shaft moves upwards, the fluid in the upper chamber of the output cylinder flows through valve 3 back into the accumulator and the low pressure side of the pump, marked L. Under ideal conditions (if the blocking pressure of the MR valves is infinite), there is no leakage flow through valves 2 and 4. However, in a real system, valves 1 and 4 permit a very small leakage flow through them. This leakage flow is very low as compared to valves 1 and 3.

Figure 4.7(b) shows the schematic for reversing the direction of motion of the output cylinder shaft. We can see in this figure that the current is to valves 1 and 3 only. This closes the fluid path in valves 1 and 3 while allowing the fluid to flow through valves 2 and 4. Thus the fluid flows from the high pressure side of the pump through valve 2 to the upper chamber of the output cylinder. This forces the cylinder shaft to move downwards as seen in the figure. As the cylinder shaft moves downwards, the fluid in the lower chamber of the cylinder moves through valve 4 to the accumulator and the low pressure side of the pump. Thus, switching the applied current from valves 2 and 4 to 1 and 3 allows the fluid to flow to the opposite sides (upper and lower) of the output cylinder, thus producing bi-directional motion.

4.2.2 MR valves

The MR valves used in this study consist of a core, flux return and an annulus through which the MR fluid flows. This can be seen in Figure 4.8. The core is wound with insulated copper wire. A current applied through the wire coiled around the bobbin creates a magnetic field in the gap between the flange and the flux return. The magnetic field increases the yield stress of the MR fluid in this gap. This increase in yield stress alters the velocity profile of the MR fluid in this gap and raises the pressure difference required for a given flow rate. If the applied magnetic field is sufficiently large, then the pressure difference across the valve is not able to surpass the yield stress of the MR fluid and the valve remains blocked. The main parts of the MR valve can be seen in Figure 4.9.

A 1-D axisymmetric analysis for the flow of MR fluids have been given by Kamath *et.al.*(1996), and an approximate rectangular duct analysis was provided by Wereley and Pang(1998). Gavin provided an analysis for annular valves with more appropriate radial field dependence (Gavin et al., 1996a). In the present study, we assume a uniform field across the valve gap and a rectangular duct analysis of Poiseuille flow through a valve system containing MR fluid (Wereley and Pang, 1998). For a Newtonian flow, the volume flux Q through the valve is a function of the area moment of inertia of the cross-section, $I = bd^3/12$, the viscosity of the MR fluid and the pressure drop over the valve length, $\Delta P/L_a$. Depending on the rheological model used, the dimensional volume flux through the valve can be determined (Wereley and Pang, 1998; Lindler and Wereley, 2000).

$$Q_N = \frac{bd^3\Delta P}{12\mu_{po}L_a} \tag{4.1}$$

$$Q_{BP} = \frac{bd^3\Delta P}{12\mu_{po}L_a}\left(1-\overline{\delta}\right)^2\left(1+\frac{\overline{\delta}}{2}\right) \tag{4.2}$$

$$Q_{BV} = \frac{bd^3\Delta P}{12\mu_{po}L_a}\left[\left(1-\overline{\delta}\right)^2\left(1+\frac{\overline{\delta}}{2}\right)+\frac{3}{2}\overline{\mu}\left(1-\frac{\overline{\delta}^2}{3}\right)\overline{\delta}\right] \tag{4.3}$$

where, Q_N is the volume flux for Newtonian flow, Q_{BP} is the volume flux for Bingham plastic flow and Q_{BV} is the volume flux for bi-viscous flow. The non-dimensional plug thickness is given by $\overline{\delta} = \delta/d$, and non-dimensional viscosity ratio, $\overline{\mu}$ is the ratio of the post-yield to pre-yield fluid viscosity. A more detailed description of the different rheological models describing MR fluids is given in the Appendix.

Key geometric properties like the bobbin shaft diameter, bobbin flange thickness and the gap between the bobbin flange outer diameter and the flux return is given in Table 4.1 and can also be seen in Figure 4.8. The flux return and bobbin were made of a high permeability material called HIPERCO to maximize the flux density. Previous studies have shown the feasibility of using magnetorheological fluid-based valves to produce the bi-directional motion of the output cylinder shaft (Yoo and Wereley, 2004). This chapter explores the capabilities of such an MR actuation system.

4.3 Scope of Work

A range of experimental studies were done on the magnetorheological actuation system. The output displacement was measured at the output cylinder shaft using an LVDT and the average output velocity was calculated as the slope of a linear fit to the displacement data. The range of experimental tests can be categorized in the following manner.

- Uni-directional tests

  - No load testing: The actuator does not work against any external load as the output cylinder shaft is allowed to move freely. These tests give the maximum obtainable volume flow rate from the actuator. By performing a frequency sweep over a range of pumping frequencies at which the Terfenol-D stack can be operated, the resonant frequency of the hydraulic system can be ascertained.
  - Load testing: The actuation system works against graduated weights are hung at the end of the output cylinder shaft. These tests give the blocked force, power output and electromechanical efficiency of the actuator.

- Bi-directional tests
  - No load testing: The actuator does not work against any external load as the output cylinder shaft is allowed to move freely. These tests give the frequency bandwidth of the actuation system.
  - Load testing: Different types of load are attached to the output cylinder shaft and the actuator is made to work against these loads.
    * Stiffness loading: Pre-loaded springs are attached to either end of the shaft so that the actuator sees a constant stiffness at all values of the output stroke. These tests measure the system performance under external stiffness loads.
    * Inertial loading: Graduated weights that are supported on linear bearings are attached to the cylinder shaft and the actuation system is activated. These tests measure the system performance as it works against pure inertial loads.

4.4 Results and Discussion

4.4.1 Uni-directional No-Load Test

In these tests, a magnetic field is applied on two MR valves of the MR Wheatstone bridge setup so that flow through them is prevented. This forces the MR fluid to flow exclusively in the other arm of the bridge, thus moving the output cylinder shaft in one direction. Referring to Figure 4.7(a) magnetic fields were applied to valves 2 and 4, thus moving the cylinder shaft in the upward direction. A sinusoidally varying current of a particular frequency is applied to the magnetizing coil around the Terfenol-D stack to induce strain in the stack to provide the pumping action to the device. The output motion is measured in the output cylinder shaft and its velocity is measured using an LVDT. In no-load testing, the output cylinder shaft is not attached to any external load and is allowed to move freely. Thus we can obtain the highest output velocity obtainable from the system. This also gives the maximum obtainable volume flow rate obtainable from the pump at that particular pumping frequency. The frequency of the actuating signal provided to the Terfenol-D stack is then changed in a systematic manner to map out the entire frequency range of interest. The results of this experiment can be seen in Figure 4.10. The legend gives the bias pressure applied to the MR fluid and the maximum current applied to each MR valve. We can see that the device resonance is at a pumping frequency of 125 Hz. Earlier tests on this actuator (Chaudhuri et al., 2006b) using a hydraulic oil shows the resonance at 600 Hz pumping frequency. The resonant frequency has come down in the present study due to the high inertia of the MR fluid in comparison with the hydraulic fluid (the density of the MR fluid is almost four times that of the hydraulic fluid). The maximum output shaft velocity obtainable from the system is around 50 mm/s at a pumping frequency of 125Hz. The maximum no-load velocity is also substantially lower than that of the case where hydraulic fluid is used (maximum no-load velocity in the case of hydraulic fluid is 89 mm/s). This is due to the greater viscous losses in the MR fluid owing to its greater viscosity.

4.4.2 Uni-directional Load Test

The procedure for these tests is the same as that of uni-directional no-load testing, which was described in the earlier sub-section titled *Uni-Directional No-Load Test*. However, graduated weights are hung at the end of the output cylinder shaft so that as the actuator pushes the output cylinder shaft, it has to work against the weight of the external load. Keeping the pumping frequency constant, the loads are gradually increased till the point where the actuator is not able to lift any more load. This process is then repeated for other values of pumping frequency to get the uni-directional load performance for all pumping frequencies in the range of interest.

We can plot the output velocity of the shaft versus the load for each pumping frequency to obtain the load line for the actuator at that particular pumping frequency. The load lines for pumping frequencies of 50, 100 and 150 Hz can be seen in Figure 4.11. The slope of the load line of the actuator is determined by the load versus displacement characteristics of the active material. Since the stiffness of the Terfenol-D stack is approximately linear, the load line of the entire actuator is also linear. The point where the load line intersects the velocity axis gives the no-load velocity obtainable from the system at that particular pumping frequency. The point where the load line intersects the load axis is called the $block\ force$ of the actuator. This point denotes the maximum load that can be lifted by the actuator and is the maximum force that can be exerted by the actuation system. We can also see that load lines drawn at multiple pumping frequencies intersect at the same approximate value of block force. This is because, the block force of the device depends primarily on the block force of the Terfenol-D stack and the area ratio between the pumping chamber and the output cylinder and is independent of pumping frequency. However, the no-load velocity is different for different values of pumping frequency. The block force of this magnetorheological actuation system is 30N.

Information obtained from load lines can also be used to calculate the maximum power output from the device. Since the actuator works on the basis of frequency rectification, the maximum power that can be obtained from the system is the area of the biggest rectangle that can be enclosed inside the linear load line (Sirohi, 2002), as seen in Figure 4.5. Thus, the maximum power output of the system is the area of the biggest rectangle OCDE that can be enclosed in the actuator load line, that is, half the area enclosed under the load line.

$$P_{out} = \frac{1}{4} \times F_{block} \times v_{no\ load} \tag{4.4}$$

This method is then used to calculate the maximum power output from the device for all the pumping frequencies investigated. The variation of power output with pumping frequency is shown in Figure 4.12. We can see from the figure that the maximum power obtainable from the system is 0.37 W at 125 Hz pumping frequency. The pumping frequency at which the fluid resonance of the circuit occurs is the point where the internal losses in the fluid are the least. This is the reason why the maximum power output and actuator resonance occur at the same pumping frequency.

The energy is consumed by the actuation system to generate the magnetic field around the Terfenol-D stack and actuate the stack. This energy is then transfered to the load through the hydraulic circuit. The magnetizing coil around the Terfenol-D stack is composed to insulated copper wire wound on a plastic core. The stack forms the core of the bobbin. The electrical impedance of the magnetizing coil is composed of two parts - resistive and inductive. The resistance of the coil is 8Ω and the inductance is $6mH$. Thus the coil consumes both active (in the resistive part) and reactive (in the inductive part) power. The active part of the power is dissipated as heat and cannot be harvested in any useful manner. The reactive part is used to generate the magnetic field. However, after using some of the reactive power to actuate the Terfenol-D stack (thus converting it to mechanical energy), the remainder of the reactive part is returned back to the amplifier. Though the net energy transfered to the actuator is only in the form of heating of the coil and the stress energy of the stack, the power supply used to provide the current to the magnetizing coil must be capable of sourcing the total current (both active and reactive). This results in a much heavier power supply than necessary. This problem can be offset to some degree through the use of well balanced capacitive resonant circuits. The intention is to add a circuit element to the magnetizing coil such that the entire circuit appears like a purely resistive circuit to the power supply. In an ideal inductive circuit (like the magnetizing coil), the current lags the voltage by 90^0. In a pure capacitor, the current leads the voltage by 90^0. Thus, an appropriate capacitor could be added to the electrical circuit to balance out the lag caused by the inductance of the magnetizing coil. Such energy conservation techniques have been reported in the literature (Ellison, 2004). Such balanced LC oscillator circuits work well only at the pumping frequency for which the circuit has been designed for. Therefore, this method of improving the efficiency of the system can only be attempted after the final design of the actuator and the operational frequency is finalized.

During the experiments, the current and voltage provided to the magnetizing coil of the Terfenol-D stack was recorded. Ideally, the expression for power is written as:

$$\overline{P} = \overline{V} * \overline{I} \quad (4.5)$$

where, $\overline{P}$, $\overline{V}$ and $\overline{I}$ are complex quantities. This expression accounts for both active and reactive power. Since the power supply has to source both parts of the power, the expression for power used here is an upper bound for equation 4.5. The input electrical power is calculated as:

$$P_{input} = V_{rms} * I_{rms} \quad (4.6)$$

Equation 4.6 can be used to calculate the power consumption at different values of pumping frequency. The ratio of the output mechanical power and the input electrical power gives the electromechanical efficiency of the device at that particular pumping frequency.

$$\eta = \frac{P_{out}}{P_{in}} \quad (4.7)$$

where, η gives the electromechanical efficiency of the system. Figure 4.13 shows the variation of efficiency with pumping frequency. We can see that the peak efficiency of the device is around 0.055% and is obtained at a pumping frequency of 50Hz. Since the electrical impedance of the magnetizing coil of the Terfenol-D stack is mostly inductive, the impedance is small at lower values of frequency and increases as the pumping frequency is increased. Thus the power consumed by the coil to generate the magnetic field increases as the frequency goes up.

4.4.3 Bi-directional No-Load Test

Bi-directional motion is produced in the output cylinder shaft by alternately applying magnetic fields to the two arms of the Wheatstone bridge. *Arms* of the Wheatstone bridge are defined as the set of valves to which identical magnetic field is applied. In this case, valves 1 and 3 comprise one arm and valves 2 and 4 comprise the other arm. Figure 4.7(a) and (b) shows the schematic for the two scenarios. The current that is applied to the two arms of the Wheatstone bridge can be seen in Figure 4.14. We can see that when a saturating current is passed through one arm, no current is supplied to the other and vice versa. Thus, the output cylinder shaft moves back and forth with the same frequency as that of the switching magnetic field. This frequency, the frequency of motion of the output cylinder shaft, will be referred to as the actuator frequency. This is different from the pumping frequency, which is the frequency of the magnetic field provided to the Terfenol-D stack. We can see in the figure that there is a demagnetizing signal added when the arm is off. The demagnetizing signal is a rapidly oscillating and rapidly decreasing signal and has to be added to the driving signal to prevent the magnetic domains in the MR particles from retaining any residual magnetic field. As the magnetic domains are not able to switch their magnetic polarity at such a high frequency, the particles in the MR fluid shed any residual magnetic fields that they carry. This helps to prevent agglomeration of the ferromagnetic particles and improve the life of the fluid in the device.

The volume flow rate from the Terfenol-D pump is constant for a particular value of pumping frequency, irrespective of the motion of the output cylinder shaft. The volume flow rate from the pump can be expressed in terms of the output cylinder shaft motion as follows:

$$Q = Shaft\ Area \times actuator\ frequency \times actuator\ stroke \tag{4.8}$$

Thus, we can see that for a given flow rate, the actuator stroke varies inversely as the actuator frequency. Figure 4.15 shows the experimental variation of actuator stroke with actuator frequency for three values of pumping frequency. As predicted by equation 4.8, the variation of output stroke with output actuator frequency is hyperbolic. Figure 4.15 allows us to estimate the frequency bandwidth of the actuator. For instance, if we require a minimum of 10 mm stroke for a particular application, we can say from this figure that the maximum actuator frequency at which we can operate this device, and still obtain the minimum stroke required, is 4Hz. Beyond this frequency, the volume flow rate is not enough to sustain the required output stroke and the stroke drops off with actuator frequency.

4.4.4 Bi-directional Load Test with Inertial Loads

All practical applications involve the use of an actuator to move a load. In aerospace applications, the loads can be both elastic and inertial. To evaluate the bi-directional performance of this actuation system under loaded conditions, the actuator was tested with both inertial and spring loads. The impact of inertial loads on the actuator performance is measured in the following way. A known mass, placed on a linear bearing, is attached to the output cylinder shaft. When the actuation system is in operation, the mass is forced to move along with the cylinder shaft. The linear bearing ensures that the weight of the load does not produce additional friction in the system. Also, unlike the uni-directional case, the weights are not hung from the cylinder shaft. Thus the load that the device experiences is a pure inertial force which depends on the instantaneous acceleration and not a constant force (the weight of the load). A picture of experimental setup can be seen in Figure 4.16. The pumping frequency was fixed at 100Hz and the variation of output stroke with output actuator frequency was measured (like bi-directional no-load testing) for different values of external mass. The results can be seen in Figure 4.17. We can see that for a given value of actuator frequency, there is a decrease in stroke with increasing inertial load. We see from the figure that for an load of 66N (15lbs), the device gives a stroke of 6mm at 3Hz output actuator frequency.

The inertial loading on the actuator is caused not merely due to the oscillatory motion of the output cylinder shaft. As mentioned earlier, the hybrid hydraulic actuator works on the principle of frequency rectification using one way reed valves.

Thus the load is pushed by the hybrid material motion twice every oscillation. Figure 4.18 shows the load displacement as a function of time for three pumping cycles. We can see that the load goes through an acceleration-deceleration cycle during every period of oscillation of the Terfenol-D stack. Thus, the effect of the inertial load is felt throughout the actuator frequency range.

4.4.5 Bi-directional Load Test with Stiffness Loads

In these tests, the bi-directional performance of the actuator is measured for stiffness loads. Pre-stressed springs are attached to the ends of the output cylinder shaft such that the cylinder shaft works against the same stiffness during the entire length of its stroke. A picture of experimental setup can be seen in Figure 4.19. The performance of the actuator is measured in terms of the variation of actuator stroke with actuator frequency. Figure 4.20 shows the relationship between actuator stroke and actuator frequency for different values of actuator stiffness. All these curves are measured at a pumping frequency of 100Hz. Unlike the earlier case (inertial loading where the effect of the load was felt at all actuator frequencies), the effect of the stiffness load is felt more at lower actuator frequencies. Stiffness force is proportional to displacement. Thus, the force applied by the stiffness load on the cylinder shaft is felt as the stroke of the cylinder shaft increases, that is, when the actuator frequency is reduced. We can see from the figure that as the stiffness is increased, the stroke appreciably reduces at lower values of actuator frequency. But the output stroke remains roughly the same at higher values of actuator frequency. Thus, for a stiffness of 68 lbs/in, the system delivers a stroke of close to 7mm for the entire actuator frequency range (0-5Hz).

4.5 Conclusions

A hybrid hydraulic actuation system was developed using a Terfenol-D driven pump as the pressure source and magnetorheological fluid valve network as a valving system. Extensive experimental studies were performed on this actuation system.

These tests ranged from no-load testing in uni-directional mode to bi-directional tests with external stiffness and inertial loads. The objective of such testing was to identify the capabilities as well as the limitation of such an actuation system.

Uni-directional tests were conducted in both no-load and loaded circumstances. No-load testing established the maximum velocity output from the system as 50mm/s. Also, a pumping frequency sweep established the system resonance frequency to be at 125Hz. The system resonant frequency is determined by the stiffness and inertia of the system. The resonant frequency of the actuation system is much lower than that of an equivalent hydraulic fluid driven system due to the high fluid inertia of the MR fluid. The commercial MR fluid used for this test, MRF-132AD, has a density of 3090 kg/m^3. Load tests were also done in uni-directional mode to ascertain the power output and efficiency of the system. Using load lines obtained from uni-directional load tests, the maximum power output of the system was calculated to be 0.35W at 125Hz pumping frequency. The overall electromechanical efficiency was calculated to be 0.055%.

Bi-directional tests were performed on the system by providing the two arms of the Wheatstone bridge with alternating square wave variation of magnetic field. The system can deliver an actuator stroke of close to 7mm at an actuator frequency of 5Hz. Beyond 5Hz, the volume flow rate of the Terfenol-D driven pump is not enough to maintain 10mm actuator stroke. Bi-directional load tests were done with both stiffness and inertial external loads. It was noted that the effect of a stiffness load is mainly to change the hyperbolic variation of the actuator stroke with actuator frequency to a more flatter one. The actuation system can sustain an output actuator stroke of 9mm for an external stiffness load of 68lbs/in for the entire actuator frequency range till 5Hz. In the case of external inertial loads, the actuation system can output a stroke of 6mm at 3Hz actuator frequency for a load of 15lbs.

There are several limitations to the magnetorheological actuation system. The power output and electro-mechanical efficiency of the device is too small for many real-life applications. The reasons for the low power output and efficiency is the

Table 4.1: MR valve parameters

Outer diameter	16.4 mm
Bobbin diameter	11.0 mm
Active length	11.6 mm
Air gap	0.5 mm
No. of windings	114 turns
Material	HIPERCO-50 A
Magnetic field(max)	0.9 T (3A)

losses incurrent in the magnetizing coil around the Terfenol-D stack and the viscous losses in the MR fluid. Also, greater volume flow rate from the pump is required to increase the frequency bandwidth of the system. The ferromagnetic particles in the MR fluids tends to settle after a few days of filling the actuator. This causes dissimilarities in the flow paths in the four valves in the bridge leading to drifting in the motion of the output cylinder shaft. Dissimilarities can be caused due to settling of the ferromagnetic particles in the MR fluid, thus alterning the composition of fluid in the different fluid paths. However, the drift can be easily corrected by controlling the magnetic current in the valves of the bridge. Also, drift is less of a concern after the actuator cycles for a number of cycles sufficient to re-disperse (remix) the ferromagnetic particles in the MR valves.

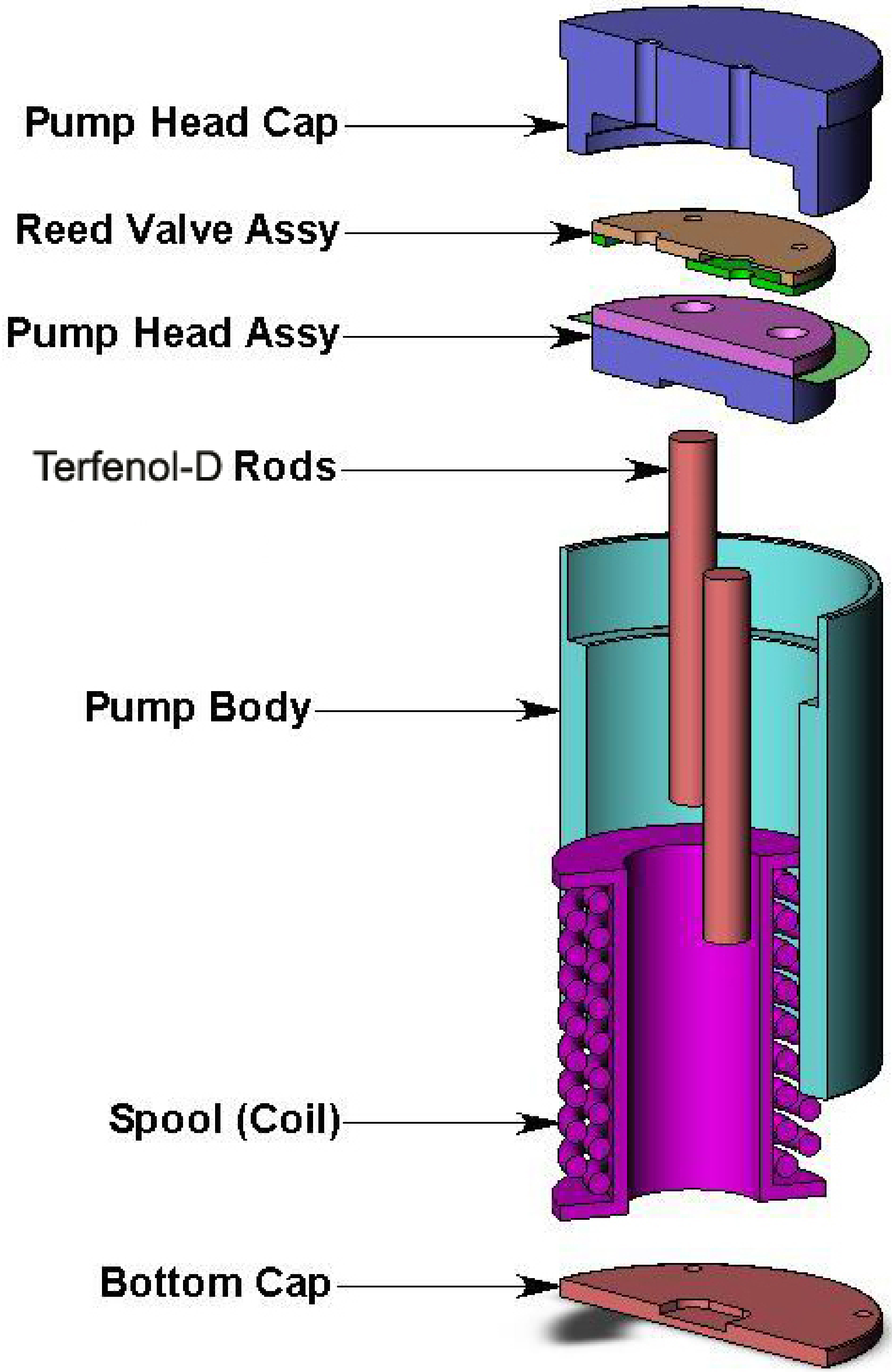

Figure 4.1: This figure shows the exploded view of the Terfenol-D driven pump

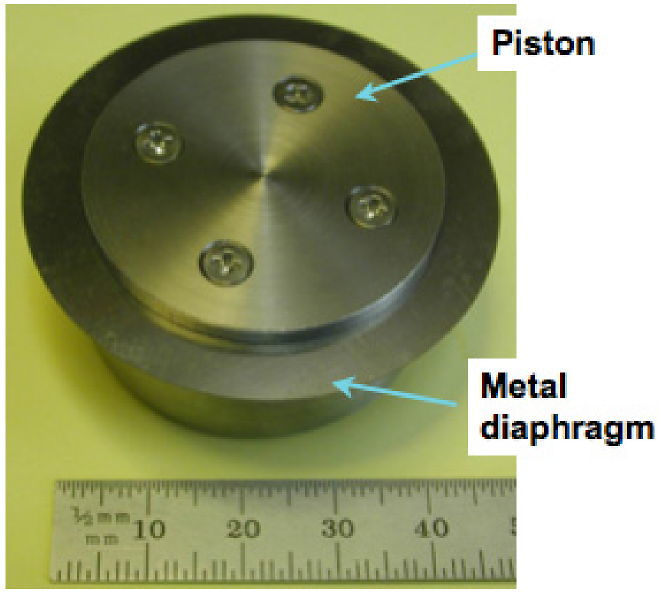

Figure 4.2: Piston assembly with metal diaphragm

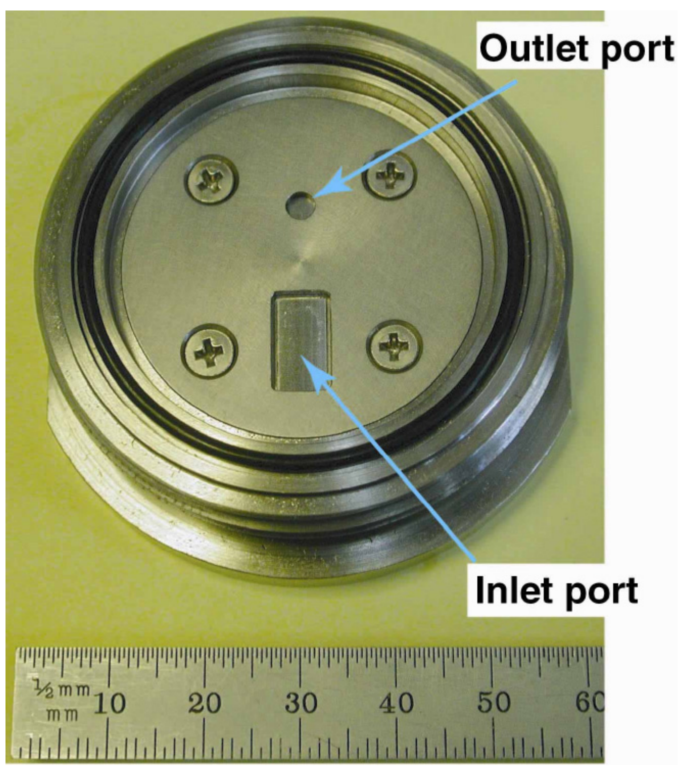

Figure 4.3: Pump head assembly showing the reed valves and ports

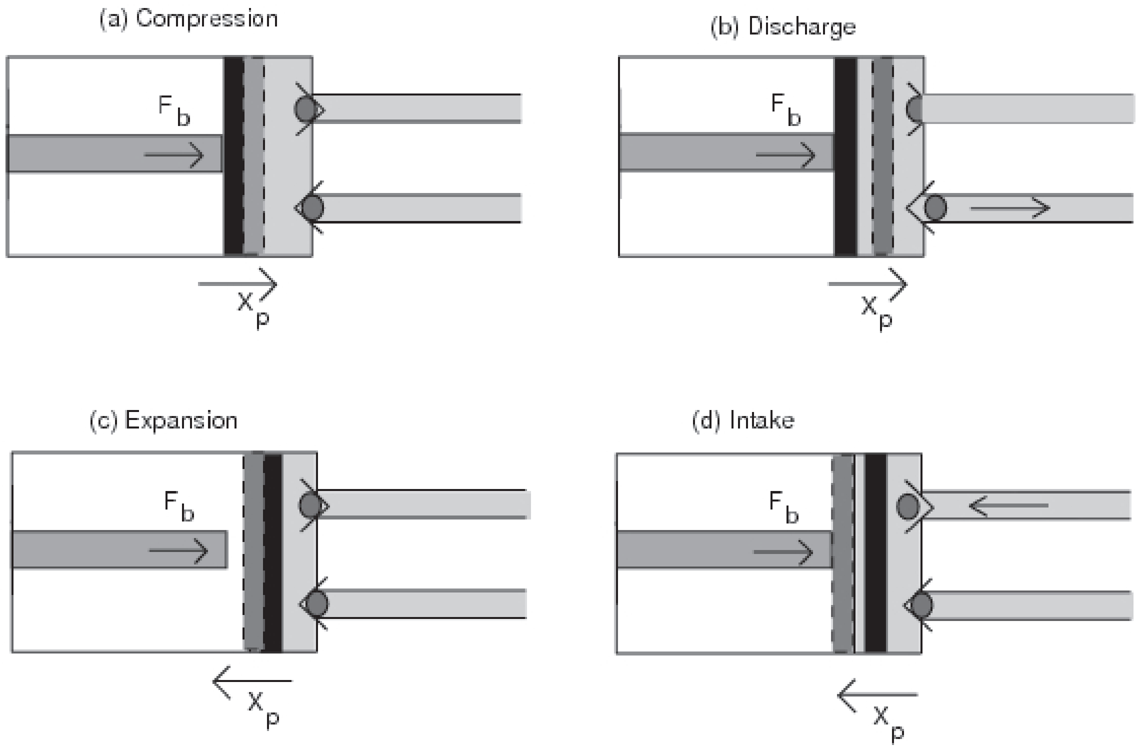

Figure 4.4: Different stages of actuator operation

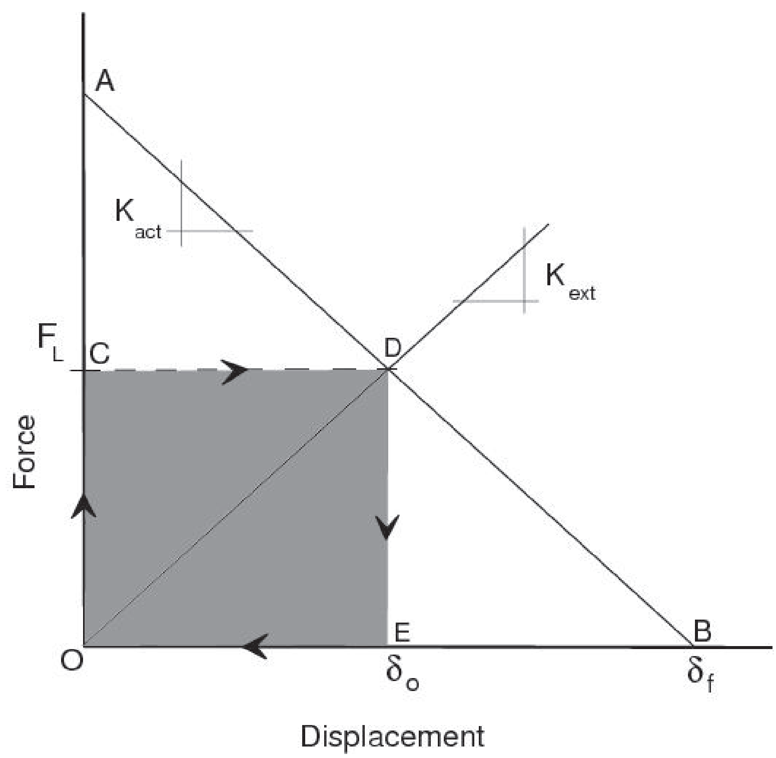

Figure 4.5: Pumping cycle for an ideal incompressible working fluid

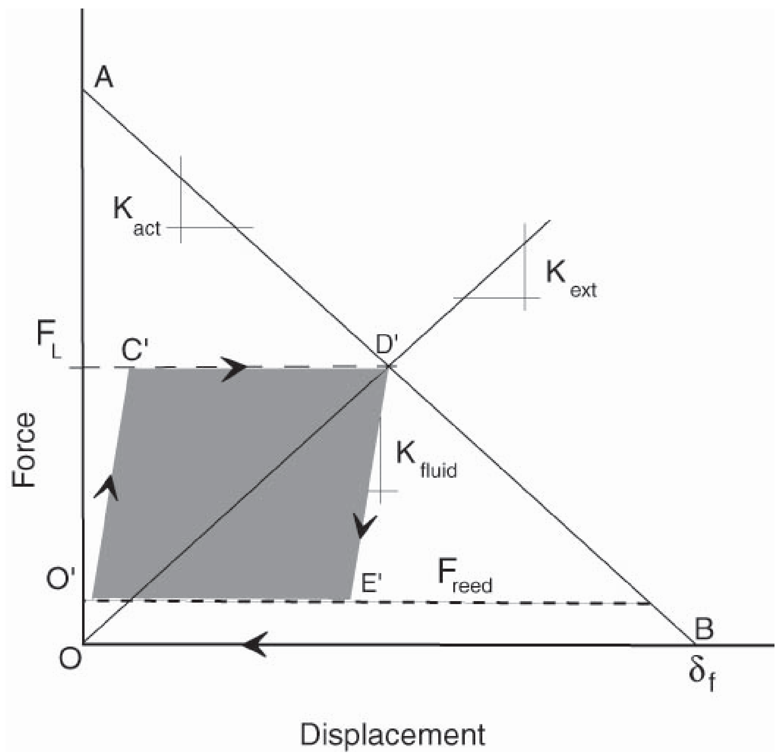

Figure 4.6: Pumping cycle for an actual compressible working fluid

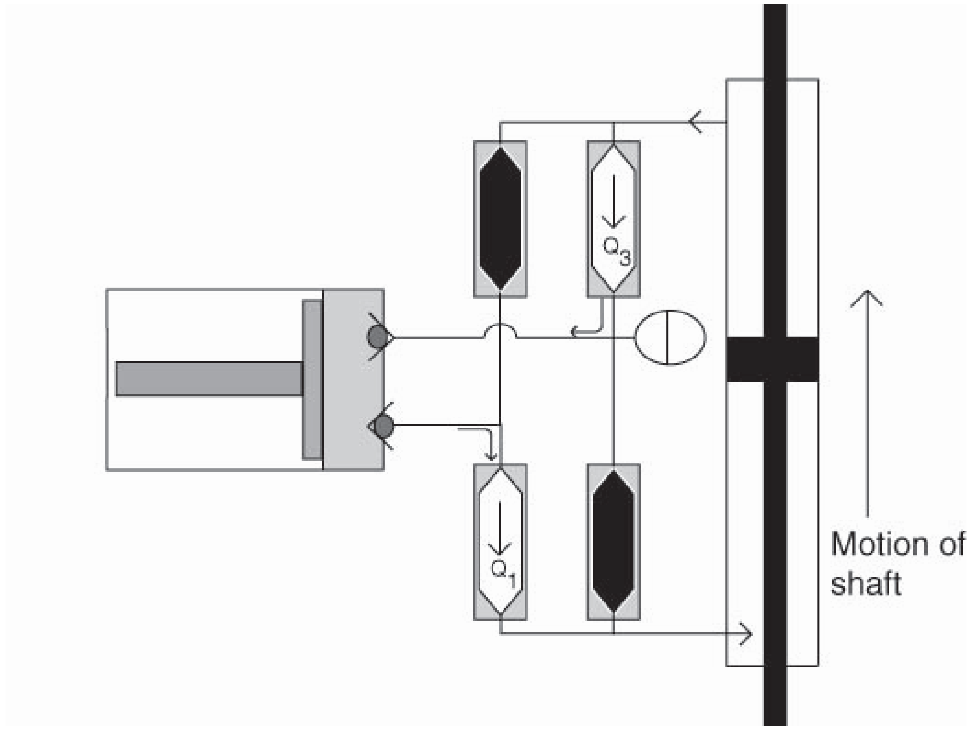

(a) Schematic for upward motion

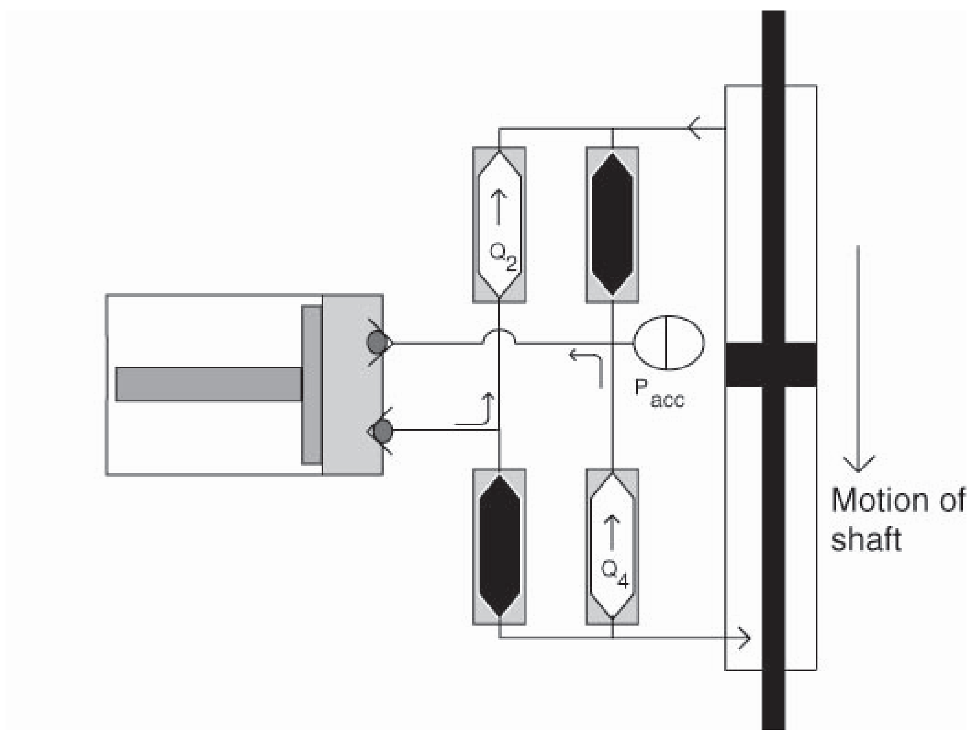

(b) Schematic for downward motion

Figure 4.7: Schematic for the active mode of the MR actuation system

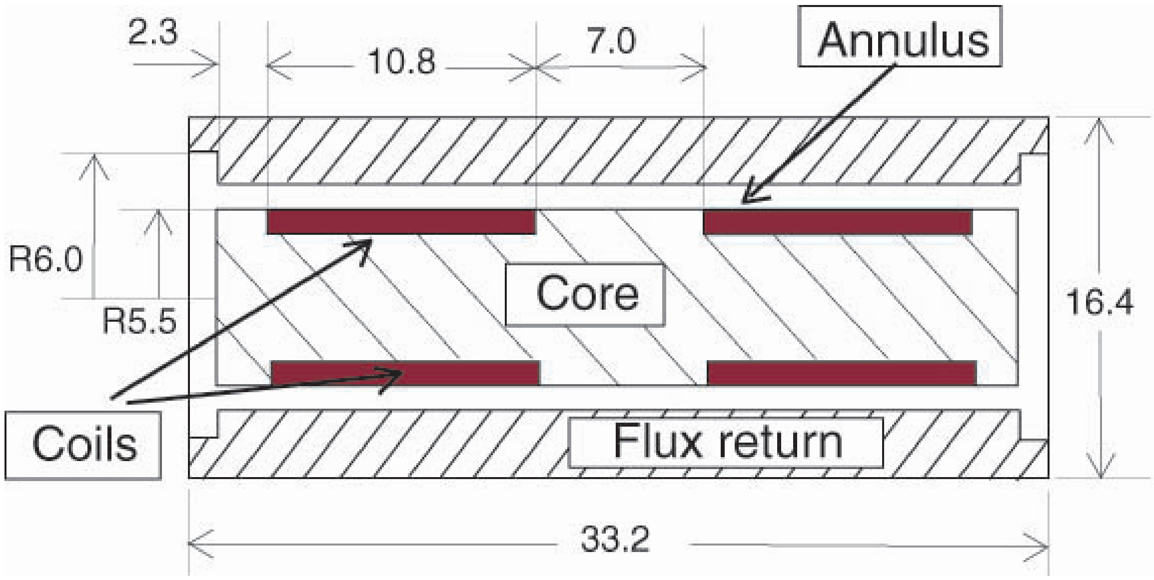

Figure 4.8: Cross-section of the MR valve with key geometrical parameters

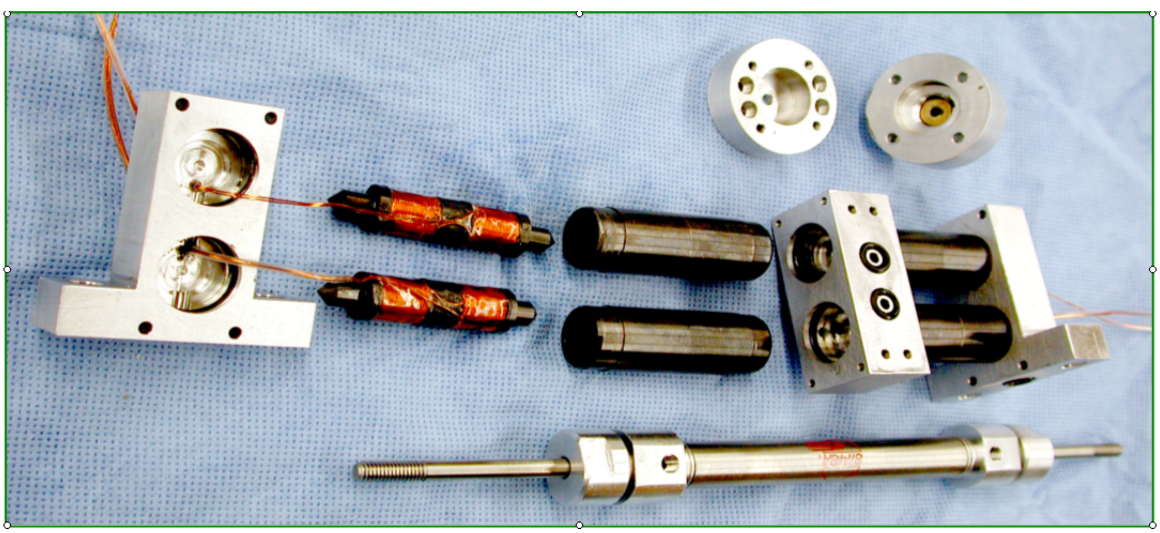

Figure 4.9: Picture showing the MR valves and Wheatstone bridge setup

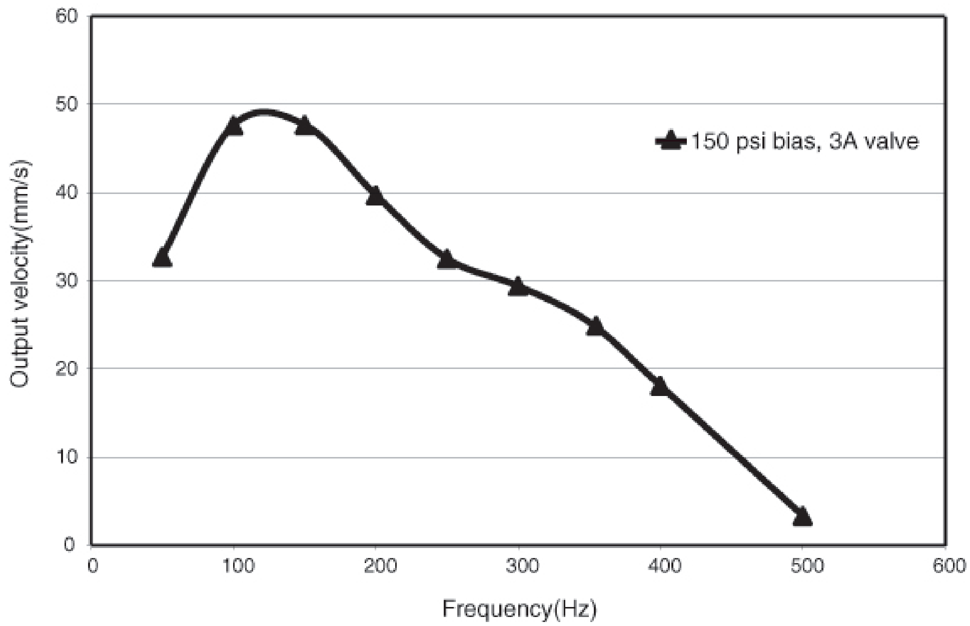

Figure 4.10: Results of uni-directional no-load testing (bias pressure = 150 psi, valve current = 3 A)

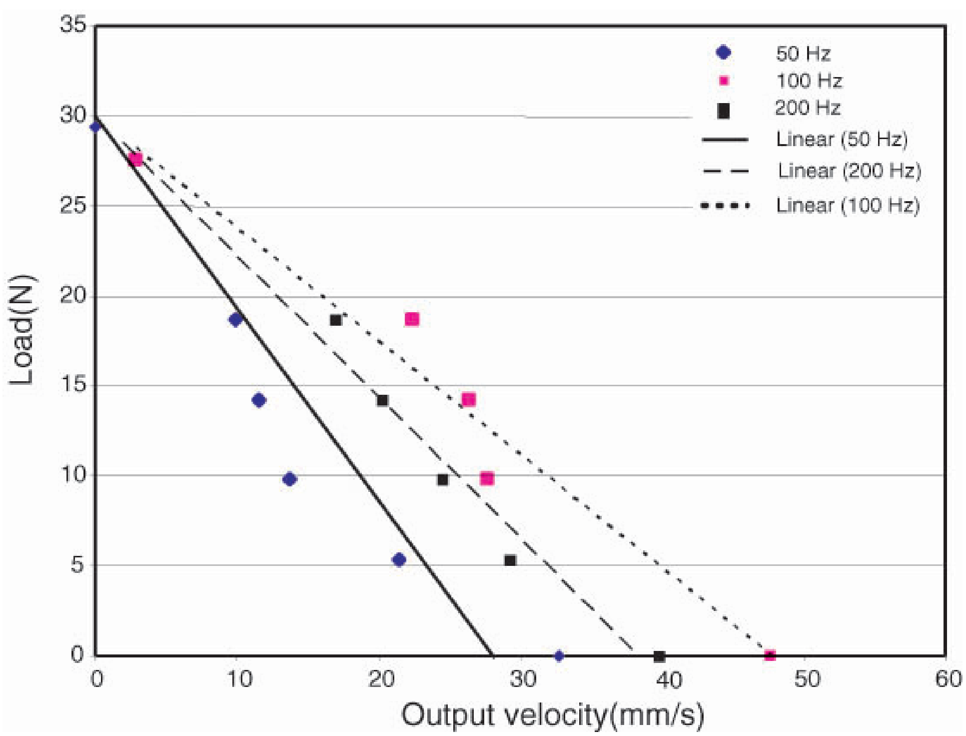

Figure 4.11: Loadline for pumping frequencies 50, 100 and 150Hz (bias pressure = 150 psi, valve current = 3 A)

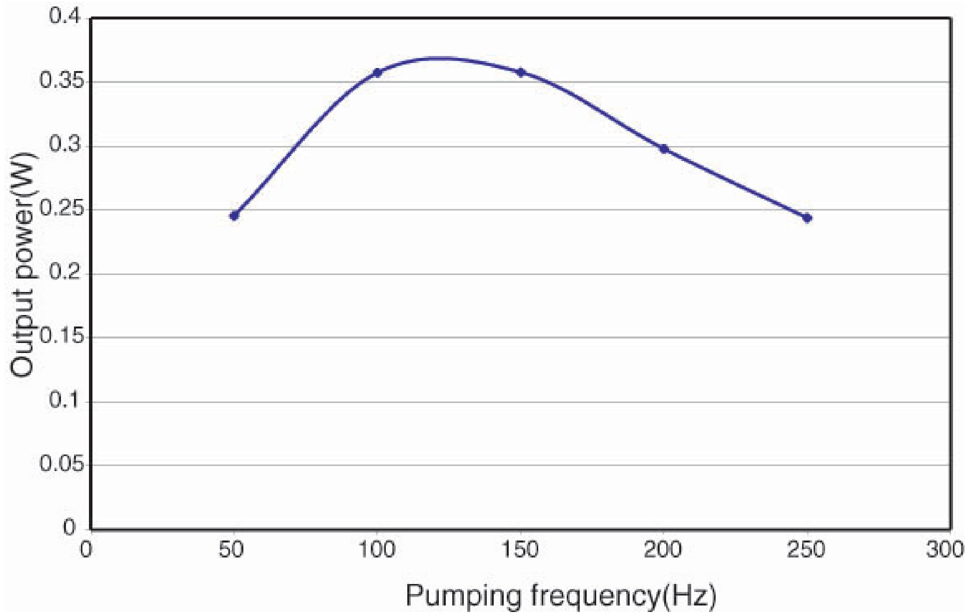

Figure 4.12: Variation of power output with pumping frequency (bias pressure = 150 psi, valve current = 3 A)

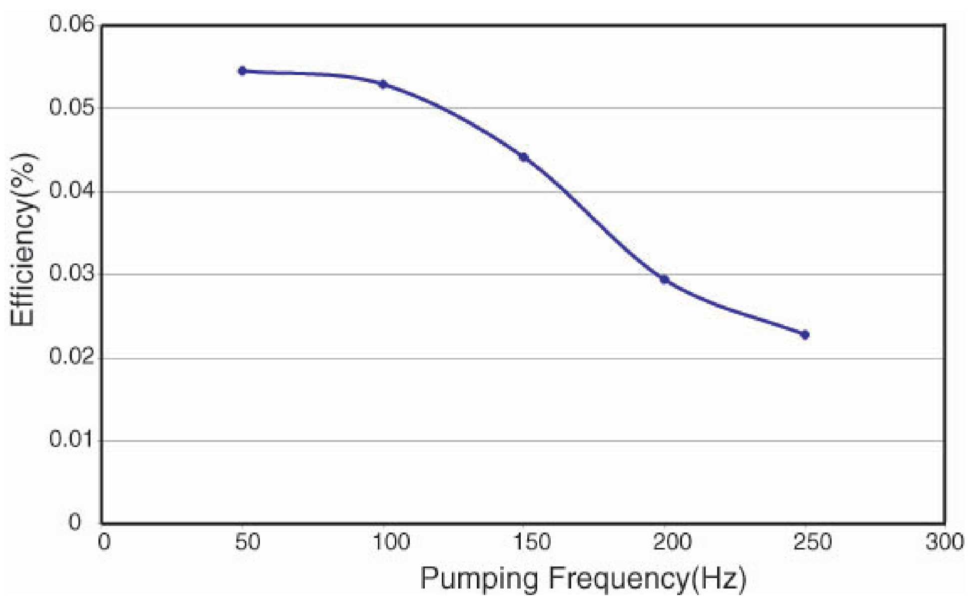

Figure 4.13: Variation of electromechanical efficiency with pumping frequency (bias pressure = 150 psi, valve current = 3 A)

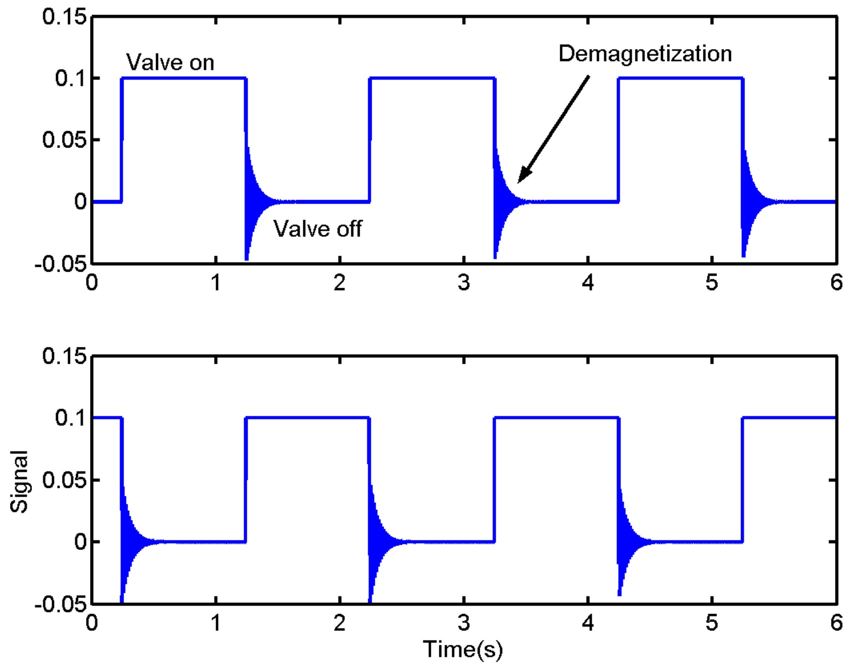

Figure 4.14: Current applied to the two arms of the Wheatstone bridge setup

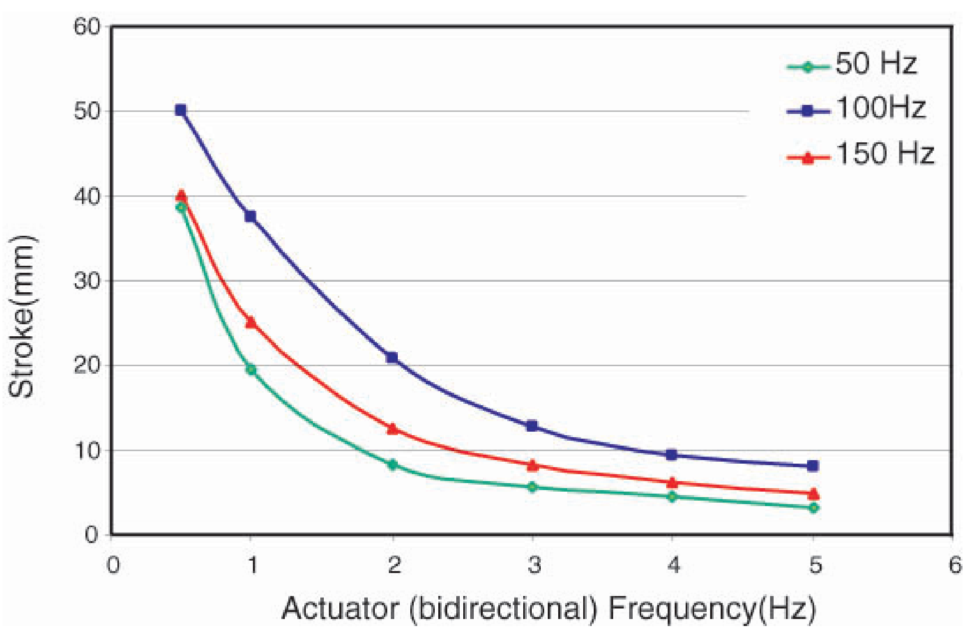

Figure 4.15: Variation of output stroke with actuator frequency (bias pressure = 150 psi, valve current = 3 A)

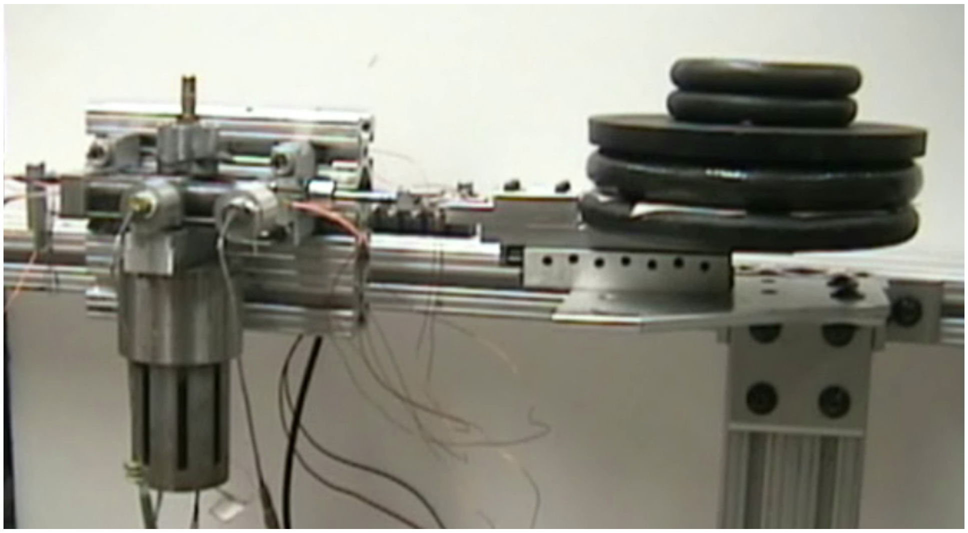

Figure 4.16: Picture of the experimental setup with inertial loads

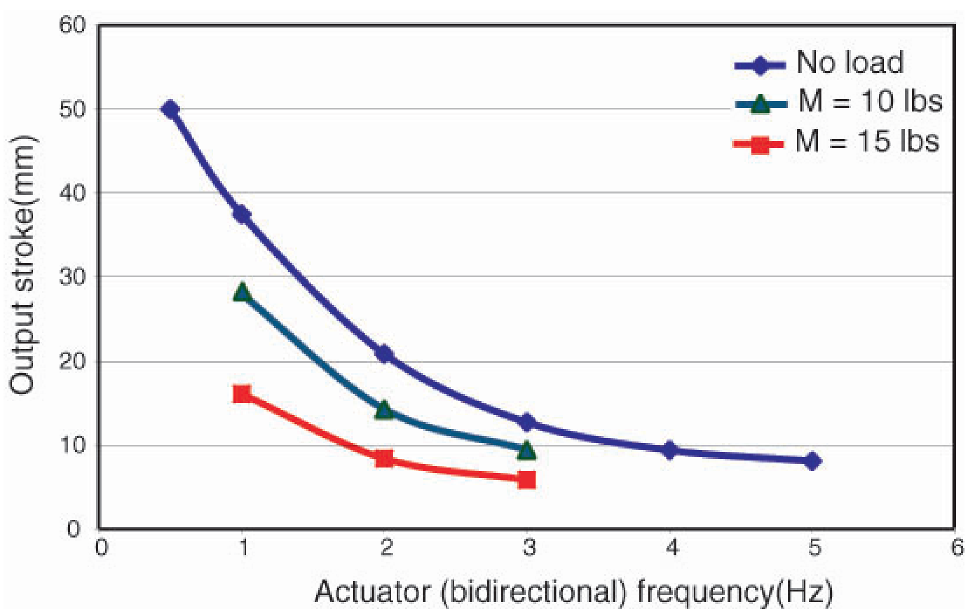

Figure 4.17: Variation of output stroke with actuator frequency for different inertial loads (pumping frequency = 100 Hz, bias pressure = 150 psi, valve current = 3 A)

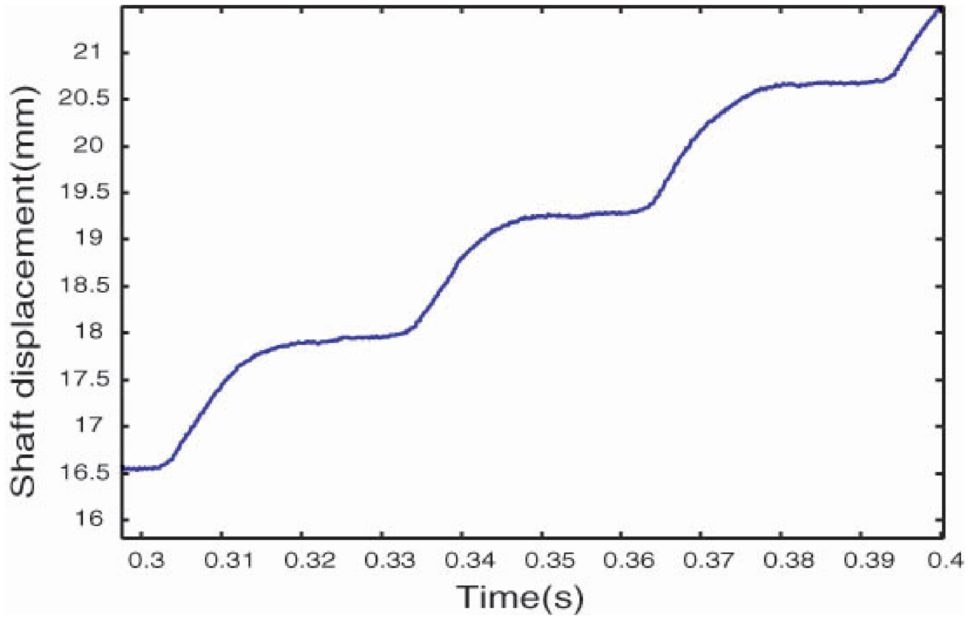

Figure 4.18: Variation of load displacement with time showing regions of alternating acceleration and deceleration (pumping frequency = 50Hz)

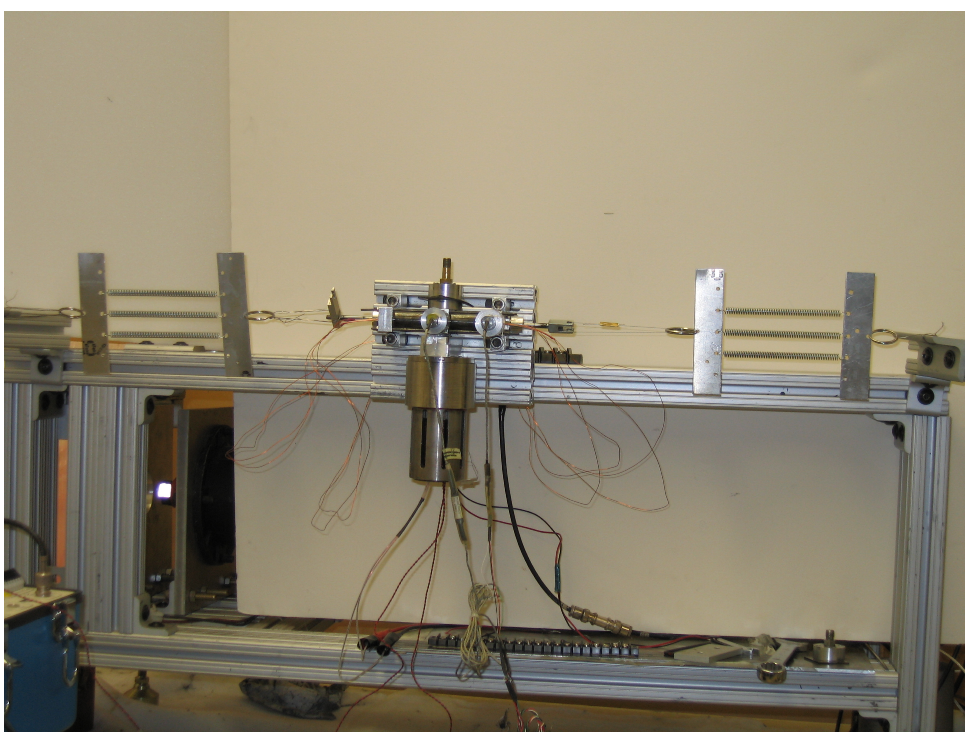

Figure 4.19: Picture of the experimental setup with stiffness loads

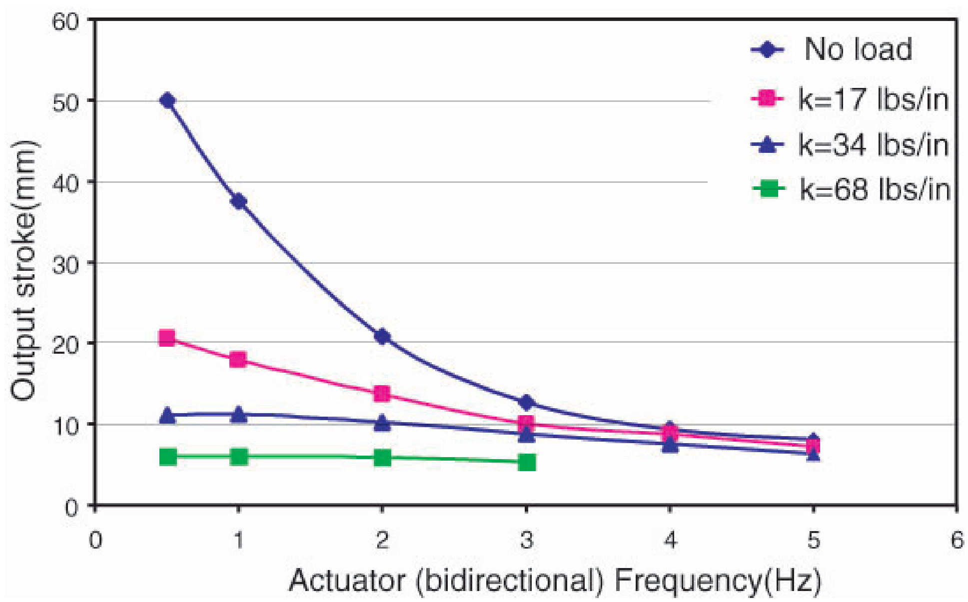

Figure 4.20: Variation of output stroke with actuator frequency for different spring loads (pumping frequency = 100 Hz, bias pressure = 150 psi, valve current = 3 A)

Chapter 5

A Hybrid Hydraulic Actuation System - Modeling

The goal of this chapter is to develop a theoretical model for the performance of the hybrid actuation system along with the MR fluid based valving system. The present system does not provide the necessary forces to actuate a rotor blade in an active pitch link application. To scale up the present actuator to provide the necessary forces and actuation bandwidth for a real-life application like the active pitch link, an accurate understanding of the different working parameters is essential. Also, a theoretical model that accounts for the different aspects of pressure loss that occurs inside the system provides invaluable information to a designer. Smart materials like Terfenol-D inherently have high energy density. To effectively use the high energy density of smart materials, the smart material has to be activated at a very high frequency. However, as the pumping frequency is increased, fluid dynamics of the fluid chambers and fluid lines become prominent. The frequency domain behavior of typical hydraulic systems exhibit resonances, where the output volume flow rate from the hybrid pump peaks at a particular value of pumping frequency of the smart material. This value of resonant frequency depends on the stiffness, inertia and damping of the system. It also has a dependence on the load that the system is working against. The resonant frequency is the optimum frequency of operation of the actuation system as the maximum power output and efficiency are obtained at the resonant frequency. Thus, an analytical model that predicts the resonant frequency of the system and the system performance over the entire frequency range of operation is essential to design the next generation of hybrid hydraulic actuation systems.

A detailed description of the operation of the actuation system was provided in the previous chapter. Hybrid actuation systems work on the principle of frequency rectification to convert the low amplitude high frequency motion of the Terfenol-D stack into a uni-directional motion of the load. Magnetorheological fluid is used as the hydraulic fluid and bi-directional motion of the load is achieved through the use of MR fluid based valves. A methodology for modeling of MR fluidic valves is developed first. The rheology of MR fluids is modeled using commonly used models like Bingham plastic and bi-viscous models. A methodology for modeling active fluidic valves was developed by Choi *et.al*. (2000). This methodology was developed using the quasi-steady assumption and was used for a uniform flow through a network of ER valves. In the hybrid hydraulic actuator, the flow that enters the valving system is pulsatile owing to the high dynamic operation of the Terfenol-D stack. Hence, the methodology was modified to include fluid inertial losses that occur as the pumping frequency is increased. The model for the entire system is then developed using mass conservation equations for different fluid sections in the actuation systems. The equations, along with the equations for the MR valves, are formulated as a state space model and solved numerically. The modeling results are then compared to the experimental results that were presented in the previous chapter.

5.1 MR Fluid Modeling

A schematic of the MR valve is shown in Figure 5.1. The valve consists of coils of insulated copper wire wound around a cylindrical core made from a high permeability material. A flux return path, also made from a high permeability material, is installed around the wound core. The flux return path and the core produces an annular region between them for the MR fluid to flow. As seen in the figure, there are two sets of coils, that are wound in opposite directions to each other. These two sets of coils produce three different sections in the flow path where there are magnetic field lines pass perpendicular to the direction of the flow. These are the three active regions of the valve. The reason for opposite direction of winding for the two sets of coils is to provide a uniform magnetic field lines in the flow section that lies between the coils. When no magnetic field is applied, the fluid flow through the annulus can be assumed to be Poiseuille flow of a Newtonian fluid. For a Newtonian flow, the pressure difference between the two ends of the valve is well know (Fox and McDonald, 1992) and can be expressed as follows:

$$\Delta P_N = \frac{12\mu L_{mr}}{bd^3}Q \tag{5.1}$$
$$= R_v Q \tag{5.2}$$

where, Q is the flow rate through the annulus, d is the thickness of the annular region where flow occurs, b is the mean circumference of the annular region, that is, $b = \pi(d_o + d_i)$, L_{mr} is the total length of the valve and μ is the viscosity of the MR fluid. The linear viscous resistance offered to the flow by the MR fluid can be represented as R_v, as in equation 5.2.

When a current is applied to the magnetizing coil, magnetic flux lines are produced, as seen in Figure 5.1. Figures 5.2(a) and (b) show the change in velocity profile of the MR fluid when a current is applied and magnetic field is generated. The magnetic field causes chains of ferromagnetic particles to form in the active section of the annulus, thus increasing the pressure difference necessary to maintain the volume flux. The velocity profile of the MR fluid changes as it encounters the active region in its flow path. The new pressure drop across the valve can be derived based on the specific rheological model used to represent the MR fluid. Two of the most common rheological models are described below.

5.1.1 Bingham Plastic Model

The Bingham plastic model (Stanway et al., 1996; Wereley and Pang, 1998) states that the MR fluid does not undergo any shear until a particular value of shear stress, called the yield stress, is reached. Once this value of shear stress is reached, the fluid behaves like a Newtonian fluid. The pressure difference across the active section of MR fluid can be written as follows:

$$\Delta P_{BP} = \frac{12\mu L_{act}}{bd^3\left(1-\bar{\delta}\right)^2\left(1+\frac{\bar{\delta}}{2}\right)}Q \tag{5.3}$$

where, ΔP_{BP} is the pressure difference across the valve, L_{act} is the length of the active section of the valve and $\overline{\delta}$ is the non-dimensionalized plug thickness.

The above equation can be rewritten as follows:

$$\begin{aligned} R_v Q &= \Delta P_{BP} \left(1-\overline{\delta}\right)^2 \left(1+\frac{\overline{\delta}}{2}\right) \\ &= \Delta P_{BP} - \frac{\Delta P_{BP}\overline{\delta}}{2}\left(3-\overline{\delta}^2\right) \end{aligned} \tag{5.4}$$

where, R_v is the linear viscous loss coefficient and is given by equation 5.2. The non-dimensional plug thickness can be expressed as:

$$\overline{\delta} = \frac{2\tau_y L_{act}}{d\Delta P} \tag{5.5}$$

Substituting equation 5.5 in 5.4 and re-arranging, we get:

$$\Delta P_{BP} = R_v Q + \frac{\tau_y L_{act}}{d}\left(3-\overline{\delta}^2\right) \tag{5.6}$$

$$= R_v Q + T_{BP} \tag{5.7}$$

where, T_{BP} is the active pressure drop and is given by

$$T_{BP} = \frac{\tau_y L_{act}}{d}\left(3-\overline{\delta}^2\right) \tag{5.8}$$

Thus, equation 5.7 shows that the total pressure drop across an MR valve comprises of two parts. The first part gives the viscous pressure drop due to the Newtonian flow of the fluid in the post-yield flow regime. The second part gives the active pressure drop that comes about due to the application of the magnetic field. This formulation allows us to explicitly calculate the pressure drop caused due to the control action, which is the current that is applied to the coils.

5.1.2 Bi-viscous Model

The bi-viscous model (Wereley et al., 2004) allows the MR fluid shear even before the value of yield stress is reached, but with a very high value of viscosity. Using the same methodology as above, we can obtain an expression for pressure loss in the case of a bi-viscous MR fluid as:

$$\Delta P_{BV} = R_v Q + T_{BV} \tag{5.9}$$

where, T_{BV} is the active pressure drop caused due to the control action and is given by

$$T_{BV} = \frac{2\tau_y L}{d}\left[\frac{3}{2} - \overline{\mu} - \frac{\overline{\delta}^2}{2}(1-\overline{\mu})\right] \quad (5.10)$$

In the above equation, $\overline{\mu}$ is the ratio of post-yield to pre-yield viscosity of the MR fluid as given by the bi-viscous model.

$$\overline{\mu} = \frac{\mu_{po}}{\mu_{pr}} \quad (5.11)$$

where, μ_{po} is the viscosity of the MR fluid in the post-yield region and μ_{pr} is the viscosity of the MR fluid in the pre-yield region. The bi-viscous model reduces to the Bingham plastic model if the pre-yield velocity is assumed to be infinite. Thus, T_{BV} converges to T_{BP} as μ_{pr} approaches infinity.

Thus, the pressure drop across an MR fluidic valve can be modeled using either equation 5.7 or 5.9. Equations 5.7 and 5.9 were derived assuming a steady fully developed flow in the active section of the MR valve. Since the high frequency operation of the active stack produces an unsteady fluid motion in the valves, equations 5.7 and 5.9 do not adequately describe the pressure loss across an MR valve. Since the density of the MR fluid is very high, the inertial effects produced due to the unsteadiness of the flow has a substantial effect on actuator performance, especially as the pumping frequency is raised. To account for the unsteady pressure losses, the pressure loss across an MR valve can be expressed as follows (Wylie et al., 1993):

$$\Delta P = R_v Q + \frac{\rho L_{MR}}{A_{MR}}\dot{Q} + T \quad (5.12)$$

The second term on the right hand side is representative of the inertial pressure loss in the system and has been derived in Chapter 3.

5.2 System Modeling

5.2.1 Conservation of Mass

All the variables used in the system modeling can be seen in the schematic diagram of the hybrid actuation system shown in Figure 5.3. The model must obey the principle of conservation of mass. Considering a control volume of fluid, we can write the equation for mass as:

$$m = \rho V \tag{5.13}$$

where, m is the mass of the fluid enclosed in the control volume, ρ is the instantaneous fluid density and V is the volume of the control region. Taking the time derivative of equation 5.13, we get:

$$\frac{d}{dt}m = \rho\frac{dV}{dt} + V\frac{d\rho}{dt} \tag{5.14}$$

Rearranging the above equation, we can get an expression for the time rate of change of fluid density:

$$\dot{\rho} = \frac{\dot{m} - \rho\dot{V}}{V} \tag{5.15}$$

where $\dot{\rho}$, $\dot{m}$ and $\dot{V}$ give the rate of change of density, mass and volume of the control volume. This formulations allows us to take into consideration the compressibility of the fluid and also the fluid flowing into and out of a particular part of the actuation system. Equation 5.15 will be used in deriving the equation for the rate of change of fluid density in the pumping chamber and the output cylinder of the system.

If we consider an enclosed volume of fluid where there is no net inflow or outflow of mass, we can rewrite equation 5.15 as,

$$\dot{\rho} = -\rho\frac{\dot{V}}{V} \tag{5.16}$$

5.2.2 Fluid Compressibility

The compressibility of the MR fluid must be taken into account in the performance simulation of the actuation system. Fluid compressibility introduces a stiffness to the hydraulic system and this stiffness is critical in predicting the resonant frequency of the hydraulic system. The bulk modulus of the fluid is defined as follows:

$$dP = -\beta\frac{dV}{V} \tag{5.17}$$

Substituting equation 5.17 in 5.16, we get,

$$dP = \beta \frac{d\rho}{\rho} \tag{5.18}$$

The above equation can be integrated to obtain an expression for the pressure in any region in the pump. Integrating equation 5.18 within limits, we get:

$$\int_{P_{bias}}^{P_1} dP = \beta \int_{\rho_{bias}}^{\rho_1} \frac{d\rho}{\rho} \tag{5.19}$$

$$P_1 - P_{bias} = \beta log\left(\frac{\rho_1}{\rho_{bias}}\right) \tag{5.20}$$

where, ρ_{bias} is the density of the fluid at the bias pressure, P_{bias}, β is the bulk modulus and P_1 and ρ_1 are the calculated values of pressure and density of the control volume.

5.2.3 Pump Piston and Pumping Chamber

Energy is provided to the system in the form of electrical energy to the Terfenol-D stack. In the stack, the electrical energy is converted into mechanical energy and the stack performs work on the hydraulic fluid, which then transfers the energy to the load. We start the modeling process by deriving the equation of motion of the Terfenol-D stack. The schematic for the pumping chamber with the active material and pump piston is shown in Figure 5.4(a). Denoting the pressure inside the pumping chamber as P_c, we can write the equation of motion of the actuator piston as follows:

$$\left(M_p + \frac{M_a}{3}\right)\ddot{x}_p + C_p\dot{x}_p + (k_a + k_d)\,x_p = k_a d_a B - P_c A_c \tag{5.21}$$

where, d_a is the magnetostrictive constant of the active material stack, B is the magnetic flux density, A_p is the area of the pump piston, k_a is the stiffness of the active stack, k_d is the stiffness of the diaphragm, M_p is the mass of the piston, M_a is the mass of the active material and C_p is the damping coefficient of the pumping chamber.

Using equation 5.15, the equation for rate of change of the density of fluid in the pumping chamber can be expressed as:

$$\dot{\rho}_c = \frac{\rho_c A_p \dot{x}_p - \rho_c \dot{Q}_{out} + \rho_0 \dot{Q}_{in}}{V_c} \tag{5.22}$$

where, ρ_c is the density of the MR fluid in the pumping chamber, A_p is the cross-sectional area of the piston, $\dot{x}_p$ is the velocity of the piston, $\dot{Q}_{out}$ is the volume flow rate flowing out of the pumping chamber, $\dot{Q}_{in}$ is the volume flow rate flowing into the pumping chamber and V_c is the instantaneous fluid volume in the pumping chamber. $\dot{Q}_{out}$ and $\dot{Q}_{in}$ is determined by the position of the reed valves. The reed valves will be modeled in the following section. We can use equation 5.20 to find out the pressure of the fluid inside the pumping chamber as follows:

$$P_c = P_{bias} + \beta log\left(\frac{\rho_c}{\rho_{bias}}\right) \tag{5.23}$$

where, ρ_{bias} is the baseline density of the MR fluid at the bias pressure of P_{bias}.

The frequency response of the current amplifier used to magnetize the Terfenol-D stack becomes important as the pumping frequency increases. This is primarily due to the inductive impedance offered by the magnetizing coil and the pump body of the actuator. Due to this, the voltage applied across the magnetizing coil reduces as the frequency increases. To account for this, a frequency sweep over the frequency range of interest was carried out. A fixed amplitude input is given to the amplifier and the magnetic flux density is measured at frequencies from 50 Hz to 500 Hz. The resulting data was fitted with a first order transfer function of the form

$$G(s) = \frac{V_{out}(s)}{V_{in}(s)} = \frac{K}{1+\tau s} \tag{5.24}$$

and its parameters were evaluated by using least squares method. Based on experimental data, the time constant, τ, of the system was estimated to be 0.7 ms.

5.2.4 Reed Valves

The uni-directional reed valves perform the function of frequency rectification, wherein the bi-directional motion of the active stack is converted into a uni-directional flow of fluid. The reed valves respond to the pressure difference across the valves. We define two critical pressures in relation to the reed valves - P_{crack} and P_{open}. P_{crack} is defined as the pressure difference at which the reed valve starts allowing fluid flow through it. P_{open} is defined as the pressure difference at while the reed valve is fully open. In practise, the reed valves allows a continuously varying flow rate through it depending on the amount of deflection of the reed. The amount of fluid allowed through the discharge and intake ports depend on the amount of deflection of the specific reed valves. This behavior of the reed valve has been modeled by Chaudhuri *et.al.* (2006b) and will be used in this study. We define an internal variable, r, which denotes the amount of deflection of the reed depending on the pressure difference. For the discharge reed valve, the opening of the valve is determined by the difference between the pressure of the fluid in the chamber, P_c, and the fluid pressure at the entrance of MR valves 1 and 2, that is, P_{ch}. We denote the pressure difference across the discharge reed valve as $\Delta P_{dis} = P_c - P_{ch}$. The location at which these variables are defined can be seen in Figure 5.3.

$$r_{dis} = \begin{cases} 0 & \text{if} \;\; \Delta P_{dis} < P_{crack} \\ \frac{\Delta P_{dis} - P_{crack}}{P_{open}} & \text{if} \;\; P_{crack} \leq \Delta P_{dis} \leq P_{open} \\ 1 & \text{if} \;\; \Delta P_{open} < P_{dis} \end{cases} \tag{5.25}$$

Similarly, we can write the equation for the opening parameter for the intake reed valve. Here, we define the pressure difference across the intake reed valve as $\Delta P_{int} = P_{acc} - P_c$.

$$r_{int} = \begin{cases} 0 & \text{if} \;\; \Delta P_{int} < P_{crack} \\ \frac{\Delta P_{int} - P_{crack}}{P_{open}} & \text{if} \;\; P_{crack} \leq \Delta P_{int} \leq P_{open} \\ 1 & \text{if} \;\; \Delta P_{open} < P_{int} \end{cases} \tag{5.26}$$

These parameters, r_{dis} and r_{in}, can be used to derive equations for the volume flow rate into and out of the pumping chamber. The pressure losses incurred in the reed valves can now be written in terms of r_{dis} and r_{in} as follow:

$$P_c - P_{ch} = \frac{\rho_C Q_{out}^2}{r_{dis}^2 A_o^2 (1-\alpha)} \tag{5.27}$$

$$P_{bias} - P_c = \frac{\rho_0 Q_{in}^2}{r_{int}^2 A_o^2 (1-\alpha)} \tag{5.28}$$

where, α is a loss coefficient associated with orifice flow. The above equations have been obtained from well know expressions for minor pressure losses in an orifice (White, 1991).

5.2.5 MR Valves

The schematic of the MR valve with the magnetic flux lines can be seen in Figure 5.1. We use the transmission line model, wherein each valve is broken up into N equal sections along its length, as seen in Figure 5.5.

The pressure drop across any section can be accounted by the effects of fluid inertia and viscous losses as follows :

$$P_i - P_{i+1} = R_v Q_i + \frac{L_{MR}/N}{A_{MR}} \rho_i \dot{Q}_i \tag{5.29}$$

where, R_v is the linear viscous loss coefficient for the individual section of the fluid line. For very low volume flow rates, as calculated in our actuation system, we can assume that the fluid volume flowing through all sections is the same i.e. $Q_i = Q \; \forall \; i = 1, 2, ...N$. Using this, we can now sum up the pressure drops over the entire length of the MR valve to get an expression for the overall loss in pressure ΔP_{MR} as a function of the volume flow rate Q as follows:

$$\Delta P_{MR} = \sum_{i=1}^{N} (P_i - P_{i+1}) \tag{5.30}$$

$$= R_v Q + \frac{L_{MR}}{A_{MR}} \left(\frac{1}{N} \sum_{i=1}^{N} \rho_i \right) \dot{Q} \tag{5.31}$$

Further, we assume that the fluid density varies linearly along the length of the valve. This allows us to replace the summation term in equation 5.30 by the arithmetic mean of the fluid densities at either end of the valve. Equation 5.30 can be simplified as:

$$\Delta P_{MR} = R_v Q + \frac{L_{MR}}{A_{MR}} \frac{(\rho_1 + \rho_N)}{2} \dot{Q} \tag{5.32}$$

As seen in Figure 5.3, we denote the volume flow rates through the four MR valves as Q_1, Q_2, Q_3 and Q_4. The pressure just downstream of the discharge reed valve is denoted as P_{ch}. The flow equations of valves 1-4 are as follows. R_v is the resistance offered by the valve to the flow. T_1, T_2, T_3 and T_4 are the pressure gradients caused due to the MR action and can be derived from either equation 5.7 or 5.9. The flow rate through an MR valve can be related to the pressure drop across the valve as follows:

$$Valve \;\; 1 : P_{ch} - P_H = R_v Q_1 + \frac{L_{MR}}{A_{MR}} \frac{(\rho_C + \rho_H)}{2} \dot{Q}_1 + T_1 \tag{5.33}$$

$$Valve \;\; 2 : P_{ch} - P_L = R_v Q_2 + \frac{L_{MR}}{A_{MR}} \frac{(\rho_C + \rho_L)}{2} \dot{Q}_2 + T_2 \tag{5.34}$$

$$Valve \;\; 3 : P_L - P_{acc} = R_v Q_3 + \frac{L_{MR}}{A_{MR}} \frac{(\rho_L + \rho_0)}{2} \dot{Q}_3 + T_3 \tag{5.35}$$

$$Valve \;\; 4 : P_H - P_{acc} = R_v Q_4 + \frac{L_{MR}}{A_{MR}} \frac{(\rho_H + \rho_0)}{2} \dot{Q}_4 + T_4 \tag{5.36}$$

In these equations we see that there are three contributing factors to the pressure drop across an MR valve. The first contributing factor is the viscous pressure loss and it depends linearly on the volume flow rate. The expression for the linear pressure loss was derived in equation 5.2. The second factor is the inertial pressure drop. Since the density of MR fluid is very high (3090 kg/m^3), accounting for the inertial pressure losses is very important. In this inertial term, we assumed that there occurs a linear variation of fluid density across the valve. A more accurate modeling could be done by considering the MR valve as a series of fluid transmission lines with distinct values of densities, pressures and flow rates. This approach was not taken in this study to avoid complexity. Also, due to the high viscosity of the MR fluid, the viscous pressure losses are more dominant than the inertial losses in the frequency range investigated in this study. The third term is the active pressure drop brought about by the application of the magnetic field across the valves. These equations are implicit as the exact value of $T1$, $T2$, $T3$ and $T4$ depends on the pressure drop across the valve itself. This will be evident from equations 5.5, 5.8 and 5.10.

5.2.6 Output Cylinder

The volume flux flowing into the high side of the pumping chamber is $Q_1 - Q_4$, as seen from Figure 5.3. The volume of fluid flowing out of the low side of the pumping chamber is $Q_3 - Q_2$. Using equation 5.15, we can write the density of the MR fluid in the high and low pressure sides of the output cylinder as follows:

$$\dot{\rho}_H = \frac{\rho_H \left(Q_1 - Q_4 - A_l \dot{x}_l\right)}{V_H} \tag{5.37}$$

$$\dot{\rho}_L = \frac{\rho_L \left(A_l \dot{x}_l - Q_3 + Q_2\right)}{V_L} \tag{5.38}$$

where, V_H and V_L denotes the instantaneous fluid volumes in the high and low sides of the output cylinder, ρ_H and ρ_L denotes the fluid densities in the high and low sides of the output cylinder, A_l is the area of cross-section of the output cylinder piston and $\dot{x}_l$ is the velocity of the output cylinder shaft. Correspondingly, we can write the expression for pressure in the high and low side of the output cylinder as follows:

$$P_H = P_{bias} + \beta log\left(\frac{\rho_H}{\rho_{bias}}\right) \tag{5.39}$$

$$P_L = P_{bias} + \beta log\left(\frac{\rho_L}{\rho_{bias}}\right) \tag{5.40}$$

The difference in fluid pressure on either side of the output cylinder piston constitute the forcing for the output cylinder shaft. The schematic for the output cylinder shaft can been seen in Figure 5.4(b). The motion of the output cylinder shaft was modeled as a one degree of freedom system.

$$M_l \ddot{x}_l + C_l \dot{x}_l + \left(L_0 - x_l\right) \frac{d}{dt}\left(\rho_l A_l \dot{x}_l\right) = \left(P_H - P_L\right) A_l - f_d \tag{5.41}$$

where, M_l is the mass of the load, C_l gives the damping coefficient of the output cylinder and f_d gives the value of dynamic friction in the shaft seals. As the cylinder shaft accelerates, the shaft experiences the inertial force exerted by the fluid column in the low pressure side of the output cylinder. The amount of fluid mass in this low pressure side varies as the cylinder shaft moves from one end to the other end of the output cylinder. This varying inertial force is modeled using the third term on the left hand side of equation 5.41. For modeling the motion of the output cylinder shaft, the friction in the shaft piston has to be accurately modeled. As with systems that experience Coulomb damping, piecewise equations have to be written to represent the motion of the cylinder shaft.

$$\ddot{x}_l = \begin{cases} 0 & \text{for } A_l\left(P_H - P_L\right) \leq f_s \\ \frac{A_l(P_H - P_L) - C_l A_l - f_d}{M_l} & \text{for } A_l\left(P_H - P_L\right) > f_s \end{cases} \tag{5.42}$$

where, f_s is the value of static friction.

5.2.7 Fluid Accumulator

The fluid accumulator consists of a chamber of fluid connected to the intake side of the pump. It is flanked on one side by a pocket of air that is separated from the fluid through a rubber diaphragm and which is pressurized to apply bias pressure of the entire system. Apart from applying the bias pressure to the system, the purpose of the fluid accumulator is to enable the pump to see a relatively constant pressure on the low pressure side and to filter out the high frequency oscillations in the system. Due to the presence of the accumulator, we can assume that the fluid in the intake tube is incompressible and has the baseline MR fluid density ρ_{bias}. Referring to Figure 5.3, we can use mass conservation equation to write the following equation for the accumulator.

$$\dot{P}_{acc} = \frac{k_{acc}\left(Q_3 - Q_{in}\right)}{A_{acc}^2} \tag{5.43}$$

where, A_{acc} is the area of cross section of the accumulator and k_{acc} is the accumulator stiffness. Typically, the stiffness of the accumulator is several orders smaller than the fluid stiffness, since the stiffness is provided by a pocket of air. This ensures that the change in the accumulator pressure during the actuator operation is very small.

5.3 State Space Formulation and Implementation

We can formulate equations 5.21, 5.22, 5.37, 5.38, 5.33, 5.34, 5.35, 5.36, 5.42 and 5.42 into a state space form. The states of the system are as follows:

$$
\begin{aligned}
x_1 &\rightarrow x_p, \text{Displacement of stack} \\
x_2 &\rightarrow \dot{x}_p, \text{Velocity of stack} \\
x_3 &\rightarrow \rho_c, \text{Density of fluid in pumping chamber} \\
x_4 &\rightarrow \rho_H, \text{Density of fluid in high side of output cylinder} \\
x_5 &\rightarrow \rho_L, \text{Density of fluid in low side of output cylinder} \\
x_6 &\rightarrow Q_1, \text{Volume flow rate through valve 1} \\
x_7 &\rightarrow Q_2, \text{Volume flow rate through valve 2} \\
x_8 &\rightarrow Q_3, \text{Volume flow rate through valve 3} \\
x_9 &\rightarrow Q_4, \text{Volume flow rate through valve 4} \\
x_{10} &\rightarrow x_l, \text{Displacement of load} \\
x_{11} &\rightarrow \dot{x}_l, \text{Velocity of load}
\end{aligned}
$$

The state space equations are as follows:

$$
\begin{aligned}
\dot{x}_1 &= \dot{x}_p \\
\ddot{x}_2 &= \left(k_a d_a B - P_C A_p - (k_a + k_d)\, x_p - C_p \dot{x}_p\right) \frac{1}{M_p + \frac{M_a}{3}} \\
\dot{x}_3 &= \frac{\rho_C}{V_C}\left(A_p \dot{x}_p - \dot{M}_{out} + \dot{M}_{in}\right) \\
\dot{x}_4 &= \frac{\rho_H}{V_H}\left(Q_1 - Q_4 - A_l \dot{x}_l\right) \\
\dot{x}_5 &= \frac{\rho_L}{V_L}\left(A_l \dot{x}_l - Q_3 + Q_2\right) \\
\dot{x}_6 &= \frac{2A_{mr}}{(\rho_C + \rho_H)\, L_{mr}}\left(P_C - P_H - R_v Q_1 - \frac{\rho_C\,(Q_1 + Q_2)^2}{r_h^2 A_o^2\,(1-\alpha)} - T_1\right) \\
\dot{x}_7 &= \frac{2A_{mr}}{(\rho_C + \rho_L)\, L_{mr}}\left(P_C - P_L - R_v Q_2 - \frac{\rho_C\,(Q_1 + Q_2)^2}{r_h^2 A_o^2\,(1-\alpha)} - T_2\right) \\
\dot{x}_8 &= \frac{2A_{mr}}{(\rho_L + \rho_0)\, L_{mr}}\left(P_L - P_{bias} - R_v Q_3 - T_3\right) \\
\dot{x}_9 &= \frac{2A_{mr}}{(\rho_H + \rho_0)\, L_{mr}}\left(P_H - P_{bias} - R_v Q_4 - T_4\right) \\
\dot{x}_{10} &= \dot{x}_l \\
\ddot{x}_{11} &= \begin{cases} 0 & \text{for } \; A_l\,(P_H - P_L) \le f_s \\ \frac{1}{M_l}\left[A_l\,(P_H - P_L) - C_l A_l - f_d\right] & \text{for } \; A_l\,(P_H - P_L) > f_s \end{cases}
\end{aligned}
\tag{5.44}
$$

5.3.1 Numerical Simulation

Equation set 5.44 are solved simultaneously using the Runge-Kutta numerical scheme. The Runge-Kutta is a well know numerical scheme to integrate ordinary differential equations by using a trial step at the mid-point of an interval to cancel out lower order error terms. A computer program was written in the language C to simulate the results. The simulations parameters are given in Table 5.1

There are some parameters in this model whose values cannot be accurately determined. They are:

- Bulk modulus of the MR fluid - β
- Stiffness of the accumulator - k_{acc}
- Damping coefficient of the fluid in the output cylinder - C_l

- Dynamic friction in the output cylinder shaft - f_s, f_d
- Loss factor of the reed valve - α
- Reed valve parameters - P_{crack}, P_{open}

These parameters will be estimated, within reasonable limits, to better fit the model to the experimental data.

5.4 Model Verification

The simulation results from the proposed model has to be verified against the experimental data to establish its usefulness as a design tool. Once the model has been verified with experimental data, a parametric analysis can be done to predict the performance trends of the actuation system.

5.4.1 Uni-directional No-load Performance

In uni-directional tests, the Terfenol-D is actuated at a particular pumping frequency and one arm of the Wheatstone bridge is provided with a saturating magnetic field to block the fluid flow through these valves to the maximum extent. A detailed explanation of the experimental procedure was given in the previous chapter. Figure 5.6 shows comparison between experimental data obtained from an LVDT connected to the output cylinder shaft and the prediction of the shaft displacement by the proposed analytical model for a pumping frequency of 100 Hz, bulk modulus of 7 kpsi and $\overline{\mu}$ of 0.0. Since the data was sampled at a high sampling frequency of 10 kHz, only 1 in 50 data points were chosen to plot this figure to ease the visualization of the graph. We can see from the figure that the model captures the overall motion and the velocity of the output cylinder shaft. The region enclosed within the rectangle shown in Figure 5.6 has been enlarged and shown in Figure 5.7. This enlarged portion shows that the model capture the step-wise motion of the output cylinder shaft. The step-wise movement, as described in Chapter 4, occurs due to the nature of the frequency rectification process performed by the passive reed valves. Due to the directionality of the reed valves, the cylinder shaft is allowed to move twice during every oscillation of the active stack. During the discharge phase of the pump, pressure builds up in the high pressure side of the output cylinder and allows the cylinder shaft to move. During the intake phase, the pressure in the low pressure side drops as fluid is allowed to flow into the pump from the accumulator. If the pressure in the low pressure side of the output cylinder drops below the value of pressure on the high pressure side of the cylinder, the cylinder shaft will move again. This will be determined by the various actuator parameters during the dynamic operation of the pump. Typically, the actuator shaft does not move appreciably during the intake phase when compared to its motion during the discharge phase.

The predicted value of the average velocity of the output cylinder shaft can be obtained for different values of pumping frequency. A comparison between the model prediction and the experimental data has been shown in Figure 5.8. The actuator resonance is located at a pumping frequency of 125Hz, beyond which, the performance of the actuator drops off. We can see that the model predicts the resonant peak at 150Hz, an over-prediction of 25 Hz.

The location of the resonant peak depends on two main factors - inertia and stiffness of the actuation system. In general, the inertia of the system consists of the inertia of the fluid, pump piston, output cylinder shaft and the external load. Figure 5.8 shows the results of actuator performance in the absence of external loads for a β 0f 7 kpsi and $\overline{\mu}$ of 0.1. In the model, the inertia of the fluid is taken into account in two ways.

- The inertia of the fluid in the MR valves is taken into account through the equations 5.33-5.36.

- The output cylinder shaft accelerates the fluid mass in the low pressure side of the cylinder. This is accounted for in equation 5.41. Any external inertial load can be coupled with the mass of the output cylinder shaft.

The pump piston mass and the output cylinder shaft mass has been accounted for in equations 5.21 and 5.41 respectively. There are, however, other stray fluid masses in the system which are not accounted for. For instance, the mass of the fluid in the fluid line leading from the accumulator to the inlet port, mass of fluid in the pumping chamber and the mass of fluid in interconnecting fluid lines between MR valves. Thus, the model under-represents the amount of fluid inertia in the system, thus showing a higher resonance frequency. We can see from the figure that the drop off in performance of the actuator after the resonance is reached has also been captured, although not accurately. Since the model accounts for most of the inertia of the system, it captures the roll off beyond the resonant frequency.

The second major factor affecting the resonance behavior of the system is the system stiffness. The stiffness arises from primarily three factors.

- Fluid stiffness arising from fluid compressibility.
- Stack stiffness.
- Fluid accumulator stiffness.

The fluid accumulator stiffness is accounted for in the model through equation 5.43. The stiffness of the Terfenol-D stack is accounted for in equation 5.21 that describes the motion of the pump piston. Since the accumulator stiffness is several orders of magnitude lower than the fluid stiffness, it has no effect on the frequency response. On the other hand, the location of the resonant peak is very sensitive to the value of bulk modulus of the MR fluid. In an ideal case, the hydraulic fluid must be incompressible, thus transferring all the energy from the active stack to the load. In reality, entrained air traps makes the fluid compressible and prevents the complete transfer of energy from the active stack to the load. A part of the energy provided to the hydraulic fluid is stored as elastic energy and then returned to the stack in the intake motion. This energy cannot be exploited as useful work. To alleviate this problem, a vacuum is applied on the MR fluid after filling the system to eliminate any air pockets or entrained air. However, the high viscosity of the MR fluid prevents all the entrained air from being extricated from the system. The value of bulk modulus used in these simulations was 47.4MPa (6000psi). Increasing the value of bulk modulus will make the fluid stiffer, thus moving the resonant peak to a higher frequency.

The estimation of damping in the system does not have a very large effect on the location of the resonant peak. However, it does affect the height of the peak. Increasing the damping in the system decreases the height of the resonant peak and also moves the frequency peak slightly leftward in the frequency scale, much like in the forced response of a single degree of freedom system. We can see that the model matches the experimental data very closely at lower frequencies.

5.4.2 Uni-directional Load Performance

The model can be used to ascertain the actuator load lines for different pumping frequencies. As described in the previous chapter, load lines show the variation of output actuator velocity for various values of output load. The intersection between the load line and the load axis gives the blocking force of the system. The load lines can then be used to calculate the power output capability of the actuation system. Figure 5.9 shows the model predicted load lines for a bulk modulus of 7 kpsi. The leakage through the MR valve is governed by the viscosity ratio, $\overline{\mu}$. As the load increases, the leakage across a saturated MR valves also increases. To account for that, the value of viscosity ratio, $\overline{\mu}$ is varied depending on the value of the load. In Figure 5.9, the value of viscosity ratio is changed from 0.1 for a no load case to 0.5 for a blocking load condition. As the external load increases, the viscosity ratio is varied using the following equation.

$$overline\mu = 0.1 + \frac{0.4}{F_{block}} F_{load} \tag{5.45}$$

where, F_{block} gives the block force of the system (30N) and F_{load} is the external load. The ascribed variation in the viscosity ratio can also be seen in Figure 5.10. We can see from the Figure 5.9 that the model over predicts the block force of the actuation system at around 30 N (3kg). The power output of the device is the half the area enclosed by the load line, as explained in Chapter 4. Figure 5.11 shows the model predicted variation of output power with pumping frequency. The figure also shows the experimentally obtained values of output power. However, the pumping frequency at which the peak output power occurs is over predicted by around 25 Hz.

5.4.3 Bi-directional No-load Performance

A detailed explanation of the bi-directional testing has been given in the previous chapter. The performance of the actuator in bi-directional mode is measured in terms of variation of output stroke versus actuator bi-directional frequency. The actuator bi-directional frequency is the frequency of switching of magnetic field applied to the arms of the Wheatstone bridge. The model was simulated for bi-directional motion at a pumping frequency of 100Hz. A comparison between the model and experimental data at an actuator frequency of 1 Hz and a pumping frequency of 100Hz is shown in Figure 5.12. We can see from the figure that the proposed model predicts the time variation of actuator stroke accurately for a no-load case.

The actuator stroke can be measured for a range of actuator frequencies. The results of comparison between the experimental results and simulations are shown in Figure 5.13. We can see that for a pumping frequency of 100Hz, the model predicts the bi-directional no-load performance of the actuator accurately. We can see from the figure that the model mildly under-predicts the stroke of the cylinder shaft. This is due to the fact that the uni-directional velocity of the actuation system was also under-predicted at a pumping frequency of 100Hz, as seen in Figure 5.8.

Figure 5.14 shows the time variation of the model predicted volume flow rates in the MR valves for a pumping frequency of 100 Hz and an actuator frequency of 1 Hz. The dotted line shows the motion of the output cylinder shaft. Bingham plastic model has been used to represent the rheological property of the MR fluids. We can see from the figure that as the magnetic field is intially applied to valves 1 and 3, Q_1 and Q_3 are zero for the initial time span of 0.5 s. At this point, the magnetic field is switched from valves 1 and 3 to valves 2 and 4, thus reducing Q_2 and Q_4

to zero for the time span from 0.5 to 1.0 s. This allows the output cylinder shaft to move in the opposite direction. We can also see that Q_3 and Q_4 are smaller in magnitude when compared to Q_1 and Q_2. This is due to the fact that the volume flow rates through valves 3 and 4 flow into the fluid accumulator, whose pressure does not change appreciably owing to its large capacity.

5.4.4 Bi-directional Performance with Inertial Load

The model can be used to predict the performance of the actuation system under an inertial load. The inertial load is added to the state space equations along with the mass of the output cylinder shaft, as shown in equation 5.46.

$$M_L = M_{L,shaft} + M_{L,external} \tag{5.46}$$

where, $M_{L,shaft}$ is the mass of the output cylinder shaft and $M_{L,external}$ is the mass of the external load. Figure 5.15 shows the comparison between the model prediction and experimental results for an inertial load of 10 lbs and 15 lbs. Though the model accurately predicts the trend in the variation of the output stroke with load mass, it over-predicts the actuator stroke for the two masses considered.

5.4.5 Bi-directional Performance with Stiffness Load

The model can also be used to predict the performance of the actuation system under a stiffness load. The external stiffness load is added to the system equations in the following way. The equation of motion of the output cylinder shaft, that is equation 5.41, is modified to account for the external stiffness.

$$M_l\ddot{x}_l + C_l\dot{x}_l + K_l x_l + (L_0 - x_l)\frac{d}{dt}(\rho_l A_l \dot{x}_l) \;\; = \;\; (P_H - P_L)\, A_l - f_d \tag{5.47}$$

Figure 5.16 shows the model prediction for bi-directional actuator performance various values of external stiffness, K_l. We can see that the effect of the external stiffness is felt more at lower values of actuator frequency. This is due to the fact that the stiffness force increases linearly with actuator stroke. Since actuator stroke is greater for lower actuator frequency, the effect of the stiffness load is felt more at lower values of actuator frequency. We can see that the trend of the actuator performance as predicted by the model is identical to the experimental trends shown in Figure 4.20. Figures 5.17 and 5.18 show the predicted variation of actuator stroke with actuator frequency for two different values of external stiffness, 34 lbs/in and 68 lbs/in. Both the lines were plotted for a β of 7 kpsi and $\overline{\mu}$ of 0.1. These figures also compare the model predictions with the experimental data. Though the model accurately predicts the trend in actuator performance, the exact values do not match the data.

5.5 Parametric Analysis

5.5.1 Effect of bulk modulus

As mentioned earlier, the location of the resonance peak of the actuation system depends on the stiffness and inertia of the fluid network along with the stiffness of the hybrid material and the external load. The bulk modulus of the fluid determines the stiffness of the fluid lines in the network. Though the reference bulk modulus of the fluid is stated to be 260 kpsi (1.8 GPa), the presence of entrained air within the system lowers the bulk modulus to around 5-20 kpsi. We can use the model to ascertain the effect of bulk modulus on the system performance. Figure 5.19 shows the model predictions for the variation actuator velocity with pumping frequencies for various values of bulk modulus. We can see that as we increase the bulk modulus, the stiffness of the fluidic system increases and the resonance peak shifts to the right of the frequency scale. There is also an increase in the velocity peak obtained. As the hybrid stack pressurizes the fluid, some energy is stored within the fluid as elastic energy owing to its compressibility. This energy cannot be obtained as useful work and is returned to the hybrid stack. As the fluid becomes stiffer, lesser amount of energy is lost to the compressibility of the fluid.

The bulk modulus of the fluid has an effect on the amount of power output of the actuation system. The comparison between the experimentally obtained output power and model predictions were made in the earlier section. Figure 5.20 shows the variation of power output of the device with pumping frequency for various values of bulk modulus. All the lines were plotted for a $\overline{\mu} = 0.0$ (Bingham-plastic). We can see from the figure that the output power increases with increasing bulk modulus. Also, the maximum output power occurs at a higher pumping frequency as the bulk modulus increases. This is due to the increase in fluid stiffness as the effect of entrained air decreases, thus allowing more energy transfer between the hybrid stack to the load. The curve for a bulk modulus of 260 kpsi (reference bulk modulus of the fluid) is the maximum obtainable power from the system as the fluid stiffness is greatest and there is no leakage through the MR valves. Figure 5.21 shows the variation of power output with nondimensional viscosity ratio for a bulk modulus of 260 kpsi. We can see from this figure that the power output of the device drops with viscosity ratio. However, unlike the bulk modulus, the location of peak power output does not change.

5.5.2 Effect of pre-yield viscosity on uni-directional performance

The bi-viscous rheological model for MR fluids states that the fluid exhibits Newtonian behavior with a finite viscosity in the pre-yield region. The post-yield behavior is also Newtonian, but with a lower viscosity than the pre-yield region. This is unlike the Bingham plastic model which states that the MR fluid has infinite viscosity in the pre-yield region. Thus, the bi-viscous model allows a small leakage flow through the MR valve at all values of magnetic field, the magnitude of which depends on the value of pre-yield viscosity. The proposed model can be used to predict the effect of pre-yield viscosity on the output velocity. Figure 5.22 shows the predicted values of output actuator displacement with time for various values of the viscosity ratio $\overline{\mu}$. The viscosity ratio, $\overline{\mu}$, is defined as the ratio of post-yield viscosity to pre-yield viscosity. The Bingham plastic model has a viscosity ratio of zero since the pre-yield viscosity is infinite. We can see that the actuator velocity decreases as the viscosity ratio increases. This is due to the fact that more leakage flow is allowed through the MR valves (which are blocked according to the Bingham plastic model) as the viscosity ratio increases.

This can be seen more clearly from Figure 5.23. Q_1, Q_2, Q_3 and Q_4 are the volume flow rates through valves 1, 2, 3 and 4. To produce uni-directional motion in the output cylinder shaft, a magnetic field is applied to valves 2 and 4. We can see that as the viscosity ratio is increased, the flow rates through valves 2 and 4, that is, Q_2 and Q_4 increase. As Q_2 and Q_4 increase, Q_1 and Q_3 decrease accordingly. This is because the discharge port of the pump is connected to valves 1 and 2. If the flow through valve 2 is completely blocked off, the entire fluid flow exiting the pump would flow through valve 1. The volume flow rate through valve 1 decreases as an increasing leakage flow is allowed through valve 2. If a leakage flow is allowed through valve 4, the amount of volume flow rate entering the output cylinder is lesser (lesser than if the flow through valve 4 were blocked). Since the volume flow rate entering the output cylinder is less, the output cylinder shaft moves a lesser amount. Since the motion of the output cylinder shaft has decreased (than the blocked condition), the volume flow rate through valve 3 is also less. Thus, the leakage flow through valves 2 and 4 decreases the volume flow rate through valves 1 and 3, thus reducing the output cylinder shaft velocity.

5.5.3 Effect of pre-yield viscosity on bi-directional performance

Leakage flow through the MR valves decreases the amount of stroke obtainable at any given value of actuator frequency. Figure 5.24 shows model prediction of output stroke for an actuator frequency of 1 Hz for different values of viscosity ratio. The figure shows that there is a deterioration in actuator stroke with increasing viscosity ratio.

5.6 Conclusions

A comprehensive model of a magnetorheological actuation system has been developed. The model is derived from a series of differential equations which represent the different sections of the system. The active material stack and pump piston are modeled as a one degree of freedom system. The forcing for the entire system is provided by the magnetic field which actuates the active stack. Equations derived from the mass conservation equation are used to represent the time rate of change of fluid densities and fluid pressures in the different areas. These equations are used together with fluid compressibility to give an accurate representation of actuator operation. The rheological properties of the MR fluid is taken into account using the Bingham plastic and the bi-viscous models. The flow rate through each of the MR valves of the Wheatstone bridge is related to the pressure difference across the valves using three pressure loss components - viscous, inertial and active.

A comparison was made between the theoretical model and the experimental results. We can see that the model over predicts the resonant frequency of the actuation system by 25 Hz. This is due to the difficulty in completely accounting for all fluid inertia in the system. We also see that the bi-directional performance is accurately modeled by this model, with a slight under-prediction.

The effect of using a bi-viscous model to represent the rheological behavior of the MR fluid has also been predicted using the model. As the bi-viscous model allows a leakage flow through the MR valve at all points of operation, the actuator performance obtainable from the actuator decreases with increasing pre-yield viscosity.

5.7 Nomenclature

α	Loss coefficient in reed valve
β	Bulk modulus of fluid
d_a	Piezomagnetic coefficient of active material
$\rho_{bias}, \rho_{ch}, \rho_H, \rho_L$	Fluid density at bias pressure, in the pumping chamber, in high and low pressure side of output cylinder
r_{dis}, r_{int}	Exhaust/intake port valve opening
x_{acc}	Displacement of accumulator diaphragm
x_p	Displacement of pumping piston
x_l	Displacement of load
A_{ch}	Cross-sectional area of pumping chamber
A_l	Cross-sectional area of output cylinder
A_t	Cross-sectional area of tubing
B	Magnetic flux density through Terfenol-D rod
C_L, C_p	Damping coefficients of load, pumping piston
E_a	Young's modulus of active material
K_a, K_{acc}, K_d, K_s	Stiffnesses of actuator, accumulator, diaphragm and pre-load spring
L_a, L_{ch}, L_o, L_{mr}	Lengths of actuator rod, pumping chamber, output cylinder and MR valve
M_L, M_p	Mass of load, piston
Q_{in}, Q_{out}	Volume flow rate through intake/exhaust valve
Q_i	Volume flow rate through MR valve number i
P_{acc}	Pressure in accumulator
P_{ch}	Pressure in pumping chamber
P_{cr}, P_{open}	Cracking and opening pressure of reed valves
P_H, P_L	Pressure in high and low pressure driving side

Table 5.1: Simulation Parameters

MR Fluid	
Density, ρ_{bias}(kg/m^3)	3090
Viscosity, μ(Pa/s)	1
Bulk modulus, β(Pa)	47.4MPa
Bias pressure, P_{bias}(Pa) 689kPa	
Terfenol-D Stack	
Stack stiffness, k_a(N/m)	76×10^6
Stack mass, M_a(kg)	0.0743
Pumping Chamber	
Chamber cross-sectional area, A_p(m^2)	0.0011
Piston mass, M_p(kg)	0.2
Chamber damping, C_p(kg.m)	0
Diaphragm stiffness, k_d(N/m)	3.6×10^3
MR Valve	
Valve length, L_{mr}(m)	33.6×10^{-3}
Valve active length, L_{act}(m)	11.2×10^{-3}
Annulus thickness, d(m)	0.5×10^{-3}
Output Cylinder	
Static friction, f_s(kgf)	2
Dynamic friction, f_d(kgf)	1
Shaft mass, M_l(kg)	30×10^{-3}
Shaft area, A_l(m^2)	7.91×10^{-5}
Cylinder damping, C_l(kg.m)	50

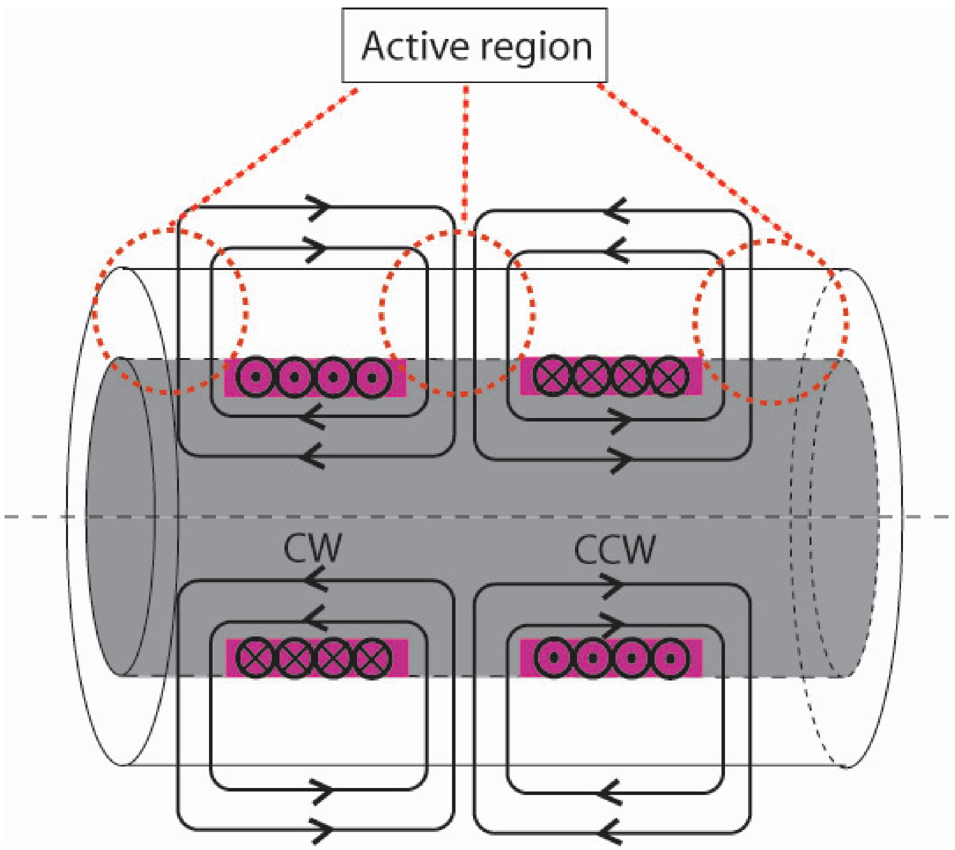

Figure 5.1: Schematic of MR valve showing the magnetic flux lines

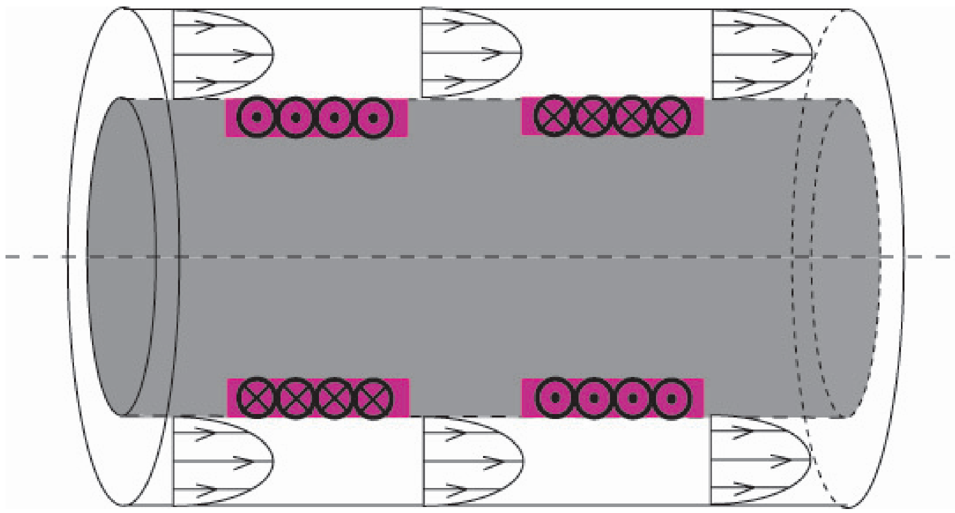

(a) Schematic for upward motion

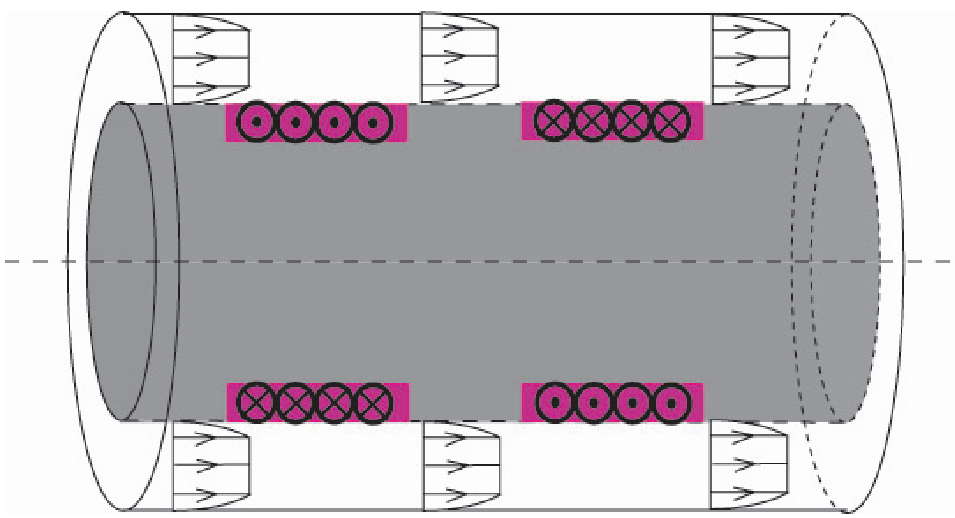

(b) Schematic for downward motion

Figure 5.2: Schematic of velocity profile of flow through the annulus of the MR valve

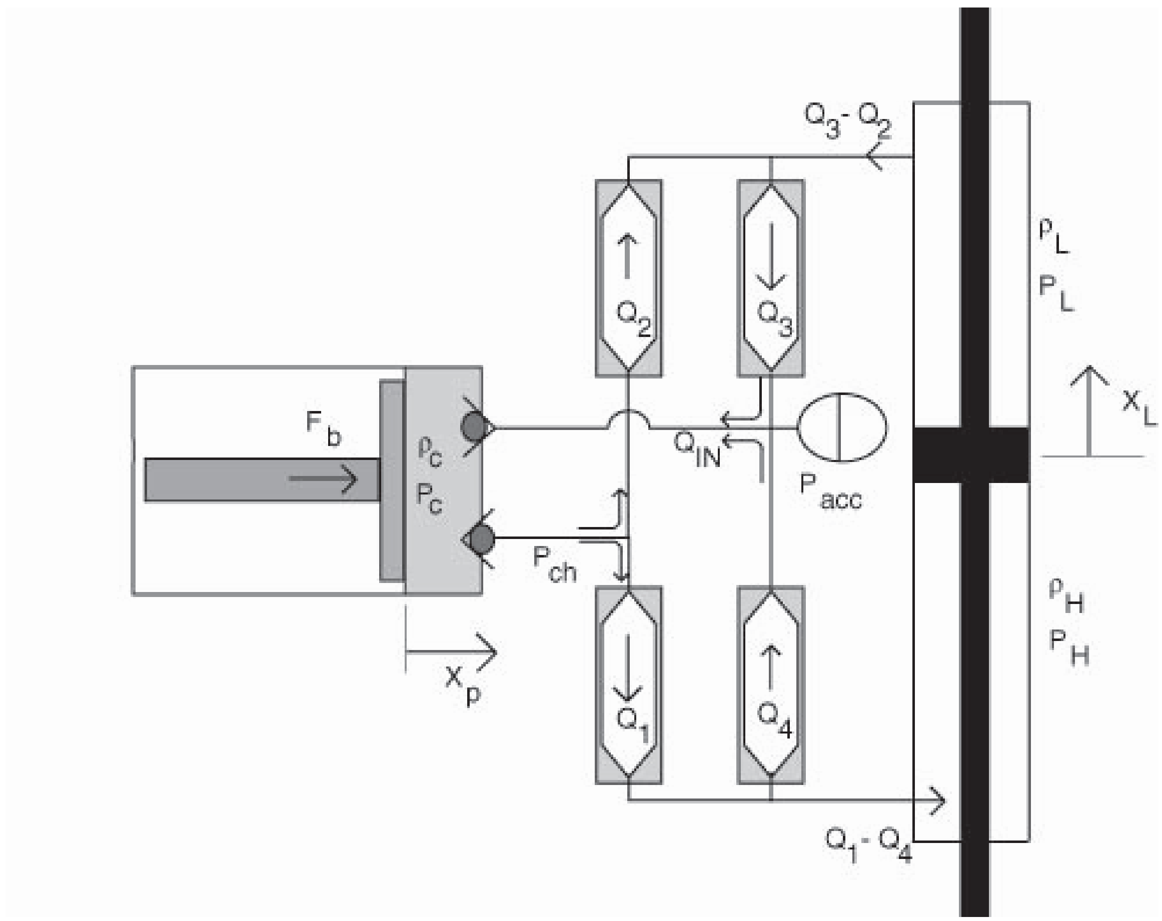

Figure 5.3: Schematic of the MR actuation system showing the variables used in the model.

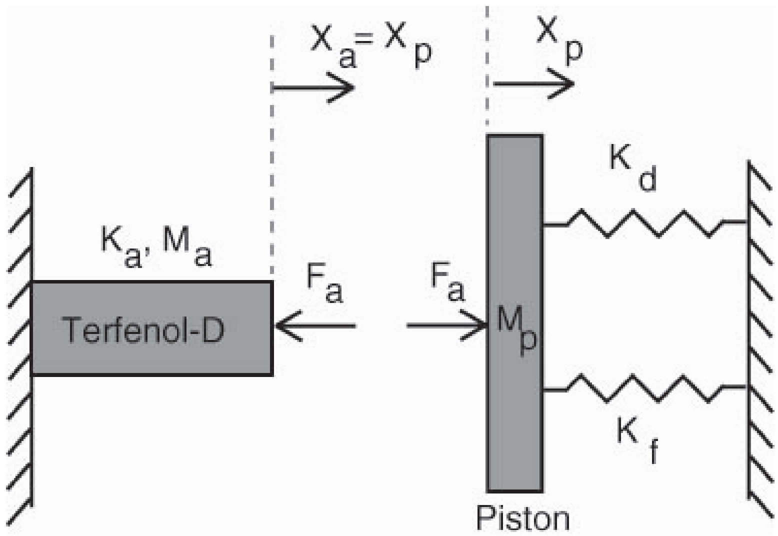

(a) Schematic for pumping chamber

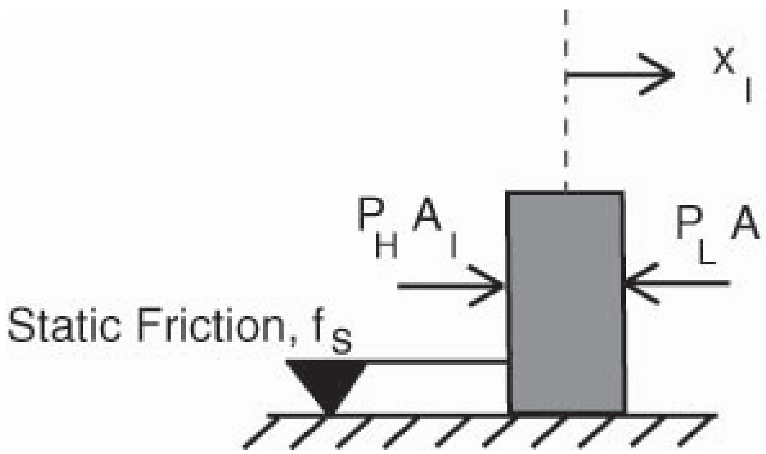

(b) Schematic for output cylinder shaft

Figure 5.4: Schematic for the pumping chamber and output cylinder shaft models

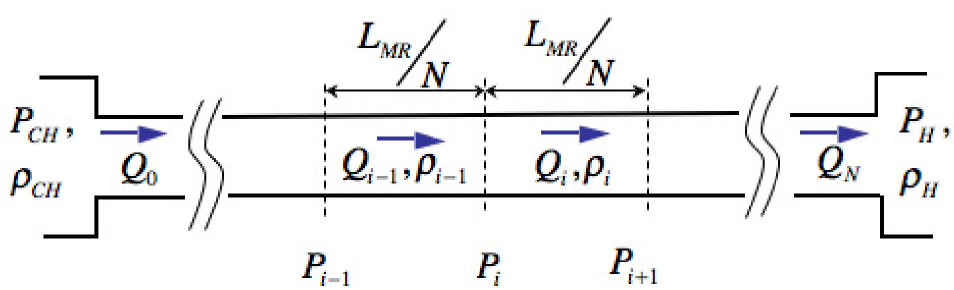

Figure 5.5: Lumped model of fluid flow through MR valve

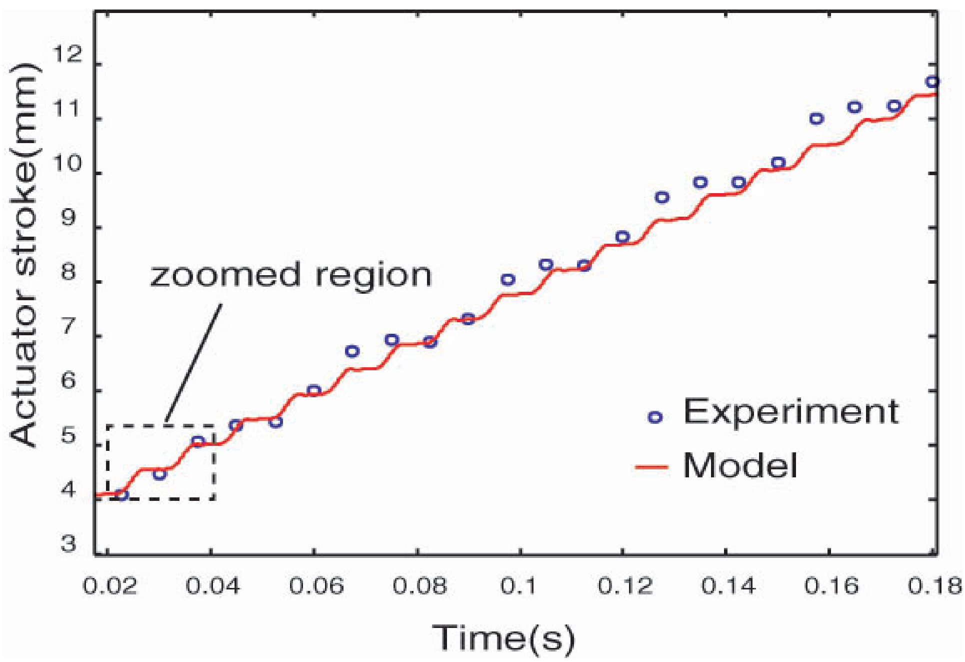

Figure 5.6: Comparison of actuator stroke data obtained from the LVDT for uni-directional motion of the output cylinder shaft and model prediction at a pumping frequency of 100Hz ($\beta = 7$ kpsi, $\overline{\mu} = 0.0$).

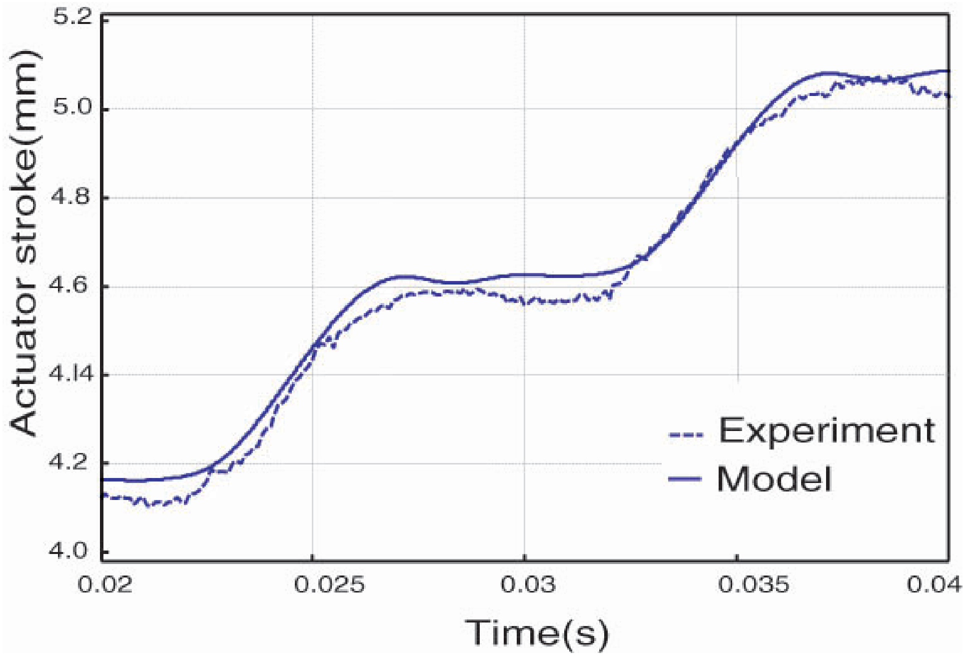

Figure 5.7: Comparison of actuator stroke data obtained from the LVDT for uni-directional motion of the output cylinder shaft and model prediction at a pumping frequency of 100Hz (zoomed region).

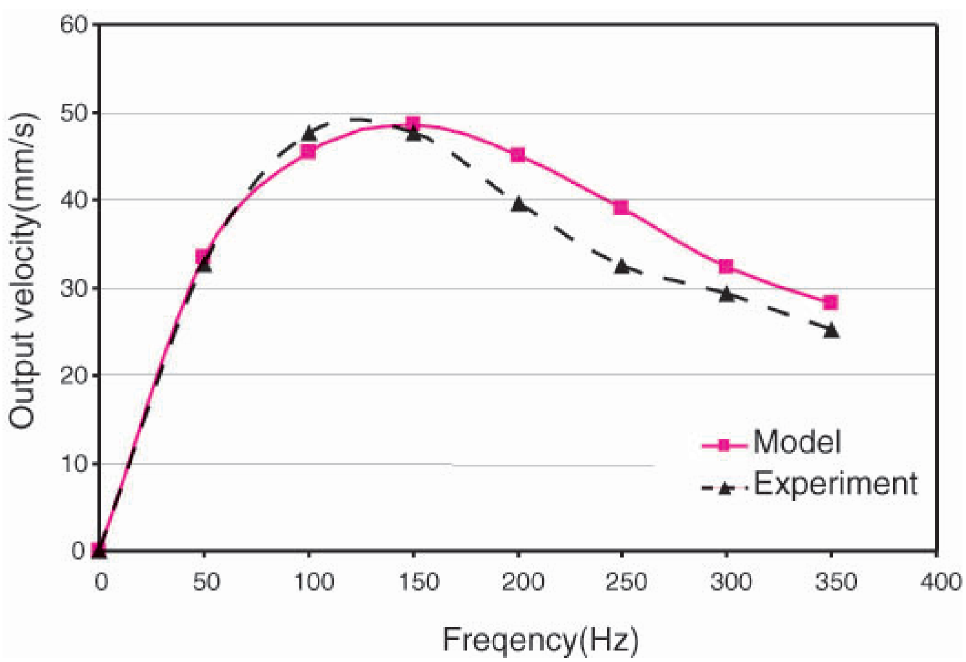

Figure 5.8: Comparison of actuator performance between experiment and model for uni-directional no-load case (β = 7 kpsi, $\overline{\mu} = 0.0$).

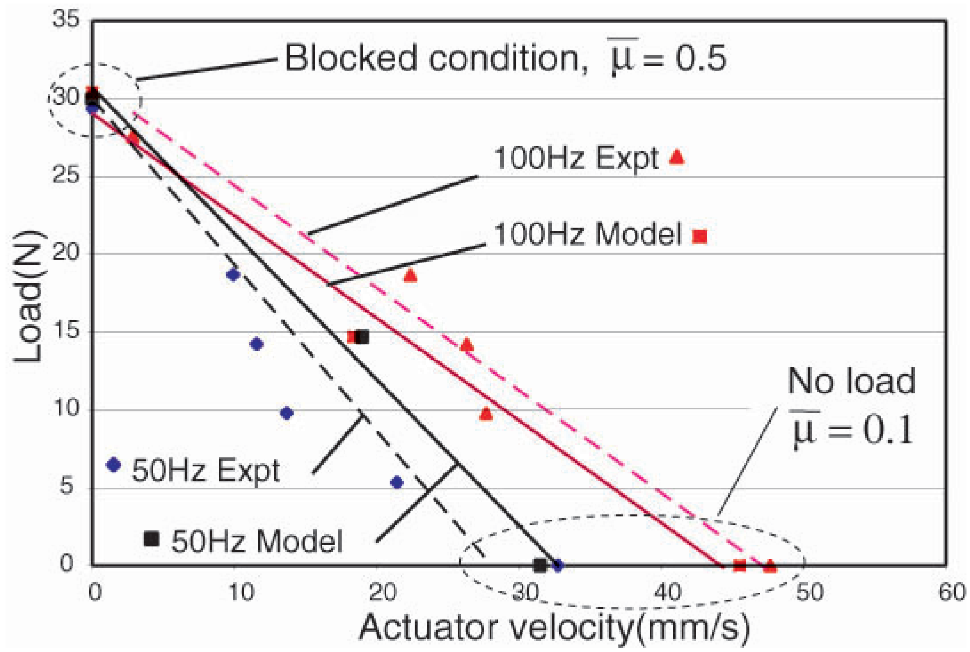

Figure 5.9: Actuator load lines for bulk modulus of 7 kpsi

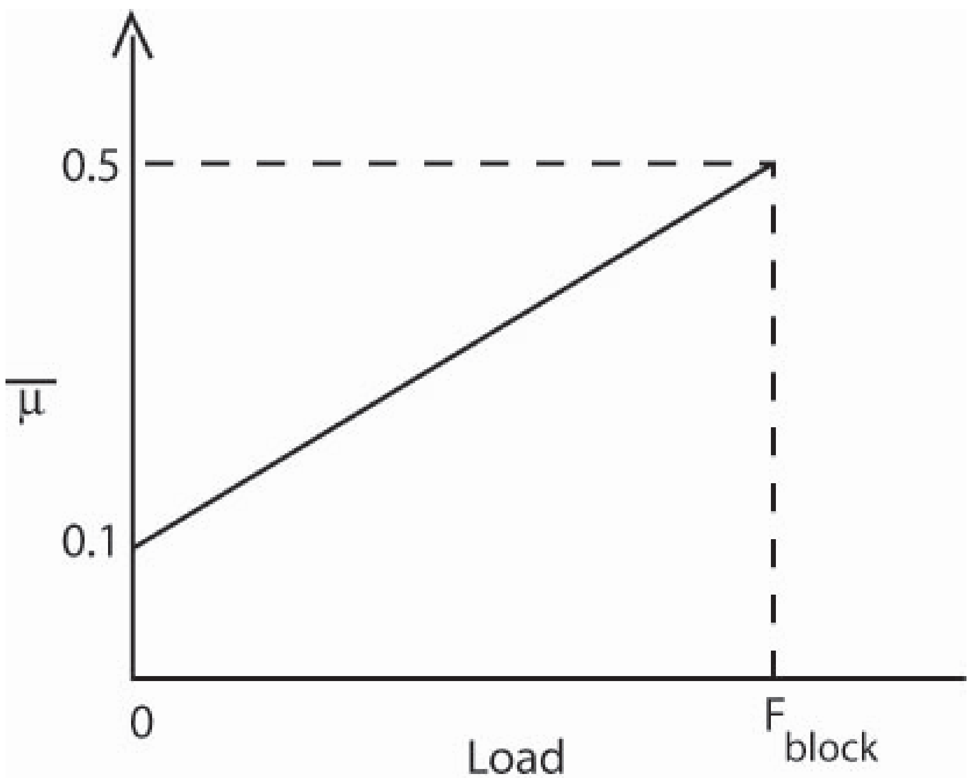

Figure 5.10: Variation in viscosity ratio used to model the actuator loadlines

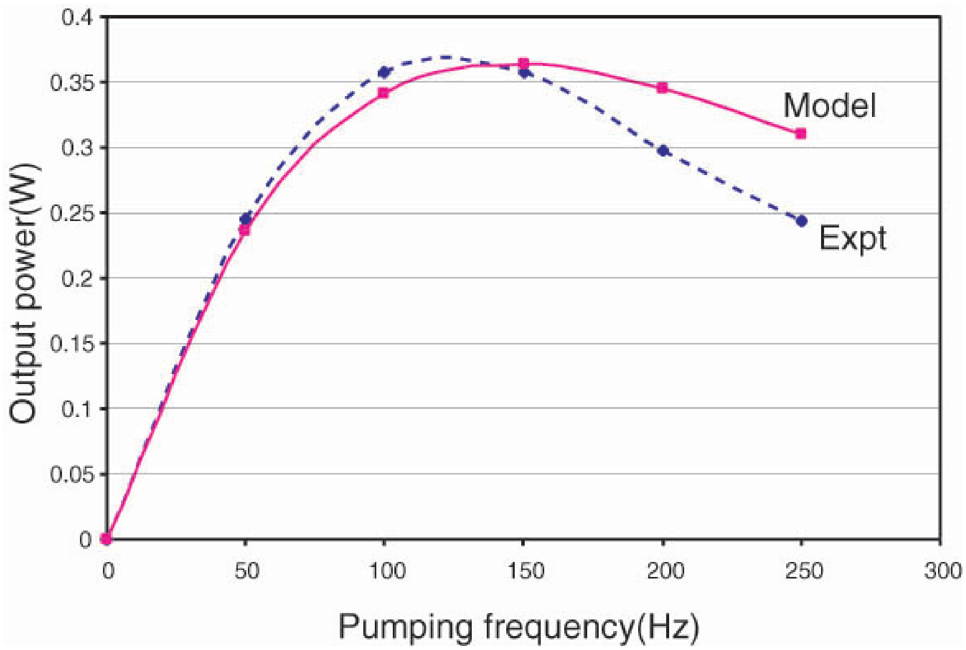

Figure 5.11: Variation of output power of the actuation system with pumping frequency and comparison with analytical model for a bulk modulus of 7 kpsi.

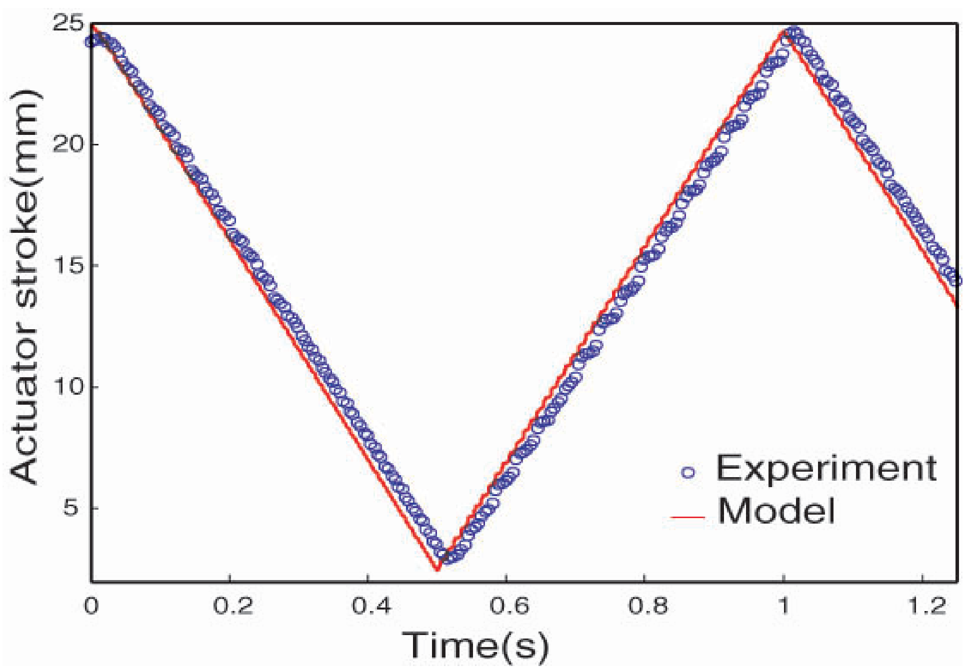

Figure 5.12: Comparison of model prediction and experimental data for time variation of actuator stroke for a pumping frequency of 100Hz and an actuator frequency of 1 Hz.

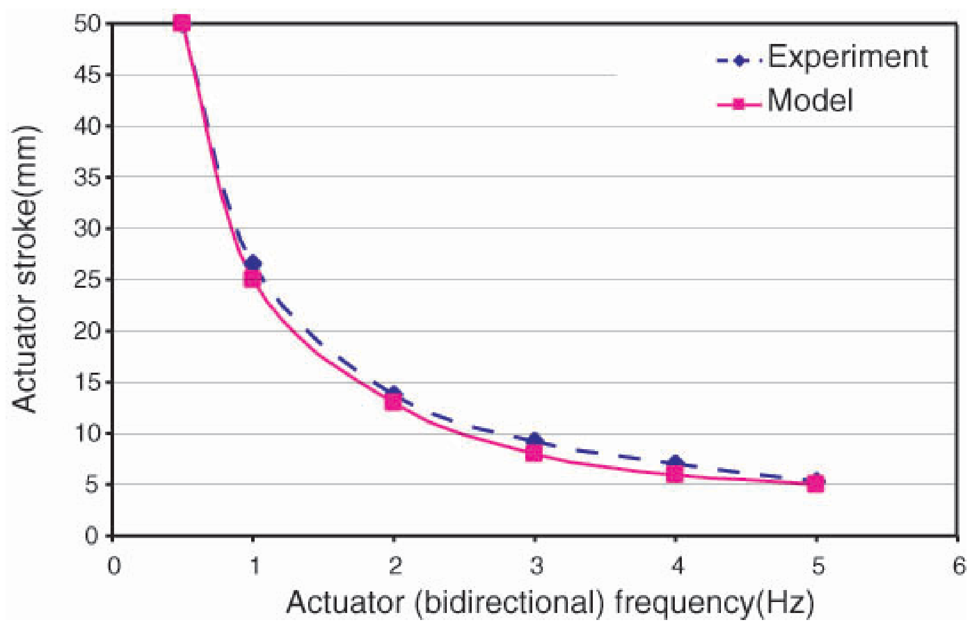

Figure 5.13: Comparison of actuator performance between experimental data and model prediction for bi-directional no-load case with a pumping frequency of 100 Hz.

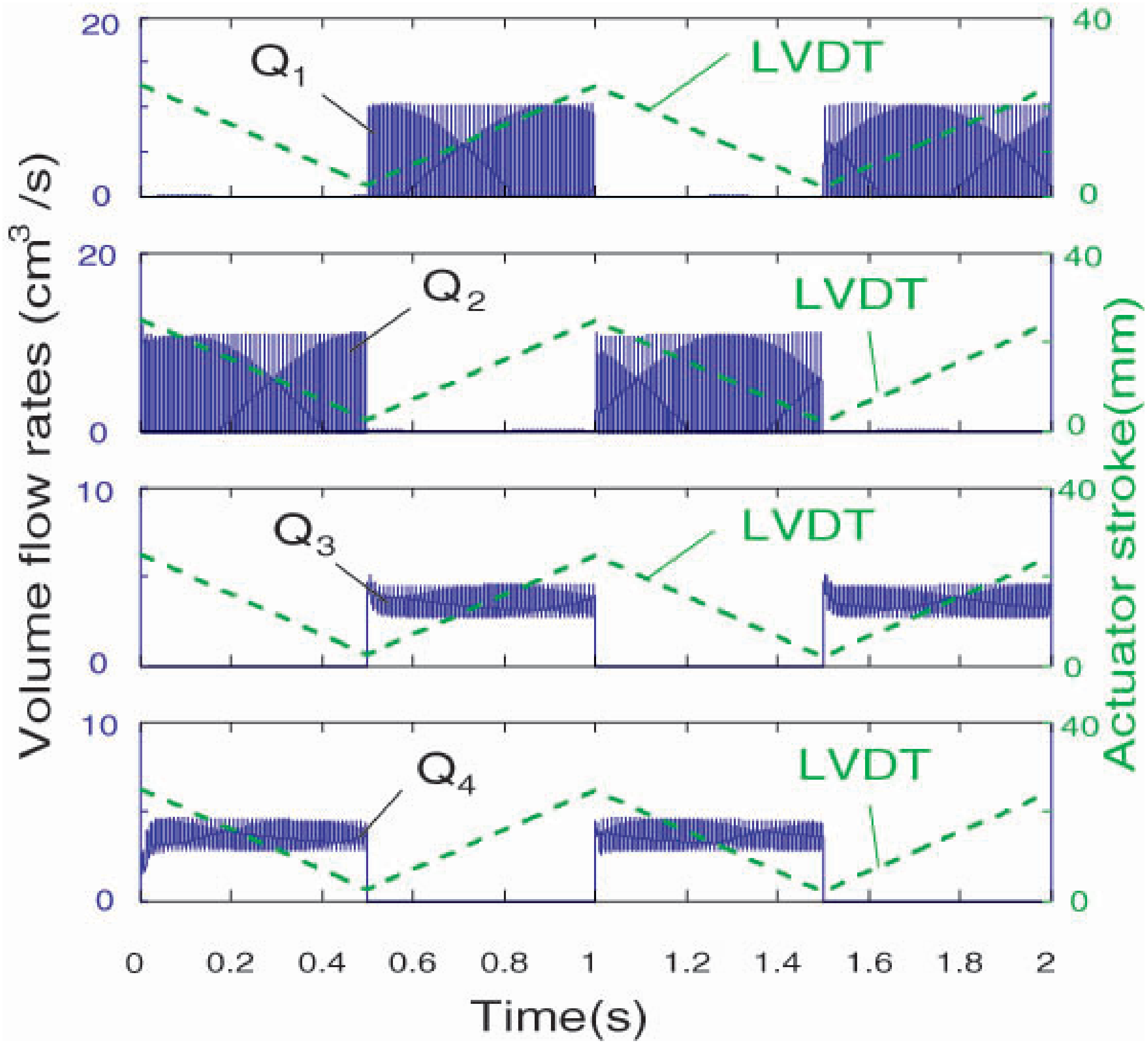

Figure 5.14: Time variation of volume flow rate through the MR valves for a pumping frequency of 100 Hz and an actuator frequency of 1 Hz.

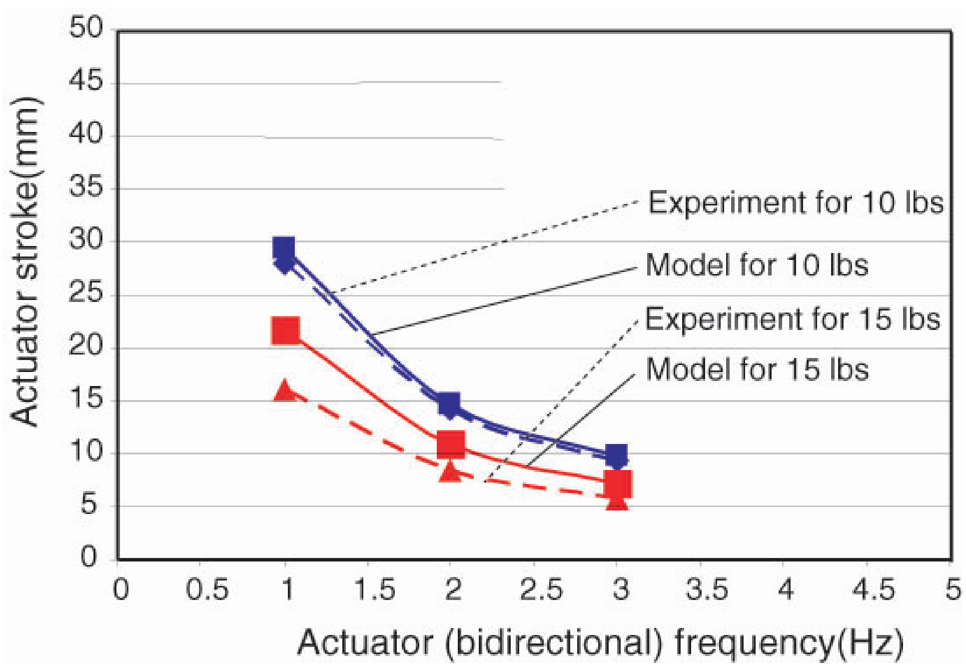

Figure 5.15: Comparison of model prediction with experimental data for the variation of actuator stroke with actuator frequency for a pumping frequency of 100 Hz

.

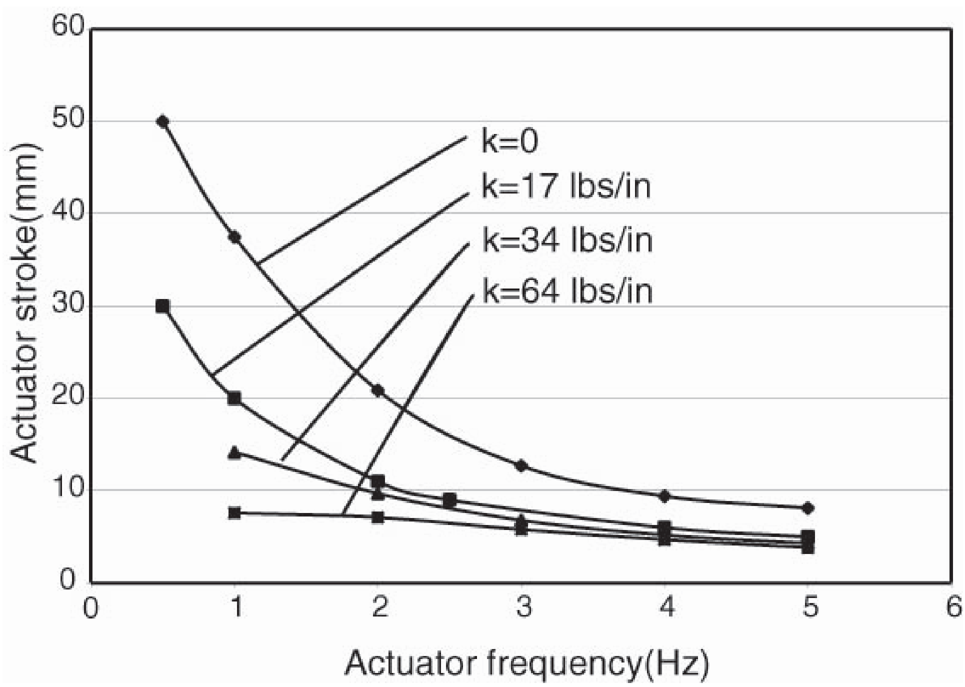

Figure 5.16: Model prediction of variation of actuator stroke with actuator frequency for various values of external stiffness for a pumping frequency of 100 Hz (β = 7 kpsi, $\overline{\mu} = 0.0$).

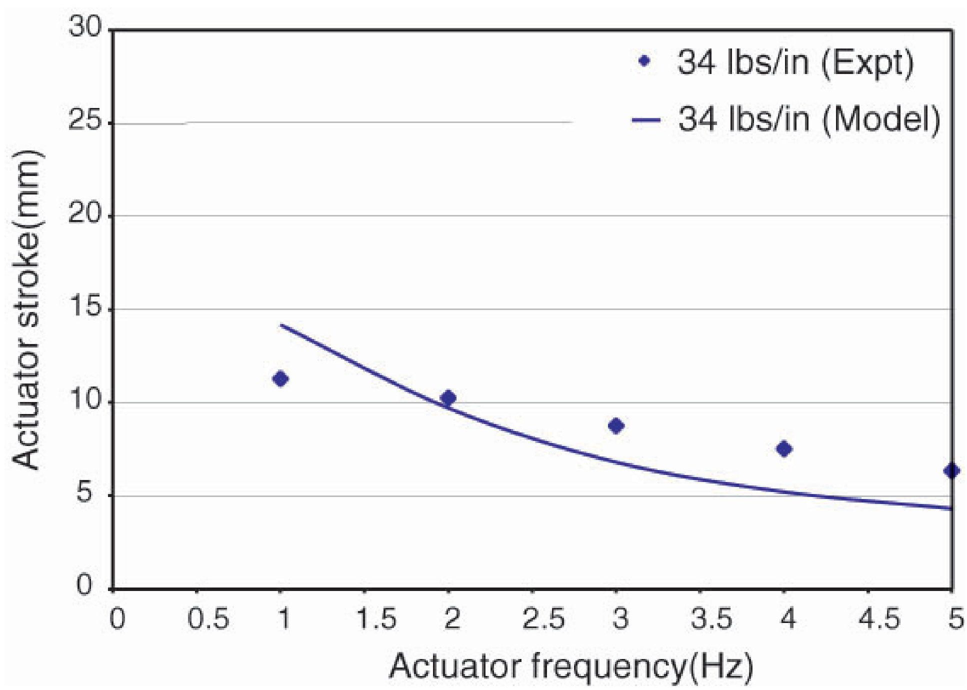

Figure 5.17: Comparison between model prediction and experimental data for an external stiffness of 34 lbs/in and pumping frequency of 100 Hz.

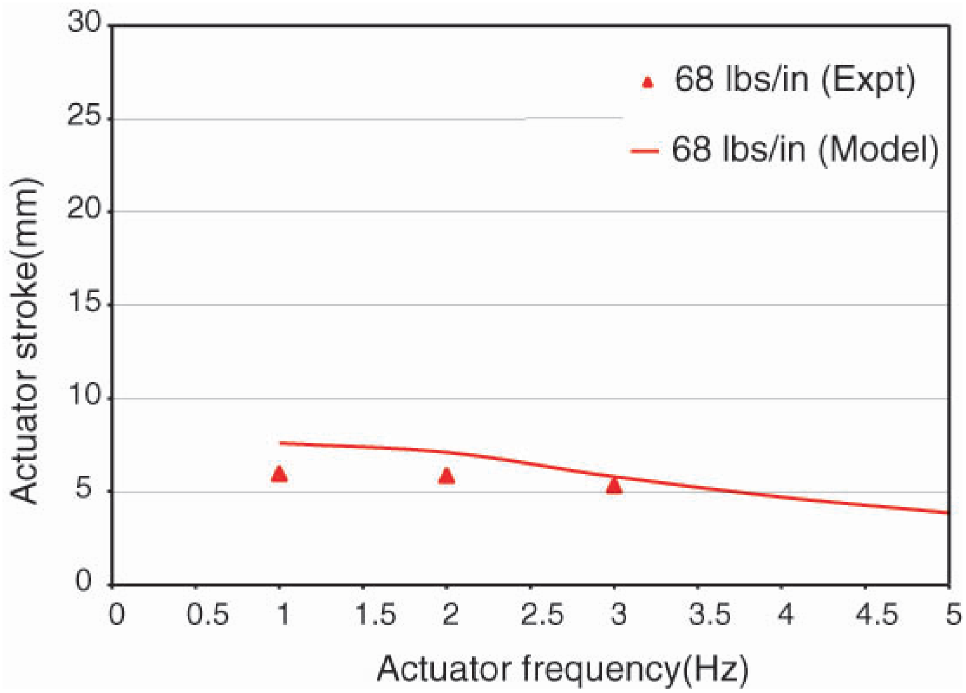

Figure 5.18: Comparison between model prediction and experimental data for an external stiffness of 68 lbs/in and pumping frequency of 100 Hz.

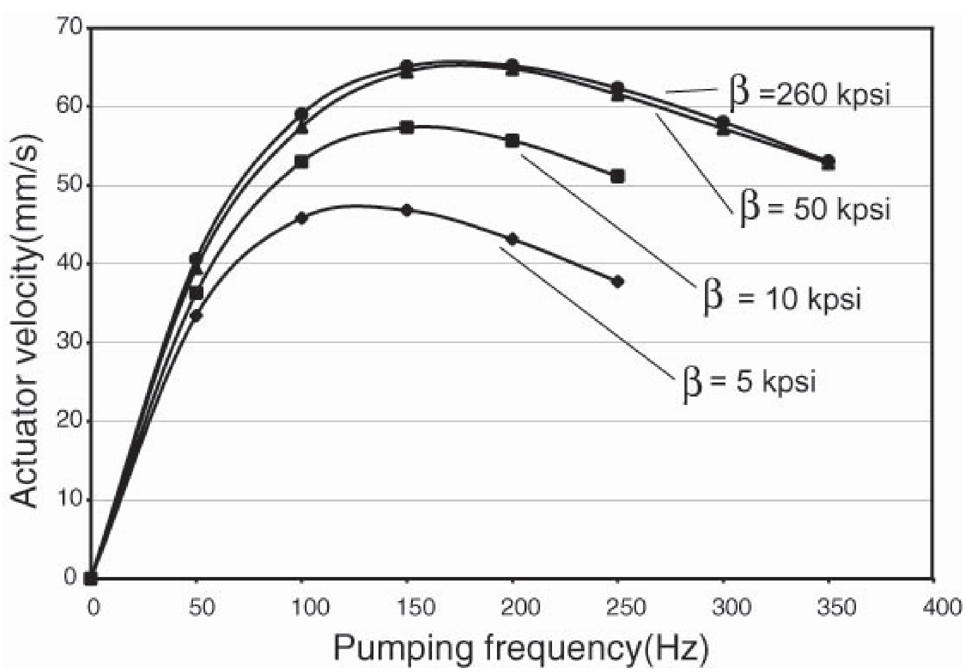

Figure 5.19: Variation of uni-directional actuator performance for various values of bulk modulus

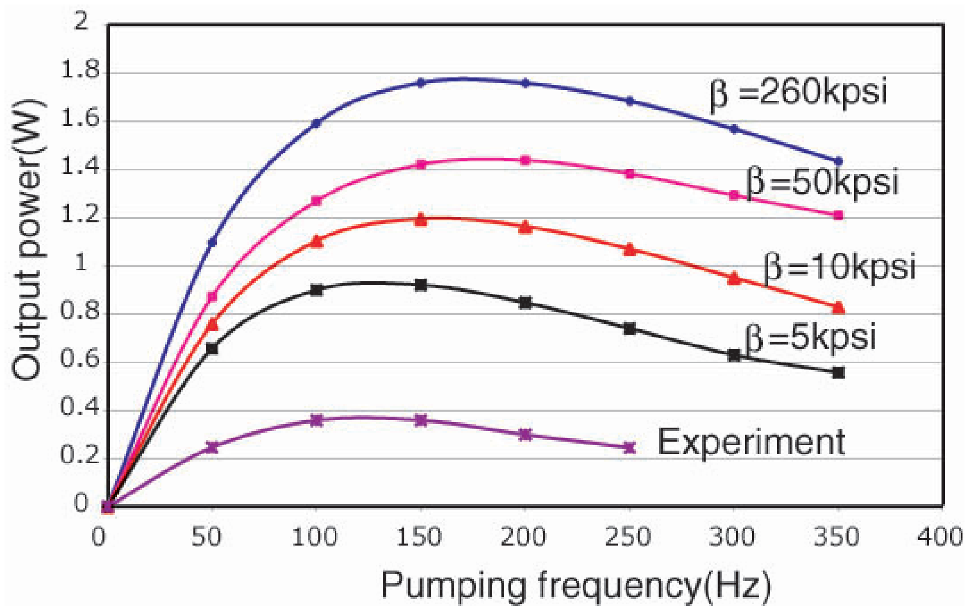

Figure 5.20: Variation of output power of the actuation system with pumping frequency for various values of bulk modulus ($\overline{\mu} = 0$).

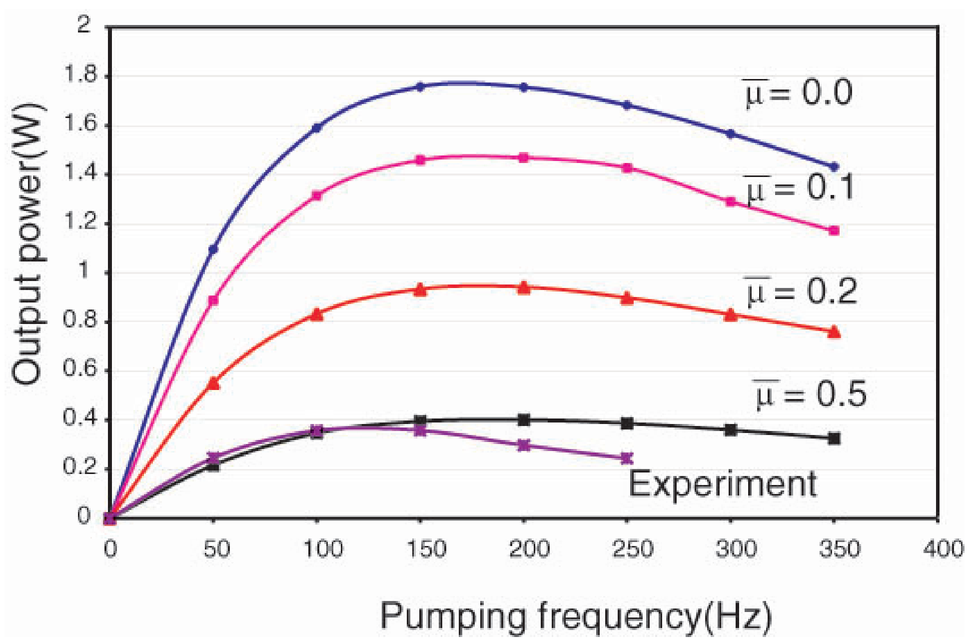

Figure 5.21: Variation of output power of the actuation system with pumping frequency for various values of viscosity ratios ($\beta = 260$ kpsi).

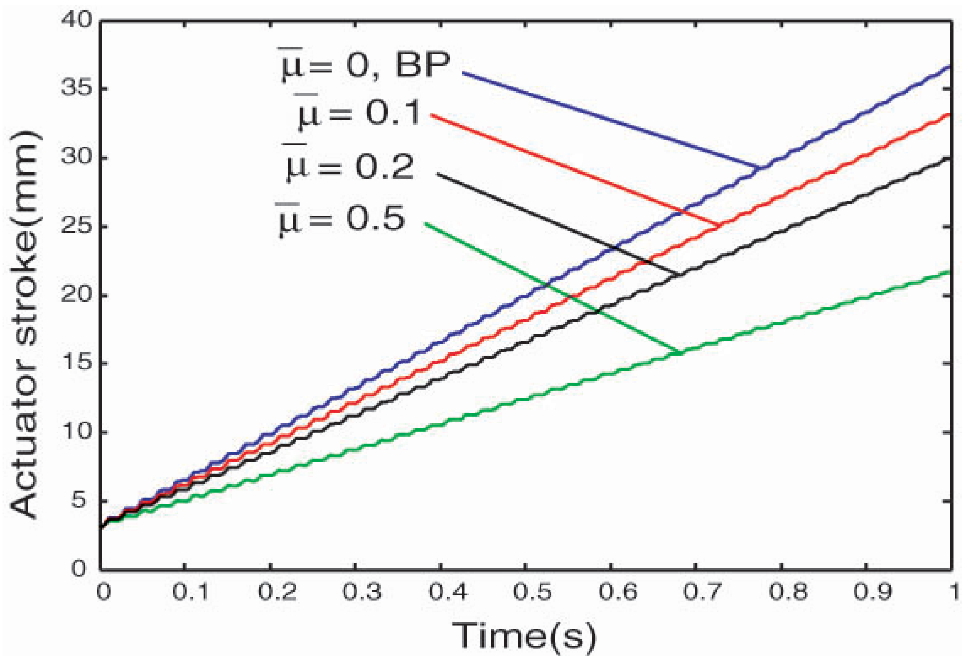

Figure 5.22: Variation of actuator displacement for various values of viscosity ratio $\overline{\mu}$. This simulation was performed for a uni-directional case with a pumping frequency of 100 Hz.

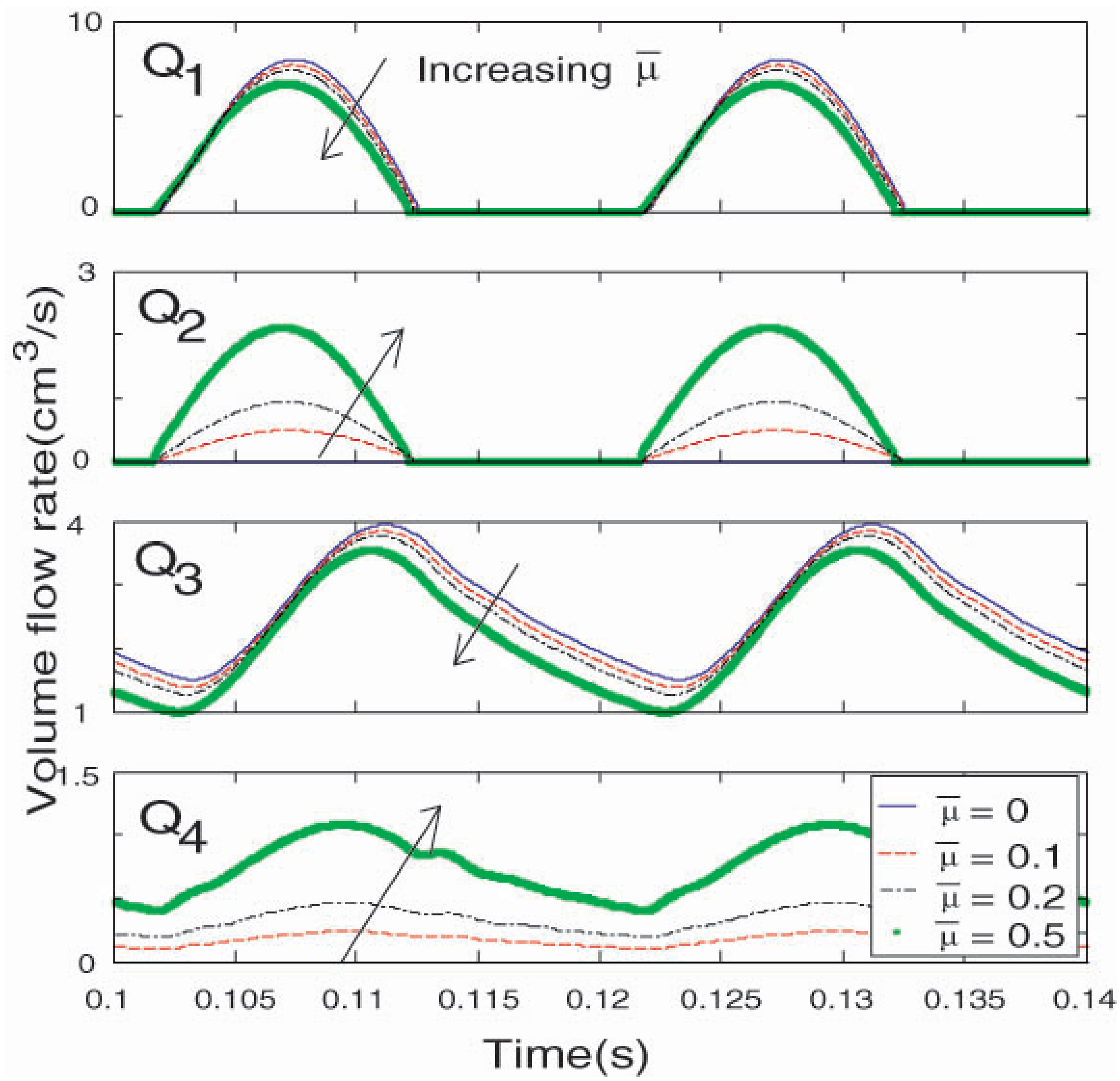

Figure 5.23: Variation of volume flow rates through MR valves for various values of viscosity ratio $\overline{\mu}$. This simulation was performed for a uni-directional case with a pumping frequency of 100 Hz.

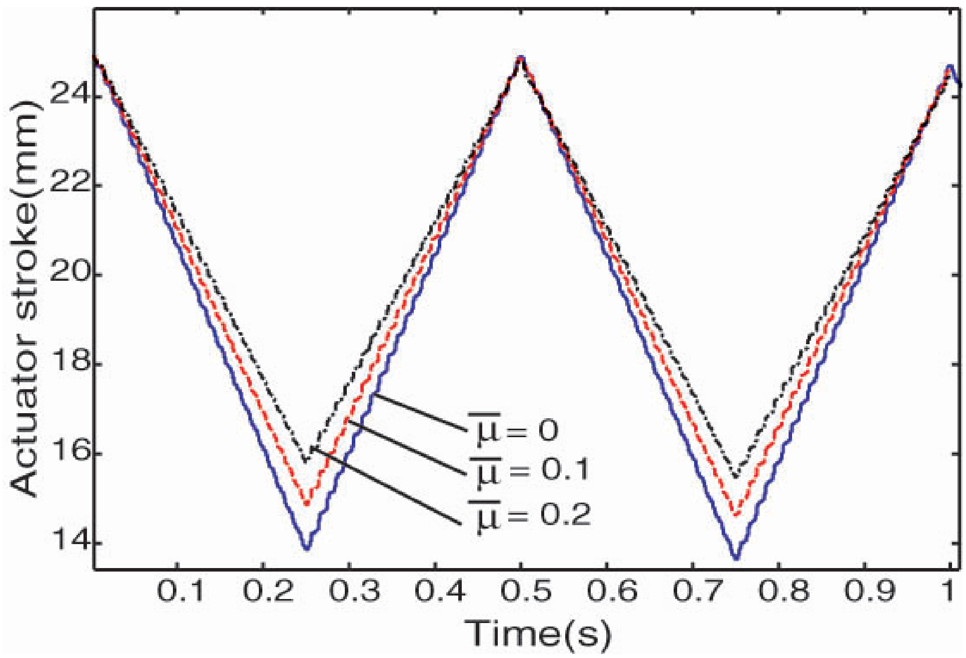

Figure 5.24: Effect of leakage flow across MR valves on the actuator stroke for a pumping frequency of 100 Hz and an actuator frequency of 1 Hz.

Chapter 6

Whirl Testing of a Hybrid Hydraulic Actuator

Helicopters typically employ a mechanical swashplate mechanism to achieve primary control and vehicle trim. The swashplate transmits control inputs from the pilot to the rotor blades by means of rigid pitch links. The swashplate assemblies are mechanically complex, bulky and consists of a large number of moving parts. As a result, it incurs a significant parasitic drag penalty in forward flight. In addition, a large amount of preventive maintenance and inspection is necessary to ensure flight safety and reliability. Recently, there has been considerable interest in achieving primary flight control without the use of a swashplate. The majority of these studies have investigated on-blade control surfaces such as trailing edge flaps (Ormiston, 2001; Roget and Chopra, 2002; Shen and Chopra, 2004; Shen et al., 2004; Falls et al., 2006; Bao et al., 2006), or active twist of the rotor blade (Chen and Chopra, 1997), to effect a change in the air-loads in the rotating frame. The major challenge of these approaches is the integration of the actuators within the blade geometry, while achieving the required power output and maintaining the weight and aeroelastic constraints of the rotor blade. In addition, as the trailing-edge flaps are typically located at around 75% blade span, the actuators must operate under large centrifugal loads. To achieve a high energy density actuation mechanism, most of the on-blade actuation concepts are based on active materials such as piezoelectrics (PZT). However, amplifying the limited stroke of active materials to the required levels presents additional practical difficulties (Chopra, 2002).

An alternate approach is to incorporate active pitch links (APL) in the rotating frame that change the blade pitch by varying their length. This approach has three major advantages. Firstly, the rotor blade is unchanged and does not require any redesign, modification or change in production method. Secondly, as the pitch links are located close to the rotor shaft, they experience a significantly lower centrifugal force than trailing edge flap actuators, and do not face stringent volumetric constraints. Thirdly, as the rotor blade does not employ a discrete control surface, the APLs do not create an additional profile drag penalty. The actuators, placed directly in the rotating frame, can also achieve vibration reduction via Individual Blade Control (IBC) over a wide band of excitation frequencies, in addition to primary control. Active Pitch link concepts have been investigated for Individual Blade Control (IBC) applications on rotorcraft, both on model scale (Lorber et al., 2001) and on full-scale rotors. These concepts involve hydraulic actuators mounted on the main rotor hub, and consequently require a hydraulic slip-ring. As a result, these systems are complicated, difficult to maintain and result in a large weight penalty. For example, on a system recently tested on the CH-53G helicopter, the pitch link actuators weighed approximately 10kg, while the overall hydraulic system including the pump, tubing and slip-ring weighed 600kg (Arnold and Strecker, 2002) .

This chapter explores the use of a hybrid hydraulic actuator as an active pitch link. By combining the hydraulic pump and actuator into a single unit, this approach will result in a localized, self-contained hydraulic actuator that can be mounted in the rotating frame without the need for a hydraulic slip-ring. Electrical power will be delivered to the actuators through an electrical slip-ring, which already exists in most rotors to service the on-blade de-icing units. This will result in a much simpler and lighter IBC actuation system.

The implementation of the APL on a rotor blade is shown schematically in Figure 6.1. The system consists of a variable length pitch link in the rotating frame, connected to the torque tube of a bearing-less rotor blade. The output shaft of a piezohydraulic actuator acts as the variable length link of the APL. Figure 6.2 presents a schematic diagram of the proposed hybrid hydraulic actuator. The actuator used in the experimental studies was driven by piezoelectric stacks. The device consists of three main assemblies: a piezoelectric pump, a manifold incorporating an accumulator and directional control valves, and a conventional hydraulic cylinder. The piezoelectric pump is a hydraulic pump driven by piezoelectric stacks that change their length in response to an applied voltage. The operation of the pump is also executed in a four-stage fashion , as described in Chapter 4. The resulting actuator is a design with no moving parts, thus significantly simplifying the construction of the actuator and increasing its reliability. The piezoelectric pump supplies pressurized hydraulic fluid to the rest of the circuit at the required flow rate and pressure. The direction of motion of the output shaft is controlled by the solenoid valves. The high frequency, low amplitude displacement of the piezostacks is effectively traded off into a low frequency, large amplitude output displacement. As the hydraulic fluid is entirely contained inside the actuator, there is no need for a hydraulic slip ring. Note that the piezoelectric stacks can be replaced by any type of high bandwidth active material.

Several researchers have designed and constructed prototype piezohydraulic actuators to establish the proof of concept and to explore the operating principle (Konishi et al., 1993b,a; Mauck and Lynch, 2000; Nasser et al., 2000). A proof-of-concept piezohydraulic actuator specifically designed for compactness and high energy density has been developed by the authors and has undergone extensive bench-top testing (Sirohi and Chopra, 2003; Sirohi et al., 2005). The geometry of this device conceptually well-suited for implementation as an APL. Figure 6.3(a) shows the actuator with the manifold and output cylinder. The pump is driven by two PI 804.10 piezostacks and has overall dimensions of 1.25" diameter, 3.5" length with a total weight of 300 g. A low viscosity hydraulic fluid was used as the working fluid. Passive reed valves achieved rectification of fluid flow. Under unidirectional operation, a blocked force of 80 N (18 lbs) and a no-load velocity of 140 mm/s (5.5 in/s) were measured.

Significant challenges remain to implement the APL system on a rotor system. A key element is to increase the bandwidth of the piezohydraulic actuator, especially by operating at high pumping frequencies. Additionally, the APL must be designed to operate in the rotor environment, under centrifugal loads. While the loads are much lower than at the location of a trailing edge flap, the main rotor hub presents a severe operational environment for the APL actuators. Vibration levels are high and centrifugal accelerations are significant (on the order of 350 g at a 0.4 m radius for a UH-60 pitch link). As a result, the actuator needs to be designed in a way that prevents seizing of the pump under centrifugal loading while ensuring consistent operation of check valves. The system must also incorporate fail-safe operation by behaving as a passive element in the event of a power loss or actuator failure.

To investigate the effect of centrifugal loads on the performance of the piezoelectric actuator, the device will be tested under rotation in the 10 foot diameter, vacuum whirl test chamber at the University of Maryland. Figure 6.3(a) shows a picture of the APL device and Figure 6.3(b) shows the device on a spin bar, with a counterweight at the other end. The radial offset of the APL is approximately 40 cm, and the actuator will be tested at rotational speeds of up to 300 RPM, which corresponds to a centrifugal loading of 400 g. Thus, the centrifugal loading experienced by the actuator will be nominally higher than the full scale centrifugal load experienced by a UH-60 pitch link.

6.1 Actuator Construction

Though the actuator used here is a piezoelectric stack driven actuator, its design is fundamentally similar to the Terfenol-D based actuator discussed in Chapters 2 and 3. A schematic of the piezoelectric actuator used here is given in Figure 6.2. The basic operation of the actuation system is executed in three stages. In the first stage, a driving signal is generated using a signal generator and is amplified and applied across the PZT stack. The changing electric field applied to the active material induces strain in the material and pushes a piston which causes the fluid in the pumping chamber to be pressurized. In the next step, two oppositely oriented uni-directional check valves respond to the fluid pressure by opening only in their preferred direction. Thus, the check valves perform the function of rectification and convert the oscillatory motion of the active material stack to a uni-directional motion of the fluid. In the third stage, the fluid is led into a hydraulic output cylinder which is connected to a load through hydraulic lines. Thus, a uni-directional motion of the output cylinder shaft is obtained. In a practical situation, there is a need for bi-directional motion of the load and this can be implemented through the use of mechanical valves (Ellison, 2004) or MR fluid based valves, as described in Chapter 4. The hydraulic circuit has an accumulator on the low pressure side, which is used to apply bias pressure to the circuit and to filter out high frequency pressure oscillations. The stack is held between the preload base and the piston. Preload can be applied to the stack using a set screw arrangement inside the preload base. The salient features of this actuator is listed in Table 6.1. The piezoelectric stack is installed inside the pump body, as shown in Figure 6.2. The hydraulic fluid is filled into the system through the accumulator port. and degassed thoroughly using a vacuum pump. Degassing, as mentioned earlier, is critical to the performance of the pump since dissolved air decreases the bulk modulus of the fluid, thus decreasing the overall efficiency of the system. A bias pressure of 1.4MPa (200psi) is applied to the fluid. Applying bias pressure reduces the risk of cavitation and also applies preload to the piezo stacks. The stacks are also preloaded using the base plate of the pump body. Unlike Terfenol-D, preload has no impact on the strain generating capability of a piezoelectric stack. In the present design of the actuator, centrifugal forces will also increase the preload on the stack. The preload is monitored using strain gages that are mounted on the stacks.

6.2 Experimental Procedure

The main objective of this chapter is the evaluation of the performance of hybrid actuator under centrifugal loading. The hybrid actuator used in the preliminary tests was an actuator powered by two piezo stacks. The actuator was coupled to a commercially available cylinder using the manifold. A hydraulic manifold is used to connect the piezohydraulic actuator to the output cylinder. The manifold can be seen in Figure 6.3(a). Owing to its stiffness, a manifold prevents stray fluid line frequency behavior to affect the overall performance of the system. It also decreases the possibility of weak points in the hydraulic circuit which might lead to leaks. The output cylinder used was purchased from Bimba Inc and had a outer diameter of

7/16” and an inner diameter of 3/16”. An LVDT is attached to the output cylinder shaft to measure the velocity of the output cylinder shaft. The performance of the actuator is characterized by the velocity of the output cylinder shaft for different values of pumping frequency.

The spin bar was constructed such that the piezohydraulic actuator is at a distance of 40 cm from the center of rotation. An assembly drawing the actuator and the spin bar used to mount the actuator in the whirl chamber is shown in Figure 6.4. When rotated to an RPM of 300, this produced a centrifugal acceleration of 400 g on the output cylinder. After assembling the actuator system, it is attached to the end of the spin bar and balanced with a counterweight for balancing. The spin bar with the actuator and the counterweight can be seen in Figure 6.3(b). The counterweight is exactly matched with that of the actuator system by balancing the spin bar on a knife edge. This can be seen in Figure 6.3(b). The spin bar and the attached actuator system is then installed inside the whirl chamber of University of Maryland and spun at various angular velocities. The spin bar was spun at a maximum RPM of 300, which corresponded to a centrifugal loading of 400 g. A slip ring around the spin shaft enables the transfer of signals to and from the whirl chamber. The required voltage for the piezoelectric stacks are fed into the power channels of the slip rings and the signals from the LVDT and the strain gage is carried by the signal channels of the slip rings. The data was recorded using a Dspace data acquisition system. Two types of tests were performed:

1. No-load tests: In the no-load testing, the spin bar was spun at 200 RPM and 300 RPM and the output cylinder shaft velocity was measured. The maximum output velocity of the actuator is obtained during no load testing as energy is lost only in overcoming the internal losses in the actuator. The shaft velocity was measured for a range of pumping frequencies. Pumping frequency is the frequency at which the piezoelectric stack is actuated.

2. Load tests: In load tests, the actuator is made to work against a spring load in a rotating environment. Springs of known stiffness (12 lbs/in and 18 lbs/in) are

attached to the output cylinder shaft such that the shaft experiences increasing spring force as it is moved by the actuator. The reason for choosing the particular values of spring stiffness was to provide a force equivalent to the blocking force of the actuator at the full stroke of the output cylinder. The full stroke of the output cylinder was 2 in and the blocked force of the actuator was calculated to be around 35 lbs (Ellison, 2004). Thus, the spring with a spring constant of 18 lbs/in will provide 36 lbs of force at a stroke of 2 in. The performance of the actuator is measured as the velocity of the cylinder shaft. The performance of the actuator was measured for only a select set of pumping frequencies. These frequencies were selected based on the actuator resonance obtained from no-load tests. Also, the actuator was tested for spin bar RPMs of 200 and 300.

6.3 Results and Discussion

Primarily, centrifugal forces are felt in the form of increased friction. The part of the actuator assembly where the effect of friction with be most experienced is the output cylinder, where the cylinder shaft and shaft piston slides in adn out of the cylinder body. Bearings support the cylinder shaft and shaft piston inside the output cylinder. Hence, the performance of the actuator is linked to the performance of the bearings in the output cylinder. The performance of the actuator was measured for two kinds of output cylinder bearings - sliding bearings and roller bearings.

6.3.1 Unidirectional no-load with sliding bearing

The output cylinder used in these tests was a commercially available cylinder purchased from Bimba Inc. In this design, the cylinder shaft was supported on two sliding bearings. The actuator and manifold are connected to this output cylinder and the entire assembly was installed inside the whirl chamber along with the spin bar and counterweight. A picture of the spin bar along with the actuator assembly and counterweight can be seen in Figure **??**. The spin bar was spun at 200 RPM and 300 RPM and the output shaft velocities were recorded through the use of an LVDT that is attached to the cylinder shaft. The results are shown in Figure 6.6. As we can see from the figure, there is a sharp drop in performance as the angular velocity is imposed on the actuator. At the pumping frequency of 800 Hz, there is a reduction of more than 50% in the output shaft velocity. Moreover, there were numerous fluid leaks around the output cylinder. The location of the fluid leak is not easily ascertained as the fluid is dispersed in the radial direction due to the rotation and the source of the leak is not evident, as in the case when the actuator is stationary.

The source of the reduction in performance had to be determined before doing additional tests. There were two possible causes for the reduction of the performance.

- The increase in preload of the piezoelectric stack due to the centrifugal load on the pump piston.

- Increased friction in the output shaft due to the centrifugal loads.

The first reason can be eliminated on the basis of the following reasoning. The centrifugal acceleration experienced at an RPM of 300 is 400 g. The net force experienced by the pump piston can be calculated as:

$$F_{CF} = m\omega^2 r \tag{6.1}$$

where, m is the mass of the piston, ω is the angular velocity and r is the radial distance from the center of rotation. Thus the net force that the piston (of mass 30g) exerts on the piezo stacks is 12 N. Since this additional force is only 0.24% of the block force of the stack (which is 5000N), we can conclude that this force is negligible and is not responsible for the drastic drop in performance. The second possible reason for the drastic change in performance is the increase in friction in the output cylinder due to the centrifugal forces. As the actuator is spun in the whirl chamber, the centrifugal force on the output cylinder shaft increases and the shaft is pressed against the copper sliding bearings inside the output cylinder. This increases the friction between the cylinder shaft and the bearing, thus, leading to a decrease in actuator performance. To alleviate this problem, a new output cylinder was constructed which has roller bearings instead of sliding bearings. Figure 6.7 shows the redesigned output cylinder.

6.3.2 Unidirectional no-load tests with roller bearings

These tests were performed using an actuator that was powered by three piezo stacks. To validate whether the increased friction in the output cylinder was the cause of the drop in performance of the actuator, an improved output cylinder with roller bearings was tested in the experimental setup. The new output cylinder had an outer diameter of 3/4" (19.05mm), and inner diameter of 1/4" (6.35mm) and a stroke of 2" (50.8mm). Since the output cylinder has a different area of cross-section compared to the earlier output cylinder, there is no direct comparison between the results. The criterion of comparison will be the percentage drop in performance with angular velocity. The results of the whirl tests are shown in Figure 6.8. As we can see from the figure, there is no appreciable drop in performance with increasing angular velocity. All the three lines are within the error bars of the baseline curve. Thus, it is ascertained that the reason for the drop in performance in the preliminary tests was the increased friction in the output cylinder shaft.

6.3.3 Load Tests

These set of tests were performed to ascertain the performance of the hybrid hydraulic actuator under load in a rotating environment. The performance of the actuator under spring loaded was analyzed. Preloaded springs were attached to the output cylinder shaft such that as the cylinder shaft moves, the springs are extended, thus forcing the actuator to work against the spring load. Two springs with different spring constants were used in this test. Spring 1 had a spring constant of 2000 N/m (12 lbs/in) and spring 2 had a spring constant of 3150 N/m (18 lbs/in). Figure 6.9 shows the actuator with one of the attached springs. Baseline data was taken when the spin bar was stationary for both cases of spring constants. The actuator was then spun at 300RPM (400 g centrifugal loading) and data was recorded for four values of pumping frequencies around the actuator resonance (700-1000Hz pumping frequency). The intention was to observe any deterioration in performance at and around the pumping frequency with the maximum performance (as seen from no-load tests). The results from the whirl testing are shown in Figure 6.10. We can see from the figure that there is no deterioration in the actuator load performance in a rotating environment for either of the springs used. Thus, we can conclude that the present actuator configuration is able to maintain baseline performance for a spring loaded case of 3150 N/m and a centrifugal loading of up to 400 g.

6.4 Conclusions

The feasibility of using a hybrid hydraulic actuator in conditions of high centrifugal loading is evaluated. Since the intended application in this study was a pitch link, the actuator was tested at a centrifugal load of 400 g, which is in excess of the full-scale load experienced by a UH-60 pitch link. Preliminary test showed a deterioration in performance with increasing centrifugal force, as well as the existence of fluid leaks in the system which are accentuated by the extreme loading case. The source of the problem was identified to be increased friction in the output cylinder shaft. To offset the problem, a new output cylinder was designed which incorporated bearings to support the centrifugal force on the cylinder shaft. Subsequent tests of this improved design showed no deterioration in performance of the actuator up to the full scale loading condition.

The performance of the actuator was also evaluated under a loaded case. Pre-stressed springs were attached to the output cylinder shaft such that as the shaft is moved, the actuator has to work against the stiffness of the spring. This setup was then spun in the chamber to full-scale loading conditions. It was found that the performance of the actuator did not deteriorate from the baseline case. Thus the existing design of hybrid hydraulic actuator driven by piezoelectric stacks is able to maintain its performance for loaded and no-load cases under a full-scale centrifugal loading environment.

Table 6.1: Pump Properties

Pump Body Assembly	
Pump body diameter(mm,in)	35.6, 1.4 O.D, 25.4, 1 I.D
Pump body length(mm,in)	50.8, 2
Piston diaphragm thickness(mm,in)	0.05, 0.002
Pumping chamber diameter (mm,in)	25.4, 1
Pumping chamber height (mm,in)	0.76, 0.030
Valve Assembly	
Valve plate thickness(mm,in)	5.1, 0.2
Reed valve thickness(mm,in)	0.051, 0.002
Hydraulic circuit	
Accumulator gas volume(mm^3,in^3)	1638.7, 0.1
Output cylinder bore(mm,in)	11.1, 7/16
Output shaft diameter(mm,in)	1.58, 3/16
Output cylinder stroke(mm,in)	50.8, 2

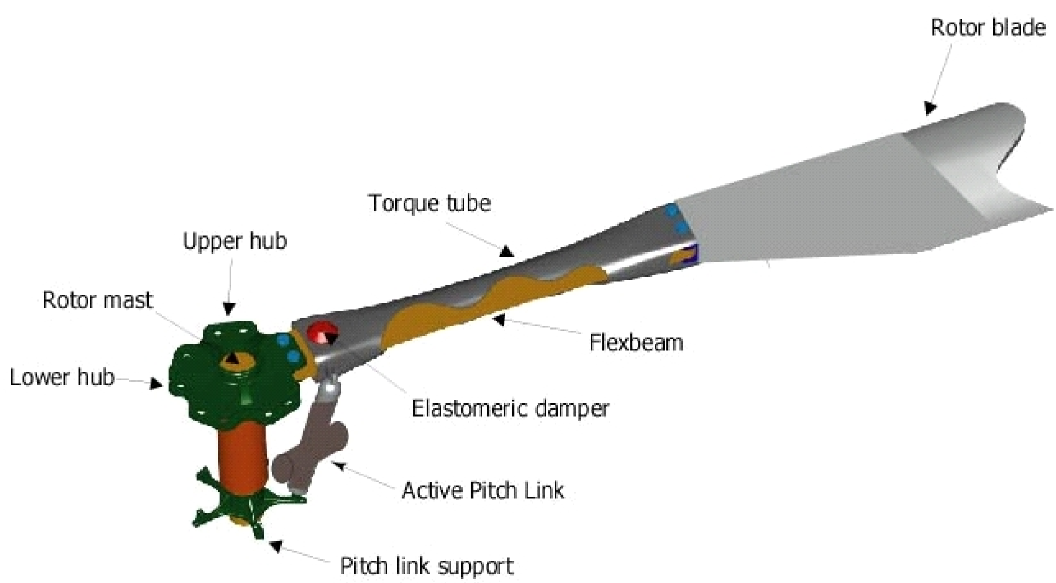

Figure 6.1: Conceptual drawing of an active pitch link

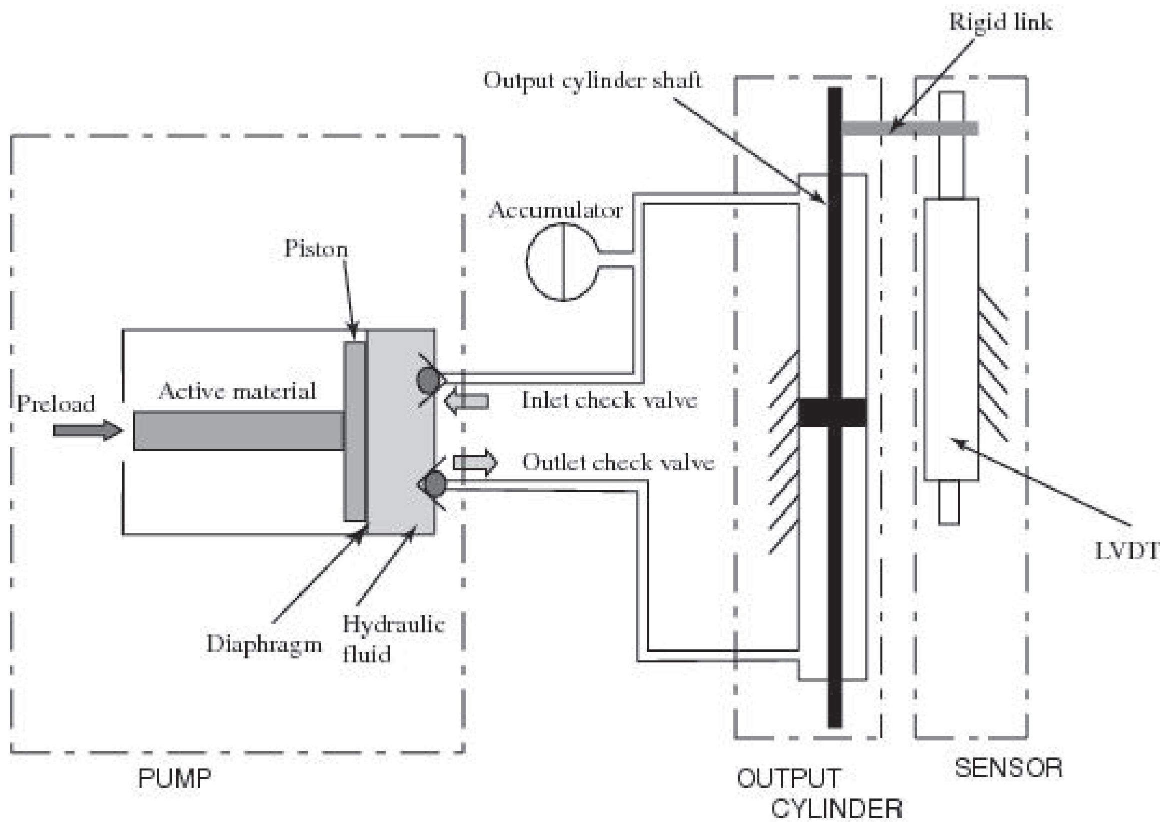

Figure 6.2: Schematic diagram of the components of the hybrid hydraulic actuator

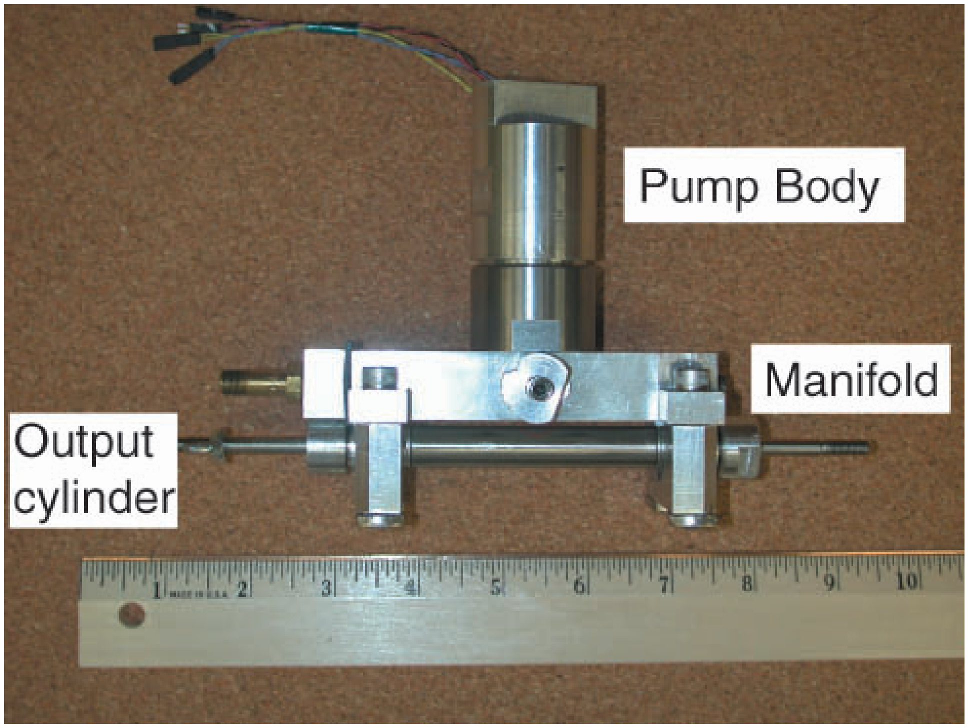

(a) Picture of a piezohydraulic actuator

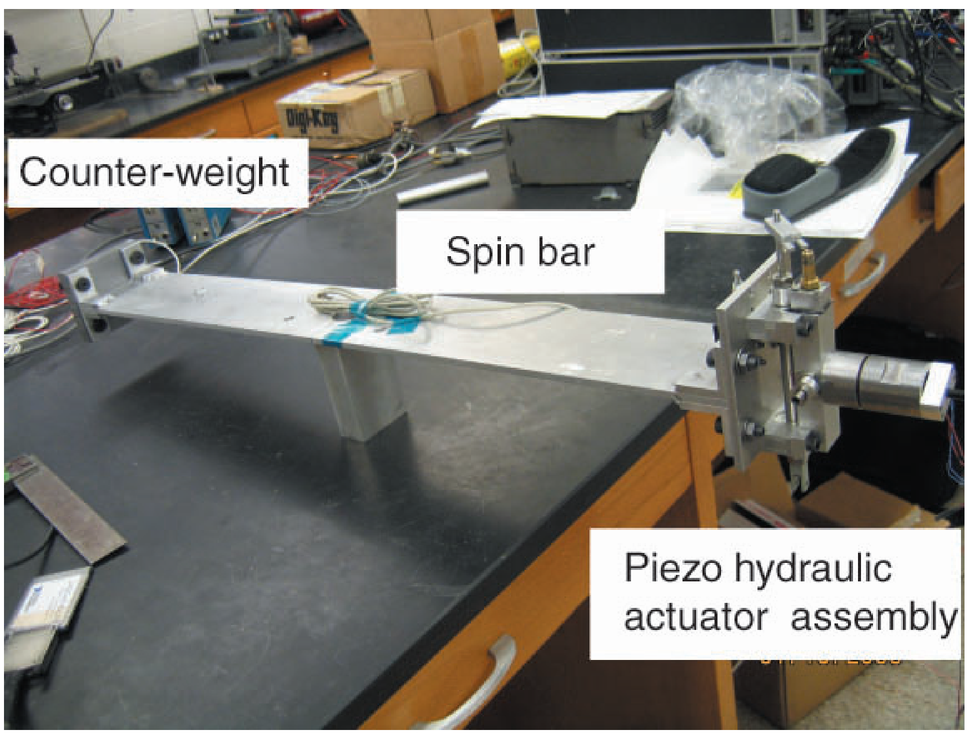

(b) Bench top testing of the device on a spin bar

Figure 6.3: Piezohydraulic actuator

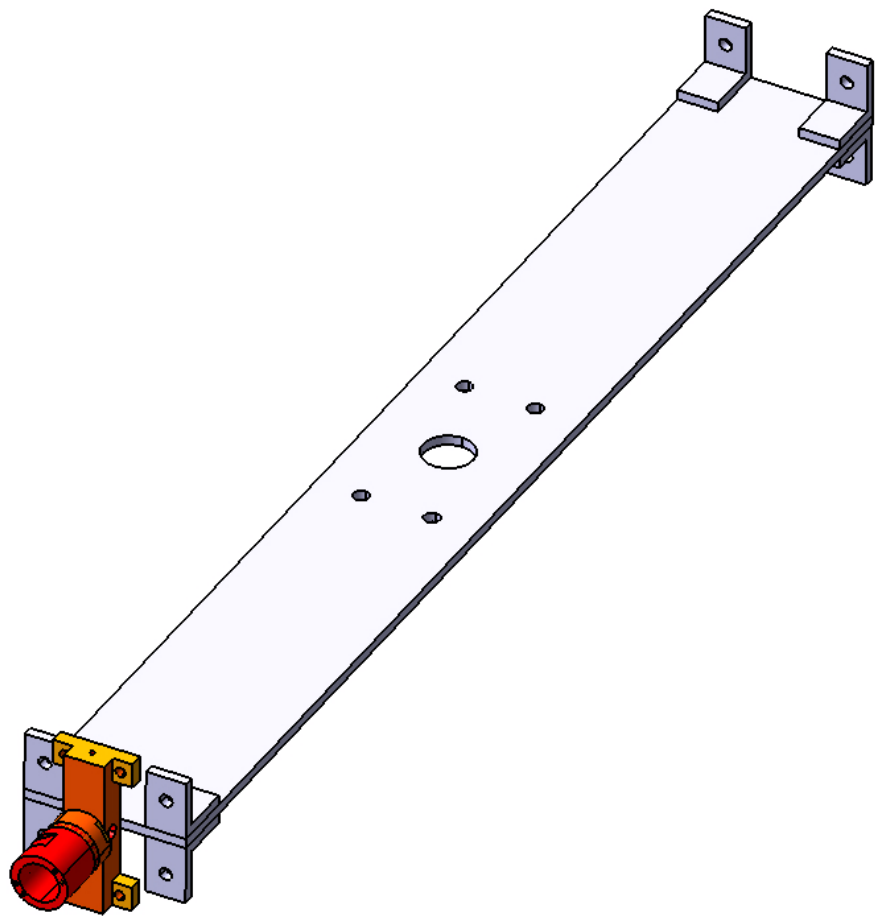

Figure 6.4: Drawing of the actuator mounted at the end of the spin bar

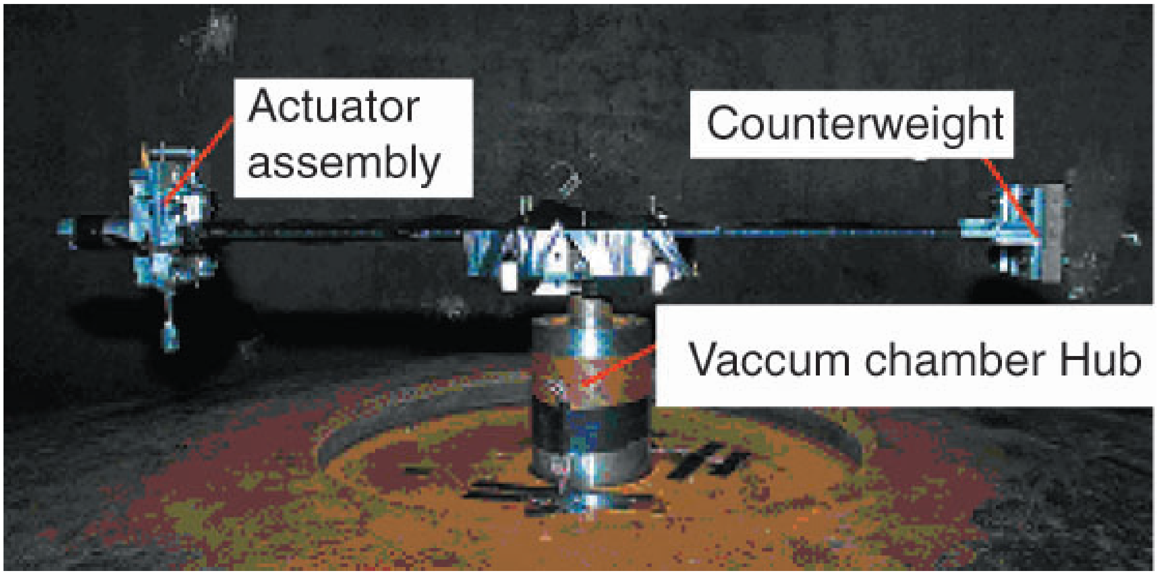

Figure 6.5: Picture showing the spin bar with counterweight and actuator assembly installed inside the whirl chamber

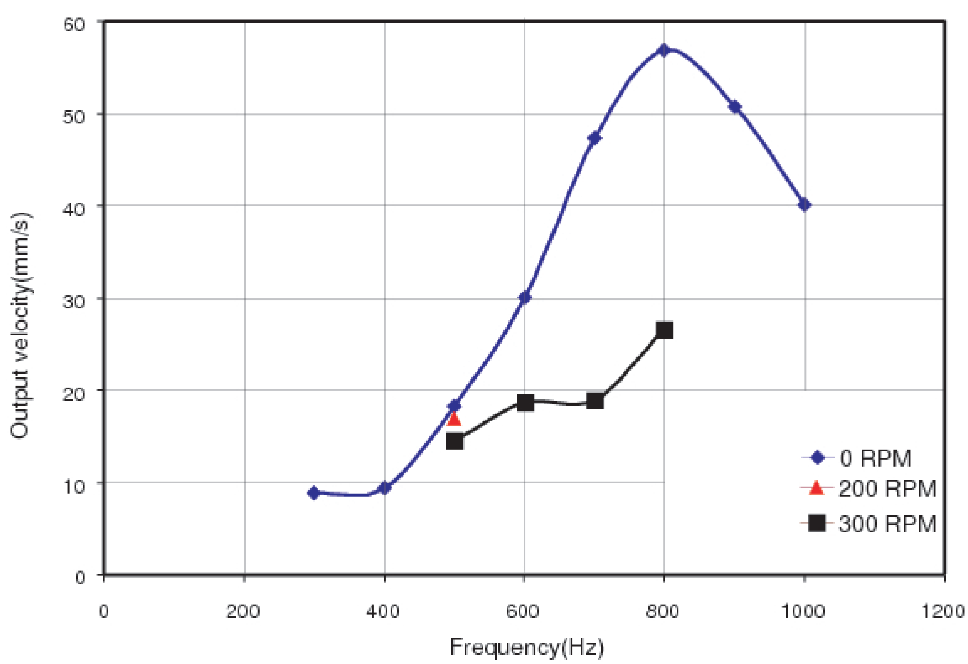

Figure 6.6: Results of whirl tests with sliding bearings

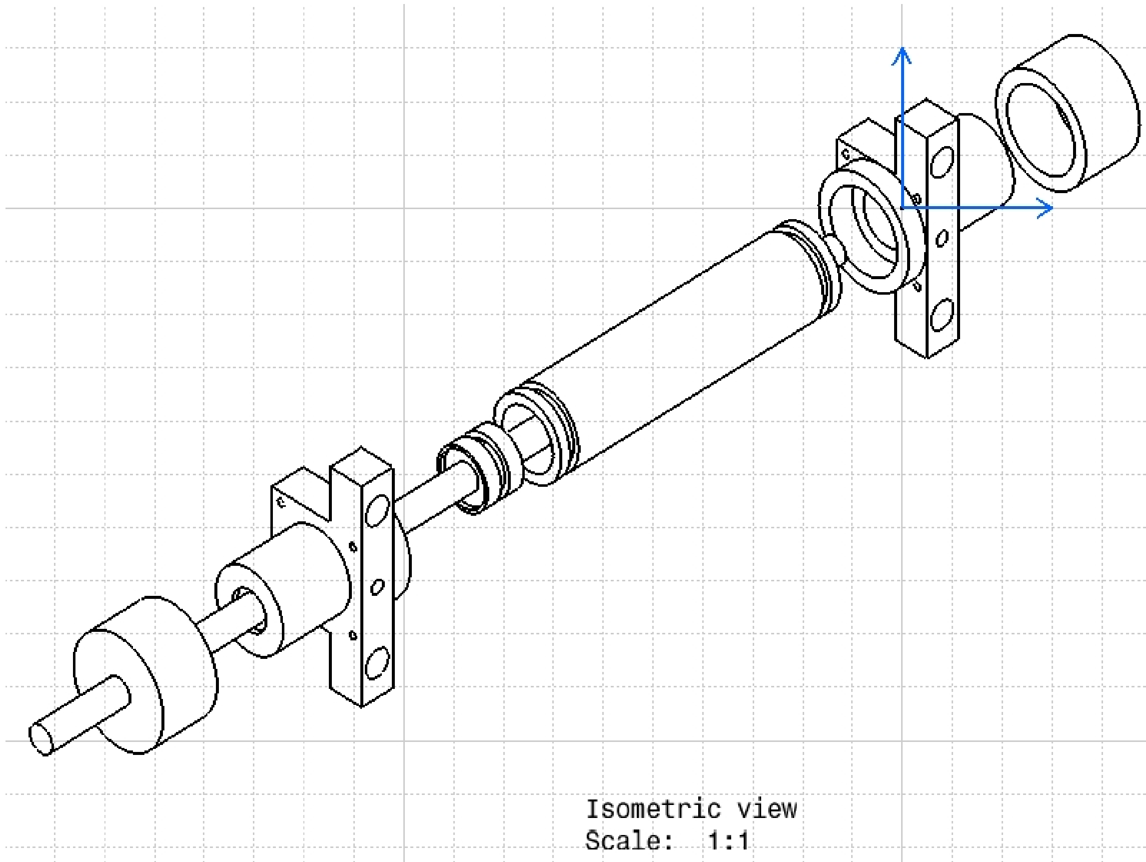

Figure 6.7: Improved design for the output cylinder with roller bearings

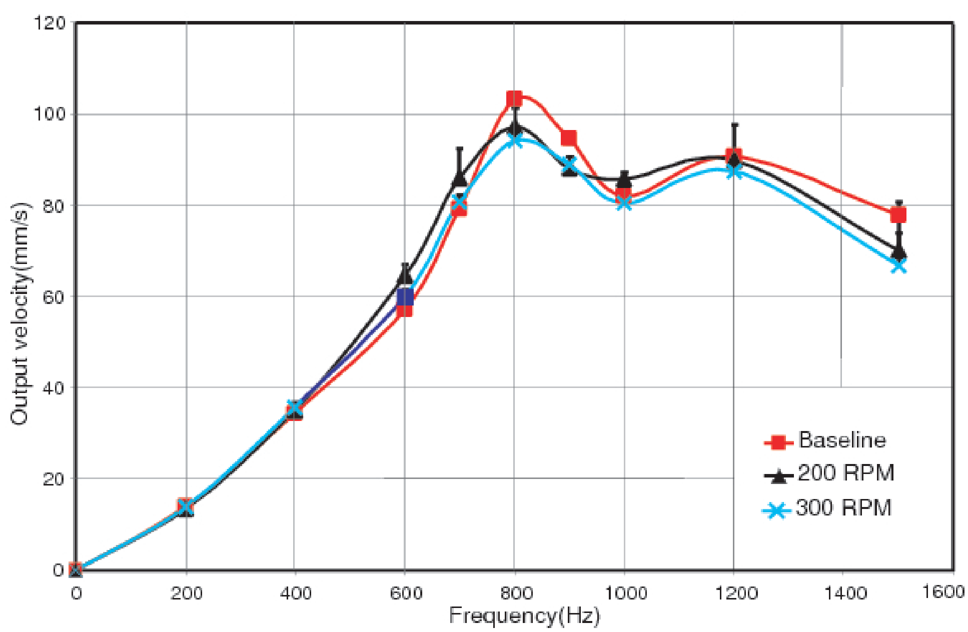

Figure 6.8: Results of whirl testing with roller bearings

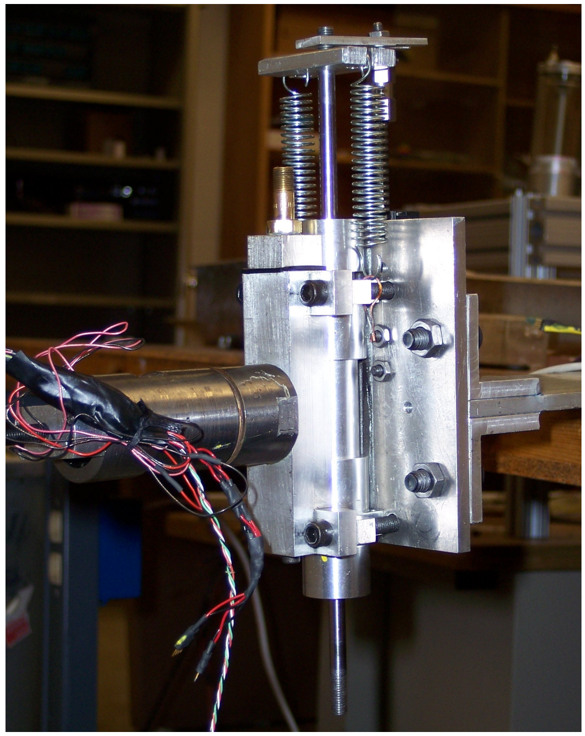

Figure 6.9: Picture of the actuator working against a stiffness of 18 lbs/in

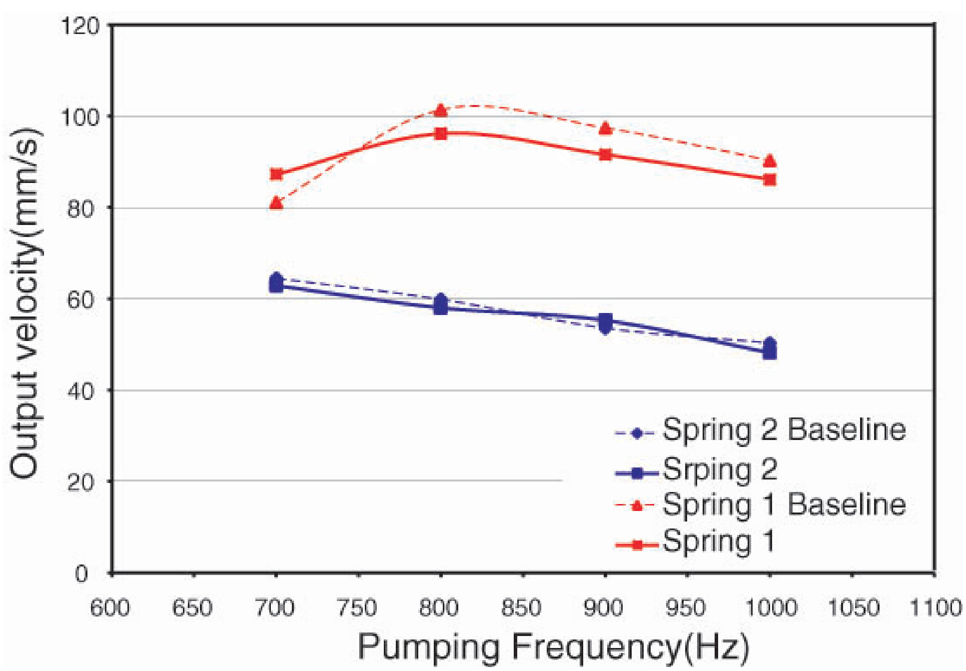

Figure 6.10: Results of whirl testing with stiffness load

Chapter 7

Conclusions and Future Work

This research focussed on exploring the applicability of a hybrid hydraulic actuation system with MR fluid based valves as an active pitch link for rotorcraft application. Such an application would enable the implementation of primary control for maneuvering the helicopter, as well as secondary control to reduce vibration and noise through IBC techniques. There were three stated broad objectives for this research.

1. Identify the major sources of pressure loss within the pumping chamber of a hybrid hydraulic actuator and the issues the come into prominence during high frequency operation. Also, what are the major design parameters that affect the fluid pressure loss in a pumping chamber.

2. To evaluate the performance of a self-contained bi-directional hybrid actuator and to model its performance using an analytical model.

3. To ascertain the effectiveness of the hybrid actuator under centrifugal loading.

The first objective was met through theoretical and computational modeling of the pumping chamber in a hybrid actuator. These results are shown in Chapters 2 and 3. The performance of a hybrid actuation system was evaluated and presented in Chapter 4 and an analytical model describing its performance is presented in Chapter 5. Finally, the effect of centrifugal load on the performance of a hybrid actuator was tested and presented in Chapter 6. The significant contributions made through this research can be categorized as follows:

7.1 Investigation of steady fluid flow in a pumping chamber

A 3D analytical model for steady flow in a pumping chamber of a hybrid hydraulic pump was developed in Chapter 2. The model was based on a typical pumping chamber geometry found in a hybrid hydraulic actuator, where the fluid chamber is flanked on one side by the pump piston (pushed by the active material stack) and on the other side by two ports (one for intake and another for discharge).

The model was derived using simplified mass and momentum conservation equations. Certain simplifying assumption regarding the nature of the flow were made. An equation describing the net change in pressure of the fluid between the inlet face and the end of the discharge tube is calculated. The three dimensionality of the geometry brings in a non-linear dependence of the pressure loss on the volume flow rate. The analytical model described the pressure loss in the pumping chamber with respect to the flow rate. The expression for pressure loss consists of two terms - 1.) a linear viscous term that depends on Q, and 2.) a non-linear term that depends on Q^2. This is a marked improvement on earlier models which were 2D. A comparison between the 3D and 2D models was also made to highlight the discrepancy in the pressure predictions between the two models.

CFD modeling is performed on the actual 3D pumping chamber geometry. A careful analysis of the CFD results showed the presence of vortices in the pumping chamber. The vortex develops in the discharge tube during discharge and in the pumping chamber during intake. These vortices have a big impact on the net pressure loss in the pumping chamber since the size of the vortex is large when compared to the dimensions of the discharge tube diameter and the pumping chamber height. The size of these vortices was also found to depend on the magnitude of the volume flow rate. The impact of the geometry of the pumping chamber on the pressure loss was also explored. The three main pumping chamber dimensions investigated were as follows:

- Pumping chamber height: It was seen that the greater the pumping chamber height, the lower the fluid pressure losses involved. A pumping chamber of larger height lowered the fluid acceleration, thus, decreasing the size of the vortex.

- Discharge tube location: It was seen that the impact of discharge tube location was not as pronounced as the other two parameters considered. This justified our earlier assumption regarding the pump geometry where the discharge tube was concentric to the pumping chamber.

- Discharge tube chamfer: A chamfering of the junction of the discharge tube and the pumping chamber decreased the pressure losses as it decreased the fluid acceleration and consequently, the size of the vortex.

The theoretical model was modified to include the effect of these vortices. The effect of vortices was accounted for in the following manner:

- Since the vortex occurs in the discharge tube during discharge, the tube diameter is modified. The modified discharge tube diameter depends on a parameter k_{dis} and the discharge volume flow rate.

- Since the vortex occurs in the fluid chamber during intake, the chamber height is modified. The modified pumping chamber height depends on a parameter k_{in} and the intake volume flow rate.

The results of the theoretical model and the CFD simulations were compared to show that using the two parameters k_{dis} and k_{in}, the steady fluid flow in a pumping chamber can be described.

CFD studies of pumping chambers have been reported in the literature. However, those studies were 2D and axisymmetric. This study performed the CFD calculations of the actual 3D geometry of pumping chambers. A theoretical model for steady fluid flow in a pumping chamber that accounts for vortices was also completed.

7.2 Three dimensional model for unsteady fluid flow in a pumping chamber

Since the effectiveness of a hybrid hydraulic actuation system depends on the high frequency operation of the active material stack, the modeling of the high frequency pumping motion is essential. The 3D model developed for a steady flow in Chapter 2 was extended to account for the high frequency motion of the stack.

Time derivatives in the Navier-Stokes equations were retained through the derivation to account for the inertia of the fluid. The 3D unsteady model results in an expression for pressure loss with three terms - 1.) a linear viscous term that depends on Q, 2.) a non-linear term that depends on Q^2, and 3.) an inertial term that depends on $\dot{Q}$. The effect of vortices during oscillatory flow is more complicated than in the steady model, as the vortices go through a cycle of formation and dissipation within the pumping chamber and the discharge tube. From the insight obtained from studies into orifice flows, a Fourier analysis was done on the expression for pressure loss. This offered valuable insight into the frequency domain behavior of the pressure losses. The pressure loss that resulted from the vortices has a non-linear quadratic relationship with the volume flow rate. Also, the pressure loss relating to the vortex has a phase difference with the driving flow rate. This is due to, what is known as, eddy inertia.

A fully coupled CFD analysis was performed on the pumping chamber geometry where there is a stress boundary condition between the fluid in the chamber and the active material stack. The forces experienced by the stack is important in determining the amount of strain displayed by the stack during dynamic operation. Plots of pressure loss in the pumping chamber versus the volume flow rates showed self-crossing behavior. These self-crossings slowly dissipated as the pumping frequency was increased. This behavior was explained using the theoretical model as the inter-play between the component of pressure loss due to inertial effects and the component due to vortices.

In conclusion, a 3D unsteady model for fluid flow in a pumping chamber was developed. The frequency domain representation of the pressure loss expression offered insight into the inter-play between the three forms of pressure loss. Also, the effect of vortices could be accounted for in the frequency domain due to the time lag involved.

7.3 Experimental studies and theoretical modeling of a hybrid hydraulic actuation system

A hybrid hydraulic actuation system was proposed for an active pitch link application in rotorcraft systems. An actuator considered for such an applications has to meet several requirements. It has to be compact and self-contained. Preferably, the actuator should have a low number of moving mechanical parts to improve reliability. The hybrid hydraulic actuation system uses the high energy density of Terfenol-D to produce a compact, frequency rectified, pressure source. An MR fluid is used as the working fluid in the device and a Wheatstone bridge fluidic valve network is used to develop a valving system with no moving parts. This study extends the preliminary work done at the University of Maryland, in which only uni-directional motion was reported. Extensive experimental tests were performed on the actuation system and can be divided broadly into two broad categories:

- Uni-directional tests: In these tests, one set of MR valves are blocked and the output cylinder produces a uni-directional motion. Two kinds of uni-directional tests were performed.
  - No-load tests: These tests were performed to evaluate the maximum obtainable output velocity from the system. The output velocity was measured over a range of pumping frequencies. The optimum pumping frequency of operation is ascertained through the location of the fluid resonance of the hydraulic circuit.
  - Load tests: The velocity of the output cylinder shaft is measured for a range of loads. Load lines can be drawn from the data obtained from load tests. The maximum power output of the actuator can be calculated

from the load lines. Also, by measuring the input power to the Terfenol-D stack, the net electromechanical efficiency can be calculated as well.

- Bi-directional tests: In these tests, signals with opposite phases are provided to the two sets of MR valves, thus producing bi-directional motion in the output cylinder shaft. Two types of bi-directional tests were performed:
  - No-load tests: Through these tests, the relationship between the stroke of the cylinder shaft and the output actuator frequency is established. This establishes the frequency bandwidth of the actuation system.
  - Load tests: The stroke of the cylinder shaft is measured as a function of the actuator frequency for two different kinds of external load - inertial and elastic. The effect of an inertial load is felt at all pumping frequencies due to the fundamental nature of a hybrid hydraulic actuator. Due to the frequency rectification process, the external load goes through an acceleration-deceleration cycle twice during every oscillation of the active stack. However, the effect of an elastic load is only felt as the stroke of the cylinder shaft is high. This is due to the fact that the elastic force is proportional to the stroke.

The development of any system is not complete without a physical model to describe its behavior. A theoretical model was derived to understand the characteristics of a hybrid hydraulic actuation system.

The actuation system is composed of two subsystems - a hybrid pump and an MR fluid based valving system. The hybrid pump was modeled using control volume equations derived for the rate of change of fluid density and pressure. The force feedback experienced by the active stack is accounted for by taking into consideration the pressure of the fluid in the pumping chamber. The reed valves that perform the task of frequency rectification is modeled using discrete equations. The fluid in the MR valves were analyzed as a fluid line with two elements. The fluid inertia, which was shown to have a major role in the pressure loss calculations, is accounted for in the MR valves. This is especially crucial for MR fluids since the density of MR fluids is high. The two sections of the output cylinder is also modeled using the control volume approach. The MR valve are modeled using a novel approach of separating the pressure drop that occurs due to leakage flow and the pressure drop that occurs due to the application of the magnetic field. Using the pressure expression derived in Chapters 3, the inertial loss of pressure in the MR fluid valves were also accounted for.

The equations were formulated as a state space system and solved numerically using a Runge-Kutta scheme. The results from the numerical simulation were compared to the experimental data. It was seen that the analytical model predicted the resonant frequency to within 25 Hz of the experimentally observed value. Also, the bi-directional no-load relationship between output stroke and output frequency was capture accurately. The accurate prediction of the bi-directional and uni-directional no-load performance proved that the analytical model captures the inertial, stiffness and damping of the system effectively. Hence, this model can be used to predict the performance of a system prior to its manufacture and to tailor the system to the particular requirements.

7.4 Evaluation of a hybrid hydraulic actuation system as an active pitch link

The pitch link of a helicopter operates in the rotating frame and encounters centrifugal acceleration of close to 350 g. To evaluate the performance of the hybrid hydraulic actuation system in a rotating environment, a piezoelectric stack driven pump was attached to a spin bar and rotated in a spin chamber.

The hybrid hydraulic actuator was tested in uni-directional mode in a rotating environment. The actuator was attached to the end of a 80 cm long spin bar. A counter-weight was added to the other end to reduce dynamic loads. When spun to 300 RPM, the centrifugal acceleration experienced by the output cylinder shaft was 400 g. This is in excess of the centrifugal acceleration experienced by a full scale pitch link on a UH-60 helicopter. The actuator was operated at various pumping frequencies and the output cylinder shaft velocity were measured using an LVDT. It was suspected that the kind of bearing in the output cylinder would be key to the performance under centrifugal loading. Two types of bearings were tested - sliding bearings and roller bearings. When the actuator was tested with an output cylinder having sliding bearings, the measured performance decreased with increasing RPM (the baseline performance was measured at 0 RPM). This is due to the increase in friction between the output cylinder shaft and the sliding bearing. the second type of bearing that was tested, roller bearings, showed no deterioration in performance between the baseline (0 RPM) case and a centrifugal acceleration of 400 g. Thus, it was proven that the current design of the hybrid hydraulic actuator was capable of sustained performance under a full-scale centrifugal load. Subsequently, the design of the output cylinder with roller bearings were chosen for further tests. Load tests were performed wherein the actuator was made to work against springs of stiffness constant 12 lbs/in and 18 lbs/in. For these two values of external stiffness, the actuator did not show any deterioration of performance from the baseline case to a rotational speed of 300 RPM.

7.5 Future work

This study dealt with the testing and modeling of a hybrid hydraulic actuation system for application as an active pitch link in rotorcraft systems. The state-of-the-art can be advanced on several fronts.

7.5.1 Advanced system modeling

The system model presented in this study works well for conditions of no-load. However, to be more useful in predicting actuator behavior in real-life cases when the actuator is working against a load. The modeling can be improved in the following ways:

1. The model has to account for the minor losses in the actuator in a more accurate way. Minor losses involve pressure lost in the working fluid due to bends and turns in the hydraulic circuit. These losses are critical in predicting the actuator performance at pumping frequencies that are not close to the

resonance. For an application like the active pitch link, it is desirable that the actuator is operated at the resonance frequency. However, there could be alternate applications of this hybrid system which might involve considerable operation at a much lower frequency.

2. The fluid line model of the MR valve that was presented in this study consisted of only one element and assumed that the variation of fluid density in the valve is linear. This assumption was made to simplify the modeling process and is not accurate. The MR fluid column in the valve has a low area of cross-section and a longer length compared to other fluid regions in the hydraulic circuit. This reduces the stiffness of the fluid column in the valve, thus making it susceptible to rapid variation in fluid density. A more accurate modeling of the fluid line is essential for accurate prediction of actuator performance.

3. The model has to be validated for a range of load cases. All real-life applications involve the actuator working against a load. Validation of the model for load cases is essential to perform scaling up studies of the actuator.

7.5.2 Feasibility of a full-scale active pitch link

The hybrid actuation system shown in this studies provides a block force of 30 N and a peak velocity of 50 mm/s. The force and stroke provided by the actuator has to be improved dramatically to be applied in a real-life application. However, there are several issues involved in scaling up the system. The size of the entire assembly is one such factor. To provide the blocking pressures necessary to actuator a rotor blade, the MR valves have to be increased in size. The prediction of the size of the MR valve has to come from careful analysis of the magnetic circuit. Such an analysis has to be done along with investigation into better and improved magnetic circuit designs.

The improvements to the analytical model suggested in the previous section only deals with the performance aspects of the system. The model cannot be used to predict the overall size of the system. The model can, however, be used to ascertain the size of the Terfenol-D (or any other active material stack) necessary for an application. Such an analysis is essential to ultimately decide the feasibility of this system.

7.5.3 Comparison between MR valves and solenoid valves

It has been mentioned in this study that typically solenoid valves are rated for frequencies less than 50 Hz. MR fluid based valves, on the other hand, can have a theoretical frequency bandwidth of close to 200 Hz. The advantage of MR valves over solenoid valves lies in the fact that MR valves do not have any moving parts. However, to establish this fact, a high flow rate actuator is necessary to produce meaningful stroke at very high actuator frequencies. Also, the ferromagnetic particles possess mass and will experience a centrifugal force in a rotating environment. The effect of this centrifugal acceleration on MR particles on the actuation system performance could be evaluated and a comparison can be made between the utility of MR valves over solenoid valves in a rotating environment.

7.5.4 Control studies of hybrid hydraulic systems

The hybrid hydraulic system that has been explored in this study can be used in a variety of other applications. For instance, this device can be used as an active/semi-active vibration suppressor. The MR valve network could be used to damp out the vibration while the pressure produced by the pump can be used to optimally bring the target back to the desired location. The model presented in this study represents the entire actuation system as a series of state space equations. This allows us to predict the performance of the system under difference control schemes like PID control and the system performance in a closed loop. Such a study can pave the way for potential application in many other areas like automobile and robotics applications.

Appendix A

Bi-Directional Actuation of a Piston Using MR Valves and a Piezoelectric Pump

A.1 Introduction

Magnetorheological fluids(MRFs) are used in optical polishing (Kordonski and Golini, 1999), fluid clutches (Lee et al., 2000; Takesue et al., 2001), vibration isolation systems and a variety of passive aerospace (Kamath et al., 1999; Marathe et al., 1998), civil(Sodeyama et al., 2001; Ribakov and Gluck, 2002) and automotive(Lam and Liao, 2003; Lindler et al., 2003) damping applications. Piezoelectric actuators (Mauck and Lynch, 2000; Nasser et al., 2000; Sirohi and Chopra, 2003) have high energy density and can provide actuation in a highly precise and controllable fashion. Active systems where MRFs are combined with an actuation mechanism have also been demonstrated (Yoo et al., 2005). In such a system, MRFs are used as the working fluid and a fluid network enables bi-directional actuation of the output cylinder through activation of magnetic fields across the flow path of MRFs. The need for such systems arise where there is a necessity to provide highly reliable, accurate and compact actuation systems in a constrained volume. These actuators coupled with a fluid network of MRFs can provide bi-directional actuation to an output cylinder. This study demonstrates the result of such a hybrid actuation system with force or motion control capability. The main components of this actuation system are the piezoelectric hydraulic pump and the MR valve network. Driving force, stroke, cut-off frequency and efficiency are the main evaluation parameters (Watton, 1989) for the actuator. The performance of this hybrid MR-piezo actuator has been determined experimentally through load tests. Dead weights are hung at the end of the output cylinder and the resulting shaft velocity is measured to determine the output power. This test is performed at various piezo excitation frequencies and MR valve activation magnetic fields. These experimental results are then compared to standard rheological models like Bingham Plastic (BP) and bi-viscous (BV) (Wereley et al., 2004) models. Experiments were also done using dummy valves to determine the efficiency of MR valves. The piezoelectric pump and MR valve system have been optimized through various studies to obtain the best performance in a constrained volume (Sirohi and Chopra, 2003; Yoo and Wereley, 2002).

A.2 Piezoelectric Hydraulic Pump

The piezoelectric pump used in this study was developed at the University of Maryland. The exploded view of this pump is shown in Figure A.1 and the schematic is shown in Figure A.2. The main components of the piezo pump are the piezo stack assembly, piston assembly, pump body, pumping head and preload assembly. The piezo stack assembly consists of two commercially availably piezo stacks (PI-804.10 made by Physik Instrumente). One end of the piezo stacks is attached to the preload assembly while the other end is free to push against the piston. The preload assembly serves to provide a compressive preload to the piezo stacks and also to align the piezostacks inside the pump body. The piston-diaphragm assembly consists of a 2.54 cm (1") diameter steel piston which has a sliding fit with the pump body. The piston is also bonded to a 0.051 mm (0.002") spring steel diaphragm. The diaphragm seals the working fluid from the pump body and the piston serves to constrain the deflected shape of the diaphragm to remain flat over most of its surface, thus maximizing the swept volume of the pump per cycle. While one face of the pumping chamber is formed by the piston, the other face is formed by the pumping head, that contains two oppositely oriented passive check valves. Each check valve opens the port as it deflects in only one preferred direction to facilitate the flow and it closes the port to prevent flow in the other direction. As a result, flow is enabled only when there is a pressure difference in the preferred direction. As the sinusoidal excitation is applied to the piezo stacks, one check valve enables fluid to be pushed out of the pumping chamber as the piezo stack pushes the fluid and the pressure inside the chamber increases (while the second check valve remains closed) and the second check valve allows the fluid to return into the pumping chamber as the piezo stack retreats and the pressure in the pumping chamber decreases (the first check valve remains closed in this period of time) (Sirohi and Chopra, 2003). Thus the reed valves rectify the flow to provide a uni-directional output flow from the pump. The salient features of the piezo pump are given in Table A.1.

A.3 MR Valve Network

The schematic of the MRF valve network is shown in Figure A.3. The network consists of four MR valves arranged in a Wheatstone's bridge configuration, an accumulator at the low pressure side of the piezo pump, and a conventional hydraulic cylinder to obtain output motion (Yoo and Wereley, 2002, 2004). The accumulator is used to apply bias pressure to the hydraulic circuit and to filter out high frequency fluid oscillations.

A.3.1 MR Valves

The MR valves used in the study consist of a core, flux return and an annulus through which MR fluid flows, as shown in Figure A.4. The core is wound using 28 gauge insulated copper wire. A current is applied through this wire to create a magnetic field at the active section. As the MR fluid flows through the active section, it encounters the magnetic field and its rheological properties change, creating a yield force (Yoo and Wereley, 2002). Flow is initiated only if the pressure difference is greater than the yield force. This blocking property enables us to used MRFs as fluidic valves.

A 1-D axisymmetric analysis was given by Kamath $et.al$ 1996, and an approximate rectangular duct analysis was provided by Wereley and Pang, 1998. Gavin $et.al$ 1996, provided an analysis for annular valves with more appropriate radial field dependence. In the present analysis, we assume uniform field across the active section. We also consider an approximate rectangular duct analysis of Poiseuille flow through a valve system containing MR fluid. For Newtonian flow, the volume flux, Q, through the annulus is a function of the area moment of inertia I ($bd^3/12$) of the valve cross-section, the fluid viscosity, and the pressure drop over the active length, $\Delta P/L_a$ in the case of the rectangular duct model. The dimensional volume flux through the valve can be determined (Lindler and Wereley, 2000; Wereley and Pang, 1998). The salient features of the MR valve are listed in Table A.2

$$Q_N = \frac{bd^3\Delta P}{12\mu_{po}L_a} \tag{A.1}$$

$$Q_{BP} = \frac{bd^3\Delta P}{12\mu_{po}L_a}\left(1-\bar{\delta}\right)^2\left(1+\frac{\bar{\delta}}{2}\right) \tag{A.2}$$

$$Q_{BV} = \frac{bd^3\Delta P}{12\mu_{po}L_a}\left[\left(1-\bar{\delta}\right)^2\left(1+\frac{\bar{\delta}}{2}\right)+\frac{3}{2}\bar{\mu}\left(1-\frac{\bar{\delta}^2}{3}\right)\bar{\delta}\right] \tag{A.3}$$

where Q_N denotes Newtonian flow, Q_{BP} denotes Bingham plastic flow and Q_{BV} denotes bi-viscous flow. Here the non-dimensionalised plug thickness , $\bar{\delta} = \delta/d$ and non-dimensional viscosity ratio, $\bar{\mu}$ which is defined as the ratio of the post-yield differential viscosity (μ_{po}) to the pre-yield differential viscosity (μ_{pr}), have been introduced. Normalizing each volume flux by the Newtonian (field off) value of volume flux yields the non-dimensional volume flux for each of the flow models.

$$\bar{Q_N} = 1 \tag{A.4}$$

$$\bar{Q_{BP}} = \left(1-\bar{\delta}\right)^2\left(1+\frac{\bar{\delta}}{2}\right) \tag{A.5}$$

$$\bar{Q_{BV}} = \left[\left(1-\bar{\delta}\right)^2\left(1+\frac{\bar{\delta}}{2}\right)+\frac{3}{2}\bar{\mu}\left(1-\frac{\bar{\delta}^2}{3}\right)\bar{\delta}\right] \tag{A.6}$$

Figure A.5 shows the variation of non-dimensional volume flux with plug thickness, $\bar{\delta}$ for the Bingham plastic and bi-viscous models. We can see that complete blockage of the valve is not possible with the biviscous model since there is a finite value of viscosity in the preyield region. Hence, as the value of $\bar{\mu}$ increases, the leakage flow through the valve increases (for a plug thickness $\bar{\delta}$ of 1).

Yield stress characteristics of an MRF change as a function of the applied magnetic field. Therefore, the magnetic field applied to these valves is a critical factor to the performance of the valve and actuator.

A.3.2 MR Valve Network Operation

In the active mode, the piezo pump functions as the pressure source to the hydraulic system. The output motion of the cylinder can be controlled by the activation of the MR valves through the application of current through the electromagnetic coils. Applying current to valves 1 and 4 activates these valves and the fluid flows predominantly from the high pressure side of the pump to the high pressure side of the output cylinder. Under ideal situation, or infinite blocking pressure, there is no flow through valves 1 and 4. However, in a real system, valves 1 and 4 permit a very small volume flow rate through them even when they are active. This leaking flow is very small compared to the volume flow rate in valves 2 and 3.

A.4 MR-Piezo Hybrid Actuator

The MR-piezo hybrid actuator consists of a piezo pump as the main fluid driver and MR fluids are used to change the direction of an output cylinder. The performance of this hybrid actuator can be evaluated using three models: 1) an idealized valve in which infinite blocking pressure is assumed, 2) a Bingham plastic model with a finite blocking pressure, and 3) a bi-viscous model.

The volume flux through each valve can be written as

$$Q_i = \frac{bd^3}{12\mu L_a}\bar{Q}_i\left(P_S - P_H\right) \tag{A.7}$$

$$Q_a = \frac{bd^3}{12\mu L_a}\bar{Q}_i\left(P_S - P_L\right) \tag{A.8}$$

In these equations, P_S, P_H and P_L are the supply pressure from the pump, pressure at high pressure end of the output cylinder and pressure at low pressure end of the output cylinder respectively. Q_i is the volume flux through the inactive (or open) valve and Q_a is the volume flux through the active (or closed) valve. The total volume flow rate Q_S from the pump and the flow rate for moving the actuator Q_W

are defined as

$$Q_S = Q_i + Q_a \tag{A.9}$$

$$Q_W = Q_i + Q_a = A_p u \tag{A.10}$$

From the force equilibrium equation at the output cylinder, the velocity of the output cylinder bore can be expressed as

$$u = \frac{bd^3 P_S}{24\mu L_a A_p}\left[\left(\bar{Q}_i - \bar{Q}_a\right) - \left(\bar{Q}_i + \bar{Q}_a\right)\frac{F}{A_P P_S}\right] \tag{A.11}$$

$\overline{Q_i}$ and $\overline{Q_a}$ are the nondimensional volume flux through the inactive and active valves respectively. Thus, the non-dimensional actuator performance equation can be stated as

$$\bar{Q}_W = \frac{12\mu Q_W L_a}{bd^3 P_S} = \frac{1}{2}\left[\left(\bar{Q}_i - \bar{Q}_a\right) - \left(\bar{Q}_i + \bar{Q}_a\right)\bar{F}\right] \tag{A.12}$$

where, $\bar{F} = F/A_P P_S$. The maximum value of $\bar{F}$ is 1 and $\bar{Q}_W$ is 0.5. When the current is applied to an appropriate set of valves, we can define $\bar{Q}_i$ and $\bar{Q}_a$ as the following.

$$\bar{Q}_a = 1 \qquad \text{Newtonian} \tag{A.13}$$

$$\bar{Q}_i = \left(1-\bar{\delta}\right)^2\left(1+\frac{\bar{\delta}}{2}\right) \qquad \text{Bingham plastic} \tag{A.14}$$

$$\bar{Q}_i = \left(1-\bar{\delta}\right)^2\left(1+\frac{\bar{\delta}}{2}\right) + \frac{3}{2}\bar{\delta}\bar{\mu}\left(1-\frac{\bar{\delta}^2}{3}\right) \text{ Bi-viscous} \tag{A.15}$$

Figure A.6 shows the actuator performance prediction based on the Bingham plastic model for different values of plug thickness. We see that on increasing the magnetic field in the valve, we increase the plug thickness and the performance approaches the ideal line. Figure A.7 shows the actuator performance prediction based on the biviscous model for various values of viscosity ratios. All these lines have been plotted for a plug thickness of 1. We see that as the value of $\bar{\mu}$ increases, the valve deviates more from the ideal line. Increasing the value of the parameter $\bar{\mu}$ means to decrease the viscosity in the preyield region. This increases the leakage flow through the valves and hence decreases the performance.

A.4.1 Efficiency

The hydraulic system efficiency, defined as the power transfered to the load divided by the power supplied to the MR valves, is given by Yoo and Wereley (2002)

$$\eta = \frac{\text{Power delivered to load}}{\text{Power supplied to the system}} \tag{A.16}$$

$$= \frac{P_H Q_i - P_L Q_a}{P_H Q_i + P_L Q_a} \tag{A.17}$$

$$= \frac{\bar{Q}_i - \bar{Q}_a}{\bar{Q}_i + \bar{Q}_a} \tag{A.18}$$

From the above, system efficiency of the actuator model can be derived asd follows.

$$\eta\left(\overline{\delta}, \overline{\mu}\right) = 1 - \frac{2\overline{Q}_a}{1 + \overline{Q}_a} \tag{A.19}$$

This equation only gives the efficiency for the hydraulic system. It is evident from the equation that the efficiency depends on the value of both plug thickness,$\bar{\delta}$ and viscosity ratio,$\bar{\mu}$. Figure A.7 shows the variation of hydraulic efficiency with plug thickness, $\bar{\delta}$ for various values of viscosity ratio, $\bar{\mu}$. We see that as the value of $\bar{\mu}$ increases, the efficiency decreases. This is due to the increased leakage flow through the valves.

A.5 Experimental Results

Experiments were performed to measure the output performance of the MR-piezo hybrid actuator. A potentiometer(LVDT, TR50 NovoTechnik) was attached to the output cylinder to measure the displacement performance. A commercially available amplifier, the AE Techron LV3620, was used to drive the piezo stacks with frequencies up to 2 kHz. Load tests were performed by hanging dead weights at the end of the output cylinder. The output cylinder was a commercially available hydraulic cylinder with an outside bore diameter of 7/16 in and inside bore diameter of 3/16 in. All experiments were performed at a bias pressure of 200 psi. The data were acquired using MATLAB and a dSPACE autobox, which were also used to generate the drive signal for the amplifiers. The MR fluid used in the experiments was MRF-132AD manufactured by the LORD Corporation. Properties of this fluid were first investigated using a parallel plate rheometer and the results are shown in Figure A.9. The preliminary results of this study have been published (Yoo and Wereley, 2004).

Figure A.10 shows the comparison of performance of an ideal blocked valve and a MR valve. First, a dummy valve was used on two arms of the Wheatstone's bridge to completely block off fluid flow in one direction. After obtaining the results for the dummy valve, these dummy valves were replaced with active MR valves and a similar test was performed where the magnetic field in these valves was saturated with a current of 3 A. From the figure, we can see that there is a decrease in the maximum output velocity by around 10 mm/s. This corresponds to the leakage flow through the valves. Additionally we also see the frequency domain behavior of MR valves in conjunction with the piezo pump. The output velocity shows a distinct peak at 1100 Hz actuation of the piezo stack.

Unidirectional load tests were performed using blocked MR valves. A typical result is shown in Figure A.11. This figure shows the variation of output cylinder velocity as a function of piezo actuation frequency for various values of currents applied to the MR valves. Piston or actuator shaft velocity drops drastically when the current applied to the MR valves is reduced. Figure A.12 shows the load lines for 700, 800 and 900Hz actuation frequencies. The performance of the system was also studied using the relation between force and the working flow rate. The comparison between the theoretical result and the experimental data for frequencies 700, 800 and 900 Hz are given in Figures A.13 - A.15.

Figure A.16 shows the output power transferred to the load as a function of the actuation frequency. From this plot, we can see that maximum power is transfered when the load is 2.5 lbs and when the actuation frequency is 800 Hz.

The piezo-MR actuator was also tested in bidirectional mode. This was done by switching alternate arms of the Wheatstone bridge at the desired frequency. This causes the flow to change direction causing the output cylinder to reverse direction. To prevent agglomeration and settling of the MR particles, a demagnetization signal is also incorporated into the valve activation waveform. A demagnetization signal consists of a rapidly oscillating and diminishing signal. This is generated by multiplying a sinusoid of high frequency with an exponentially decreasing function. Such a rapidly changing magnetic field randomizes the magnetic dipole directions of the particles and prevents them from agglormerating. Figure A.17 shows the signals given to both sets of MR valves. The signals to both sets of valves are identical in amplitude and frequency. However, they are phased 180 degrees opposite to each other. Figure A.18 shows the variation of stroke with bidirectional frequency. In an ideal case, since the piezo pump is operating at a contant voltage and frequency, the flow rate provided to the output cylinder is a contant. The flowrate coming into the output cylinder can be written as a product of the cylinder frequency and the volume swept in each stroke as shown in Equation A.20- A.22. Since the area of cross-section of the output cylinder remains constant, the product of output stroke and frequency must be a constant. The results follow the hyperbolic trend as expected.

$$V_{piston} \times f = Q \tag{A.20}$$

$$A_p \times d_{piston} \times f = Q \tag{A.21}$$

$$d_{piston} \times f = constant \tag{A.22}$$

A.6 Conclusions

A smart actuation system using MR fluids as the transmission fluid and piezoelectric stacks as the driving element is studied. A Wheatstone bridge arrangement of MR valves enables bidirectional actuation of the output cylinder. The driving pressure is produced by the high frequency motion of piezo stacks and the resulting fluid motion is rectified into bidirectional actuation of the output cylinder through MR valves. The actuation system was tested in unidirectional and bidirectional mode and a comparison was made between the effectiveness of MR valves and ideal valves.

From the results, we can conclude that the output power is dependent on the mechanical load and the MR valve driving current. The load dependence comes as a result of impedance matching criteria. The final design of the actuator and the valves have to take the load into account for optimised design. When the magnetic field in the valve is less than the optimum valve, the leakage flow through the valve decreases its hydraulic efficiency. The system is also limited by a finite blocking pressure since MR fluid has a finite yield force. From the bi-directional tests, we see that we get appreciable stroke for frequencies up to 10 Hz. The stroke is limited by the flow rate that the piezo pump can output.

Though the capabilities of this actuator are limited at the present time, it offers significant potential for localized actuation and vibration reduction through the control of the active valves.

A.7 Nomenclature

A_p	Output piston area
b	Breadth of active
d	Height of active section
L_a	Length of active section
Δ P	Pressure differential between two positions
F	Output force of cylinder
μ_{po}	Post-yield viscosity
μ_{pr}	Preyield viscosity
$\bar{\delta}$	Non-dimensionalised plug thickness
$\bar{\mu}$	Ratio of preyield and postyield viscosity
Q	Volume flux
η	Efficiency as a function of plug thickness
F	Force
$\overline{F}$	Nondimensional force
Q_w	Working volume flux
$\overline{Q_w}$	Nondimensional working volume flux
Q_i	Volume flux through the inactive valve
Q_a	Volume flux through the active valve
P_S	Supply pressure at the pump
P_H	Pressure at high pressure side of the output cylinder
P_L	Pressure at low pressure side of the output cylinder

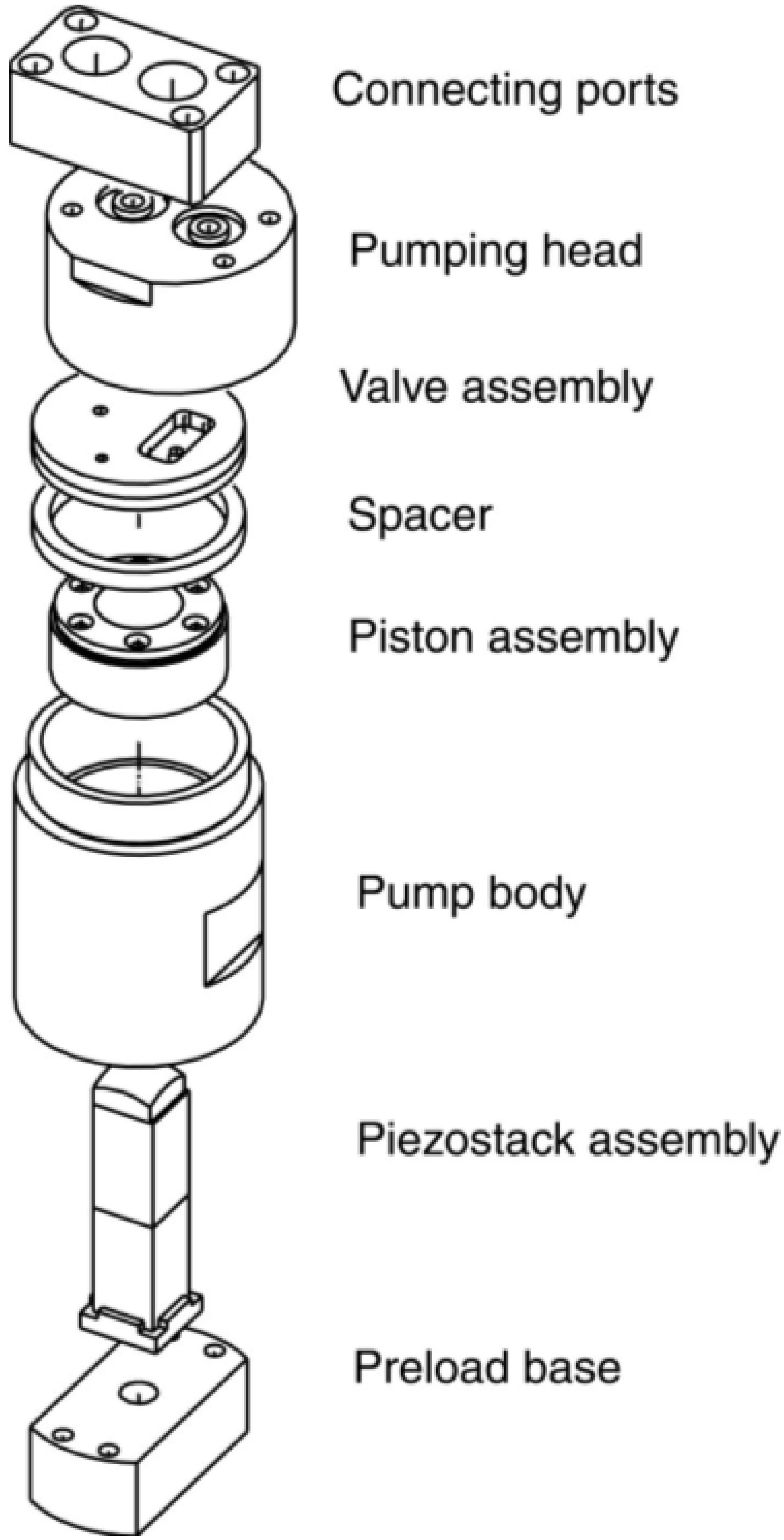

Figure A.1: Exploded view of the different piezo pump parts

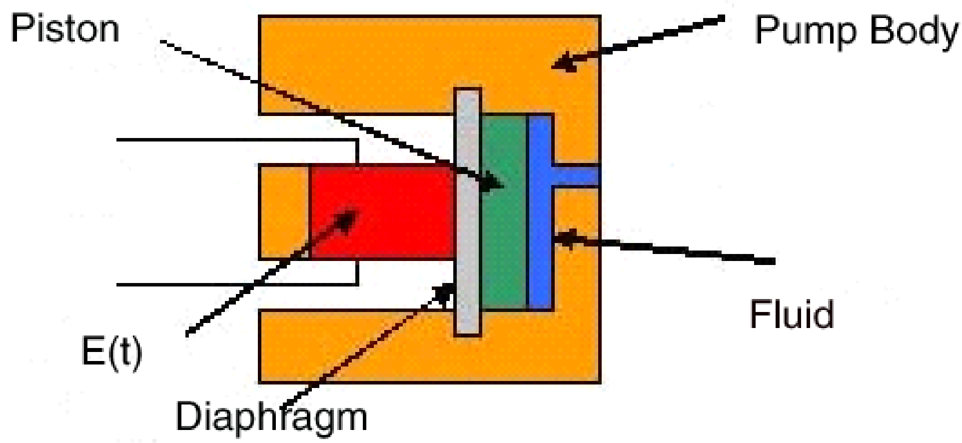

Figure A.2: Piezo pump schematic diagram

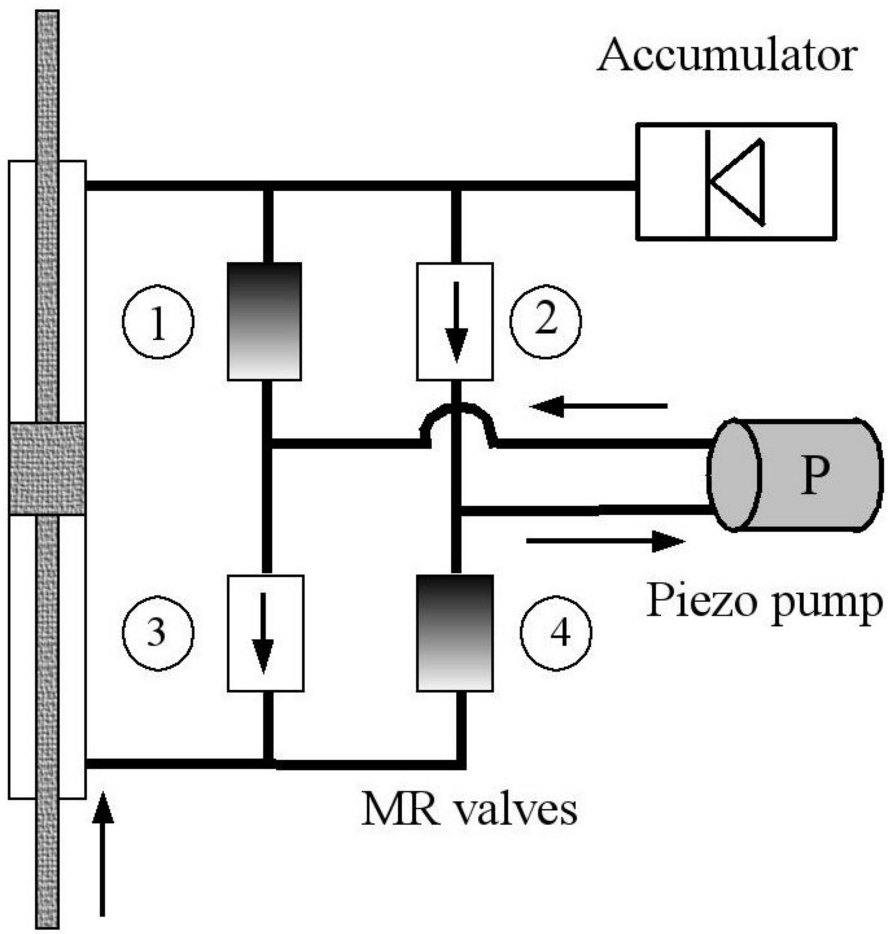

Figure A.3: Active mode

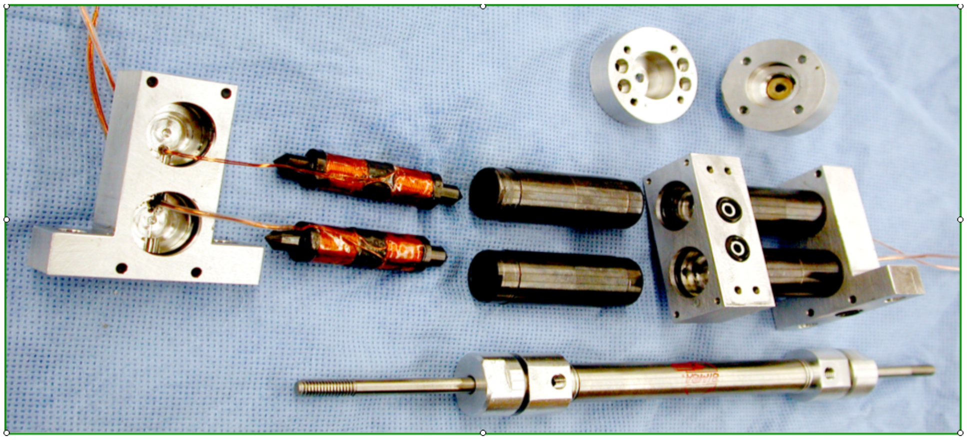

Figure A.4: MR valves and manifold

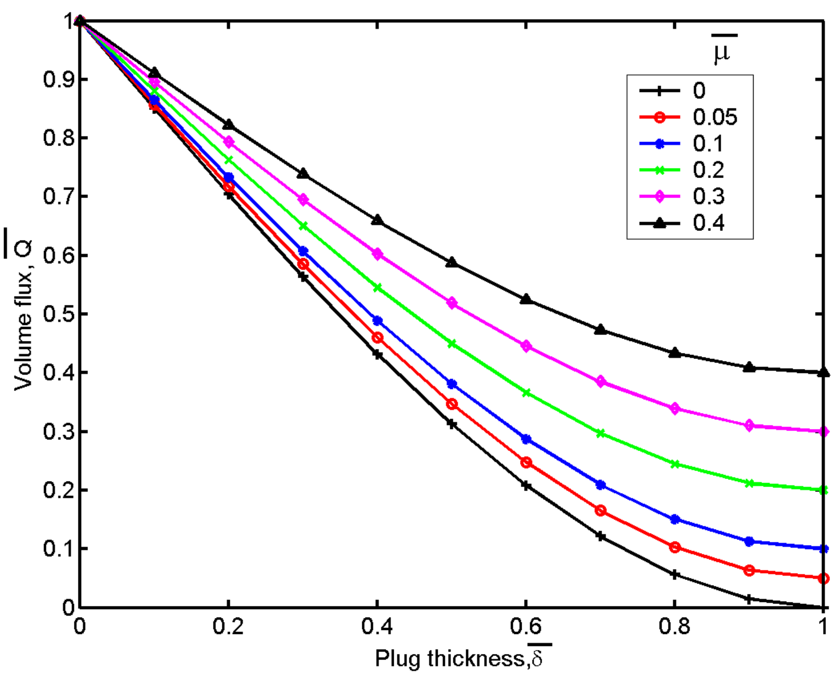

Figure A.5: Non-dimensional volume flux as a function of plug thickness

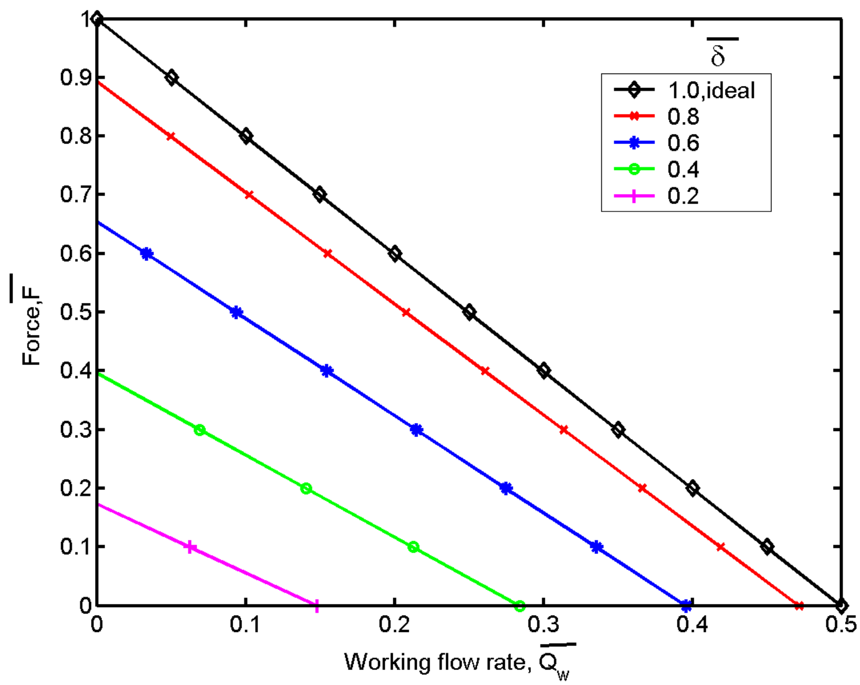

Figure A.6: Non-dimensionalised force as a function of working flow rate, as predicted by Bingham plastic model. For all cases shown here, $\overline{\mu}$=0

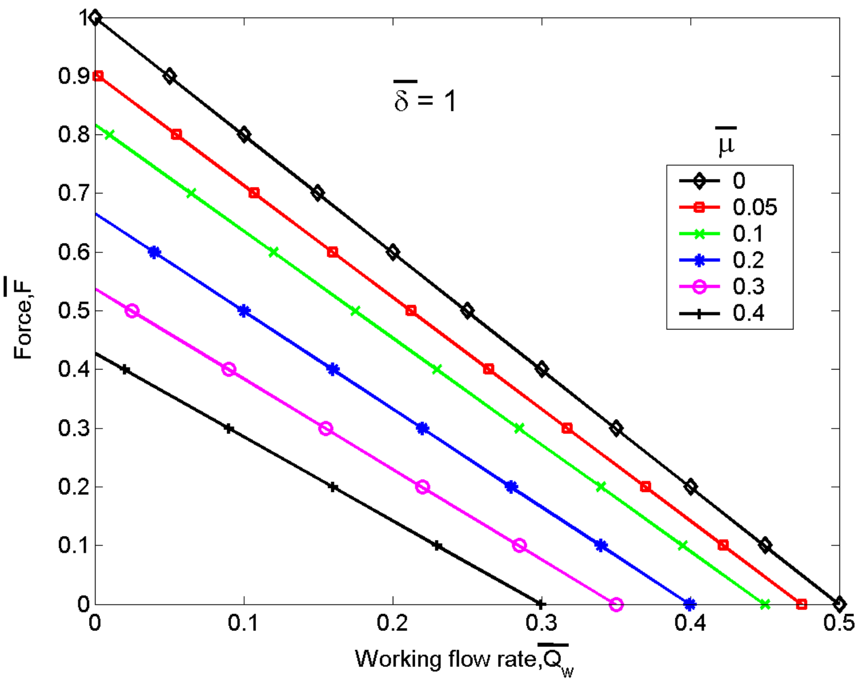

Figure A.7: Non-dimensionalised force as a function of working flow rate, as predicted by the bi-viscous model. For all cases shown here, $\overline{\delta}$=1

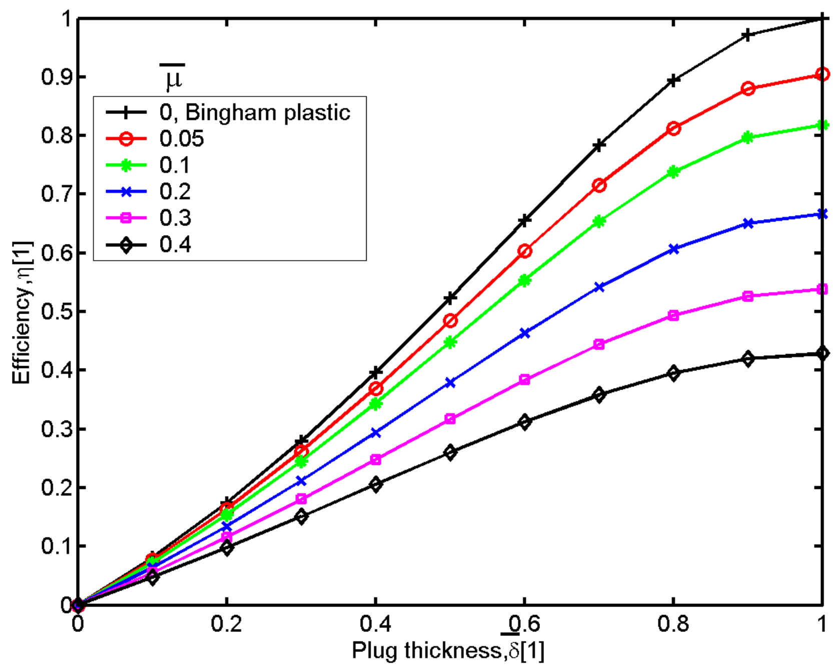

Figure A.8: Efficiency as a function of plug thickness $\bar{\delta}$ for various values of viscosity ratio, $\bar{\mu}$

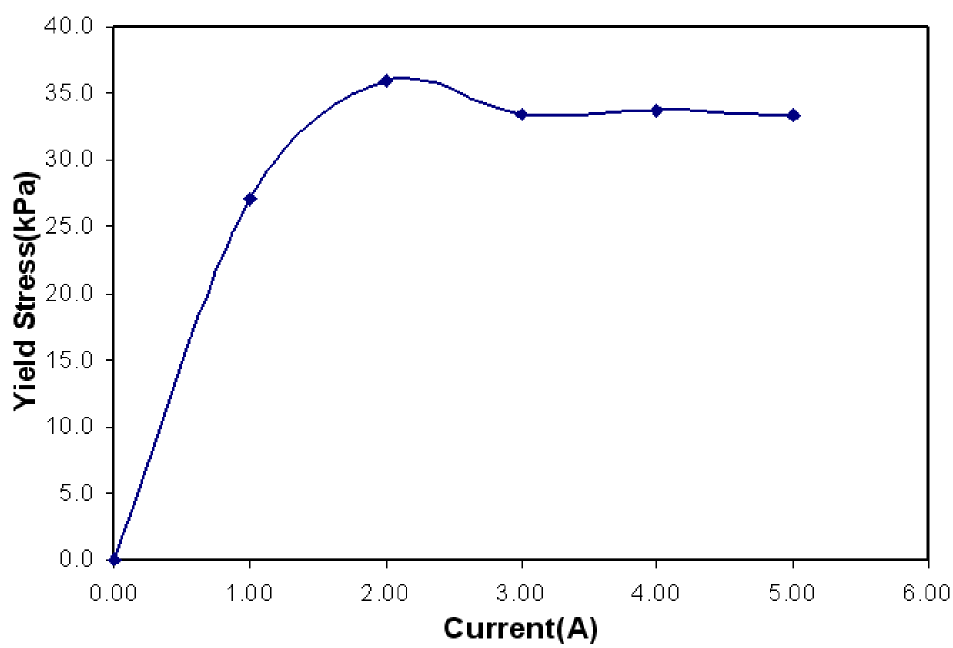

Figure A.9: Variation of yield stress of MRF-132AD with current

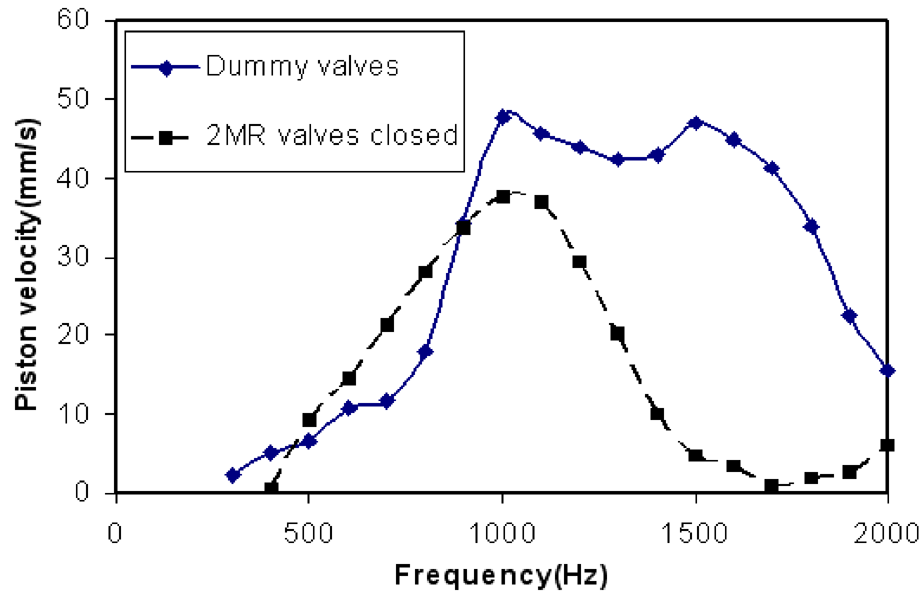

Figure A.10: Comparison of MR and ideal valves

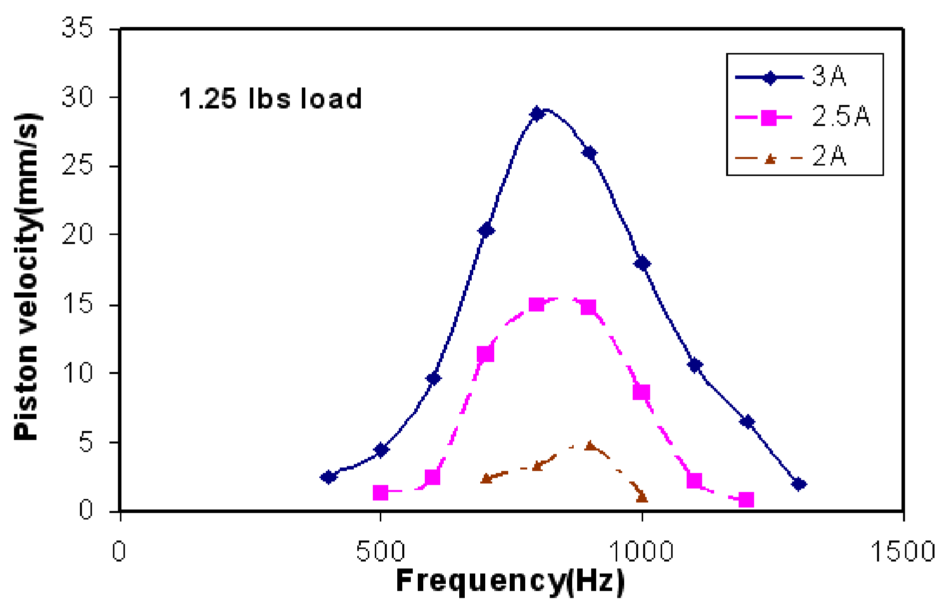

Figure A.11: Output velocity as a function of actuation frequency for a 1.25 lbs load

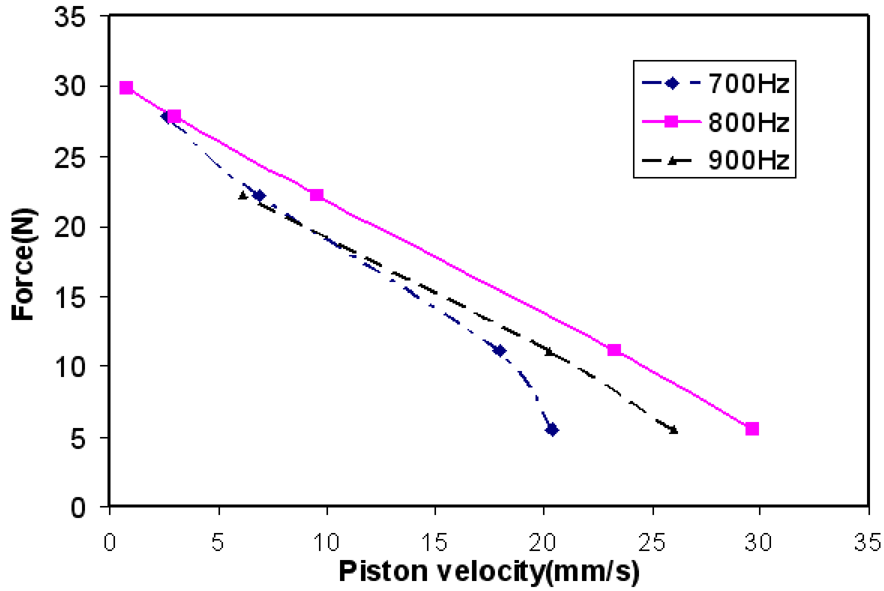

Figure A.12: Load line at 700, 800 and 900 Hz actuation frequencies

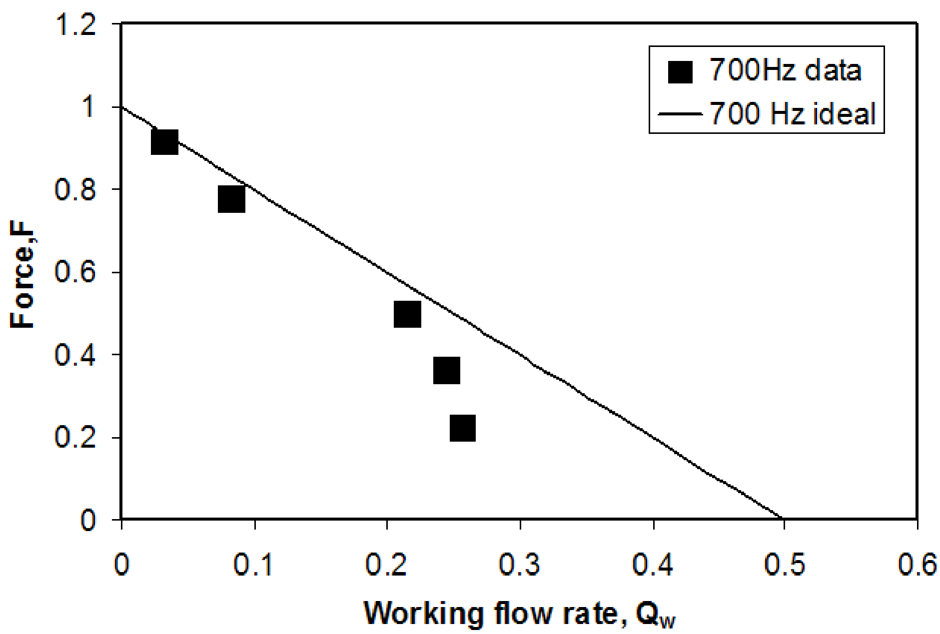

Figure A.13: Force as a function of working flow rate for 700 Hz piezo actuation

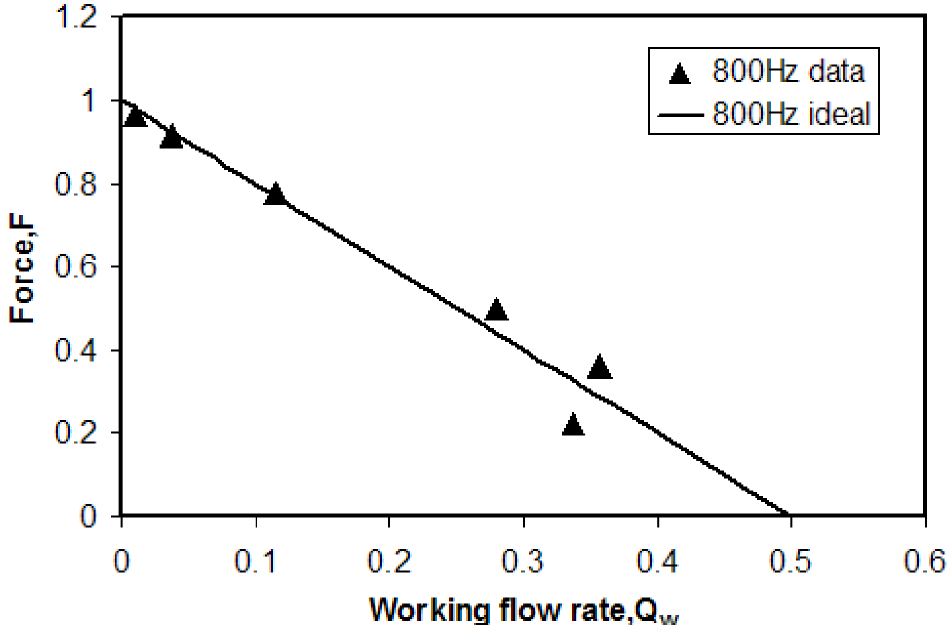

Figure A.14: Force as a function of working flow rate for 800 Hz piezo actuation

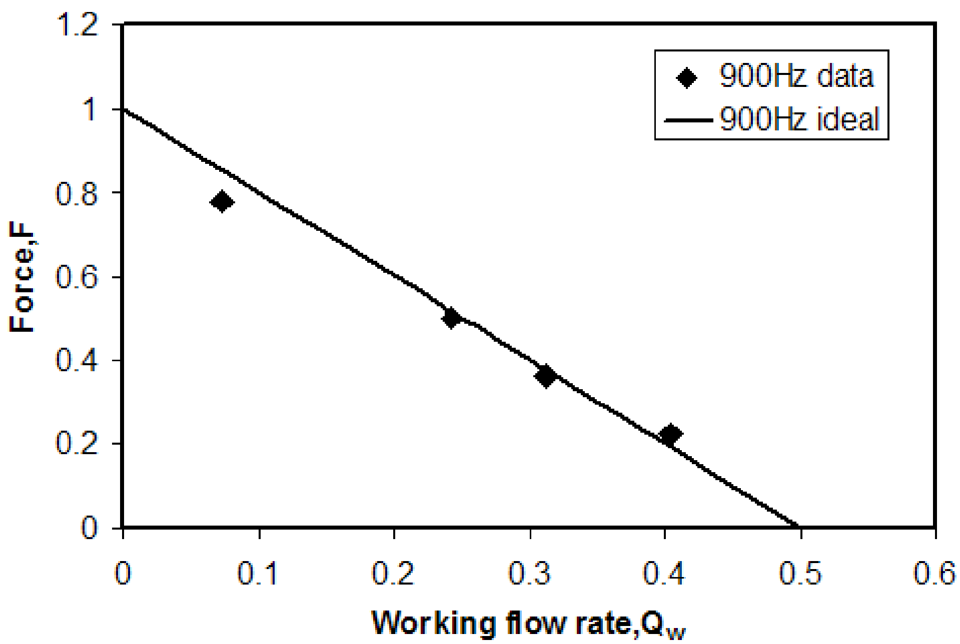

Figure A.15: Force as a function of working flow rate for 900 Hz piezo actuation

Table A.1: Piezo pump parameters

Piezostacks	PI P-804.10
No. of stacks	2
Length	0.3937 in
Width	0.3937 in
Height	0.7087 in
Blocked force (0-100V)	1133 lbs
Free displacement (0-100V)	0.5 mil
Maximum voltage	140V
Minimum voltage	-20V
Capacitance	7 μF
Pumping chamber diameter	1 in
Pumping chamber height	0.05 in

Table A.2: MR valve parameters

Outer diameter	16.4mm
Bobbin diameter	11.0mm
Active length	11.6mm
Air gap	0.5 mm
No. of windings	114 turns
Material	HIPERCO-50A
Magnetic field (max)	0.9T (3A)

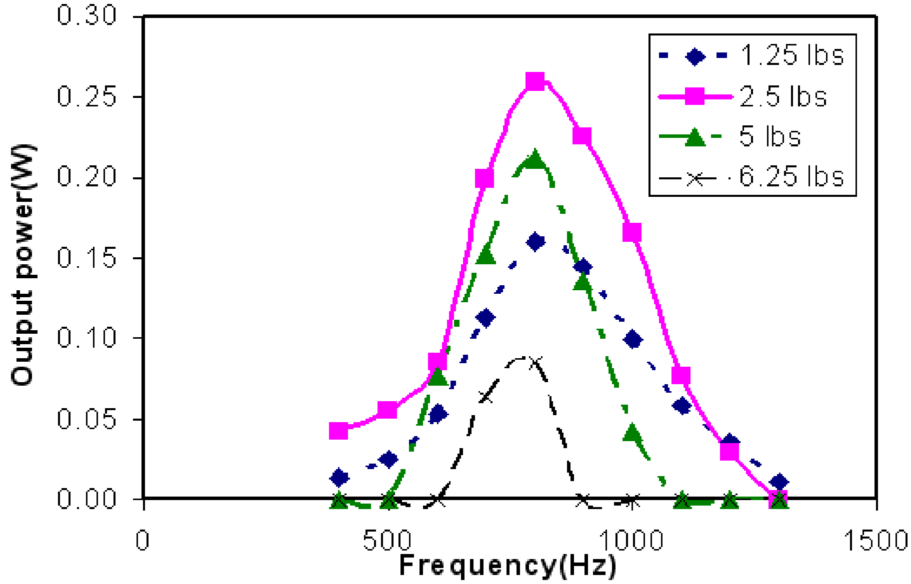

Figure A.16: Load line at 700, 800 and 900 Hz actuation frequencies

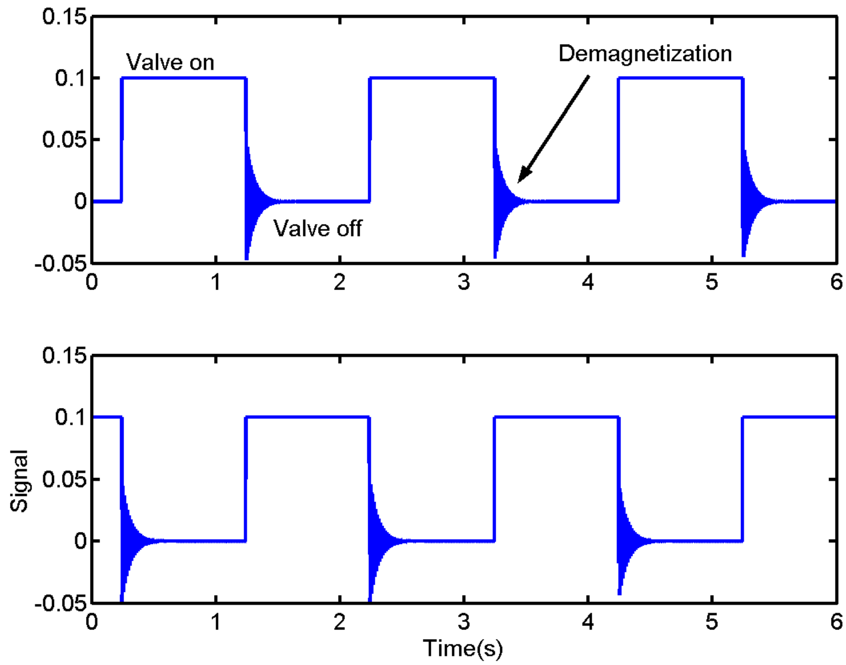

Figure A.17: Bi-directional valve drive signal

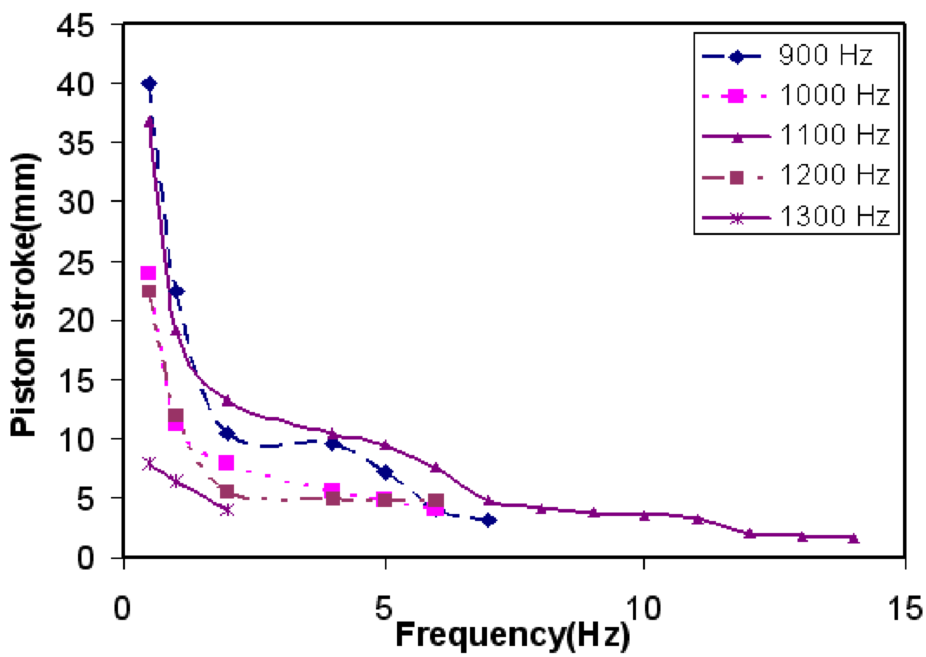

Figure A.18: Variation of stroke with output cylinder frequency in bidirectional mode

Appendix B

Comparison of Piezoelectric, Magnetostrictive and Electrostrictive Hybrid Hydraulic Actuators

B.1 Introduction

Active materials are materials that undergo an induced strain due to the application of an electric, magnetic or thermal field. Within this broad classification of active materials, we investigate the properties of electro-active and magneto-active materials, which respond to electric and magnetic fields, respectively. In recent years, hybrid actuators have exploited the high energy density, large blocked force and large actuation bandwidth capability of active materials by using them as primary driving elements in actuators. Additionally, hybrid actuators can be designed to have a very low number of moving parts, thus improving their reliability. Actuation systems based on active materials find applications in rotorcraft (Prechtl and Hall, 1999), automobile (Lam and Liao, 2003) and biomedical (Shoji and Esashi, 1994) engineering. Despite their high energy density and actuation bandwidth, the factor that limits the use of such actuators is their low induced strain. Frequency rectification methods overcome the low induced strain by trading high frequency motion of the active material for a low frequency motion of the load through the use of active or passive means. Examples of such frequency rectified devices are ultrasonic motors (Sashida and Kenjo, 1993; Uchino, 1997), rotary piezoelectric motors (Duong and Garcia, 1996; Frank et al., 2003) and inch-worm motors (Hemsel and Wallaschek, 2000; Galante et al., 2000). Because such devices use friction for rectification, they are highly prone to rapid wear and tear. Hybrid hydraulic devices are another class of devices that use frequency rectification techniques to convert low amplitude, high frequency motion of the active material into a high amplitude, low frequency motion of the load. In these actuators, the active material is used to pressurize a hydraulic fluid in an enclosed pumping chamber. The bi-directional motion of this pressurized fluid, resulting from the excitation of the active material, is then rectified using one-way valves. These one-way valves, which act in a similar manner to electric diodes, allow flow in only one direction depending on the pressure difference across them. This results in a uni-directional flow exiting the pump and thus, a uni-directional motion of the output load. To obtain bi-directional motion of the output load, an additional valving system (active or passive) must be introduced. Several such hybrid hydraulic devices have been developed in recent years by various research groups (Mauck and Lynch, 2000; Nasser, Leo and Cudney, 2000; Sirohi and Chopra, 2003). These different prototypes of the hybrid hydraulic actuator vary in the output power capability and frequency range of operation.

A variety of models have been developed to predict the performance of hydraulic hybrid actuators, such as quasi-static approaches (Mauck, Oates and Lynch, 2001; Cadou and Zhang, 2003), lumped parameter approaches using electrical analogies (Nasser and Leo, 2000) and mechanical analogies (Oates, Mauck and Lynch, 2002), lossless transmission line (Sirohi, Cadou and Chopra, 2003) approaches, CFD methods (John et al., 2006; Oates et al., 2002) and integration of the mass conservation equations (Konishi et al., 1997; Regelbrugge et al., 2003). Such models attempt to address the overall performance of the actuators vis-a-vis fluid losses, hydraulic resonances, output power and electromechanical efficiency. The performance of hybrid hydraulic actuation systems depends on several factors like pump head design, hydraulic circuit dynamics and electric drive circuit design. The properties of the active driving material are also highly critical to the performance of a hybrid hydraulic actuator. Therefore, investigation into the impact of different active material stacks on the performance of hybrid hydraulic actuator systems becomes important. There have been several studies that compared the bulk material properties - mechanical and electrical - of different active materials (Pan et al., 2000; Zhao and Zhang, 1996; Pomirleanu and Giurgiutiu, 2004). Studies into a comprehensive comparison of these active materials from an application point of view have been few (Janocha et al., 1994; Ellison, 2004; Damjanovic and Newnham, 1992).

A frequency rectified device makes use of the high bandwidth capability of the active material by driving the active material stack at high frequencies. This ensures that the maximum volume of fluid is displaced at a very high frequency to result in maximum obtainable volume flow rate from the pumping chamber. The limitations of operating at higher pumping frequencies are the increase in input power required and the reduction in flow rate after resonance of the hydraulic circuit is reached. The resonance of the hydraulic circuit depends on the inertia and stiffnesses of the fluid lines, the active material stack and the load. The maximum flow rate is obtained at the resonant frequency of the actuator system. Raising the pumping frequency beyond this value results in a decrease in the performance of the actuator. The amount of energy transfered from the active material to the fluid is governed primarily by the impedance matching condition between the active material stack and the fluid in the pumping chamber. Thus, to transfer the maximum energy from the active material to the fluid, the active material stack stiffness should match the fluid chamber stiffness (Sirohi, 2002). The overall electromechanical efficiency of the actuator determines the total amount of energy transfered to the load as a ratio of the amount of energy put into the material. In this study, this energy is measured in terms of the rate of work done, *i.e.* power. The stiffness of the active material stack also affects the overall electromechanical efficiency since the energy output of the device is affected by the material stiffness. The input energy depends on the inherent characteristics of the active material and the electric or magnetic drive circuit. The amount of energy consumed by electro-active materials such as piezoelectrics and electrostrictives, depends on the capacitance of the stack. The amount of energy consumed by a magneto-active material depends on the resistance and inductance of the field generating coil. Thus, the design of the magnetic circuit becomes an important consideration for magneto-active materials. Preliminary investigation into the issues of coil design was done in a previous work (Ellison, 2004) and will not be addressed in this paper.

This study compares different active materials from an actuator system performance standpoint while constraining the active volume of the active material and the volume of the actuator as a whole. Most applications place geometric and volumetric constraints on the actuator. Thus its necessary to compare the active material stacks on the basis of their active length, cross-sectional area, active volume and overall actuator dimensions. The active material stacks used in study had an active length of around 54 mm and a cross-sectional area of 25 mm^2. The actuation system used in this study was developed at the Alfred Gessow Rotorcraft Center (Sirohi and Chopra, 2003). By adapting the different materials to be used in the same actuator, the overall dimensions of the actuator were also held constant. This provides the basis for a direct comparison between these materials.

B.2 Material Properties

Active materials vary widely in their basic mechanism of strain generation as well as their elasticity, stiffness, strain, hysteresis and electrical impedance properties. The stiffness and the amount of strain generated by the material are the major factors that determine the power output of the actuator. The stiffness of the stack - dictated by Young's modulus of elasticity of the pure active material and the insulating material as well as the cross-sectional area and length of the stack - determines the amount of energy transferred by the stack to the fluid in the pumping chamber through an impedance matching criteria. The free displacement determines the amount of volumetric displacement produced by the stack under no-load conditions. The input electrical energy required by the stack depends on the electrical impedance of the stack or the coil and the hysteresis in the active material. Hysteresis constitutes the part of the input energy that is dissipated within the material and is a characteristic of the bulk material. The rest of the energy is available to be transmitted to the load as useful mechanical work. In the case of electro-active stacks, this part of the input energy (non-dissipative part) is determined by the electrical impedance of the stack, which is capacitive in nature. For magnetostrictive stacks, the non-dissipative part of the input energy depends on the inductance of the magnetic field generating coil. Both electro-active and magneto-active materials shall be referred to as *stacks* in this study.

Electro-active materials produce induced strain on the application of an electric field. The two types of electro-active materials considered for this study are piezoelectric and electrostrictive materials.

- Piezoelectric materials generate strain when an electric field is applied in a prescribed direction. This effect is also called the *converse* effect. The most common form of piezoceramics is based on Lead-Zirconate-Titanate(PZT) compounds. In piezoceramics, the unit cell has a certain degree of asymmetry which gives it a permanent dipole. A poling operation is done on a bulk material to orient all the dipoles in a preferred direction to produce a net polarization. Once polarized, an applied electric field in the poling direction produces a temporary expansion in the poling direction, thus producing induced strain. The piezoelectric stack used in this study was a commercially available stack PST 150-5x5x54 obtained from American Piezo International Ltd. The free strain and modulus of elasticity of the stack as provided by the manufacturer are 1600 μs and 20 GPa. The stack has a length of 54 mm, a cross-sectional area of 25 mm^2 and is rated for voltages ranging from -20 to 150V. Figure B.1(a) presents the results of static tests done on the PZT stack and shows that the strain is nearly proportional to the voltage applied to the stack. As mentioned earlier, the energy consumption of a stack depends on its electrical impedance. The electrical impedance of piezoelectric stacks is capacitive in nature and has a value of 5.4μF. Due to the capacitive nature of the impedance, the impedance decreases with increase in frequency and the current required to maintain a constant voltage increases.

- Electrostrictive materials also exhibit strain on the application of electric field. The phenomenon of electrostriction, however, is fundamentally different from the converse piezoelectric effect. The unit cell in an electrostrictive material is centro-symmetric and hence, the strain exhibited by such a material is not due to the change in structure, but is inherent in the material itself. The basic mechanism of actuation is a separation of charged ions in the unit cell of the material. The electrostrictive stack used in this study was a commercially obtained stack TRS PMN-5%PT, a Lead-Magnesium-Niobate compound, from TRS Ceramics Inc. The free strain and modulus of elasticity of this stack as provided by the manufacturer are 2000μs and 20GPa respectively. The stack has an overall length of 59mm, a cross-sectional area of 24mm^2. The relationship between strain and applied voltage for this stack is shown in Figure B.1(a). Electrostriction is fundamentally similar to magnetostriction and exhibits many of the common characteristics. Typically, the strain exhibited by an electrostrictive material has a quadratic relationship with the applied field and shows the property of *frequency doubling*. This phenomenon will be further explained in relation to the magnetostrictive stack. Ideally, an electrostrictive stack can operate under both positive and negative electric fields. However, due to the recommendations of the manufacturer, the electrostrictive stack used in this study was rated only for the voltage range of -20 to 500V. The electrical impedance of an electrostrictive stack, like a piezoelectric stack, is capacitive in nature and has a value of 0.37μF. Because the PMN stack has a lower capacitance than the PZT stacks, its energy consumption at a given voltage and frequency will be reduced.

Application of preload does not have a marked effect on the strain output of piezoelectric or electrostrictive materials. Preload is generally applied to these stacks to ensure that the stack always remains in contact with the actuator piston during high frequency operation. Application of preload also offsets the effect of extensional strain in the stack. Extensional strains are highly detrimental to the integrity of the stacks. Special care is required while mounting the stack in the actuator body as the slightest misalignment can produce a bending moment on the stack. Especially in stacks with a large aspect ratio (ratio of length to cross-sectional width), this bending moment can result in extensional stresses during high frequency operation. To mitigate the effect of extensional strains produced by bending moments, ball ends are used as the contact points on either end of the stack.

The type of magneto-active material considered in this study are magnetostrictive alloys. Magnetostrictive materials require an externally applied magnetic field to exhibit strain. This effect, called *Joule* effect, is generated from the realignment of magnetic domains in the material. Without an external field, the magnetic domains in a magnetostrictive material stacks will be aligned randomly. When an external magnetic field is applied, the domains realign in the preferred orientation parallel to the external magnetic induction B of the coil. This realignment causes a change in dimension. The response bandwidth magnetostrictive materials are typically large ($\sim$1kHz). In contrast to piezoelectrics or electrostrictives, preloading a magnetostrictive material has a significant effect on the induced strain obtained from the sample. The strain obtained from a magnetostrictive material increases substantially with an increase in preload. The magnetic domains tend to align under the effect of the preload and strain can be obtained from the stack by applying a magnetic field large enough to offset this initial domain alignment. This effect is a marked difference when compared to electro-active materials, where there is no significant effect of preload on the strain obtained. A typical static behavior of a magnetostrictive material is shown in Figure B.1(b). In addition to the longitudinal extension in length, the magnetostrictive material also undergoes a lateral contraction. The net result is a zero change in net volume of the material. Another distinctive feature of magnetostrictive materials is that the displacement of the material in its normal direction is always positive, regardless of the applied magnetic field direction. This can also be seen in Figure B.1(b). Thus, the strain has a quadratic dependence on the applied field. This means that when a purely AC sinusoidal signal is applied to the sample, the output strain will have a frequency which is double that of the input signal. This property of magnetostrictive material can be used to perform a *frequency doubling* of the stack. Because of this phenomenon, a bi-directional motion of the stack can obtained only by operating about a bias point. At the bias point, the magnetic domains are preferentially oriented. Thus, the length of the sample can be increased or decreased by increasing or decreasing the applied magnetic field about this zero point. Two types of magnetostrictive material were used in this study.

- Terfenol-D is an inter-metallic alloy of Terbium, Dysprosium and Iron that is produced as a near-single crystal. Terfenol-D is highly brittle and is likely to crack after prolonged operation. It has a maximum free strain and Young's modulus value of 1000 μs and 35-50 GPa, respectively. This material was a commercially available product provided by Etrema Products Inc.

- Galfenol, an alloy of Gallium and Iron, and unlike Terfenol-D, has a much better ductility than Terfenol-D, and so has a high degree of structural integrity. Galfenol has been shown to be machinable and has a maximum free strain and Young's modulus of 300 μs and 20-25 GPa, respectively. This research material was manufactured by Tom Lograsso of Iowa State University.

Both stacks had a length of 54.8mm and a cross-sectional area of 31mm^2. As opposed to electro-active stacks, the maximum free strain obtainable from a magnetostrictive stack is a strong function of the applied preload. The required magnetic field is applied using a field generating coil wound using 24 gage copper wire. It is also necessary to have flux return paths for the magnetic field lines. The main body of the pump is made of steel and thus acts as the flux return. The energy consumption of a magnetostrictive material depends on the electrical impedance of the coil, which is predominantly inductive in nature. An important fact to remember in the magnetic circuit around a magnetostrictive material is that for a given current, the magnetic field experienced by each stack depends on its magnetic permeability. Thus, equivalence in applied current does not translate to an equivalence in magnetic field as experienced by the different magnetostrictive stacks.

A table showing the salient material properties of the four samples is shown in Table B.1. The overall geometrical properties of the actuator were held constant in all four cases. Figure B.2 shows a picture of the active material stacks used in this study.

B.3 Experimental Setup

A schematic of the hybrid actuator used in this study is given in Figure B.3. The basic operation of the actuation system is executed in three stages. In the first stage, a driving signal is generated using a signal generator and is amplified and applied across the PMN/PZT stack or the coil surrounding the Terfenol-D/Galfenol stack. The changing electric/magnetic field applied to the active material produces induced strain in the material and pushes a piston which causes the fluid in the pumping chamber to be pressurized. In the next step, two oppositely oriented uni-directional check valves respond to the fluid pressure by opening only in their preferred direction. Thus, the check valves perform the function of rectification and convert the oscillatory motion of the active material stack to a uni-directional motion of the fluid. In the third stage, the fluid is led into a hydraulic output cylinder and the load through hydraulic lines. Thus, a uni-directional motion of the output cylinder shaft is obtained. In a practical situation, there is a need for bi-directional motion of the load and this can be implemented through the use of mechanical valves (Ellison, 2004) or MR fluid based valves (Yoo, Sirohi and Wereley, 2005). The hydraulic circuit has an accumulator on the low pressure side, which is used to apply bias pressure to the circuit and to filter out high frequency pressure oscillations. The stack is held between the preload base and the piston. Preload can be applied to the stack using a set screw arrangement inside the preload base. Since the length was nominally the same for each of the four active material stacks, the same pump body was used for all cases. The field generating coil for magnetostrictive stacks was designed to fit inside the pump body of the same pump. Thus, the overall dimensions of the actuator were the same for all four stacks. The salient features of this actuator is listed in Table B.2. An isometric view of the pump showing its various components is shown in Figure B.4.

The detailed operating procedure is as follows. The active material stack is mounted inside the pump body, as shown in Figure B.4. In the case of the magnetostrictive stacks, the coil and the stack were designed to fit the same pump body. The hybrid actuator was then filled with the transmission fluid through a reservoir connected to the accumulator port and degassed thoroughly using a vacuum pump. Degassing is very critical to the performance of the pump since dissolved air decreases the bulk modulus of the fluid thus decreasing the amount of work that can be done on to the load. Compressibility in the transmission fluid decreases the overall efficiency of the system. The reservoir was then disconnected from the pump manifold and a bias pressure of 1.4 MPa (200 psi) was applied via an accumulator. The bias pressure mitigates the effects of entrained air and also applies a preload to the active material stack. Another major reason for application of bias pressure is to prevent cavitation in the hydraulic fluid. Cavitation will result in vaporization of the hydraulic fluid and the resulting two-phase system will cause a decrease in the performance of the actuator. The preload base was screwed tightly onto the pump body and the preload on the active material was further increased by tightening the set screw inside the preload base. The amount of applied preload was monitored using a strain gage mounted on the stack. This basic procedure was identical for both electro-active and magneto-active stacks.

In the case of electro-active materials, the stack was actuated using a amplified DC-biased sine signal of a particular frequency. The DC bias is required since electric fields with a polarity opposite to that of the poling direction of the stack can depole the material. In the case of magnetostrictive stacks, a pure sinusoidal signal of a particular frequency was sent to a power amplifier, which provided the coils with the necessary current to produce the magnetic field for actuation. There is no danger of depoling in the case of magnetostrictive materials. As mentioned earlier, due to the quadratic dependence of strain on the applied field, a pure sinusoidal input signal will produce a magnetic field at twice its frequency in the stack, and hence, induced strain also at twice the frequency. The resulting motion of the output cylinder shaft was measured using a TR50 Novotechnik linear potentiometer. The voltage amplifier used was AE Techron, LV 3620 Linear Amplifier. The current amplifier used was a commercially available audio amplifier QSC Audio RMX 2450 Professional Power Amplifier. All the data acquisition and appropriate signal generation was done through a dSPACE Autobox Real Time system.

Three types of tests were performed on each stack:

1. Static Tests: The static tests were performed on the active material stack (but not on the actuator system). The objective of these tests was to determine the maximum free strain obtainable from the material under normal operating conditions and the calibration of the strain gage on the stacks. This test also served to verify the free strain values specified by the manufacturer. In the case of electro-active materials, a constant DC voltage was applied to the stack and the displacement was measured through the use of a laser sensor and corroborated with the signal received from a quarter-bridge strain gage that was mounted on the stack.

   The power amplifier used for the testing of magneto-active stacks was an audio amplifier. Since audio amplifiers are typically not capable of amplifying DC signals, only a quasi-steady test could be performed on the magneto-active stacks. Hence, a sinusoidal signal of very low frequency ($\ll$1 Hz) was amplified and applied across the field generating coil. This produced a very slowly varying magnetic field and simulates a quasi-steady condition. Elongation of the stack was then measured using a laser sensor and compared with the corresponding strain gage data.

2. No-load Tests: These tests determine the flow rate generated by the active material in the absence of any external load. The flow rate was determined by measuring the shaft velocity of the output cylinder. Since the active material was not working against an external load, useful power output was zero. The input power was used to overcome the internal losses in the actuator and to accelerate the mass of the shaft and piston inside the output cylinder. Additionally, hysteresis curves obtained from no-load tests can be used to ascertain the amount of energy dissipation in the material.

3. Loaded Tests: These tests were done to measure the performance of the pump in the presence of external loads. Graduated weights were hung from the shaft

of the output cylinder to simulate the effect of external loads. Upon actuation of the active material, the output cylinder shaft moves, along with the load, at a particular velocity. By measuring the output velocity of the load, we can determine the useful power output from the actuator. This was done for various pumping frequencies and loads. The weights were gradually increased till the blocking load for the actuator was reached. This data was then used to deduce the load line and output power of the actuator. The input power to the actuator was also measured at each tested pumping frequency.

B.4 Results

B.4.1 Static tests

As mentioned in the previous section, static tests were performed on the different stacks to experimentally identify the maximum value of free strain obtainable from the sample within the safe operating range specified by the manufacturer. For electro-active stacks, this test was performed by applying a constant DC voltage to the stacks. This was done using a DC power supply capably of supplying voltages up to 400V. Figure B.1(a) shows the results for PZT and PMN stacks. We see that the PZT stack (rated for maximum 150V) exhibited strain of 1300 μs at 140V and the PMN stack (rated for a maximum voltage of 500V) gives a strain of 1600 μs at a excitation voltage of 350V. To ensure the integrity of the stacks during further dynamic tests, the values of voltage used for static testing were less than the maximum rated operating voltages. From these values, we can say with sufficient confidence that the maximum free strain values provided by the manufacturer are accurate. Figure B.1(b) shows the results of quasi-static tests performed on the magnetostrictive samples. The stack was placed inside the magnetic field generating coil such that the magnetic field lines run along the length of the stack. A very slowly varying magnetic field was applied to the stack at a very low frequency. The Terfenol-D stack shows a strain of 750μs at a current of 4A, while the Galfenol stack shows a strain of only 250 μs at a current of 0.5A. We can see evidence for the slow varying nature of the magnetic field in the hysteresis loops seen in the quasi-steady data. The stacks were not tested beyond these values of current as the quasi-static curve showed signs of saturation at the higher values of current. Also, the ohmic heating produced in the coil at these high values of current is substantial. Sufficient time has to be provided between tests to sufficiently cool the field generating coil.

The free strain values provided by the manufacturer were verified via these static tests. Thus, we conclude the PMN stack exhibits the maximum free strain (of about $2000\mu\epsilon$), followed by PZT ($1600\mu\epsilon$), Terfenol-D ($1000\mu\epsilon$) and Galfenol ($300\mu\epsilon$). We can see from these values that the free strain obtained from PMN was 20% greater than PZT and 50% greater than Terfenol-D stacks and that the strain obtained from Galfenol was 70% less than that of the Terfenol-D stack. Purely by consideration of volumetric displacement, we could conclude that PMN will produce the greatest velocity in the output cylinder shaft under no-load conditions. However, when the stack is pushing the fluid enclosed inside the pumping chamber, the force that the fluid exerts on the stack is also important. Thus, volumetric displacement alone does not determine the work output of the actuator. The free strain has to considered together with the stiffness of the stack to determine the amount of energy that is transferred by the stack to the hydraulic fluid and ultimately to the load.

B.4.2 No-load tests

During no-load testing, the output cylinder shaft was permitted to move freely in the absence of any external load. No useful work was done during these tests and all the energy transfered by the stack to the fluid goes towards overcoming internal viscous losses in the pumping chamber and fluid paths in the actuator, frictional losses in the O-rings and lip seals in the output cylinder shaft, and in the motion of the shaft and piston mass of the output cylinder. In these tests, the active material was first mounted inside the pump body and preloaded. The stack was then actuated at various pumping frequencies causing the output cylinder shaft to move at different velocities. The velocity of the output cylinder shaft was measured using an LVDT. Figure B.5 shows the comparison of velocity under no-load conditions for PZT, PMN and Terfenol-D.

From this figure, we can see that the PMN stack produces the highest no-load velocity of 270mm/s. The Terfenol-D stack also has a very high no-load velocity of 250mm/s. The PZT stack has the least no-load velocity of about 70mm/s. As mentioned earlier, the amount of energy transfered between the stack and the fluid is dictated by the free displacement and the stiffness of the stack in comparison with the stiffness of the fluid column in the pumping chamber. The stiffness of the fluid in the pumping chamber is given by Equation B.1.

$$k_{fluid} = \frac{\beta A}{l} \tag{B.1}$$

where, k_{fluid} is the stiffness of the fluid column in the pumping chamber, β is the bulk modulus of the fluid, A is the area of cross-section of the pumping chamber and l is the height of the pumping chamber. Using the geometrical values of the pump used in this study from Table B.2 and a Bulk modulus of 137.9MPa (20000 psi), we obtain a fluid stiffness of 140 MN/m. When we compare this value of fluid stiffness to the values of stack stiffness listed in Table B.1, we can see that all the stacks are considerably softer than the fluid column. Since none of the stacks have a more favorable impedance matching condition than the others, we can conclude that the highest no-load velocity shown by the PMN stack is due to its superior free strain capability compared to the other stacks. However, we see that the PZT stacks shows a much lower no-load velocity than Terfenol-D, despite the fact that its free strain value is higher. The reason for this lies in the way in which stacks are made. Adjacent layers of piezoelectric material are glued together with alternating layers of insulating material to prevent short circuiting between the layers. The type and thickness of each insulating material layer depends on the choice of the manufacturer. Hence, the overall stiffness of the stack depends on the relative stiffness of the piezoelectric material and the insulating material. Since the value of overall stiffness of a stack is not provided by the manufacturer, the values listed in Table B.1 were calculated considering a stack which consists only of the pure material. Magnetostrictive stacks are not affected by this issue as they are not made by layering the active material. Magnetostrictive material are usually single-crystalline or polycrystalline bulk material grown in cylindrical or cuboidal form. Though the Young's modulus of the raw PZT material is greater than that of PMN or Terfenol-D, the overall stack stiffness of PZT was lesser than PMN or Terfenol-D, thus lowering its no-load velocity. This factor will also manifest itself in loaded tests as a decrease in the output power.

These tests also enable us to compare the hysteresis characteristics of the different active materials. Hysteresis quantifies the internal material losses within the stack and is a characteristic of the material. The area under a hysteresis plot is indicative of the amount of energy lost internally in the material due to rearrangement of domains and polarized particles. Figure B.6(a) shows the hysteresis curve of the Terfenol-D sample at 100Hz. This plot shows the variation of strain with the current supplied to the coil. We can see that hysteresis curve of Terfenol-D has a characteristic butterfly shape showing a quadratic behavior, wherein a negative magnetic field produces a positive strain in the stack. Figure B.6(b) shows the hysteresis characteristics of PMN and PZT stacks and plots the variation of strain with the applied voltage. We can quantify the hysteresis by normalizing the area under the hysteresis plot by the product of the peak values of voltage and strain. This quantity gives the area enclosed by the hysteresis loop as a fraction of the area of the smallest rectangle which encloses the loop. The value of this normalized hysteresis index is 0.18 for PMN and 0.06 for PZT. Thus, we can conclude that PMN exhibits higher hysteretic losses than PZT.

When the stacks were placed inside the pump and tested, the Galfenol stack failed to move the output cylinder shaft. Considering the low free strain shown by Galfenol, the lack of sufficient volumetric displacement of fluid to overcome the internal friction in the actuator could be a possible reason. This becomes evident from Figure B.7. In this experiment, Terfenol-D was placed inside the pump and actuated by providing varying values of current to the coil. The output velocity was measured for progressively decreasing values of coil current. As the coil current decreases, the magnetic field applied to the stack decreases and induced strain decreases. This causes a decrease in the no-load output velocity. The applied magnetic field is decreased till the output cylinder shaft just tends to move. At this value of magnetic field, the stack produces just enough volumetric displacement in the hydraulic fluid to overcome the various internal frictions in the actuator. Consequently, magnetic fields below this value fail to produce any motion in the output cylinder shaft. Figure B.7 shows that when the magnetic field applied to the Terfenol-D stack was decreased to give a strain of 400μs, the actuator does not produce any output motion. Thus, we can conclude that the Galfenol stack, which gives a maximum free strain of 300μs, does not produce sufficient volumetric displacement in the fluid chamber to produce output motion in the particular actuator design that was used in this study. As a result, Galfenol was not tested further in this study. However, Galfenol would be a promising and feasible material for an actuation system with lower internal friction. The non-linear nature of the trend in Figure B.7 is due to the coulomb damping in the output cylinder shaft and piston. The effect of this frictional force becomes a more significant part of the total force as the forcing from the active element is reduced.

B.4.3 Load Tests

Load tests were performed to ascertain the capability of different active materials to do useful work. In these tests, graduated weights are hung from the output cylinder shaft. When the active material was actuated, the output cylinder shaft lifted the weight, thus performing useful work. The output power of the actuator system can be calculated by multiplying the load by the shaft velocity. As the output load increases, the actuator reaches the block force limitations of the active material stack. The blocking load of the actuator system depends on the block force of the active material stack and the ratio of the cross-sectional areas of the output cylinder piston to that of the pumping chamber. The information gained from the relationship between output velocity and output load can be used to plot load lines at particular pumping frequencies.

Figure 4.5 shows a typical load line curve for an active material driven actuator.

A load line is drawn at a particular pumping frequency and plots the variation of output velocity with the load. For pumping frequencies below the fluid resonance point, load lines are typically linear. This is due to the fact that the load line of the actuator bears a close relationship with the static load line of the active material, which is typically linear. Point A represents the blocked force of the actuator while point B denotes free displacement in the absence of load. The line OD denotes the stiffness of all the elements of the actuator, namely that of the hydraulic fluid, active material stack, accumulator and the piston diaphragm. The intersection point D marks the static equilibrium point for the whole system. As the voltage to the active material is varied, the load line shifts upwards, while remaining parallel to the original load line and the equilibrium point shifts along the line OD. In a loaded operation, energy is transferred from the active element to the load and is shown in Figure 4.5 as OCDEO, and the work done by the active material every cycle is the area shown in the shaded region. Thus, the maximum work obtainable from the actuator at a particular pumping frequency can be obtained by calculating half of the area under the load line OABO. This method can been used to compare the output power of the stacks. Experimentally obtained load lines for PMN, PZT and Terfenol-D stacks are shown in Figure B.8(a), (b) and (c). These plots were obtained by actuating the active material at a particular frequency and changing the load on the output cylinder shaft. The measured output velocity is then plotted against the load to obtain the load line at that particular pumping frequency. We can infer from these figures that the blocking force of the PMN is highest among the three active materials considered. The blocking load of the PMN-based actuator 13 lbs, while the blocking load of the PZT-based actuator was the least among the three active materials at 7 lbs. The Terfenol-D based actuator showed a blocking load of around 10 lbs.

As explained in the previous paragraph, the maximum output power of the actuation system can be obtained from load lines by calculating one half of the area under the load line. A comparison of output power gives us a comparison of capacity of different actuators to do useful work. These power output values are plotted against pumping frequency in Figure B.9. We see from the figure that PMN and Terfenol-D stacks have a maximum output power of around 2.5W. We see that the maximum output power occurs at different pumping frequencies. Maximum power output is obtained at the resonant frequency of the actuator system. The resonant frequency of the actuator system depends on the stiffness of the active material stack, the dynamics of the hydraulic fluid lines in the system and the load. Since the stiffness varied among different stacks tested in this study, the resonant frequencies are also different.

As the pumping frequency increased, the force exerted by the fluid on the stack also increased. This is due to higher inertial and damping forces of the fluid. The PMN and Terfenol-D stacks were able to sustain substantial stack displacement even at higher pumping frequencies owing to their greater stack stiffness, thus exhibiting greater power output. Since the PZT stack is softer when compared with PMN and Terfenol-D stacks, it was not able to sustain the strain levels measured under quasi-steady conditions. The output power capability of the PZT stack was therefore lower than the other stacks at around 0.5W at an pumping frequency of 700Hz.

B.4.4 Overall electromechanical efficiency

Overall electromechanical efficiency defines the ratio of the amount of useful mechanical energy obtained from the actuation system to the electrical energy put into the active material stack. The input work is measured in terms of apparent power, which is defined as the product of the R.M.S values of voltage and current drawn by the active material stack. The power drawn by electro-active materials depends on the stack capacitance. Thus, the PZT stack requires greater input power than PMN for a given voltage, owing to its higher capacitance. The electrical power consumed by the magnetostrictive stacks is determined by the electric impedance of the coils. This electrical impedance appears as a predominantly inductive component from the coils and a resistance of the metallic wire used in the coil. Due to the large inductive component of the impedance, larger voltages are required to produce the same magnetic field over the active material at higher frequencies (since magnetic field produced by the coil is proportional to the current in the coil). This results in power losses as a result of ohmic heating in the coils. The resistance of the coils also changes with temperature, thus altering the electrical impedance. Another major cause of power losses in magnetic circuits, in addition to ohmic losses, is eddy currents. As a result of alternating magnetic induction and a conducting magnetic flux return path, eddy current loops are generated. The formation of such loops cause power losses due to ohmic heating in the flux return paths. In the actuator used in this study, the pumping body, made of steel, was used as the magnetic flux return path and hence, forms an ideal conducting path for eddy currents. To prevent the effect of such current loops, a narrow slit was machined lengthwise in the pump body. This prevents the formation of such loops to a large extent and mitigates losses due to ohmic heating.

The current and voltage across the active material is recorded during load tests. This enables us to calculate the input power to the material. These experimental results obtained are shown in Figure B.10. The PMN stack was tested up to a maximum pumping frequency of 500Hz to maintain the integrity of the stack (as recommended by TRS Ceramics Inc.). We see that at 200 Hz pumping frequency, the PMN based actuator is five times as efficient as the PZT based actuator and seven times more efficient than the Terfenol-D based actuator. Though the PMN stack exhibits greater hysteretic losses than PZT, it is much more electromechanically efficient due to its lower power consumption.

B.5 Conclusions

The goal of this study was to compare the actuator properties of two kinds of active materials - electro-active (PMN and PZT) and magneto-active(Terfenol-D and Galfenol) materials for our hydraulic hybrid actuator configuration. The materials were tested as active elements in a hybrid hydraulic actuator developed at the University of Maryland and their performance was evaluated in terms of metrics like static displacement, no-load velocity, output power and electromechanical efficiency. Since most of the applications of such hydraulic hybrid actuators involve overall geometrical constraints, the overall length of the active material as well as the whole actuator system was held constant in all four cases.

The maximum static displacement obtained from the PMN stacks was around 100μm (350V). The free displacement of PMN was much higher than was obtained from PZT, Terfenol-D or Galfenol stacks. Greater free displacement results in greater volumetric displacement of fluid in the pump and this manifests as a higher no-load velocity. The maximum no-load velocity obtained with PMN stacks was 270mm/s (at 400 Hz pumping frequency) while the PZT and Terfenol stacks generated a maximum no-load velocity of 75mm/s (at 600Hz pumping frequency) and 250mm/s (at 600Hz pumping frequency). The Galfenol stack failed to provide any output motion in the actuator system used for this study. This was due to the fact that the free strain capability of Galfenol was insufficient to overcome the internal frictional and stiffness losses in the actuator system.

The measured blocked force for the PMN actuator was around 13 lbs (57.8N), the PZT actuator was 7.5 lbs (62.3N) and Terfenol-D actuator was 10 lbs. The stiffness of the stack greatly influenced the blocked force of the actuator. Though the stiffness value of the PZT stack that was provided by the manufacturer is higher than PMN, the presence of insulating layers in the stack decreased its overall stiffness, thus making the blocked force much lower than that of a PMN based actuator. From tests under load, output power and overall system efficiency was determined. The maximum power output from the PMN actuator was around 2.5W at 400Hz, the PZT actuator generated almost 0.5W at 700Hz pumping frequency and Terfenol-D generated 2.5W at 600Hz pumping frequency. However, the PMN actuator generated this power at a far greater efficiency than the PZT or Terfenol-D based actuator. The overall electromechanical efficiency of the PMN actuator was around 7% at 200Hz pumping frequency while the PZT and Terfenol-D based actuators were only 2.5 % and 0.5 % efficient. Although the output power from the different materials was not very different, the low input power required for the PMN based actuator improved its efficiency. Thus, PMN shows superior performance in terms of output power and overall electromechanical efficiency. A comparison of the major

Table B.1: Manufacturer supplied Material Properties

Parameter	**PZT**	**PMN**	**Terfenol-D**	**Galfenol**
Length(mm)	54	59	54.8	54.8
Cross-sectional area(mm^2)	25	24	31	31
Free strain(μs)	1600	2000	1000	300
Field required for Max.strain	120V	500V	80kA/m	25 kA/m
Young's modulus(GPa)	70	20	35-50	20-25
Stiffness of stack(MN/m)	20	8.1	28.3	14.2
Blocked force(N)	1700	900	1550	310
Capacitance(μF)	5.4	0.37	-	-
Magnetic permeability	-	-	3-10	300
Robustness	robust	brittle	brittle	machinable

performance results are listed in Table B.3.

Table B.2: Pump Properties

Pump Body Assembly	
Pump body diameter(mm,in)	35.6, 1.4 O.D, 25.4, 1 I.D
Pump body length(mm,in)	50.8, 2
Piston diaphragm thickness(mm,in)	0.05, 0.002
Pumping chamber diameter (mm,in)	25.4, 1
Pumping chamber height (mm,in)	0.76, 0.030
Valve Assembly	
Valve plate thickness(mm,in)	5.1, 0.2
Reed valve thickness(mm,in)	0.051, 0.002
Hydraulic circuit	
Accumulator gas volume(mm^3,in^3)	1638.7, 0.1
Output cylinder bore(mm,in)	11.1, 7/16
Output shaft diameter(mm,in)	1.58, 3/16
Output cylinder stroke(mm,in)	50.8, 2
Coil Parameters	
Wire gauge	20
Wire diameter(mm,in)	0.02, 0.00081
Coil length(mm,in)	50.8, 2
Coil diameter(mm,in)	22.86, 0.9
Total mass(g)	113
DC resistance(Ω)	1.2
Inductance(mH)	2.1

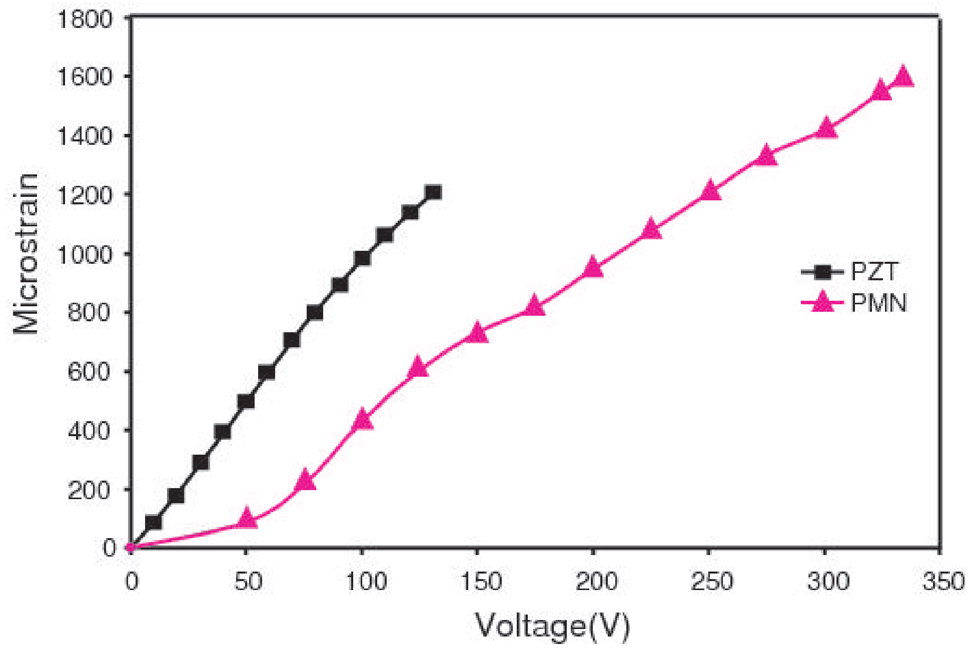

(a) Electro-active stacks

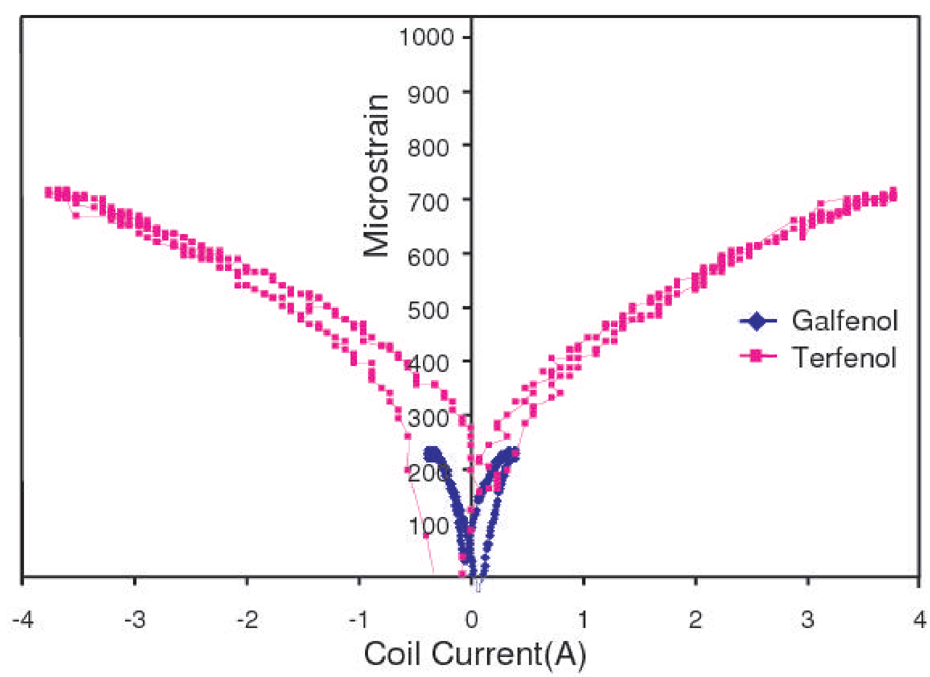

(b) Magneto-active stacks

Figure B.1: This figure shows the static relationship between strain in the material and applied excitation field

Table B.3: Performance Results

Parameter	PZT	PMN	Terfenol-D	Galfenol
Blocked force(N,lbs)	33.7, 7.5	57.8, 13	44.5, 10	-
Max. no load velocity(mm/s)	75	270	250	-
Max. output power(W)	0.5	2.5	2.5	-
Max. efficiency(%)	2.5	7	0.5	-
Mass of active material(g)	13.6	16.8	14.8	11.2
Mass of coil(g)	NA	NA	113	113

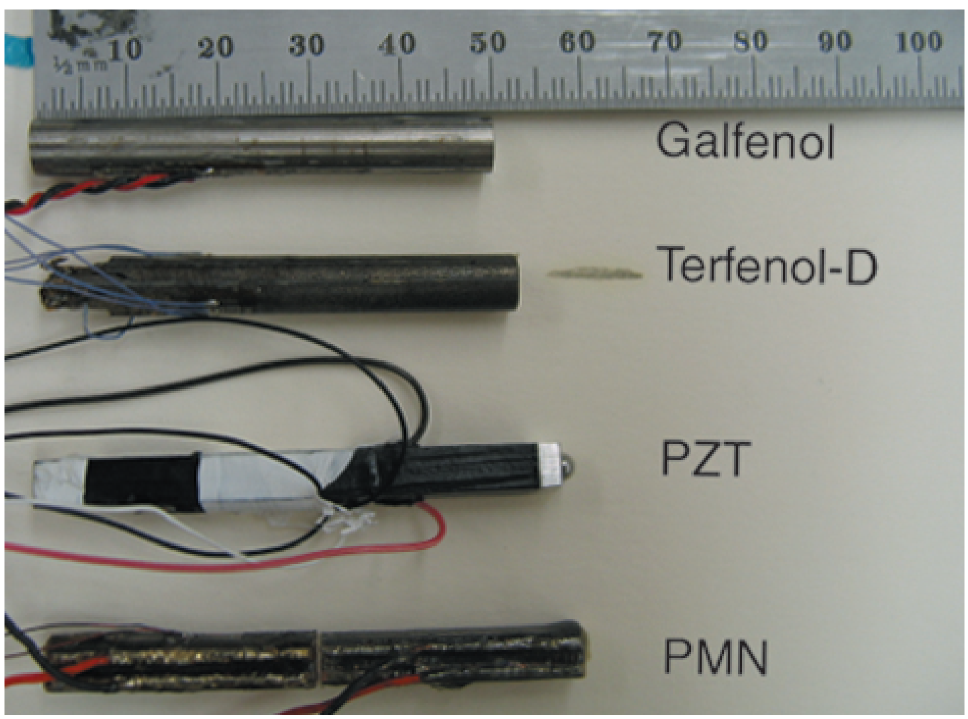

Figure B.2: Picture of the four active material stacks used in this study.

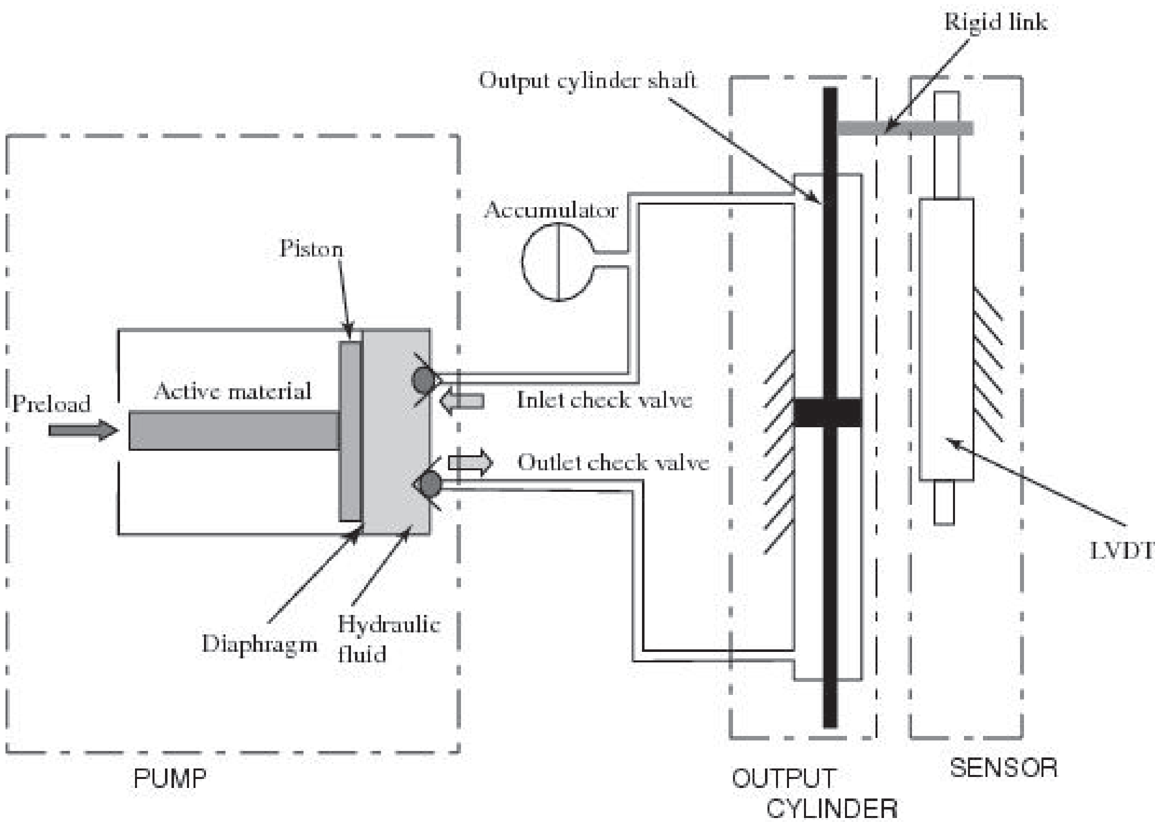

Figure B.3: Schematic diagram of the components of the hybrid hydraulic actuator

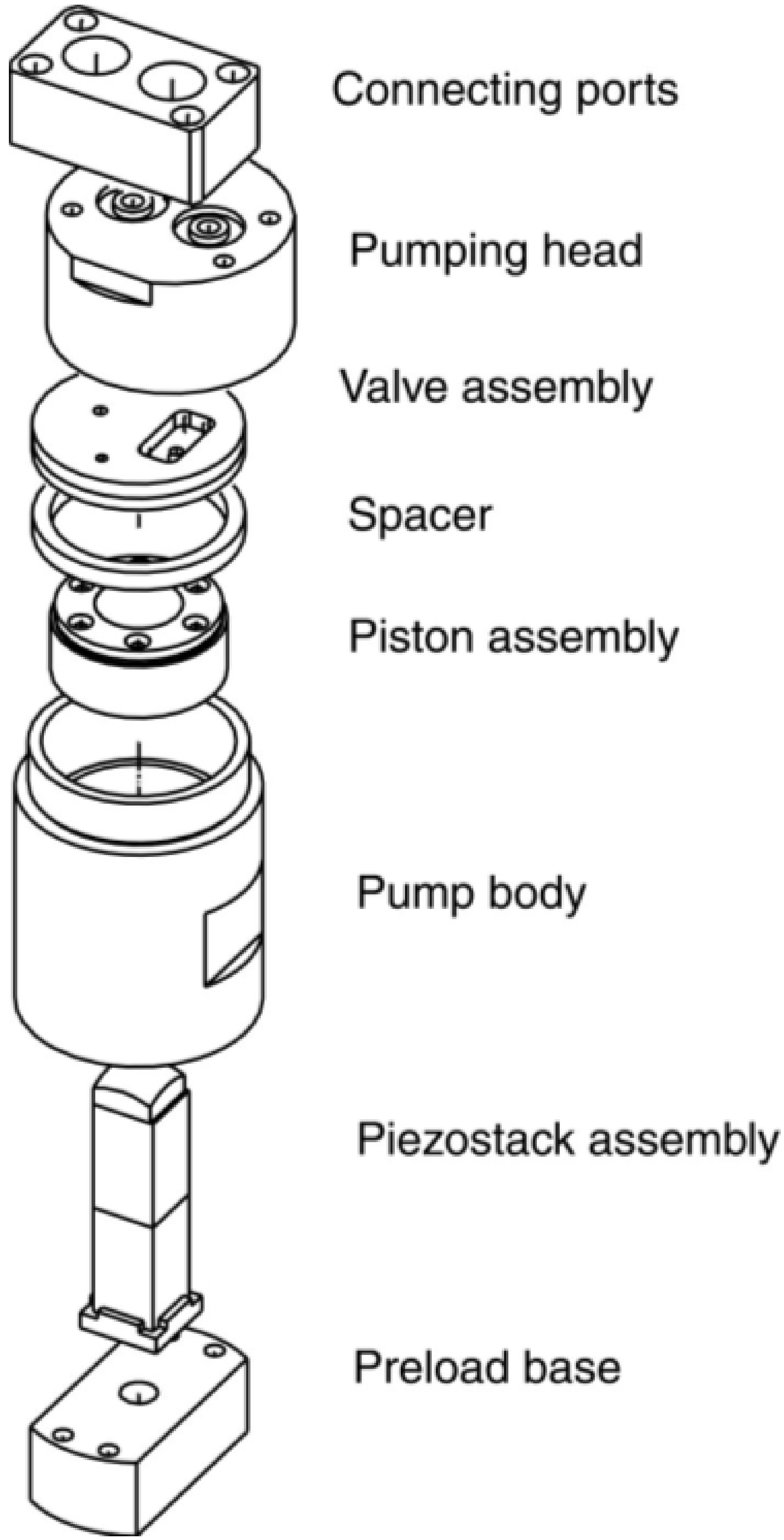

Figure B.4: Isometric view of the prototype hybrid actuator

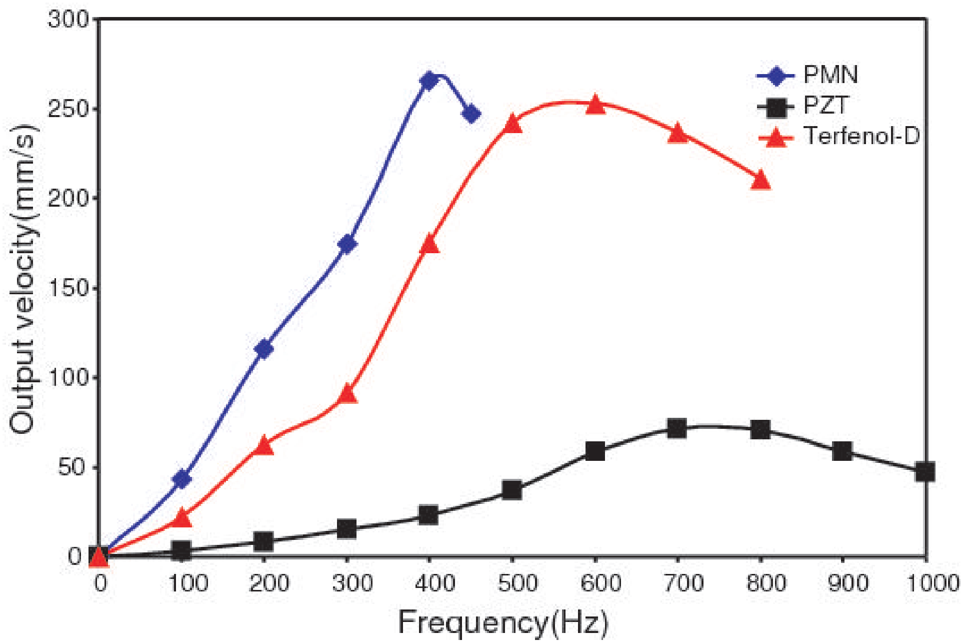

Figure B.5: Comparison of no-load output velocity for PMN, PZT and Terfenol-D stacks as a function of pumping frequency

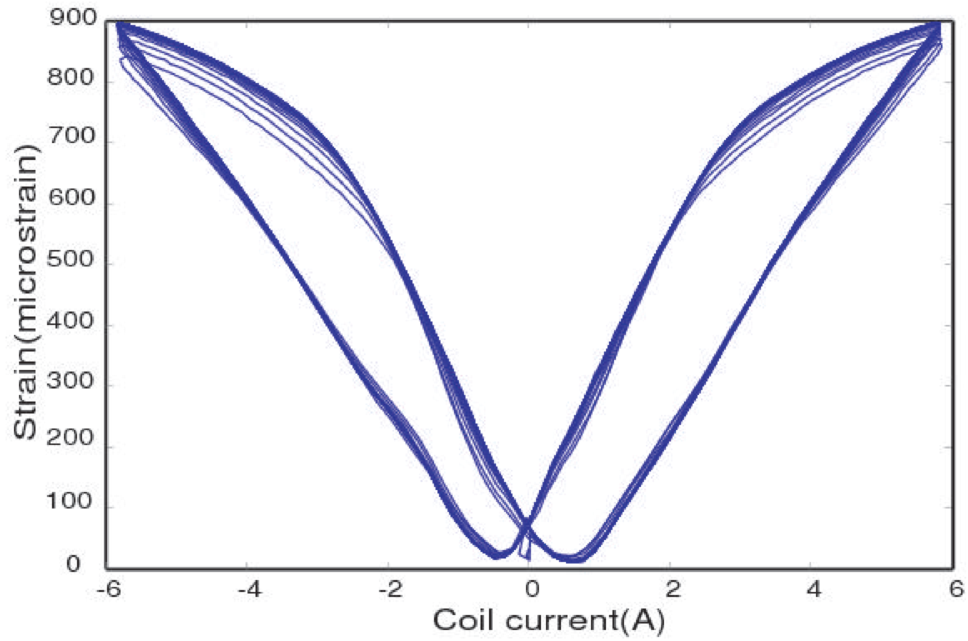

(a) Magneto-active stacks

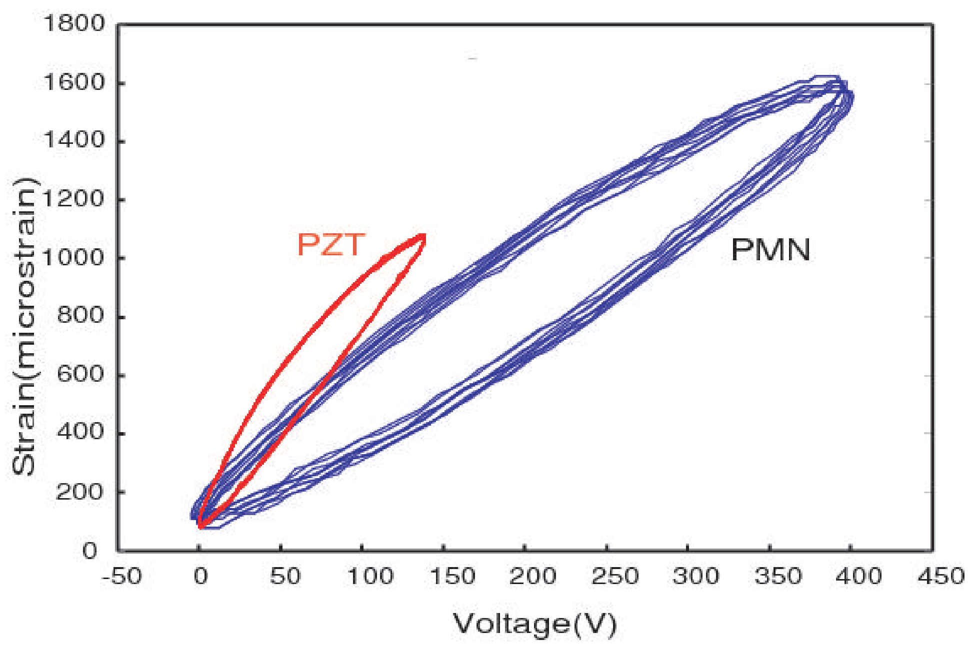

(b) Electro-active stacks

Figure B.6: This figure shows hysteresis loops obtained for Terfenol-D, PMN and PZT stacks when driven at an pumping frequency of 100Hz

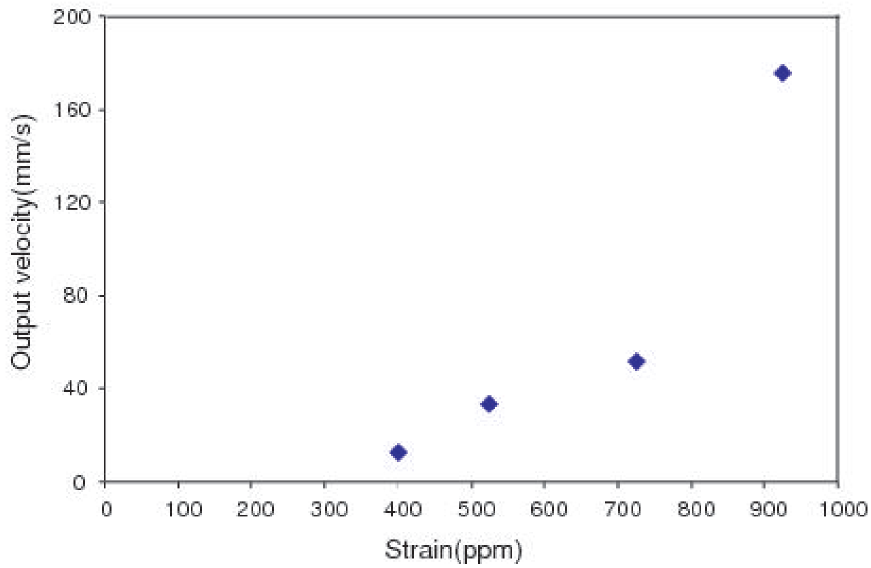

Figure B.7: This figure shows the results of output velocity versus the strain generated in a Terfenol-D stack.

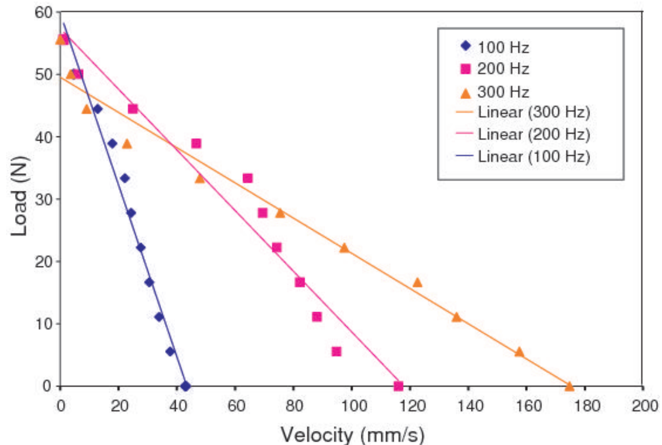

(a) Load line for PMN

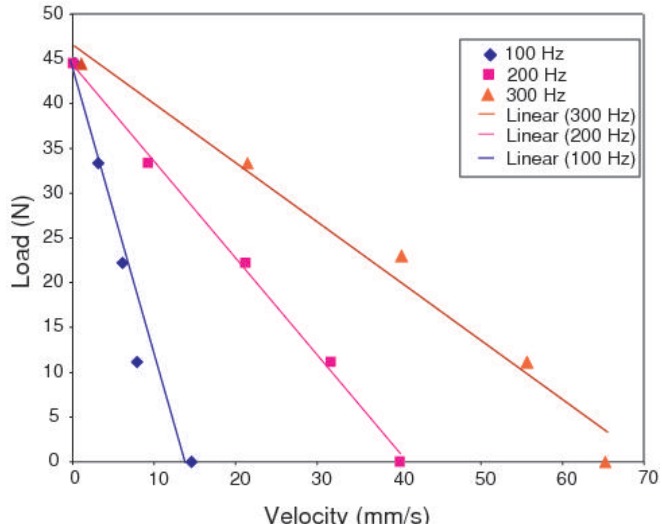

(b) Load line for PZT

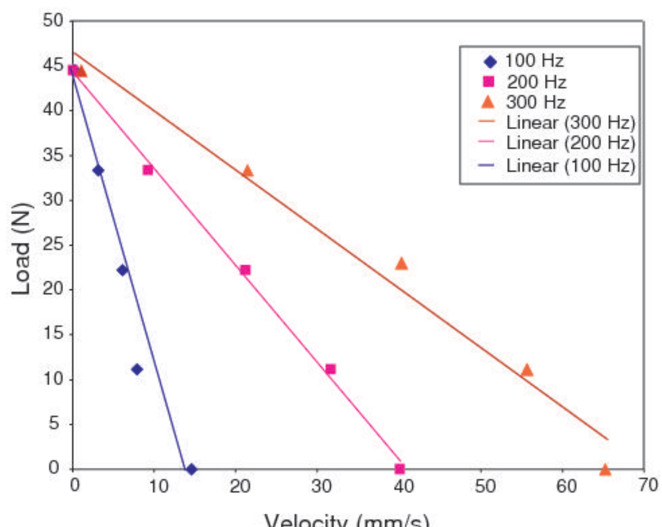

(c) Load line for Terfenol-D

Figure B.8: Load lines for electro-active and magneto-active stacks as a function of pumping frequency(100, 200, 300Hz).

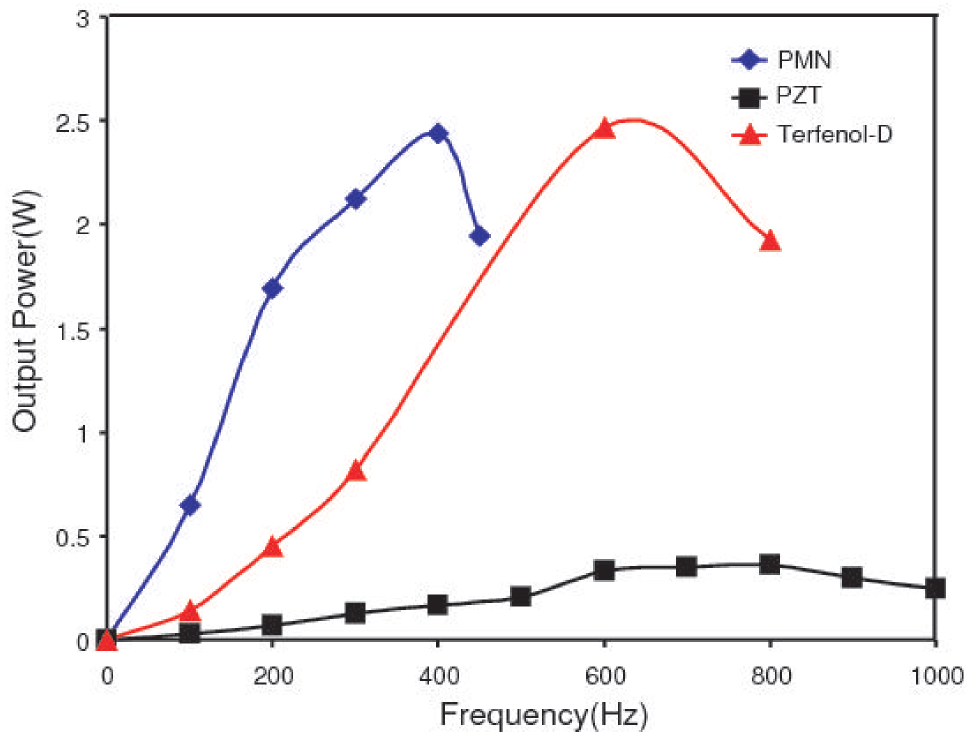

Figure B.9: Comparison of measured output power from the actuator driven by PMN, PZT and Terfenol-D as a function of pumping frequency.

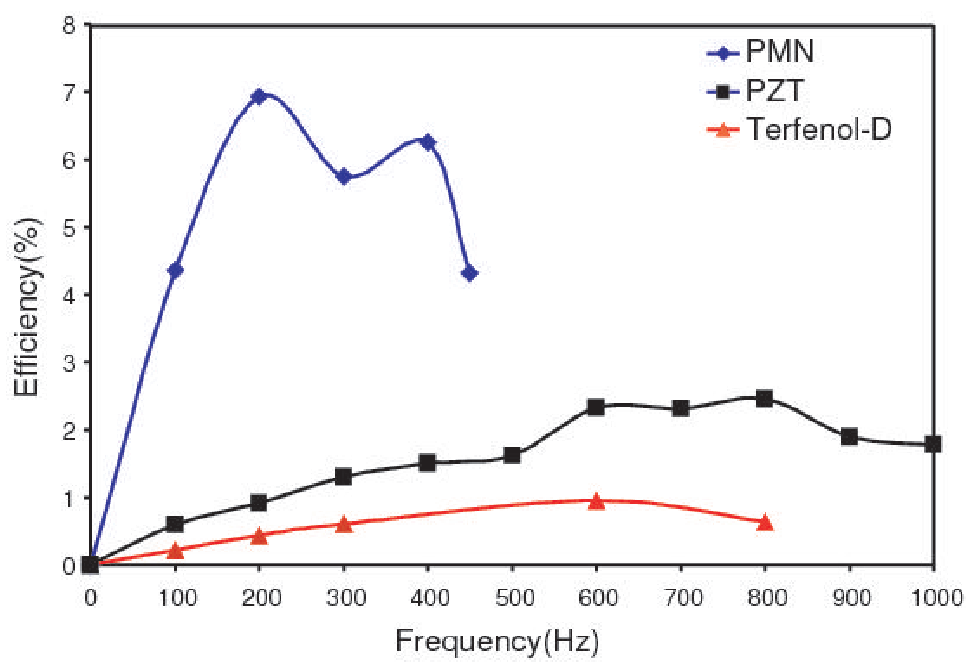

Figure B.10: Comparison of electromechanical efficiency of the hybrid actuator with PMN, PZT and Terfenol-D as a function of pumping frequency.

Appendix C

A Unifying Perspective on the Quasi-Steady Analysis of Magnetorheological Dampers

Abstract

An MR fluid, modeled as a Bingham-plastic material, is characterized by a field dependent yield stress, and a (nearly constant) postyield plastic viscosity. Based on viscometric measurements, such a Bingham-plastic model is an idealization to physical magnetorheological behavior, albeit a useful one. A better approximation involves modifying both the preyield and postyield constitutive behavior as follows: (1) assume a high viscosity preyield behavior when the shear stress is less than the transition stress, and (2) assume a power law fluid (i.e., strain rate dependent viscosity) when the shear stress is greater than the transition stress. Assuming a power law fluid in postyield allows the model to account for shear thinning behavior exhibited by MR fluid at higher strain rates. Such an idealization for MR fluid constitutive behavior is called a viscous-power law model, or a Herschel-Bulkley model with preyield viscosity. This study develops a quasi-steady analysis for such a constitutive MR fluid behavior applied to a magnetorheological (MR) flow mode damper. Closed form solutions are developed for the fluid velocity, as well as key performance metrics such as damping capacity and dynamic range (ratio of field on to field off force). For given fluid properties and flow mode damper geometry, the fluid velocity profile and gradient, and the relationship of the damper force and piston velocity are analyzed. Also, specializations to existing models such as the Herschel-Bulkley, Biviscous, and Bingham-plastic models, are shown to be easily captured by this model when physical constraints (idealizations) are placed on the rheological behavior of the MR fluid.

C.1 Introduction

Magnetorheological (MR) or Electrorheological (ER) fluids present a significant increase in yield stress when magnetic or electric field is applied. The field-dependent yield stress of MR or ER fluids can be effectively utilized in semi-active damping control systems. Semi-active devices utilizing MR or ER fluids have the advantages of continuously controllable damping, quiet operation, simple configuration, low power consumption, and high control stability (Stanway et al., 1996; Carlson et al., 1996). An important characteristic of MR and ER dampers is their rapid response times, which are nominally less than 10 ms, in response to step changes in field (Choi and Wereley, 2002; Koo et al, 2006). Such response enable effective control systems for numerous applications (Ahmadian et al 2006). MR and ER fluids can be effectively utilized in shock absorbers for vehicle or train suspensions (Lee and Choi, 2000; Lam and Liao, 2003; Liao and Wang, 2003; Sims and Stanway, 2003; Karakas et al., 2004), isolation systems (Choi, Wereley and Jeon, 2005), seismic dampers for building and civil structures (Dyke et al, 1996; Yi et al., 2001; Hiemenz, Choi and Wereley, 2003, Xu and Guo, 2006), impact dampers for recoil systems (Ahmadian and Poyner, 2001; Facey et al., 2003; Facey et al., 2005), mounts for flexible structural systems (Hong et al., 2002; Hong and Choi, 2005), and helicopter lag dampers (Kamath, Wereley and Jolly, 1999; Marathe, Gandhi and Wang, 1998, Hu et al, 2007). A common requirement for all of these applications is the need to design or size the MR or ER device given the required force-stroke profile. Quasi-steady models provide such an analytical design tool.

MR or ER dampers have been designed on the basis of four operation modes of the fluids: shear mode (Couette flow) (Stanway et al., 1996; Wereley and Pang, 1998), flow mode or Poiseuille flow (Stanway et al., 1996; Gavin et al., 1996a, 1996b; Peel et al., 1996; Wereley and Pang, 1998; Lindler and Wereley, 1999; Hong et al., 2003), squeeze (squeeze-flow) mode (Stanway et al., 1996; Jolly and Carlson, 1996; Sims et al., 2001, Ai et al, 2006), and mixed mode (combined Poiseuille and Couette flow) (Yang et al., 2002). Shear mode dampers have two moving surfaces (magnetic poles or electrodes) where one of the surfaces can translate or rotate relative to the other, and develops damping forces via shear resistance of the fluids. Flow mode dampers are designed by exploiting Poiseuille flow through fixed surfaces (or a valve), and develop damping force via pressure drop of the fluid as it flows through the valve. Mixed mode dampers combine flow and shear mode operations, and develop the damping force from pressure drop through the valve, as well as by direct shearing of the fluid. In squeeze mode dampers, the gap distance between the two surfaces varies and the fluid filled in the gap is squeezed by a normal force, and the damping force is developed via flow resistance of the fluid. From a practical design perspective, flow or mixed mode dampers can be designed with smaller surface area than shear mode damper cases. Moreover, application of squeeze mode dampers appears to be limited to systems subjected to small magnitude vibrations (low stroke) in order to avoid contact of the two plates. Thus, most MR or ER dampers have been developed on the basis of flow or mixed mode operations, so that high force and long stroke can be realized.

The rheological behavior of MR or ER fluids has been typically treated as Bingham plastic material in steady fully developed laminar flow (Stanway et al., 1996; Wereley and Pang, 1998). For a Bingham plastic fluid, shearing motion cannot occur in the preyield condition, defined as the condition where the applied shear stress is less than the dynamic yield stress, because the fluid is assumed to be rigid. In the postyield condition, defined as the condition where the shear stress exceeds the dynamic yield stress, shearing motion can occur. In the postyield condition, the shear stress is proportional to the shear strain, and the slope of the stress versus strain curve, or postyield viscosity, of the Bingham plastic fluid is assumed to be constant.

Because of its simplicity and usefulness, the Bingham plastic model has been widely used to describe MR or ER fluid behavior in dampers. Phillips (1969) developed a nondimensional analysis for the flow and mixed mode operation of the fluids based on Bingham plastic flow, which was refined by Gavin et al. (1996a, 1996b). Stanway et al. (1996) and Peel et al. (1996) studied an alternative nondimensional analysis for flow mode dampers utilizing the friction coefficient, the Reynolds number, and the Hedström number. Wereley and Pang (1998) presented a nondimensional analysis for flow and mixed mode dampers utilizing the Bingham number, the nondimensional plug thickness, and the equivalent viscous damping coefficients (dynamic range). Solution procedures for the above nondimensional analyses result in a polynomial root finding problem for determining the pressure drop in the MR or ER valves. Hong et al. (2003) developed a nondimensional design scheme for flow mode dampers utilizing nondimensional design variables of the Bingham number, the nondimensional geometric parameter, the nondimensional damping force, and the dynamic range.

Based on viscometric measurements of MR or ER fluids (e.g. Chaudhuri et al, 2006), a refined approximation involves modifying both the preyield and postyield constitutive behavior of the Bingham plastic model as follows: (1) assume a high viscosity preyield behavior when the shear stress is less than the yield stress similar to a biviscous model (Stanway et al., 1996; Wereley et al., 2004; Williams et al., 1993), and (2) assume a power law fluid (i.e., variable viscosity) when the shear stress is greater than the yield stress so that the model can account for high shear rate shear thinning behavior similar to a Herschel Bulkley model (Wolf-Jesse and Fees, 1998; Wang and Gordaninejad, 1999; Lee and Wereley, 1999). In this work, viscosity is defined as the instantaneous time rate of change of shear stress over shear rate. Shear thinning and shear thickening can be seen in Figure C2. Even though the results shown in this paper pertain only to shear thinning, the model can be extended to cases of shear thickening as well. Prior work (Wereley, 2003) presented a nondimensional analysis based on the Herschel-Bulkley model for flow mode dampers utilizing nondimensional variables as those used for the Bingham plastic analysis (Wereley and Pang, 1998), with the addition of the flow index. Here, the flow index is a measure of the shear thinning or thickening behavior of the fluid. The Herschel-Bulkley analysis can better describe MR or ER damper behavior in the high shear rate condition by introducing the flow index. Wang and Gordaninejad (1999) also developed a dimensional form of the damper force model utilizing a Herschel-Bulkley model, and their model validation demonstrated that the flow index is useful to predict the damper force behavior in the high velocity condition. Williams et al. (1993) presented a nondimensional analysis scheme based on the biviscous model for the disc type squeeze-flow damper. This nondimensional model consists of the dimensionless pressure gradient, the dimensionless radius, and the ratio of the postyield viscosity to the preyield viscosity. Wereley et al. (2004) studied a biviscous damping behavior of flow mode dampers utilizing the same three nondimensional variables (Wereley and Pang, 1998) as used for the Bingham plastic analysis, with the addition of the ratio of the postyield viscosity to the preyield viscosity. The biviscous behavior of the damper in the low velocity condition was favorably described by the nondimensional analysis model.

In this study, quasi-steady analysis is undertaken for a flow mode MR damper based on a viscous Herschel-Bulkley model, that is preyield viscosity, coupled with a postyield viscous-power law model. The proposed nondimensional analysis model accounts for both a preyield viscosity when shear stress is less than the transition stress, and a power law postyield viscosity when the shear stress is above the transition stress of the MR fluids. Five nondimensional parameters are required for the analysis: the Bingham number, the nondimensional preyield region thickness, the equivalent damping coefficient, the flow index, and the stress coefficient are utilized for the analysis. Here, the flow index and the stress coefficient are introduced to account for the Herschel-Bulkley behavior in the postyield condition and the biviscous behavior in the preyield condition, respectively. The influences of the flow index and the stress coefficient on the Bingham number, the nondimensional preyield thickness, and the equivalent damping coefficient are analytically investigated. The fluid velocity profile and its gradient across the valve, and the relationship of the damper force and the piston velocity, are also analyzed. Specializations of the proposed model to existing models such as the Herschel-Bulkley (HB), Biviscous (BV), and Bingham-plastic models (BP) are presented.

C.2 Nondimensional Modeling

C.2.1 Flow Mode Damper

Flow mode MR dampers are basically designed by utilizing an MR valve, a hydraulic cylinder, and a piston/rod assembly. The MR valve normally consists of two concentric tubular magnetic poles, that form the annulus through which the MR fluid flows. Figure C1 shows a typical MR damper that has an MR valve inside the piston head. The MR fluid fills a hydraulic cylinder and annular gap, and the electromagnetic coil is used to provide a magnetic field to the MR fluid. The MR fluid flows from one chamber, through the MR valve, and into the chamber on the opposite side of the piston as a result of piston motion. Thus, the pressure drop due to the flow resistance of the MR fluid in the gap can be obtained. If no magnetic field is applied, the MR damper only produces a force exerted by the flow resistance associated with the viscosity of the MR fluid. However, if the MR fluid is activated by the magnetic field, the MR damper produces a controllable damping force due to the yield stress of the MR fluid.

C.2.2 Governing Equation

To simplify the analysis, the 1D axisymmetric annular duct geometry of the MR valve will be approximated as a rectangular duct. If the annular gap is small relative to the annular radius, then the error associated with hydrodynamic analysis is small (Wereley and Pang, 1998; Gavin et al., 1996a). Therefore, we adopt the simple rectangular duct analysis and develop physical and analytical insight into flow mode damper behavior. Approximating the 1D axisymmetric annular duct geometry by a rectangular duct, then the governing equation obtained from force equilibrium simplifies to

$$\frac{d\tau}{dy} = -\frac{\Delta P}{L} \tag{1}$$

Here, τ is the shear stress, y is the coordinate measured from the center of the valve to the wall of the valve, L is the length of the valve, ΔP is the pressure drop from the flow inlet to the flow outlet of the valve, and $\Delta P = F / A_p$ where F is the damper force and A_p is the piston head area.

C.2.3 Constitutive Model

Constitutive models, such as the Bingham-plastic (BP) model, Herschel-Bulkley (HB) model, biviscous (BV) model, which have been used to describe rheological behaviors of MR or ER fluids, are schematically presented in Figure C2 in terms of their shear stress vs. shear rate (flow curve) diagram. The BP model is characterized by a dynamic yield stress and postyield viscosity and represented. The constitutive shear flow relationship for the Bingham-plastic model is expressed as (Wereley and Pang, 1998)

$$\tau = \tau_y \operatorname{sgn}\left(\dot{\gamma}\right) + \mu_{po}\dot{\gamma} \tag{2}$$

Here, τ_y is dynamic yield stress, μ_{po} is postyield viscosity, $\dot{\gamma}$ is shear rate. In the preyield condition, $|\tau| < \tau_y$, the fluid does not shear (i.e., zero shear rate, $\dot{\gamma}=0$) because the shear stress of the fluid is less than the dynamic yield stress. In the postyield condition, the shear stress exceeds the dynamic yield stress, $|\tau| > \tau_y$, so that the fluid begins to shear flow, or the shear rate is greater than zero, or $\dot{\gamma}>0$. The postyield viscosity of the BP model is assumed to be independent of the shear rate.

The Herschel-Bulkley (HB) model is characterized by a power law fluid above the dynamic yield stress. The constitutive shear flow relationship for the HB model is expressed as (Skelland, 1967)

$$\tau = \left[\tau_y + \kappa \left|\dot{\gamma}\right|^n\right] \mathrm{sgn}\left(\dot{\gamma}\right) \tag{3}$$

Here, κ is consistency (a parameter analogous to viscosity), and n is the flow index. For the case where $n=1$, (1) the consistency, κ, specializes to the postyield viscosity, μ_{po}, of the BP model, and (2) the postyield behavior of the HB model specializes to the BP model. The preyield behavior of the HB and BP models are identical. Both models induce plug flow in the case of Poiseuille flow, where the plug is a semi-solid of unyielded material across which the shear rate is zero.

The HB model is a general approach to the analysis of postyield behavior of MR or ER fluid flow. Depending on the flow index, n, the model can account for postyield shear thinning or thickening as below:

(1) $n>1$: dilatant or shear thickening behavior

(2) $0<n<1$: pseudoplastic or shear thinning behavior

(3) $n=1$: Bingham-plastic behavior

The biviscous (BV) model is characterized by a high viscosity preyield behavior over a low strain range and a low viscosity postyield behavior over a high strain range. The transition from the preyield to the postyield condition occurs once the shear stress exceeds a transition stress. The constitutive shear flow relationship for the biviscous model is expressed as (Stanway et al., 1996)

$$\tau = \begin{cases} \tau_y \operatorname{sgn}\left(\dot{\gamma}\right) + \mu_{po}\,\gamma & for \quad |\tau| > \tau_t \quad or \left|\dot{\gamma}\right| > \gamma_t \\ \mu_{po}\,\dot{\gamma} & for \quad |\tau| \le \tau_t \quad or \left|\dot{\gamma}\right| \le \gamma_t \end{cases} \tag{4}$$

Here, τ_t is the static yield stress or transition stress, $\dot{\gamma}_t$ is the transition shear rate, and μ_{pr} is the preyield plastic viscosity. In this model, the material is assumed to have high viscosity when the local shear stress is less than the static yield stress, or $|\tau| < \tau_t$ or the preyield condition. The dynamic yield stress, τ_y, and the transition stress, τ_t, are different quantities and have the relationship below

$$\bar{\tau} = \frac{\tau_y}{\tau_t} = 1 - \bar{\mu} \tag{5}$$

Here, $\bar{\tau}$ is the stress coefficient and defined by the ratio of the dynamic yield stress to the transition stress. $\bar{\mu}(= \mu_{po}/\mu_{pr})$ is the viscosity coefficient and defined by the ratio of the postyield viscosity to the preyield viscosity (Wereley et al., 2004). For the case where $\bar{\tau} = 1$ or $\bar{\mu} = 0$, the preyield viscosity approaches infinity or the dynamic yield stress equals the transition stress, and the preyield behavior of the BV model reduces to that of the BP model.

The BV model is a general approach to the analysis of preyield viscous behavior in MR fluid flow. Depending on the viscosity or stress coefficients, $\bar{\mu}$ or $\bar{\tau}$, the model can account for different preyield behaviors as below:

(1) $0 < \bar{\tau} = 1 - \bar{\mu} < 1$: biviscous behavior

(2) $\bar{\tau} = 1 - \bar{\mu} = 1$: Bingham-plastic behavior

The Herschel-Bulkley model with preyield viscosity, represented in Figure C2, is obtained by modifying both the preyield and postyield constitutive behaviors as follows: (1) assume a high viscosity preyield behavior when the shear stress is less than the transition stress, and (2) assume a power law fluid when the shear stress is above the transition stress that accounts for the shear thickening or thinning behaviors exhibited by MR fluids in postyield. This idealization to the MR fluid's constitutive behavior is a viscous-power law model, or a Herschel-Bulkley model with preyield viscosity (HBPV). The constitutive equation of the HBPV model is expressed by

$$\tau = \begin{cases} \left[\tau_y + \kappa \left|\dot{\gamma}\right|^n\right] \operatorname{sgn}\left(\dot{\gamma}\right) & for \quad |\tau| > \tau_t \quad or \left|\dot{\gamma}\right| > \gamma_t \\ \mu_{pr}\, \dot{\gamma} & for \quad |\tau| \le \tau_t \quad or \left|\dot{\gamma}\right| \le \gamma_t \end{cases} \tag{6}$$

The Herschel-Bulkley model with preyield viscosity generalizes the rheological behaviors of the MR fluid in both the preyield and postyield regions as follows

(1) $n > 1$ and $0 < \bar{\tau} < 1$: shear thickening behavior with preyield viscosity

(2) 0< $n < 1$ and $0 < \bar{\tau} < 1$: shear thinning behavior with preyield viscosity

(3) $n = 1$ and $0 < \bar{\tau} < 1$: biviscous behavior

(4) $n > 1$ and $\bar{\tau} = 1$: shear thickening behavior

(5) $n < 1$ and $\bar{\tau} = 1$: shear thinning behavior

(6) $n = 1$ and $\bar{\tau} = 1$: Bingham-plastic behavior

The relationship between the dynamic yield stress and the transition stress of the HBPV model with preyield viscosity can be expressed as

$$\bar{\tau} = \frac{\tau_y}{\tau_t} = \frac{\tau_t - \kappa \dot{\gamma}_t^{\,n}}{\tau_t} = 1 - \frac{\kappa \dot{\gamma}_t^{\,n}}{\mu_{pr}\dot{\gamma}_t} \tag{7}$$

For the case where $n = 1$, the stress coefficient of the HBPV model in Equation (7), reduces to that for the BV model in Equation (5).

C.2.4 Preyield Region

A schematic of the velocity profile, velocity gradient, and shear stress profile for the HBPV model in the valve annulus is shown in Figure C3. It is assumed that the pressure is applied to the left side of the valve, producing a velocity profile that moves to the right. There are three distinct flow regions. Region 1 and region 3, which adjacent to the valve walls, are postyield regions where $|\tau| > \tau_t$, while region 2 is the central preyield region where $|\tau| < \tau_t$. The velocity profile is symmetrical about the horizontal centerline of the valve because it was assumed that (1) the pressure is uniform perpendicular to the flow direction or the pressure is uniform across the gap, and (2) cylindrical or 1D axisymmetric duct geometry may be approximated by rectangular duct geometry.

The shear stress constitutive equations for each region are

$$\begin{aligned} \tau_1(y) &= \tau_y + \kappa \dot{\gamma}^{\,n} \\ \tau_2(y) &= \mu_{pr}\dot{\gamma} \\ \tau_3(y) &= -\tau_y - \kappa\left(-\dot{\gamma}\right)^n \end{aligned} \tag{8}$$

The width of the preyield region, or the preyield thickness, δ, can be determined from Equation (1) and the shear stress boundary conditions. Using symmetry condition for the rectangular duct geometry, the preyield region is located symmetrically about the flow velocity axis or u axis. Integrating Equation (1) yields the shear stress in the gap as below:

$$\tau = -\frac{\Delta P}{L} y + C \tag{9}$$

Here, C is integration constant to be determined using the shear stress boundary conditions:

$$\tau\left(-\frac{\delta}{2}\right) = \tau_t \text{ and } \tau\left(\frac{\delta}{2}\right) = -\tau_t \tag{10}$$

which yield the system of equations below:

$$\begin{aligned} \tau_t &= \frac{\Delta P}{L}\frac{\delta}{2} + C \\ -\tau_t &= -\frac{\Delta P}{L}\frac{\delta}{2} + C \end{aligned} \tag{11}$$

Adding the two equations shows that $C = 0$. Thus,

$$\tau(y) = -\frac{\Delta P}{L} y \tag{12}$$

Subtracting the two equations yield an expression for the nondimensional preyield thickness, $\bar{\delta}$, which is the ratio of the preyield thickness, δ, to the gap, d, so that

$$\bar{\delta} = \frac{\delta}{d} = \frac{2L\tau_t}{\Delta P d} \tag{13}$$

As applied field increases, it follows that the transition stress and the preyield thickness also increase.

C.2.5 Velocity Gradient and Velocity Profile

Since three distinct regions exist, fluid velocity profiles of each region need to be considered separately. The velocity profile in the ith region is denoted as $u_i(y)$. The velocity profile must satisfy the boundary conditions and compatibility conditions. No slip boundary conditions at the upper and lower walls of the gap are assumed, so that

$$u_3\left(\frac{d}{2}\right)=0$$
$$u_1\left(-\frac{d}{2}\right)=0 \tag{14}$$

The velocity compatibility conditions are

$$u_1\left(-\frac{\delta}{2}\right)=u_2\left(-\frac{\delta}{2}\right)$$
$$u_3\left(\frac{\delta}{2}\right)=u_2\left(\frac{\delta}{2}\right) \tag{15}$$

The velocity gradient compatibility conditions are

$$u_1'\left(-\frac{\delta}{2}\right)=u_2'\left(-\frac{\delta}{2}\right)$$
$$u_3'\left(\frac{\delta}{2}\right)=u_2'\left(\frac{\delta}{2}\right) \tag{16}$$

Substituting for the constitutive relationship, Equation (8), of each region, into the force equilibrium equation of Equation (1) and rearranging yields the velocity gradient for each region:

$$u_1'(y)=\left(\frac{C_1}{\kappa}-\frac{\Delta P}{\kappa L}y\right)^{\frac{1}{n}}$$
$$u_2'(y)=-\frac{\Delta P}{\mu_{pr}L}y+\frac{C_2}{\mu_{pr}} \tag{17}$$
$$u_3'(y)=-\left(-\frac{C_3}{\kappa}+\frac{\Delta P}{\kappa L}y\right)^{\frac{1}{n}}$$

Here, C_1, C_2, and C_3 are integration constants. Integrating the velocity gradients yield the velocity profiles across each region:

$$u_1(y) = -\frac{n}{n+1}\left(\frac{\Delta P}{\kappa L}\right)^{-1}\left(\frac{C_1}{\kappa} - \frac{\Delta P}{\kappa L}y\right)^{\frac{n+1}{n}} + D_1$$

$$u_2(y) = -\frac{1}{2}\frac{\Delta P}{\mu_{pr}L}y^2 + \frac{C_2}{\mu_{pr}}y + D_2 \qquad (18)$$

$$u_3(y) = -\frac{n}{n+1}\left(\frac{\Delta P}{\kappa L}\right)^{-1}\left(-\frac{C_3}{\kappa} + \frac{\Delta P}{\kappa L}y\right)^{\frac{n+1}{n}} + D_3$$

Here, D_1, D_2, and D_3 are integration constants. The integration constants are obtained by satisfying the boundary conditions and compatibility conditions of Equations (14-16). The resulting velocity gradients are expressed as

$$u_1'(y) = \left(\frac{\Delta P}{\kappa L}\right)^{\frac{1}{n}}\left[-\left(\frac{\delta}{2} + y\right) + \left(\frac{\Delta P}{\kappa L}\right)^{-1}\left(\frac{\Delta P}{\mu_{pr}L}\right)^{n}\left(\frac{\delta}{2}\right)^{n}\right]^{\frac{1}{n}}$$

$$u_2'(y) = -\left(\frac{\Delta P}{\kappa L}\right)\left(\frac{k}{\mu_{pr}}\right)y \qquad (19)$$

$$u_3'(y) = -\left(\frac{\Delta P}{\kappa L}\right)^{\frac{1}{n}}\left[-\left(\frac{\delta}{2} - y\right) + \left(\frac{\Delta P}{\kappa L}\right)^{-1}\left(\frac{\Delta P}{\mu_{pr}L}\right)^{n}\left(\frac{\delta}{2}\right)^{n}\right]^{\frac{1}{n}}$$

The velocity profile is expressed as

$$u_1(y) = \frac{n}{n+1}\left(\frac{\Delta P}{\kappa L}\right)^{\frac{1}{n}}\left\{\left[-\left(\frac{\delta}{2} - \frac{d}{2}\right) + \left(\frac{\Delta P}{\kappa L}\right)^{-1}\left(\frac{\Delta P}{\mu_{pr}L}\right)^{n}\left(\frac{\delta}{2}\right)^{n}\right]^{\frac{n+1}{n}} - \left[-\left(\frac{\delta}{2} + y\right) + \left(\frac{\Delta P}{\kappa L}\right)^{-1}\left(\frac{\Delta P}{\mu_{pr}L}\right)^{n}\left(\frac{\delta}{2}\right)^{n}\right]^{\frac{n+1}{n}}\right\}$$

$$u_2(y) = \frac{1}{2}\left(\frac{\Delta P}{\kappa L}\right)\left(\frac{\kappa}{\mu_{pr}}\right)\left[\left(\frac{\delta}{2}\right)^2 - y^2\right]$$
$$+ \frac{n}{n+1}\left(\frac{\Delta P}{\kappa L}\right)^{\frac{1}{n}}\left\{\left[-\left(\frac{\delta}{2} - \frac{d}{2}\right) + \left(\frac{\Delta P}{\kappa L}\right)^{-1}\left(\frac{\Delta P}{\mu_{pr}L}\right)^{n}\left(\frac{\delta}{2}\right)^{n}\right]^{\frac{n+1}{n}} - \left[\left(\frac{\Delta P}{\kappa L}\right)^{-1}\left(\frac{\Delta P}{\mu_{pr}L}\right)^{n}\left(\frac{\delta}{2}\right)^{n}\right]^{\frac{n+1}{n}}\right\}$$

$$u_3(y)=\frac{n}{n+1}\left(\frac{\Delta P}{\kappa L}\right)^{\frac{1}{n}}\left\{\left[-\left(\frac{\delta}{2}-\frac{d}{2}\right)+\left(\frac{\Delta P}{\kappa L}\right)^{-1}\left(\frac{\Delta P}{\mu_{pr}L}\right)^{n}\left(\frac{\delta}{2}\right)^{n}\right]^{\frac{n+1}{n}}-\left[-\left(\frac{\delta}{2}-y\right)+\left(\frac{\Delta P}{\kappa L}\right)^{-1}\left(\frac{\Delta P}{\mu_{pr}L}\right)^{n}\left(\frac{\delta}{2}\right)^{n}\right]^{\frac{n+1}{n}}\right\}$$

(20)

A convenient nondimensional form of velocity gradient and velocity profile of Equations (19) and (20) can be obtained by defining following:

$$\bar{y}=\frac{y}{d} \tag{21}$$

$$\bar{u}'=u'\left[\left(\frac{\Delta P}{\kappa L}\right)^{\frac{1}{n}}\left(\frac{d}{2}\right)^{\frac{1}{n}}\right]^{-1} \tag{22}$$

$$\bar{u}=u\left[\frac{n}{n+1}\left(\frac{\Delta P}{\kappa L}\right)^{n}\left(\frac{d}{2}\right)^{\frac{n+1}{n}}\right]^{-1} \tag{23}$$

Here, $\bar{y}$ is nondimensional gap coordinate and $\bar{u}$ is nondimensional velocity profile. Furthermore, the term $(\Delta P/\kappa L)^{-1}(\Delta P/\mu_{pr}L)^{n}(\delta/2)^{n}$ in Equations (19) and (20) is expressed as a function of the stress coefficient and preyield thickness by considering the Equations (7) and (13) as below:

$$\begin{aligned}\left(\frac{\Delta P}{\kappa L}\right)^{-1}\left(\frac{\Delta P}{\mu_{pr}L}\right)^{n}\left(\frac{\delta}{2}\right)^{n}&=\left(\frac{\tau_t}{\kappa\delta}\right)^{-1}\left(\frac{\tau_t}{\mu_{pr}\delta}\right)^{n}\left(\frac{\delta}{2}\right)^{n}=\left(\frac{\tau_t}{\kappa}\right)^{-1}\left(\frac{\tau_t}{\mu_{pr}}\right)^{n}\left(\frac{\delta}{2}\right)\\&=\left(\frac{\kappa}{\mu_{pr}}\right)\left(\frac{\dot{\gamma}^{n}}{\dot{\gamma}}\right)\left(\frac{\delta}{2}\right)=\left(\frac{\kappa}{\mu_{pr}}\right)\left(\frac{\tau_t}{\mu_{pr}}\right)^{-1}\left(\frac{\tau_t}{\mu_{pr}}\right)^{n}\left(\frac{\delta}{2}\right)\\&=\left(1-\frac{\tau_y}{\tau_t}\right)\left(\frac{\delta}{2}\right)=(1-\bar{\tau})\left(\frac{\delta}{2}\right)\end{aligned} \tag{24}$$

Rearranging Equation (19) with the consideration of Equations (21), (22), and (24) yields the nondimensional velocity gradient:

$$\bar{u}_1{}' = \left[-2\bar{y} - \bar{\tau}\bar{\delta}\right]^{\frac{1}{n}}$$
$$\bar{u}_2{}' = -2\left(\frac{\bar{y}}{\bar{\delta}}\right)\left[(1-\bar{\tau})\bar{\delta}\right]^{\frac{1}{n}} \tag{25}$$
$$\bar{u}_3{}' = -\left[2\bar{y} - \bar{\tau}\bar{\delta}\right]^{\frac{1}{n}}$$

Rearranging equation (20) with the consideration of equations (21), (23), and (24) yield the nondimensional velocity profile:

$$\bar{u}_1 = \left[1 - \bar{\tau}\bar{\delta}\right]^{\frac{n+1}{n}} - \left[-2\bar{y} - \bar{\tau}\bar{\delta}\right]^{\frac{n+1}{n}}$$
$$\bar{u}_2 = \frac{1}{2}\frac{n+1}{n}\left[(1-\bar{\tau})\bar{\delta}\right]^{\frac{1}{n}}\left(\bar{\delta} - 4\frac{\bar{y}^2}{\bar{\delta}}\right) - \left[1 - \bar{\tau}\bar{\delta}\right]^{\frac{n+1}{n}} - \left[(1-\bar{\tau})\bar{\delta}\right]^{\frac{n+1}{n}} \tag{26}$$
$$\bar{u}_3 = \left[1 - \bar{\tau}\bar{\delta}\right]^{\frac{n+1}{n}} - \left[2\bar{y} - \bar{\tau}\bar{\delta}\right]^{\frac{n+1}{n}}$$

Given the nondimensional preyield thickness $\bar{\delta}$, flow index, n, and stress coefficient, $\bar{\tau}$, the nondimensional velocity gradient and velocity profile across the valve can be calculated.

C.2.6 Volume Flux

The volume flux of the fluid in the annulus, Q_d, is the sum of volume flux in each region of the annulus and is expressed by

$$Q_d = 2Q_1 + Q_2 = 2b\int_{-d/2}^{-\delta/2} u_1(y)dy + b\int_{-\delta/2}^{\delta/2} u_2(y)dy$$
$$= -2b\frac{n}{n+1}\frac{n}{2n+1}\left(\frac{\Delta P}{\kappa L}\right)^{\frac{1}{n}}\left[-\left(\frac{\delta}{2} - \frac{d}{2}\right) + \left(\frac{\Delta P}{\kappa L}\right)^{-1}\left(\frac{\Delta P}{\mu_{pr}L}\right)^{n}\left(\frac{\delta}{2}\right)^{n}\right]^{\frac{2n+1}{n}}$$

$$+2b\frac{n}{n+1}\frac{n}{2n+1}\left(\frac{\Delta P}{\kappa L}\right)^{\frac{1}{n}}\left[\left(\frac{\Delta P}{\kappa L}\right)^{-1}\left(\frac{\Delta P}{\mu_{pr}L}\right)^{n}\left(\frac{\delta}{2}\right)^{n}\right]^{\frac{2n+1}{n}}$$

$$+2b\frac{n}{n+1}\left(\frac{\Delta P}{\kappa L}\right)^{\frac{1}{n}}\left[-\left(\frac{\delta}{2}-\frac{d}{2}\right)+\left(\frac{\Delta P}{\kappa L}\right)^{-1}\left(\frac{\Delta P}{\mu_{pr}L}\right)^{n}\left(\frac{\delta}{2}\right)^{n}\right]^{\frac{n+1}{n}}\frac{d}{2} \tag{27}$$

$$+\frac{2}{3}b\left(\frac{\Delta P}{\kappa L}\right)^{\frac{1}{n}}\left[\left(\frac{\Delta P}{\kappa L}\right)^{-1}\left(\frac{\Delta P}{\mu_{pr}L}\right)^{n}\left(\frac{\delta}{2}\right)^{n}\right]^{\frac{1}{n}}\left(\frac{\delta}{2}\right)^{2}$$

$$-b\frac{n}{n+1}\left(\frac{\Delta P}{\kappa L}\right)^{\frac{1}{n}}\left[\left(\frac{\Delta P}{\kappa L}\right)^{-1}\left(\frac{\Delta P}{\mu_{pr}L}\right)^{n}\left(\frac{\delta}{2}\right)^{n}\right]^{\frac{n+1}{n}}\delta$$

Here, b is the annulus or gap width. Substituting Equation (24) into Equation (27), and rearranging Equation (27) yields the concise form of volume flux through the valve:

$$Q_d=\frac{bdn}{2n+1}\left(\frac{\Delta P}{\kappa L}\right)^{\frac{1}{n}}\left(\frac{d}{2}\right)^{\frac{n+1}{n}}\left\{-\frac{n}{n+1}\left[1-\overline{\tau}\overline{\delta}\right]^{\frac{2n+1}{n}}+\frac{n}{n+1}\left[(1-\overline{\tau})\overline{\delta}\right]^{\frac{2n+1}{n}}+\frac{2n+1}{n+1}\left[1-\overline{\tau}\overline{\delta}\right]^{\frac{n+1}{n}}\right.$$
$$\left.+\frac{2n+1}{3n}\left[(1-\overline{\tau})\overline{\delta}\right]^{\frac{1}{n}}\overline{\delta}^{2}-\frac{2n+1}{n+1}\left[(1-\overline{\tau})\overline{\delta}\right]^{\frac{n+1}{n}}\overline{\delta}\right\} \tag{28}$$

C.2.7 Equivalent Damping

By equating volume flux through the valve annulus, Q_d, to the volume flux displaced by the piston, $Q_p = A_p v_p$, the damper force can be determined in terms of the piston velocity. v_p is the piston velocity. From $Q_d = Q_p$, the pressure drop, ΔP, is obtained as

$$\Delta P=\frac{\kappa L\left(\frac{2n+1}{bdn}\right)^{n}\left(\frac{2A_p}{d}\right)^{n+1}\frac{v_p^n}{A_p}}{\left[-\frac{n}{n+1}\left[\left(1-\overline{\tau}\overline{\delta}\right)^{\frac{2n+1}{n}}-\left((1-\overline{\tau})\overline{\delta}\right)^{\frac{2n+1}{n}}\right]+\frac{2n+1}{n+1}\left[\left(1-\overline{\tau}\overline{\delta}\right)^{\frac{n+1}{n}}-\left((1-\overline{\tau})\overline{\delta}\right)^{\frac{n+1}{n}}\overline{\delta}\right]+\frac{2n+1}{3n}\left((1-\overline{\tau})\overline{\delta}\right)^{\frac{1}{n}}\overline{\delta}^{2}\right]^{n}} \tag{29}$$

Noting that $F = \Delta P A_p$, yields an expression for the damper force as a function of the velocity, as below:

$$F = C_{eq} v_p \tag{30}$$

where

$$C_{eq} = \frac{\kappa L \left(\frac{2n+1}{bdn}\right)^n \left(\frac{2A_p}{d}\right)^{n+1} v_p^{n-1}}{\left[-\frac{n}{n+1}\left[(1-\bar{\tau}\bar{\delta})^{\frac{2n+1}{n}} - ((1-\bar{\tau})\bar{\delta})^{\frac{2n+1}{n}}\right] + \frac{2n+1}{n+1}\left[(1-\bar{\tau}\bar{\delta})^{\frac{n+1}{n}} - ((1-\bar{\tau})\bar{\delta})^{\frac{n+1}{n}}\bar{\delta}\right] + \frac{2n+1}{3n}((1-\bar{\tau})\bar{\delta})^{\frac{1}{n}}\bar{\delta}^2\right]^n} \tag{31}$$

The equivalent viscous damping, C_{eq}, is a measure of the field dependent damping or controllable damping. The damper force in the absence of field is $F_0 = C_0 v_p$, which that implied that $\bar{\delta} = 0$, so that where

$$C_0 = \kappa L \left(\frac{2n+1}{bdn}\right)^n \left(\frac{2A_p}{d}\right)^{n+1} v_p^{n-1} \tag{32}$$

It is noted that the damping coefficient in the absence of field, or $\bar{\delta} = 0$, does not contain the stress coefficient, $\bar{\tau}$. An expression for the damping coefficient, or the ratio of the field dependent damping, C_{eq}, to the damping in the absence of field, C_0, as below:

$$\frac{C_{eq}}{C_0} = \frac{1}{\left[-\frac{n}{n+1}\left[(1-\bar{\tau}\bar{\delta})^{\frac{2n+1}{n}} - ((1-\bar{\tau})\bar{\delta})^{\frac{2n+1}{n}}\right] + \frac{2n+1}{n+1}\left[(1-\bar{\tau}\bar{\delta})^{\frac{n+1}{n}} - ((1-\bar{\tau})\bar{\delta})^{\frac{n+1}{n}}\bar{\delta}\right] + \frac{2n+1}{3n}((1-\bar{\tau})\bar{\delta})^{\frac{1}{n}}\bar{\delta}^2\right]^n} \tag{33}$$

Note that the equivalent damping coefficient, C_{eq}/C_0, of Equation (33) is the principal nondimensional representation of the MR damper characteristics with respect to the Herschel-Bulkley behavior with preyield viscosity for a flow mode MR damper. The equivalent damping coefficient, C_{eq}/C_0, can be evaluated by the three nondimensional parameters of the nondimensional preyield thickness, $\bar{\delta}$, flow index, n, and stress coefficient, $\bar{\tau}$. The postyield and preyield characteristics of the fluid are accounted into the equivalent damping coefficient, C_{eq}/C_0, by the flow index, n, and the stress coefficient $\bar{\tau}$, respectively. The nondimensional preyield thickness, $\bar{\delta}$, is a key parameter to describe the action of the MR valve. As such, the preyield thickness, $\bar{\delta}$, is proportional to the transition stress, which is in turn a function of the applied field. For small values of preyield thickness, $\bar{\delta}$, the equivalent damping coefficient, C_{eq}/C_0, is close to one, meaning that the flow across the gap behaves according to the fluid's postyield properties and indicating that the damper has virtually no controllable damping. As the preyield thickness, $\bar{\delta}$, increases, the preyield region is manifested across the center of the gap, where the flow behaves according to the fluid's preyield characteristics such as high viscosity flow or semi solid plug flow. Then the equivalent damping coefficient, C_{eq}/C_0, also increases.

C.2.8 Preyield Thickness Polynomial and Bingham Number

Based on the flow rate continuity, the piston velocity can be expressed by

$$v_p = \frac{A_d}{A_p} v_d \tag{34}$$

Here, $A_d (= bd)$ is the cross-sectional area of the MR valve annulus gap, v_d is the average fluid velocity in the valve gap. From Equation (13), the damper force, F, can be expressed as

$$F = \Delta P A_p = \frac{2L\tau_t A_p}{\bar{\delta} d} \tag{35}$$

Substituting Equations (34) and (35) into Equation (30), and rearranging Equation (30) yields a characteristic polynomial for the nondimensional preyield thickness as below:

$$\Lambda(\bar{\delta}) = \left[-\frac{n}{n+1}\left[\left(1-\bar{\tau}\bar{\delta}\right)^{\frac{2n+1}{n}} - \left(\left(1-\bar{\tau}\right)\bar{\delta}\right)^{\frac{2n+1}{n}} \right] + \frac{2n+1}{n+1}\left[\left(1-\bar{\tau}\bar{\delta}\right)^{\frac{n+1}{n}} - \left(\left(1-\bar{\tau}\right)\bar{\delta}\right)^{\frac{n+1}{n}}\bar{\delta} \right] + \frac{1}{3}\frac{2n+1}{n}\left(\left(1-\bar{\tau}\right)\bar{\delta}\right)^{\frac{1}{n}}\bar{\delta}^2 \right]^n - \left[\frac{2(2n+1)}{n}\right]^n \frac{\bar{\tau}\bar{\delta}}{\mathrm{Bi}(n)} = 0 \tag{36}$$

The generalized Bingham number, $\mathrm{Bi}(n)$, is defined as the ratio of the dynamic yield stress to the viscous shear stress (Prager, 1961; Wereley, 2003), or

$$\mathrm{Bi}(n) = \frac{\tau_y}{\kappa\left(v_d/d\right)^n} = \frac{\tau_y}{\mu_{eq} v_d/d} \tag{37}$$

where

$$\mu_{eq} = \kappa\left(\frac{v_d}{d}\right)^{n-1} \tag{38}$$

Here, μ_{eq} is the equivalent (linearized) viscosity. The Bingham number, $\mathrm{Bi}(n)$, is large when the yield stress, τ_y, is high, or the equivalent viscosity, μ_{eq}, and the piston velocity, v_d, are low. The large Bingham number, $\mathrm{Bi}(n)$, implies that the damper operates close to a preyield condition and the preyield thickness is large. The small Bingham number, $\mathrm{Bi}(n)$, implies that the damper operates in a strongly post-yield condition and the preyield thickness is small. The nondimensional preyield thickness, $\bar{\delta}$, can be determined as the root of $\Lambda(\bar{\delta}) = 0$ in its domain $0 < \bar{\delta} < 1$ for given the flow index, n, the generalized Bingham number, $\mathrm{Bi}(n)$, and the stress coefficient, $\bar{\tau}$, Then, the equivalent damping coefficient, C_{eq}/C_0, can be calculated from Equation (33) by using the nondimensional preyield thickness, $\bar{\delta}$.

Specializations of nondimensional analysis models, for Herschel-Bulkley model with preyield viscosity, to existing models such as the Herschel-Bulkley, the Biviscous, and the Bingham-plastic models, are summarized in the Appendix. Thus, the existing models are easily captured by the proposed analysis model when physical constraints (idealizations) are placed on the rheological behavior of the MR fluid.

C.3 Analysis Results

C.3.1 Equivalent Damping Coefficient vs. Nondimensional Preyield Thickness

Figure C4 represents the relationship between the equivalent damping coefficient, C_{eq}/C_0, and the nondimensional preyield thickness, $\bar{\delta}$, with the influence the stress coefficient, $\bar{\tau}$, and flow index, n, obtained by using Equation (33). Figure C4 (a) shows the case where $\bar{\tau}=1$ with variation of the flow index. This is the Herschel- Bulkley (HB) model case (Wereley, 2003). The nondimensional preyield thickness ranges from zero to one, and the equivalent damping coefficient ranges from one to infinity. For $\bar{\delta}=0$, the flow through the MR valve is zero field flow. Thus, the damper behaves as a passive viscous damper. For $\bar{\delta}=1$, the plug is fully developed inside the gap and the flow does not occur. Thus, the damping coefficient approaches to infinity. The curve of $n=1$ corresponds to the Bingham plastic (BP) case or linear postyield damping. For $n<1$, or shear thinning, the equivalent damping coefficient is below the Bingham plastic case. It is noted that most of MR fluids show the shear thinning behaviors. As the flow index, n, further decreases, the equivalent damping coefficient also further falls below. For $n>1$, or shear thickening, the equivalent damping coefficient is above the Bingham plastic case.

Figure C4 (b) shows the case of $n=1$, or of linear postyield damping, with variation of the stress coefficient. This is the biviscous (BV) model case (Wereley et al., 2004). The curve of $\bar{\tau}=1$ corresponds to the Bingham plastic (BP) model case or preyield viscosity of infinity. As the stress coefficient decreases, that is the preyield viscosity decreases, the equivalent damping coefficient also decreases. For $\bar{\delta}=1$, the flow in the gap is Newtonian or high viscosity flow of preyield condition. Thus, in contrast to the Herschel-Bulkley or Bingham plastic models where the damping approaches infinity as the nondimensional preyield thickness close to one, the equivalent damping coefficient of biviscous model approaches to a finite value as below:

$$\lim_{\bar{\delta}\to 1}\left(\frac{C_{eq}}{C_0}\right)_{BV} = \frac{1}{1-\bar{\tau}} \qquad (39)$$

Figure C4 (c) and (d) show the cases of $n = 0.9$ and 0.8, or the power-law postyield viscosity, with variation of the stress coefficient. As the stress coefficient decreases, the damping coefficient decreases for given flow index and preyield thickness. As the flow behavior decreases, the damping coefficient falls below for given stress coefficient and preyield thickness. Thus, for $\bar{\tau} < 1$ and $0 < \bar{\delta} < 1$, both the high viscosity in the preyield region and the power-law viscosity in the postyield region can be accounted into the equivalent damping coefficient at the same time. As the nondimensional preyield thickness approaches to one, the equivalent damping coefficient of Herschel-Bulkley model with preyield viscosity approaches to a finite value as below:

$$\lim_{\bar{\delta} \to 1} \left(\frac{C_{eq}}{C_0} \right)_{HBPV} = \frac{1}{\left[\frac{1}{3} \frac{2n+1}{n} (1 - \bar{\tau})^{\frac{1}{n}} \right]^n} \tag{40}$$

As it can be seen from Figure C4, as the flow index decreases, the equivalent damping coefficient falls below, and as the stress coefficient decreases, the equivalent damping coefficient decreases. Both the flow index and the stress coefficient have effects on the equivalent damping coefficient for given the nondimensional preyield thickness.

C.3.2 Nondimensional Preyield Thickness vs. Bingham Number

Figure C5 represents the relationship between the nondimensional preyield thickness, $\bar{\delta}$, and the Bingham number, $\mathrm{Bi}(n)$, with the influence of the stress coefficient, $\bar{\tau}$, and flow index, n, obtained by using equation (36). The curves in Figure C5 are the solution of the nondimensional preyield thickness polynomial (36). Figure C5 (a) shows the case of $\bar{\tau} = 1$ with the variation of the flow index, or the Herschel- Bulkley model case (Wereley, 2003). For the case of $\mathrm{Bi}(n) = 0$, the flow through the MR valve is zero field flow, and corresponding nondimensional preyield thickness is zero. As the Bingham number increases, the nondimensional preyield thickness also increases. This implies that as the ratio of the yield stress over the viscous shear stress increases, the extent of plug flow in the valve will grow. By increasing the Bingham number, a high nondimensional preyield thickness can be obtained and approaches to one. Consequently, the equivalent damping coefficient approaches to infinity as shown in Figure C4 (a). The curve of $n=1$ corresponds to the Bingham plastic case. For $n<1$, or shear thinning, the postyield viscosity of the fluid is smaller than the case of $n=1$ in entire shear rate range. Thus, the plug or preyield flow can be easily developed and the nondimensional preyield thickness is above the Bingham plastic case. As the flow index further decreases, the nondimensional preyield thickness further falls above. For $n>1$, or shear thickening, the equivalent damping coefficient falls above the Bingham plastic case.

Figure C5 (b) shows the case of $n=1$, the biviscous model case (Wereley et al., 2004). The curve of $\bar{\tau}=1$ corresponds to the Bingham plastic model case. As the stress coefficient decreases, the nondimensional preyield thickness increases for a given Bingham number. In other words, the preyield region of the biviscous model grows easily when the stress coefficient, or the preyield viscosity is low. The range of the Bingham number corresponding to $\bar{\delta}=1$ for the biviscous model is expressed by

$$\bar{\delta}=1, \text{ for } \mathrm{Bi} \geq \frac{6\bar{\tau}}{1-\bar{\tau}} \tag{41}$$

Figure C5 (c) and (d) show the cases of $n=0.9$ and 0.8, or Herschel- Bulkley model with preyield viscosity. As the stress coefficient decreases, the nondimensional preyield thickness increases for given flow index and Bingham number. As the flow behavior decreases, the nondimensional preyield thickness falls above for given stress coefficient and Bingham number. Thus, the relationship between the nondimensional preyield thickness and the Bingham number of the Herschel-Bulkley model with preyield viscosity accounts for the characteristics of both Herschel-Bulkley model and biviscous model. The range of the Bingham number corresponding to $\bar{\delta}=1$ for the Herschel-Bulkley model with preyield viscosity is expressed by

$$\bar{\delta}=1, \text{ for } \mathrm{Bi}(n) \geq \frac{6^n\,\bar{\tau}}{1-\bar{\tau}} \tag{42}$$

C.3.3 Equivalent Damping Coefficient vs. Bingham Number

Figure C6 represents the relationship between the equivalent damping coefficient, C_{eq}/C_0, and the Bingham number, $\mathrm{Bi}(n)$, with the influence of the stress coefficient, $\bar{\tau}$, and flow index, n, obtained by using Equations (33) and (36). Figure C6 (a) shows the case of $\bar{\tau}=1$ with the variation of the flow index, or the Herschel- Bulkley model case (Wereley, 2003). For $\mathrm{Bi}(n)=0$, and corresponding equivalent damping coefficient is one. As the Bingham number increases, the equivalent damping coefficient also increases. The curve of $n=1$ corresponds to the Bingham plastic case. For $n<1$, or shear thinning, the equivalent damping coefficient is above the Bingham plastic case. As the flow index further decreases, the nondimensional preyield thickness further falls above. For $n>1$, or shear thickening, the equivalent damping coefficient falls below the Bingham plastic case.

Figure C6 (b) shows the case of $n=1$, or the biviscous model case (Wereley et al., 2004). The curve of $\bar{\tau}=1$ corresponds to the Bingham plastic model case. As the stress coefficient decreases, the equivalent damping coefficient decreases for given Bingham number. For $0<\bar{\tau}<1$, the equivalent damping coefficient increases with respect to the Bingham number, and approaches to finite value, or the gap is entirely high viscosity preyield flow. The limiting value of the equivalent damping coefficient and corresponding range of the Bingham number is expressed by

$$\left(\frac{C_{eq}}{C_0}\right)_{BV}=\frac{1}{1-\bar{\tau}}, \text{ for } \mathrm{Bi}\geq\frac{6\bar{\tau}}{1-\bar{\tau}} \tag{43}$$

Figure C6 (c) and (d) show the cases of $n=0.9$ and 0.8, or Herschel- Bulkley model with preyield viscosity. As the stress coefficient decreases, the equivalent damping coefficient decreases for given flow index and Bingham number. As the flow behavior decreases, the nondimensional preyield thickness falls above for given stress coefficient and Bingham number. The limiting value of the equivalent damping coefficient can be obtained as

$$\left(\frac{C_{eq}}{C_0}\right)_{HBPV}=\left(\frac{3n}{2n+1}\right)^n\frac{1}{1-\bar{\tau}},\ \text{for}\ \ \mathrm{Bi}(n)\geq\frac{6^n\,\bar{\tau}}{1-\bar{\tau}} \tag{44}$$

It is shown that the relationship between the equivalent damping coefficient and the Bingham number of the Herschel-Bulkley model with preyield viscosity accounts for the characteristics of both Herschel-Bulkley model and biviscous model. When the fluid has preyield viscosity, the equivalent damping coefficient approaches to constant value as the Bingham number increases.

C.3.4 Damper Force vs. Piston Velocity

The quasi-static relationship between the damper force, F, and piston velocity, v_p, is investigated. For the simulation, the yield stress, τ_y, is assumed to be $10\,\mathrm{kPa}$ with magnetic field and $0\,\mathrm{kPa}$ without magnetic field. The postyield viscosity, κ, is assumed to be $1.0\,\mathrm{Pa\cdot s}^n$. Then, the corresponding transition stress, τ_t, and preyield viscosity, μ_{pr}, are also assumed by the stress coefficient, $\bar{\tau}(=1.00, 0.98, 0.96)$, and flow index, $n(=1.00, 0.90, 0.80)$. By using those parameters and Equation (6), the shear stress versus shear rate is represented in Figure C7. Figure C7 (a) is for the Herschel-Bulkley behavior, Figure C7 (b) is for the biviscous behavior, Figure C7 (c) and (d) are for the Hershel-Bulkley with preyield viscosity behavior. For the cases where $\tau_y=0\,\mathrm{kPa}$, there is no preyield viscosity, and shear stress curves of different stress coefficients are the same. The geometry of the MR valve is assumed as follows: the gap length, L, is $50\,\mathrm{mm}$, the gap size, d, is $0.8\,\mathrm{mm}$, the gap width, b, is $94\,\mathrm{mm}$, the piston head area, A_p, is $706\,\mathrm{mm}^2$. Given the fluid properties and the piston velocity, the Bingham number, $\mathrm{Bi}(n)$, is calculated from Equation (37), and the nondimensional preyield thickness, $\bar{\delta}$, can be determined from Equation (36) using a root finding algorithm. The physically sensible root is the root that satisfies $0<\bar{\delta}\leq 1$. Then the pressure drop, ΔP, in the valve can be calculated from Equation (31), and the force exerted by the MR damper can be obtained by the product of the pressure drop and the piston head area.

Figure C8 (a) shows the case of $\bar{\tau}=1$ with the variation of the flow index, or the Herschel-Bulkley model case (Wereley, 2004). It is evident that the damper force of higher yield stress is larger than the damper force of lower yield stress for given flow index and piston velocity. As the flow index decreases for given yield stress and piston velocity, the slope, or magnitude, of the damper force also decreases. For $\tau_y = 0\,\text{kPa}$ and $n = 1.00$, the flow through the MR valve is Newtonian, and the corresponding damper force, proportional to the piston velocity, behaves as a linear viscous damper.

Figure C8 (b) shows the case where $n = 1$, or the biviscous model case (Wereley et al., 2004). For the cases where $\tau_y = 0\,\text{kPa}$, there is no preyield viscosity, and damper force curves of different stress coefficients are the same. For the case where $\tau_y = 10\,\text{kPa}$, the influence of the stress coefficient on the damper force is clearly observed. The curve of $\bar{\tau} = 1$ corresponds to the Bingham plastic behavior case. For $\bar{\tau} < 1$, there are two domains where the slope of the force versus velocity curve is high in the low velocity domain and the slope of the force is low in the high velocity domain. In the high slope domain, the gap is entirely full of high viscosity or preyield viscosity flow, and equivalent damping coefficient and Bingham number satisfy the condition expressed in Equation (43). As the stress coefficient decreases, the damper force magnitude also decreases, and the velocity limit of the high slope force domain shifts to higher velocity. Thus, the piston velocity where the transition from high slope domain to low slope domain takes place is a function of stress coefficient, and can be found from Equations (37) and (43) as below

$$v_p = \frac{A_d}{A_p} \frac{d}{6} \frac{\tau_y}{\mu_{po}} \frac{1-\bar{\tau}}{\bar{\tau}} \tag{45}$$

In the high velocity domain, the effect of the stress coefficient on the damper force behavior becomes weakened.

Figure C8 (c) and (d) show the cases of $n = 0.9$ and 0.8, or Herschel- Bulkley model with preyield viscosity. For the cases where $\tau_y = 0\,\text{kPa}$, damper force curves of different stress coefficients are the same for given flow index. For the cases where $\tau_y = 10\,\text{kPa}$, the effects of both the flow index and the stress coefficient on the damper force is clearly observed. As the stress coefficient decreases, the damper force decreases for given flow index and piston velocity. As the flow behavior index decreases, the damper force also decreases for given stress coefficient and piston velocity. For a given stress coefficient, as the flow behavior index decreases, the slope of the damper force decreases, and velocity at which the flow changes from preyield to postyield changes to a higher velocity. This is can be expected from the shear stress versus shear rate data, shown in Figure C8. The piston velocity where the transition from high slope domain to low slope domain takes place is a function of stress coefficient and flow index, and can be found from Equations (37) and (44) as below

$$v_p = \frac{A_d}{A_p}\frac{d}{6}\left(\frac{\tau_y}{\kappa}\frac{1-\bar{\tau}}{\bar{\tau}}\right)^{\frac{1}{n}} \tag{46}$$

C.3.5 Fluid Velocity Profile and Velocity Gradient

Figure C9 shows the velocity profile and gradient of the fluid in the valve. Equations (22) and (25) are used for the calculation of velocity gradient, and Equations (23) and (26) are for the velocity profile. The fluid properties, such as yield stress and postyield viscosity, and valve geometry are the same as the cases of Figures C7 and C8. The piston velocity is assumed to be $0.02\,\mathrm{m/s}$. Figure C9 (a) and (b) show the fluid velocity profiles and gradients at $\tau_y = 0\,\mathrm{kPa}$. For $n = 1.00$, the velocity profile and gradient are parabolic and linear functions of gap coordinate, which are indicatives of Newtonian shear flow. For the cases where $n = 0.90$, these velocity profiles and gradients seem to be close to the case where $n = 1.00$, but those are not parabolic and linear functions of gap coordinate. Furthermore, as the flow index decreases, the peak velocities also decrease. Because there is no preyield flow for the case where $\tau_y = 0\,\mathrm{kPa}$, the stress coefficient does not affect the damper characteristics, including velocity profile and gradient.

Figure C9 (c) and (d) show the fluid velocity profiles and gradients at $\tau_y = 10\,\mathrm{kPa}$. For $n = 1.00$ and $\bar{\tau} = 1.00$, the plug flow is developed in the central region of the gap due to the yield stress. In the plug flow region, the fluid velocity is constant and velocity gradient is zero through the gap coordinate. In the outer region, or postyield region, the flow velocity profile and gradient are parabolic and linear functions of gap coordinate. For $n = 0.90$ and $\bar{\tau} = 1.00$, the plug flow is also developed in the central region of the gap due to the yield stress. In the outer region, or postyield region, the velocity profile and gradient are not parabolic and linear functions of gap coordinate as discussed in Figure C9 (a). For $n = 1.00$ and $\bar{\tau} = 0.98$, the high viscous flow is developed in the central region of the gap due to the preyield viscosity. The velocity profiles and gradients in the preyield and postyield regions are parabolic and linear functions of gap coordinate. For $n = 0.90$ and $\bar{\tau} = 0.98$, the high viscous flow is also developed in the preyield region. In the postyield region, the velocity profile and gradient are affected by the shear stress coefficient and the flow index.

C.4 Conclusion

Nondimensional analysis of a flow mode MR damper based on a Herschel-Bulkley model with preyield viscosity was presented. Based on the nondimensional modeling and analysis undertaken in this study, the following conclusions are made:

1. On the basis of the Herschel-Bulkley model with preyield viscosity, a nondimensional analysis model that can favorably characterize the flow mode MR damper behavior was developed. The analysis model consists of the Bingham number, Bi, the nondimensional preyield thickness, $\bar{\delta}$, the equivalent damping coefficient, C_{eq}/C_0, the flow index, n, and the stress coefficient $\bar{\tau}$. The flow index and the stress coefficient could account for the Herschel-Bulkley behavior in the postyield condition and the biviscous behavior in the preyield condition, respectively.

2. The influences of the flow index and the stress coefficient on the relationships of the Bingham number, the nondimensional plug thickness, and the equivalent damping coefficient were analyzed. As the flow index decreases, the equivalent damping coefficient decreases for a given nondimensional preyield thickness, and the equivalent damping coefficient and the nondimensional plug thickness increase for a given Bingham number. As the stress coefficient decreases, the equivalent damping coefficient decreases for a given nondimensional preyield thickness, and the equivalent damping coefficient decreases and the nondimensional plug thickness increase for a given Bingham number.

3. For the case where $0<\bar{\tau}<1$ and $n\neq 1$, the proposed analysis model represent the flow mode damper behavior characterized by both the power law postyield viscosity and the preyield viscosity. For $\bar{\tau}=1$, the proposed analysis model reduces to the Herschel-Bulkley case. For $0<\bar{\tau}<1$ and $n=1$, the proposed analysis model reduces to the biviscous case. For $\bar{\tau}=1$ and $n=1$, the proposed model reduces to the Bingham plastic case.

4. For a given fluid properties and flow mode damper geometry, the fluid velocity profile and gradient, and the relationship of the damper force and piston velocity were analyzed. The analysis shows that the flow behavior in the gap and damper performance are sensitive to the flow index, n, and the stress coefficient, $\bar{\tau}$.

C.5 Special Cases

The nondimensional quantities of the velocity gradient (25), the velocity profile (26), the equivalent damping coefficient (33), the plug thickness polynomial (37) reduce to simpler forms of the Herschel-Bulkley model, the biviscous model, the Bingham model for given the stress coefficient and the flow index. The results are identical to results presented in earlier studies (Wereley and Pang, 1998; Wereley et al., 2004; Wereley, 2003) and the nondimensional quantities of four models are summarized:

C.5.1 Velocity Gradient

(1) Herschel-Bulkley model with preyield viscosity

$$\begin{aligned}
\bar{u}_1' &= \left[-2\bar{y}-\bar{\tau}\bar{\delta}\right]^{\frac{1}{n}} \\
\bar{u}_2' &= -2\left(\frac{\bar{y}}{\bar{\delta}}\right)\left[(1-\bar{\tau})\bar{\delta}\right]^{\frac{1}{n}} \\
\bar{u}_3' &= -\left[2\bar{y}-\bar{\tau}\bar{\delta}\right]^{\frac{1}{n}}
\end{aligned} \tag{47}$$

(2) Herschel-Bulkley model $(\bar{\tau}=1)$

$$\bar{u}_1{}' = \left[-2\bar{y} - \bar{\delta}\right]^{\frac{1}{n}}$$
$$\bar{u}_2{}' = 0 \tag{48}$$
$$\bar{u}_3{}' = -\left[2\bar{y} - \bar{\delta}\right]^{\frac{1}{n}}$$

(3) Biviscous model $(n = 1)$

$$\bar{u}_1{}' = -2\bar{y} - \bar{\tau}\bar{\delta}$$
$$\bar{u}_2{}' = -2\bar{y}(1 - \bar{\tau}) \tag{49}$$
$$\bar{u}_3{}' = -2\bar{y} + \bar{\tau}\bar{\delta}$$

(4) Bingham-Plastic model $(\bar{\tau} = 1, n = 1)$

$$\bar{u}_1{}' = -2\bar{y} - \bar{\delta}$$
$$\bar{u}_2{}' = 0 \tag{50}$$
$$\bar{u}_3{}' = -2\bar{y} + \bar{\delta}$$

C.5.2 Velocity Profile

(1) Herschel-Bulkley model with preyield viscosity

$$\bar{u}_1 = \left[1 - \bar{\tau}\bar{\delta}\right]^{\frac{n+1}{n}} - \left[-2\bar{y} - \bar{\tau}\bar{\delta}\right]^{\frac{n+1}{n}}$$
$$\bar{u}_2 = \frac{1}{2}\frac{n+1}{n}\left[(1 - \bar{\tau})\bar{\delta}\right]^{\frac{1}{n}}\left(\bar{\delta} - 4\frac{\bar{y}^2}{\bar{\delta}}\right) - \left[1 - \bar{\tau}\bar{\delta}\right]^{\frac{n+1}{n}} - \left[(1 - \bar{\tau})\bar{\delta}\right]^{\frac{n+1}{n}} \tag{51}$$
$$\bar{u}_3 = \left[1 - \bar{\tau}\bar{\delta}\right]^{\frac{n+1}{n}} - \left[2\bar{y} - \bar{\tau}\bar{\delta}\right]^{\frac{n+1}{n}}$$

(2) Herschel-Bulkley model $(\bar{\tau} = 1)$

$$\bar{u}_1 = \left[1 - \bar{\delta}\right]^{\frac{n+1}{n}} - \left[-2\bar{y} - \bar{\delta}\right]^{\frac{n+1}{n}}$$
$$\bar{u}_2 = -\left[1 - \bar{\delta}\right]^{\frac{n+1}{n}} \tag{52}$$
$$\bar{u}_3 = \left[1 - \bar{\delta}\right]^{\frac{n+1}{n}} - \left[2\bar{y} - \bar{\delta}\right]^{\frac{n+1}{n}}$$

(3) Biviscous model $(n = 1)$

$$\bar{u}_1 = \left[1-\bar{\tau}\bar{\delta}\right]^2 - \left[-2\bar{y}-\bar{\tau}\bar{\delta}\right]^2$$
$$\bar{u}_2 = \left[(1-\bar{\tau})\bar{\delta}\right]\left(\bar{\delta}-4\frac{\bar{y}^2}{\bar{\delta}}\right) - \left[1-\bar{\tau}\bar{\delta}\right]^2 - \left[(1-\bar{\tau})\bar{\delta}\right]^2 \tag{53}$$
$$\bar{u}_3 = \left[1-\bar{\tau}\bar{\delta}\right]^2 - \left[2\bar{y}-\bar{\tau}\bar{\delta}\right]^2$$

(4) Bingham-Plastic model $(\bar{\tau}=1, n=1)$

$$\bar{u}_1 = \left[1-\bar{\delta}\right]^2 - \left[-2\bar{y}-\bar{\delta}\right]^2$$
$$\bar{u}_2 = -\left[1-\bar{\delta}\right]^2 \tag{54}$$
$$\bar{u}_3 = \left[1-\bar{\delta}\right]^2 - \left[2\bar{y}-\bar{\delta}\right]^2$$

C.5.3 Equivalent Damping Coefficient

(1) Herschel-Bulkley model with preyield viscosity

$$\frac{C_{eq}}{C_0} = \frac{1}{\left[-\frac{n}{n+1}\left[\left(1-\bar{\tau}\bar{\delta}\right)^{\frac{2n+1}{n}} - \left((1-\bar{\tau})\bar{\delta}\right)^{\frac{2n+1}{n}}\right] + \frac{2n+1}{n+1}\left[\left(1-\bar{\tau}\bar{\delta}\right)^{\frac{n+1}{n}} - \left((1-\bar{\tau})\bar{\delta}\right)^{\frac{n+1}{n}}\bar{\delta}\right] + \frac{1}{3}\frac{2n+1}{n}\left((1-\bar{\tau})\bar{\delta}\right)^{\frac{1}{n}}\bar{\delta}^2\right]^n} \tag{55}$$

(2) Herschel-Bulkley model $(\bar{\tau}=1)$

$$\frac{C_{eq}}{C_0} = \frac{1}{\left(1-\bar{\delta}\right)^{n+1}\left(1+\frac{n}{n+1}\bar{\delta}\right)^n} \tag{56}$$

(3) Biviscous model $(n=1)$

$$\frac{C_{eq}}{C_0} = \frac{1}{\left(1-\bar{\delta}\right)^2\left(1+\frac{\bar{\delta}}{2}\right) + \frac{3}{2}\left(1-\bar{\tau}\right)\left(1-\frac{\bar{\delta}^2}{3}\right)\bar{\delta}} = \frac{1}{\left(1-\bar{\delta}\right)^2\left(1+\frac{\bar{\delta}}{2}\right) + \frac{3}{2}\bar{\mu}\left(1-\frac{\bar{\delta}^2}{3}\right)\bar{\delta}} \tag{57}$$

(4) Bingham-Plastic model $(\bar{\tau}=1, n=1)$

$$\frac{C_{eq}}{C_0} = \frac{1}{\left(1-\bar{\delta}\right)^2\left(1+\frac{\bar{\delta}}{2}\right)} \tag{58}$$

C.5.4 Preyield Thickness Polynomial and Bingham Number

(1) Herschel-Bulkley model with preyield viscosity

$$\Lambda(\bar{\delta}) = \left[-\frac{n}{n+1}\left[\left(1-\bar{\tau}\bar{\delta}\right)^{\frac{2n+1}{n}} - \left(\left(1-\bar{\tau}\right)\bar{\delta}\right)^{\frac{2n+1}{n}} \right] + \frac{2n+1}{n+1}\left[\left(1-\bar{\tau}\bar{\delta}\right)^{\frac{n+1}{n}} - \left(\left(1-\bar{\tau}\right)\bar{\delta}\right)^{\frac{n+1}{n}} \bar{\delta} \right] + \frac{1}{3}\frac{2n+1}{n}\left(\left(1-\bar{\tau}\right)\bar{\delta}\right)^{\frac{1}{n}}\bar{\delta}^2 \right]^n$$

$$-\left[\frac{2\left(2n+1\right)}{n}\right]^n \frac{\bar{\tau}\bar{\delta}}{\mathrm{Bi}(n)} = 0$$

$$\mathrm{Bi}(n) = \frac{\tau_y}{\kappa\left(v_d / d\right)^n}$$

(59)

(2) Herschel-Bulkley model $(\bar{\tau} = 1)$

$$\Lambda(\bar{\delta}) = \left(1-\bar{\delta}\right)^{n+1}\left(1+\frac{n}{n+1}\bar{\delta}\right)^n - \left[\frac{2\left(2n+1\right)}{n}\right]^n \frac{\bar{\delta}}{\mathrm{Bi}(n)} = 0$$

$$\mathrm{Bi}(n) = \frac{\tau_y}{\kappa\left(v_d / d\right)^n} \qquad (60)$$

(3) Biviscous model $(n = 1)$

$$\Lambda(\bar{\delta}) = \left(1-\bar{\delta}\right)^2\left(1+\frac{\bar{\delta}}{2}\right) + \frac{3}{2}\left(1-\bar{\tau}\right)\left(1-\frac{\bar{\delta}^2}{3}\right)\bar{\delta} - 6\frac{\bar{\tau}\bar{\delta}}{\mathrm{Bi}}$$

$$= \left(1-\bar{\delta}\right)^2\left(1+\frac{\bar{\delta}}{2}\right) + \frac{3}{2}\bar{\mu}\left(1-\frac{\bar{\delta}^2}{3}\right)\bar{\delta} - 6\frac{\left(1-\bar{\mu}\right)\bar{\delta}}{\mathrm{Bi}} = 0 \qquad (61)$$

$$\mathrm{Bi} = \frac{\tau_y}{\mu_{po} v_d / d}$$

(4) Bingham-Plastic model $(\bar{\tau} = 1, n = 1)$

$$\Lambda(\bar{\delta}) = \left(1-\bar{\delta}\right)^2\left(1+\frac{\bar{\delta}}{2}\right) - 6\frac{\bar{\delta}}{\mathrm{Bi}} = 0$$

$$\mathrm{Bi} = \frac{\tau_y}{\mu_{po} v_d / d} \qquad (62)$$

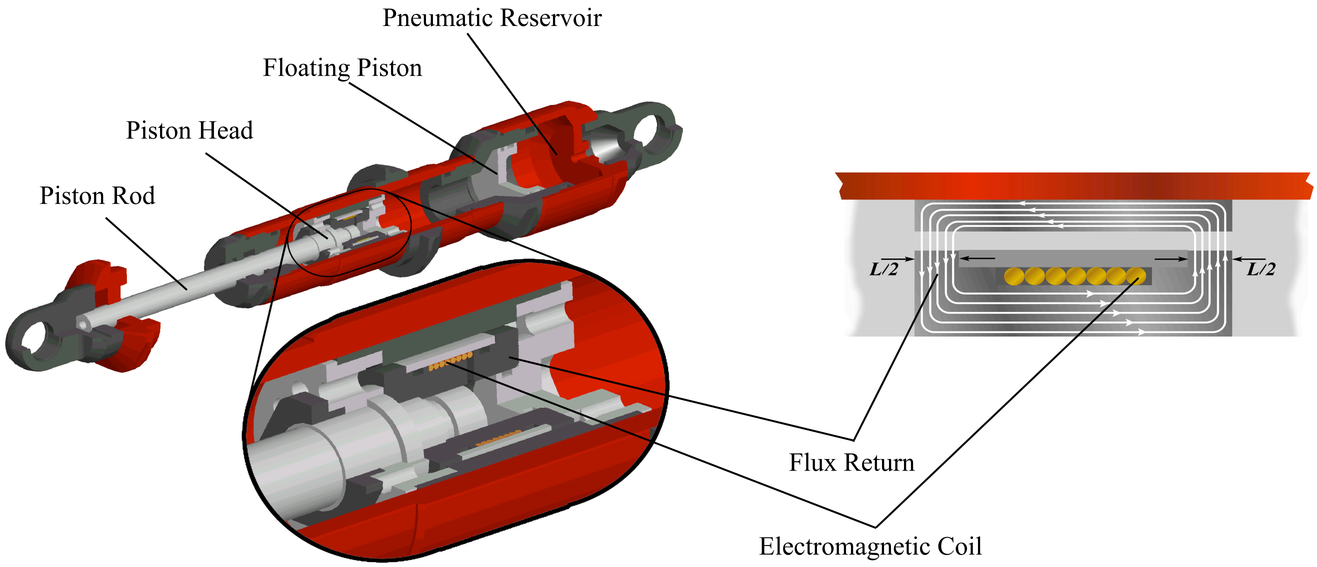

Figure C1 Configuration of typical MR damper

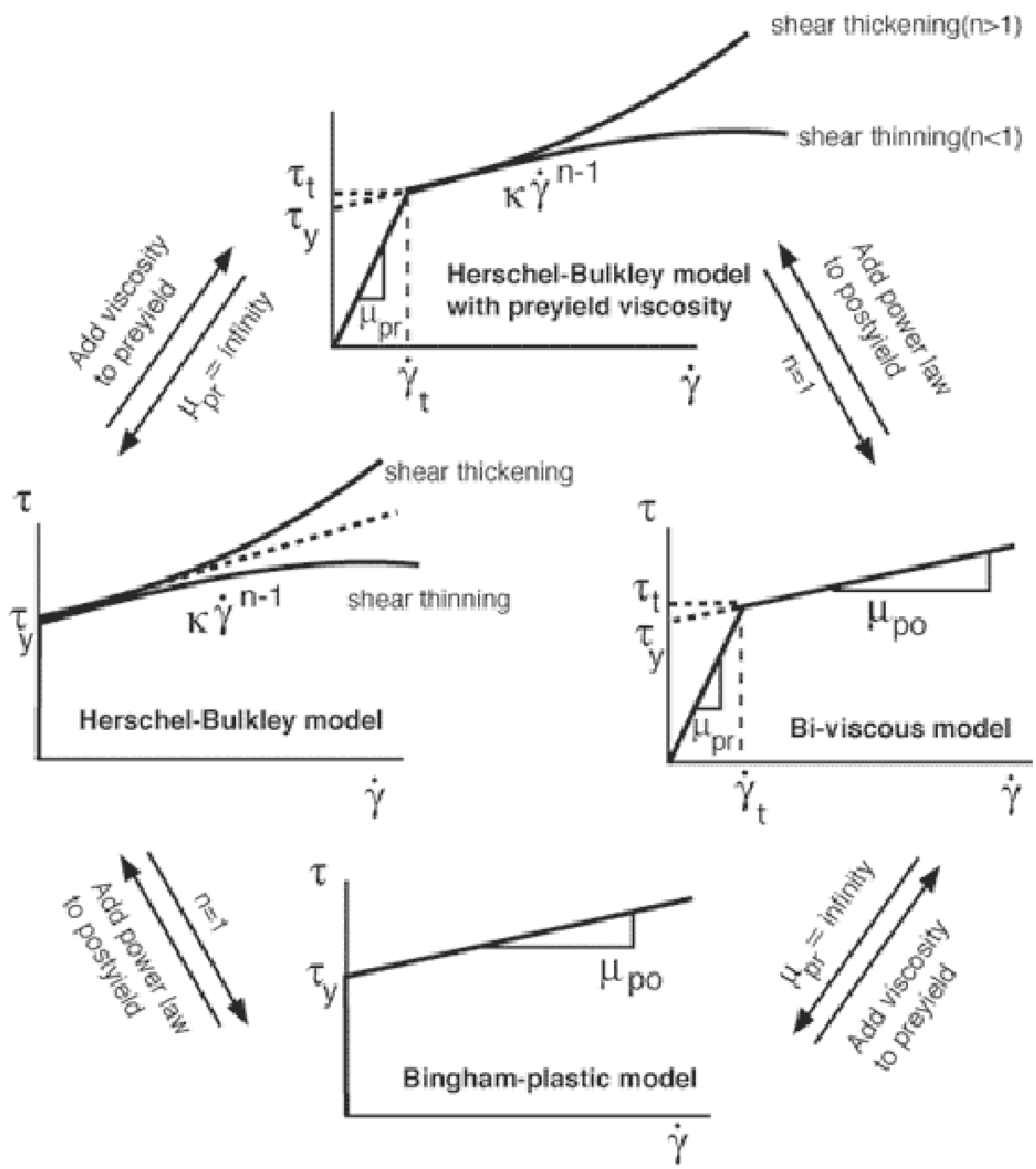

Figure C2 Relationship of constitutive rheological models for MR fluid

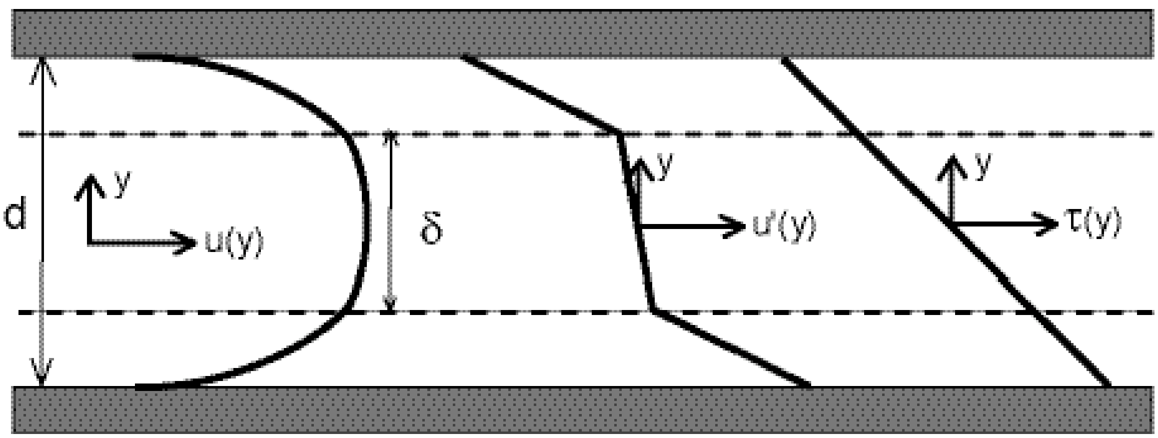

Figure C3 Typical velocity profile, velocity gradient, and shear stress profile in the MR valve

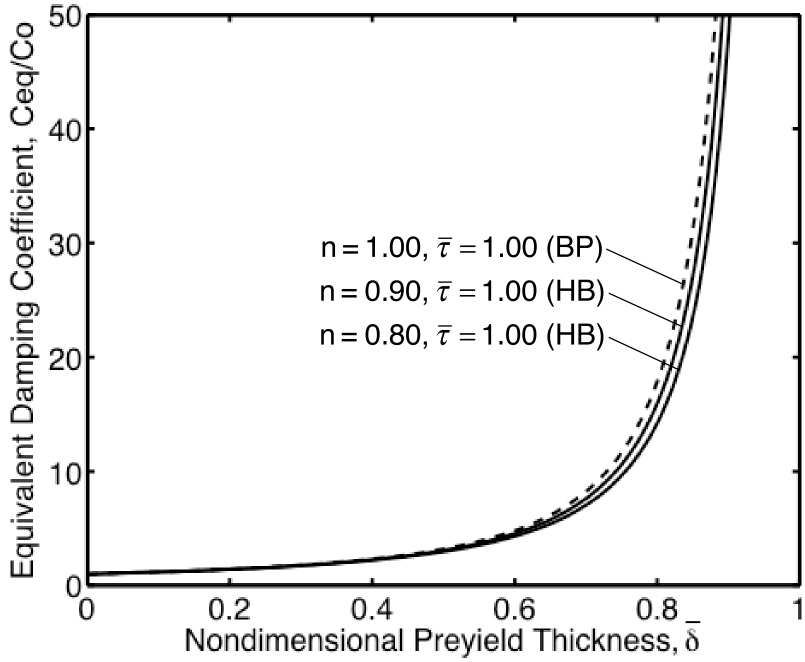

(a) variation of n with $\bar{\tau} = 1$

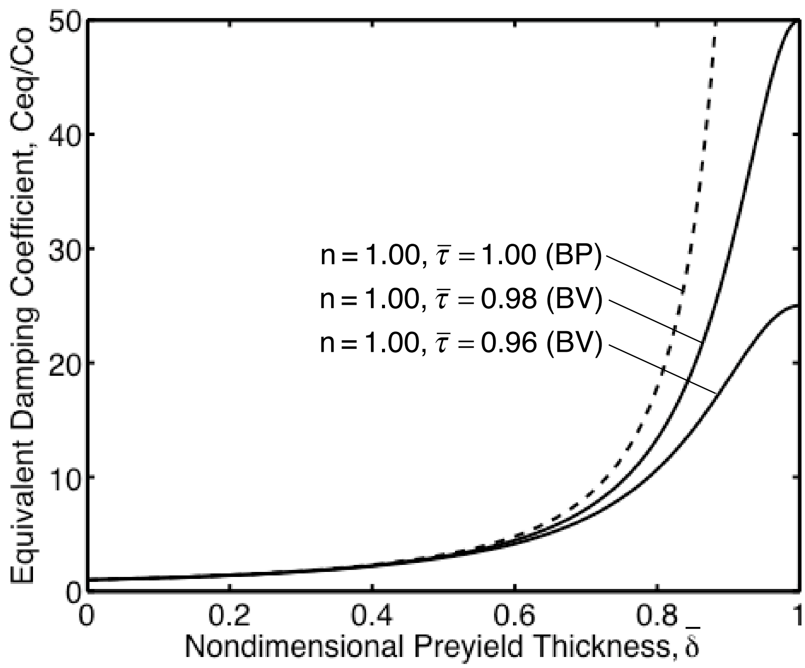

(b) variation of $\bar{\tau}$ with $n = 1$

Figure C4 Equivalent damping coefficient versus nondimensional preyield thickness

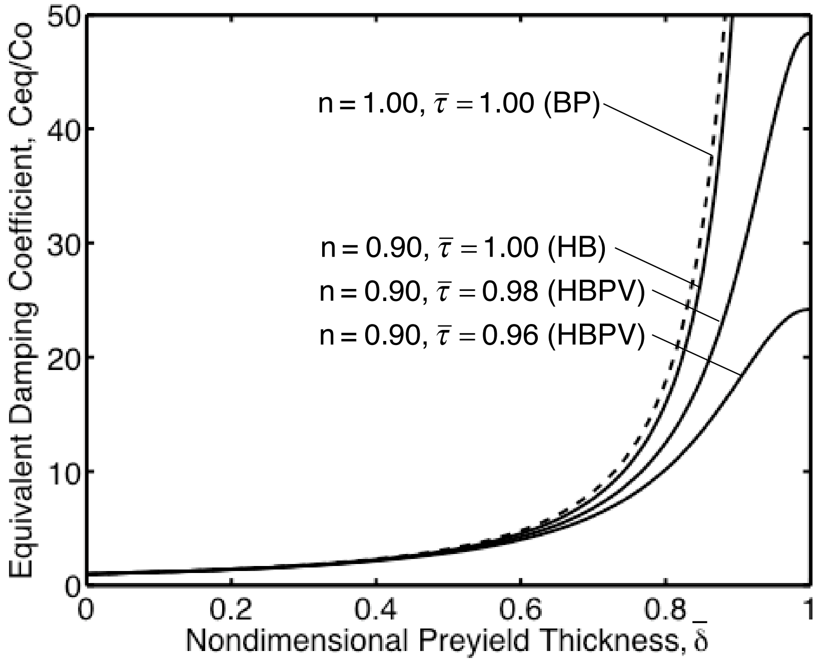

(c) variation of $\bar{\tau}$ with $n = 0.90$

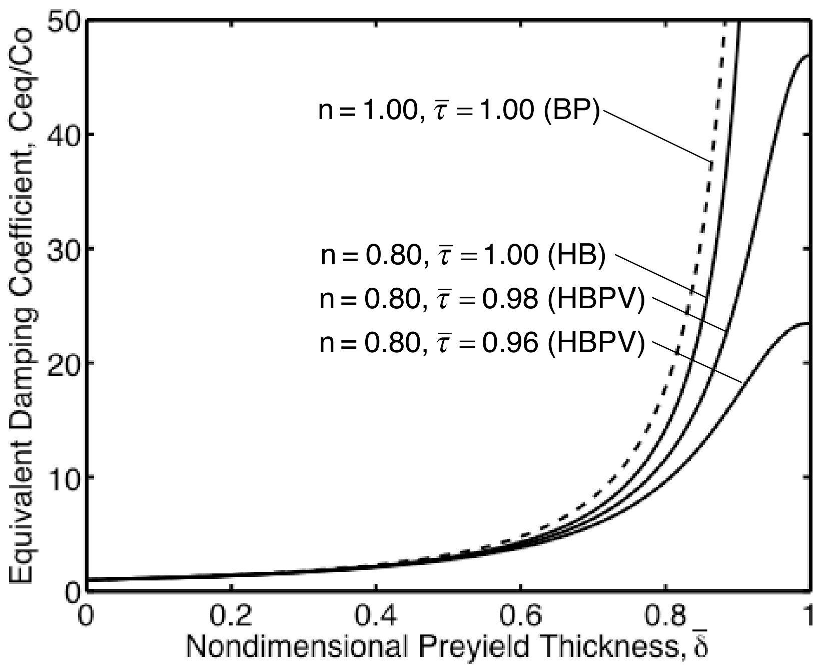

(d) variation of $\bar{\tau}$ with $n = 0.80$

Figure C4 Continued

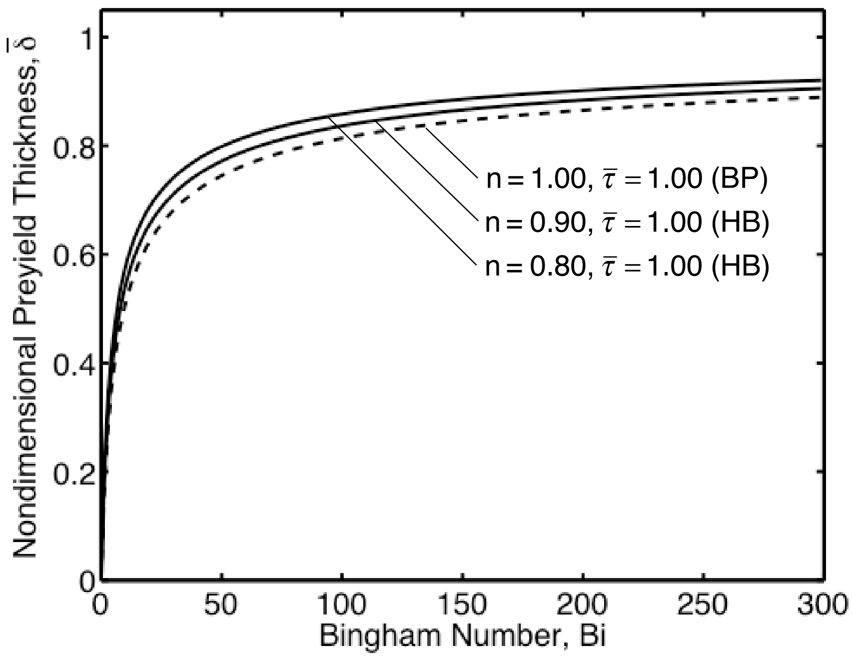

(a) variation of n with $\bar{\tau} = 1$

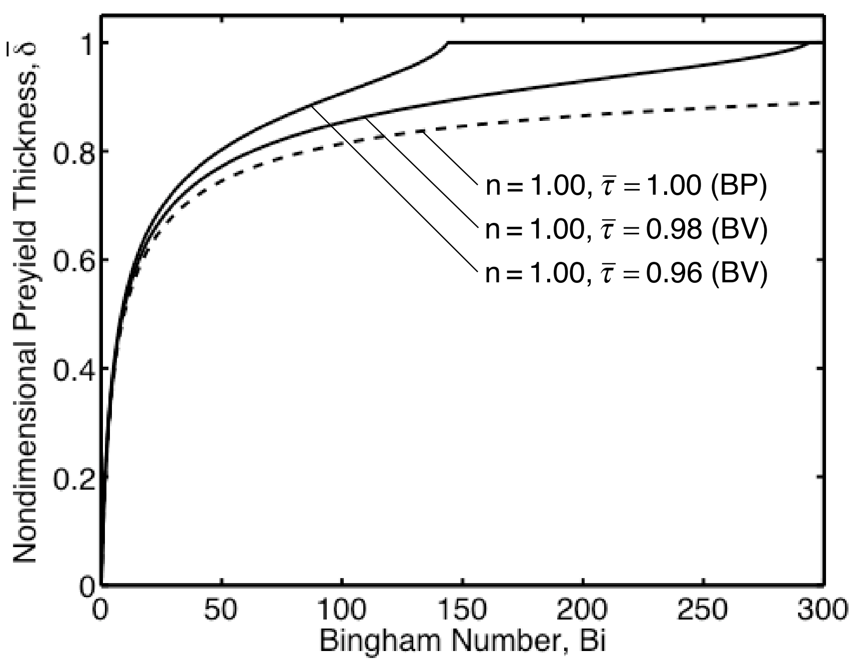

(b) variation of $\bar{\tau}$ with $n = 1$

Figure C5 Nondimensional preyield thickness versus Bingham number

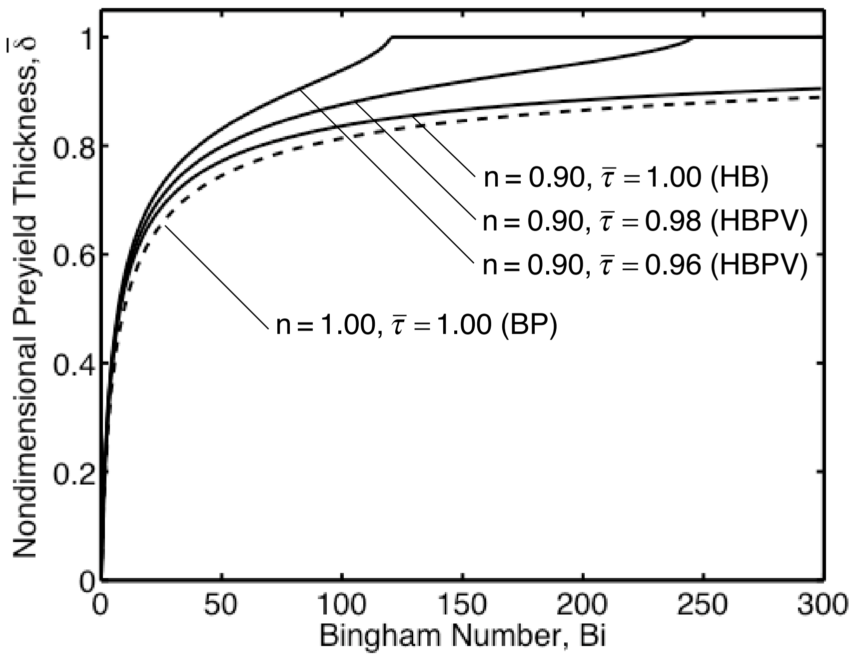

(c) variation of $\bar{\tau}$ with $n = 0.90$

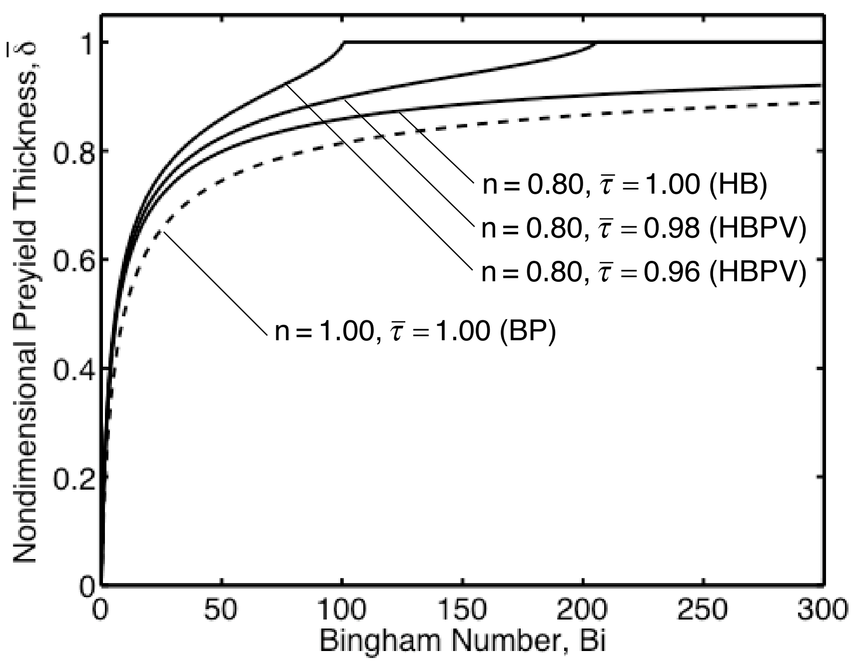

(d) variation of $\bar{\tau}$ with $n = 0.80$

Figure C5 Continued

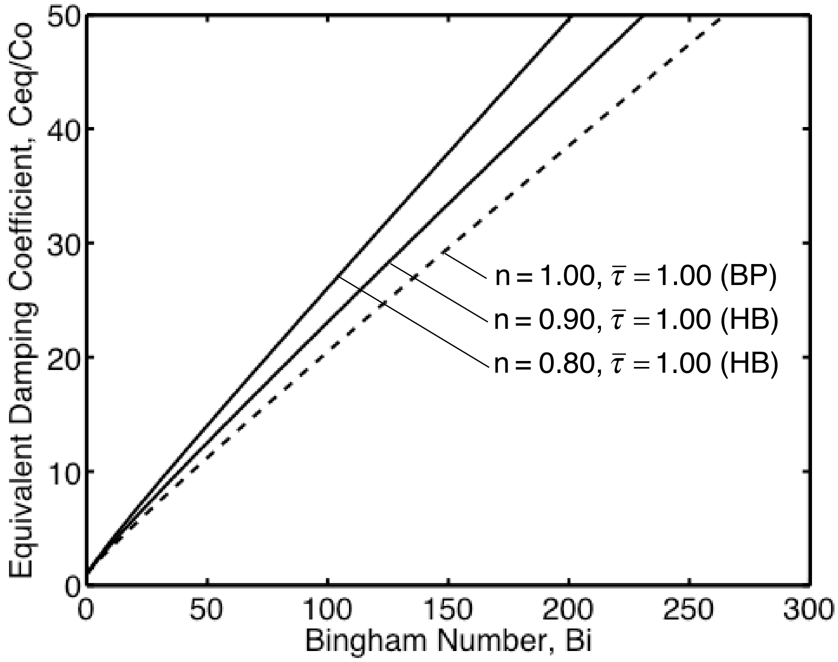

(a) variation of n with $\bar{\tau} = 1$

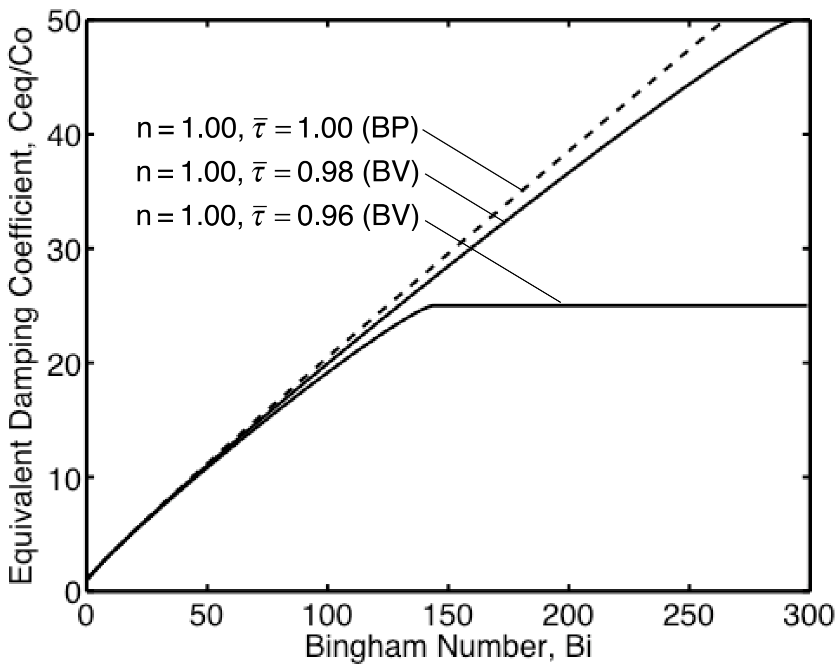

(b) variation of $\bar{\tau}$ with $n = 1$

Figure C6 Equivalent damping coefficient versus Bingham number

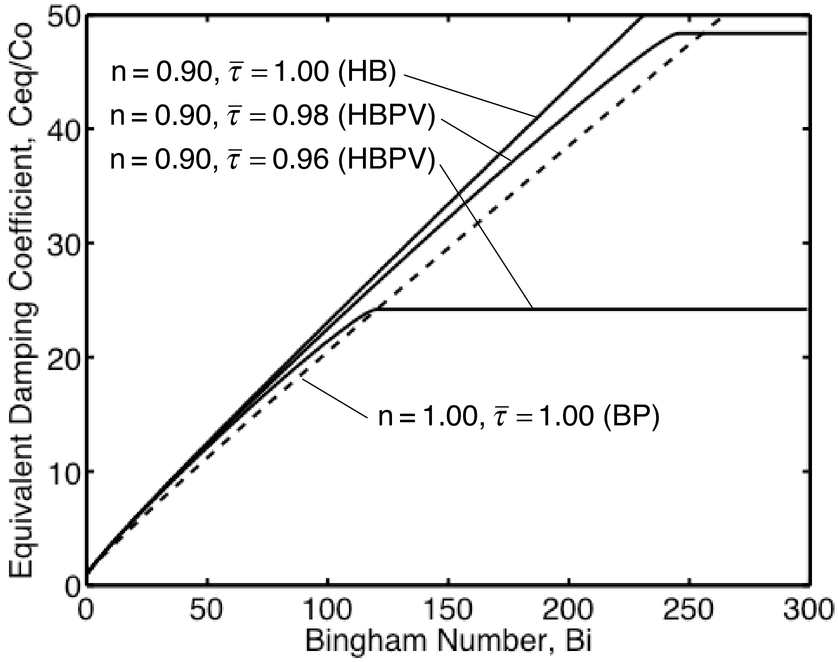

(c) variation of $\bar{\tau}$ with $n = 0.90$

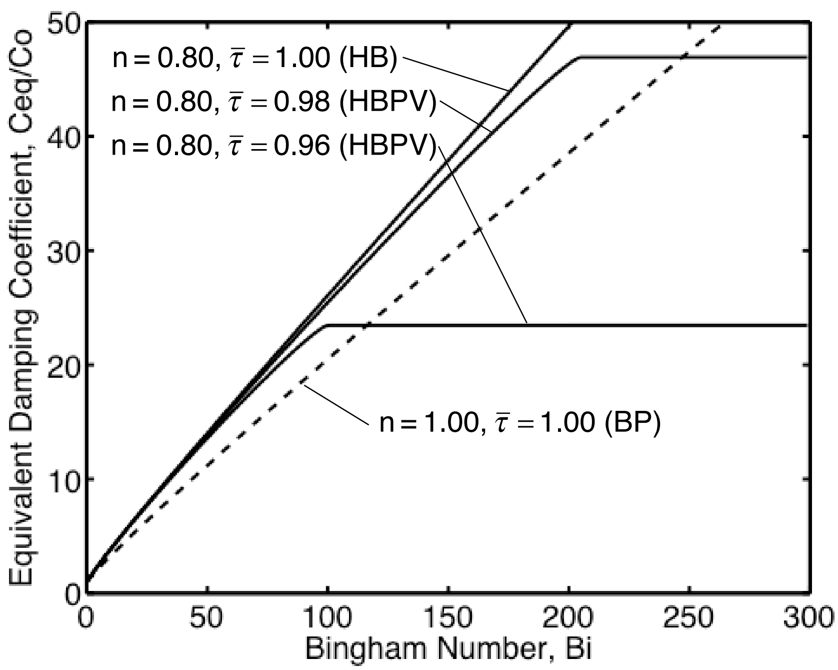

(d) variation of $\bar{\tau}$ with $n = 0.80$

Figure C6 Continued

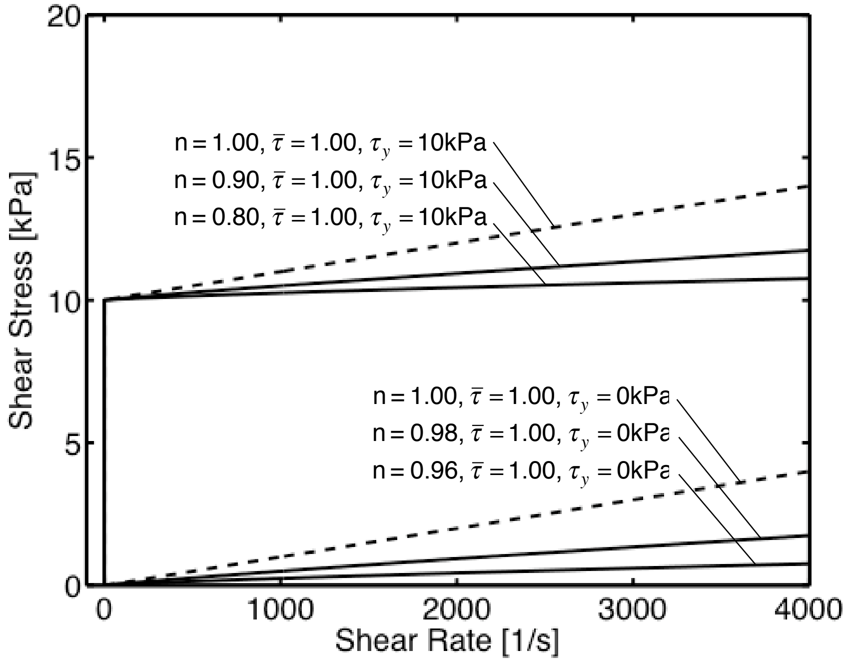

(a) variation of n with $\bar{\tau} = 1$

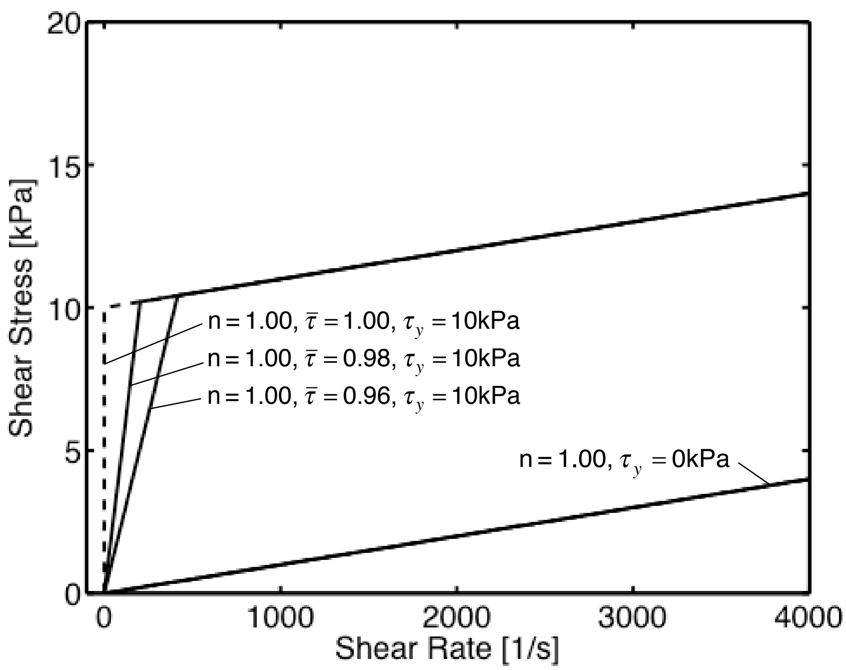

(b) variation of $\bar{\tau}$ with $n = 1$

Figure C7 Shear stress versus shear rate of MR fluid used for analysis

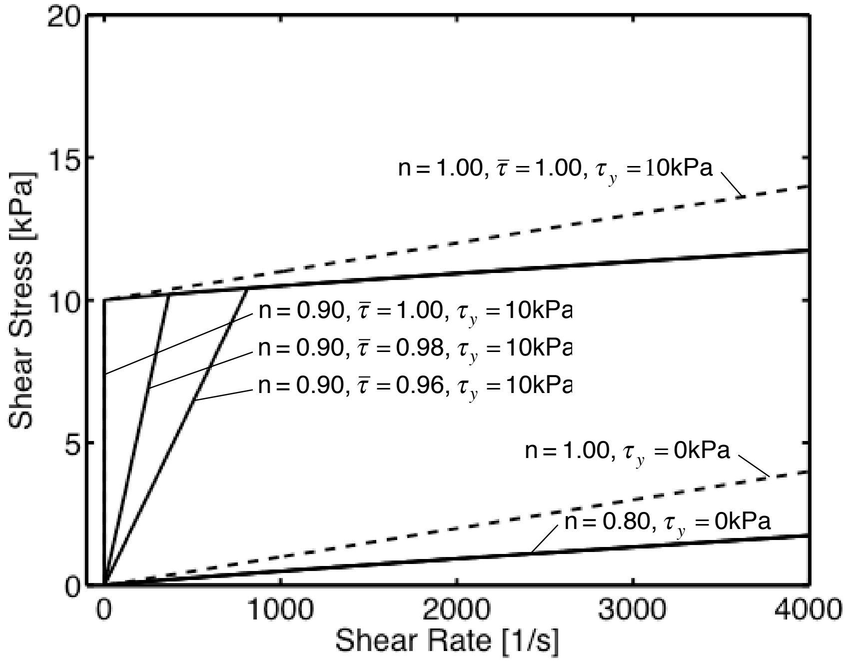

(c) variation of $\bar{\tau}$ with $n = 0.90$

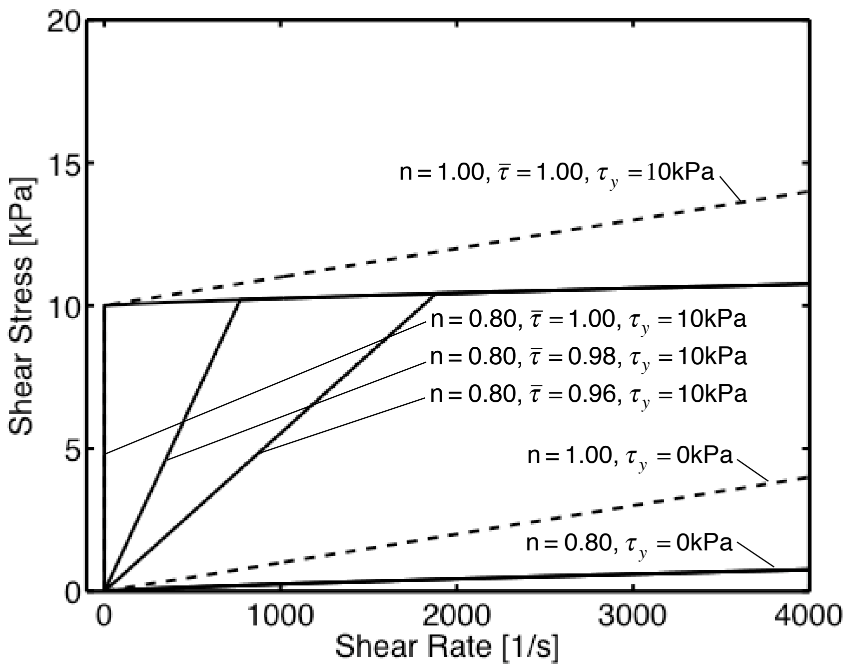

(d) variation of $\bar{\tau}$ with $n = 0.80$

Figure C7 Continued

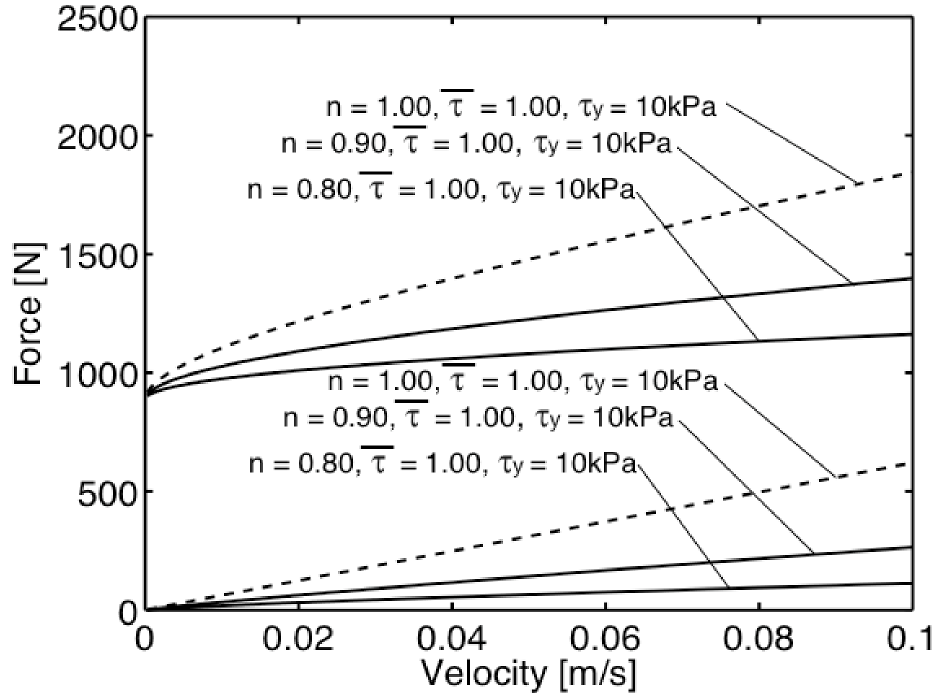

(a) variation of n with $\overline{\tau} = 1$

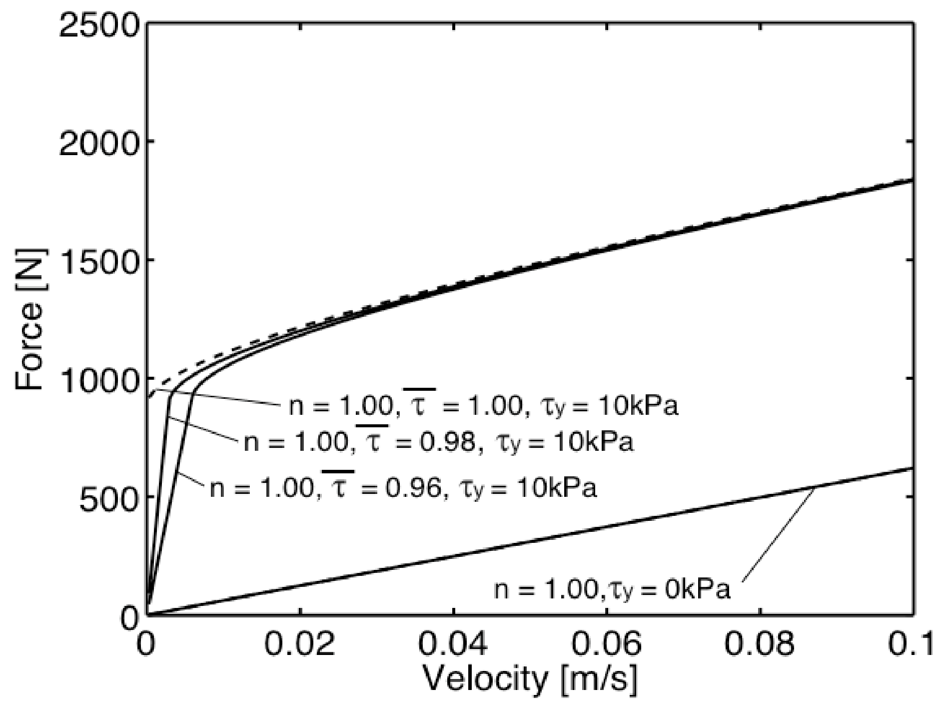

(b) variation of $\overline{\tau}$ with $n = 1$

Figure C8 Damper force versus piston velocity

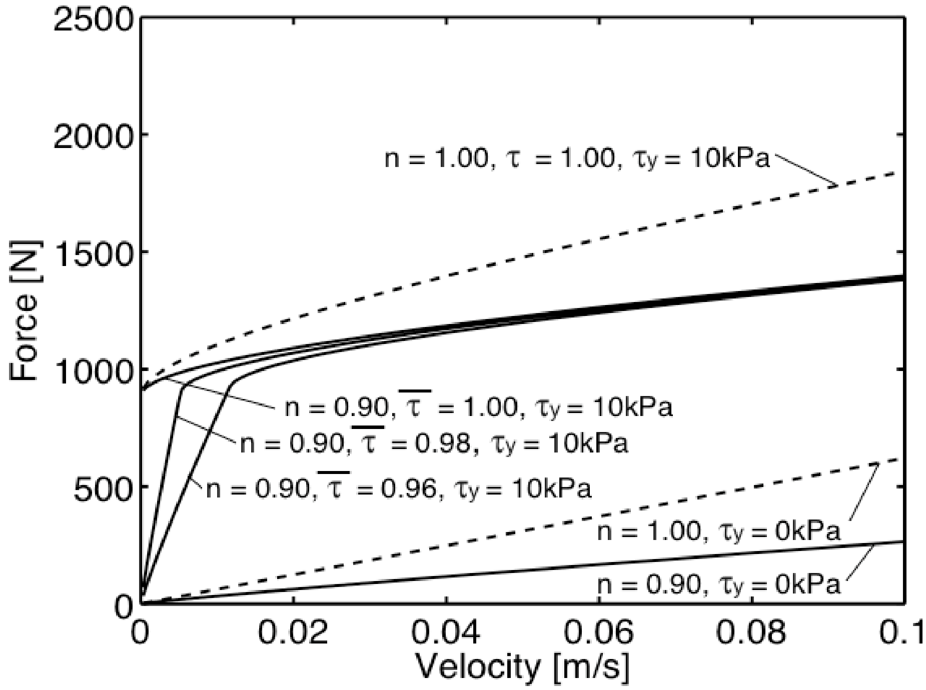

(c) variation of $\bar{\tau}$ with $n = 0.90$

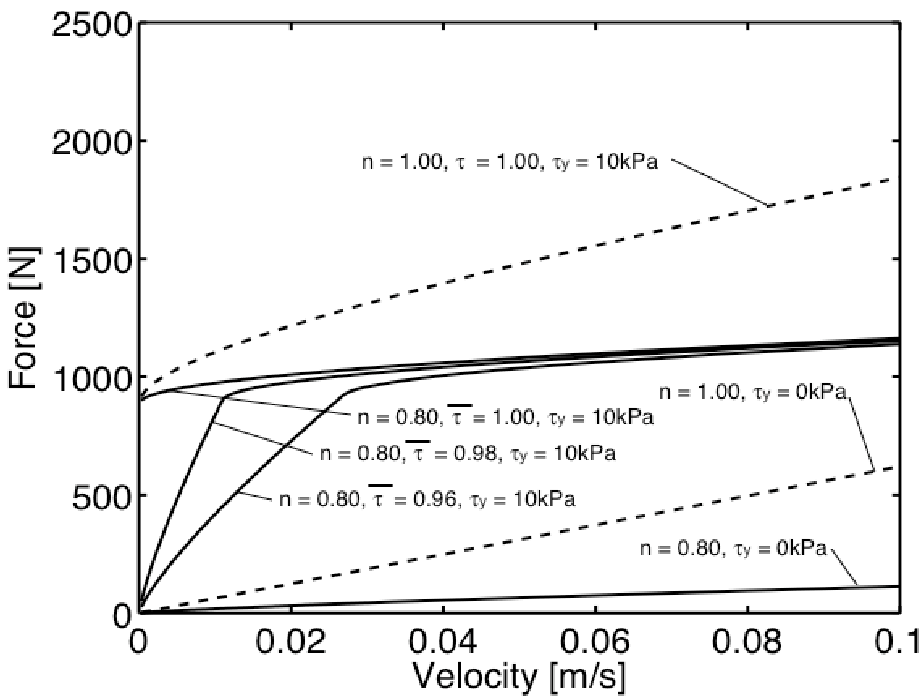

(d) variation of $\bar{\tau}$ with $n = 0.80$

Figure C8 Continued

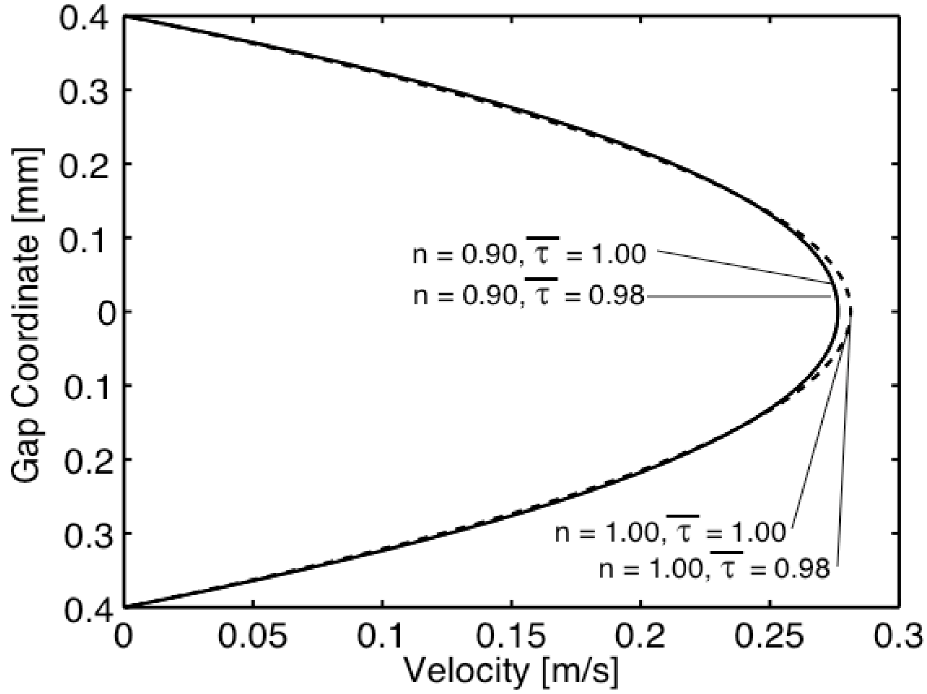

(a) velocity profile of $\tau_y = 0\,\mathrm{kPa}$

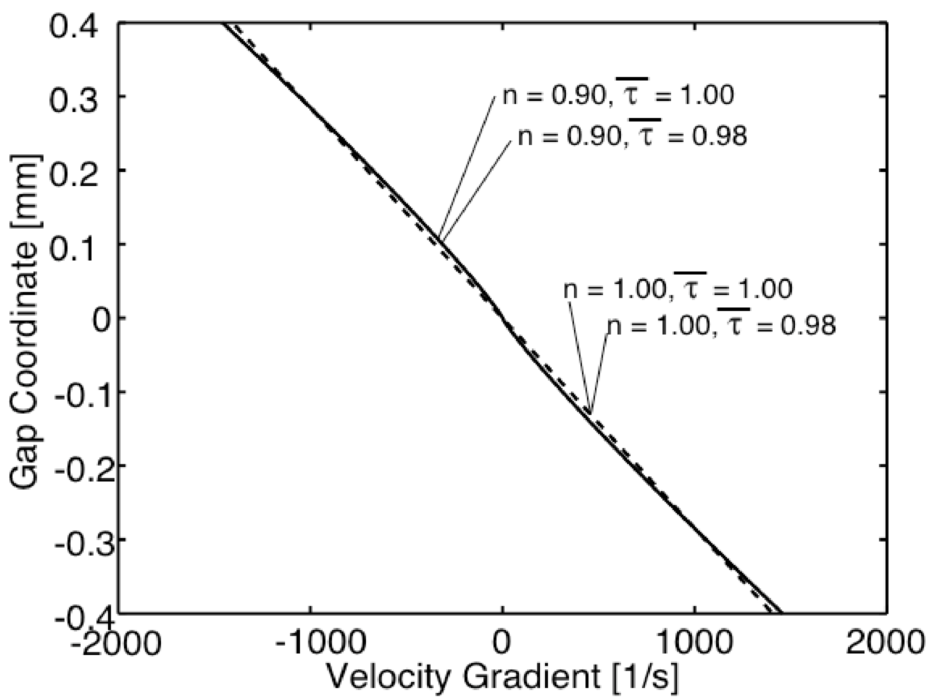

(b) velocity gradient of $\tau_y = 0\,\mathrm{kPa}$

Figure C9 Fluid velocity profile and velocity gradient in the MR valve

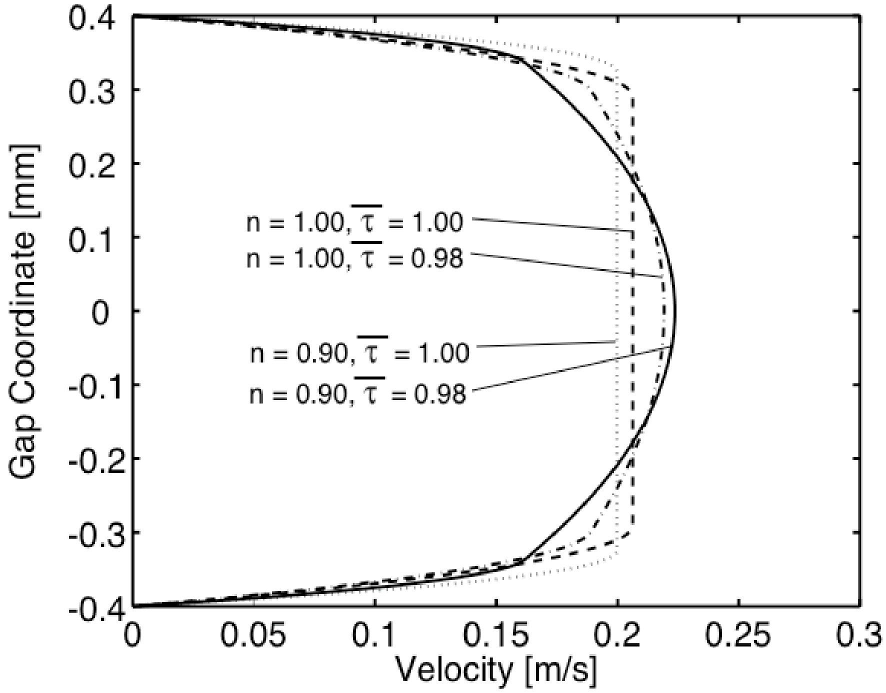

(c) velocity profile of $\tau_y = 10\,\mathrm{kPa}$

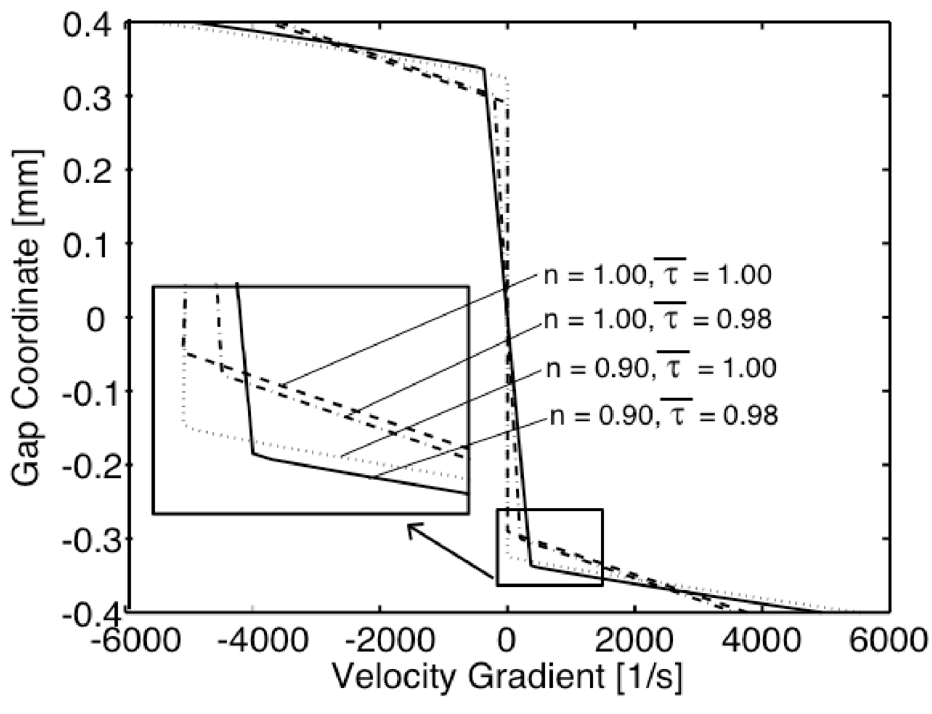

(d) velocity gradient of $\tau_y = 10\,\mathrm{kPa}$

Figure C9 Continued

BIBLIOGRAPHY

Achache, M. and Polychroniadis, M. 1986. "Higher Harmonic Control: Flight Tests on an Experimental System on an SA-349 Research Gazelle," *In Proceedings of the 42nd Forum of the American Helicopter Society, Washington, D.C.*, 2:811–820.

Amer, K. B. and Neff, J. R. 1974. "Vertical Plane Pendulum Absorbers for Minimizing Helicopter Vibratory Loads," *Journal of the American Helicopter Society*, 19(4):44–48.

Anderson, E. H., Bales, G. L. and White, E. V. 2003. "Application of Smart Material-Hydraulic Actuators," *Proceedings of SPIE : Industrial and Commercial Applications of Smart Structures Technologies*, 5054:73–84.

Arnold, U. and Strecker, G. 2002. "Certification, Ground and Flight Testing of an Experimental IBC System for the CH-53G Helicopter," *In Proceedings of the 58th Annual Forum of the American Helicopter Society*, 58(Part I):297–308.

Bachtold, M. 1997. "Efficient 3D Computation of Electrostatic Fields and Forces in Microsystems," *Diss.Swiss Federal Institute of Technology Zurich*.

Bao, J., Allen, K. and Chopra, I. 2006. "Design and Test of a Mach Scale Swashplateless Rotor Using Smart Trailing-Edge Flaps," *In Proceedings of the 62nd Annual Forum of the American Helicopter Society*, 3:1519–1530.

Bao, J., Nagaraj, V. T., Chopra, I. and Bernhard, A. P. F. 2002. "Development of a Low Vibration Mach Scale Rotor with Composite Coupling," *In Proceedings of the* 58th *Annual Forum of the American Helicopter Society*, 2:2081–2094.

Beckman, J. B. and Blickstein, M. J. 1984. "Apparatus and Method for Piezoelectric Pump," *US Patent Specification 4,449,893*, US Patent Office, Washington, DC.

Beckman, J. B. and Blickstein, M. J. 1985. "Piezoelectric Pump with Internal Load Sensor," *US Patent Specification 4,519,751*, US Patent Office, Washington, DC.

Bernhard, A. 2000. *Smart Helicopter Rotor with Active Blade Tips(SABT)*, Ph.D. thesis, Department of Aerospace Engineering, University of Maryland at College Park.

Bernhard, A. and Chopra, I. 1999. "Trailing Edge Flap Activated by a Piezo-Induced Bending-Torsion Coupled Beam," *Journal of the American Helicopter Society*, 44(1):3–15.

Bishop, R. P., Face, B. R., Face, S. A., Clark, S. E. and Rose, N. S. 2000. "Piezoelectrically Actuated Piston Pump," *US Patent Specification 6,071,088*, US Patent Office, Washington, DC.

Bitman, L., Choi, S. B., Choi, Y. T. and Wereley, N. M. 2005. "Electrorheological Damper Analysis Using an Eyring-Plastic Model," *Smart Materials and Structures*, 14(1):237–246.

Bothwell, C. M., Chandra, R. and Chopra, I. 1995. "Torsional Actuation with Extension-Torsional Composite Coupling and Magnetostrictive Actuators," *AIAA Journal*, 33(4):723–729.

Bousmann, W. 1999. "Putting the Aero Back into Aeroelasticity," *Eighth ARO Workshop on Aeroelasticity of Rotor Systems*.

Bridger, K., Cooke, A. V., Crowne, A. V., Lutian, J. L., Sewell, J. M., Small, G. E. and George, L. 2004a. "Compact Hybrid Actuator," *US Patent Specification 6,751,954*, US Patent Office, Washington, DC.

Bridger, K., Sewell, J. M., Cooke, A. V., Lutian, J. L., Kohlhafer, D., Small, G. E. and Kuhn, P. M. 2004b. "High-Pressure Magnetostrictive Pump Development: A comparison of Prototype and Modeled Performance," *In Proceedings of SPIE, Smart Structures and Materials 2004 - Industrial and Commercial Applications of Smart Structures Technologies*, 5388:246–257.

Cadou, C. and Zhang, B. 2003. "Performance Modeling of a Piezo-Hydraulic Actuator," *Journal of Intelligent Materials and Structures*, 14(3):149–160.

Calkins, F. T., Dapino, M. J. and Flatau, A. B. 1997. "Effect of Prestress on the Dynamic Performance of a Terfenol-D Transducer," *Proceedings of the SPIE-Smart Structures and Materials 1997: Smart Structures and Integrated Systems*, 3041:293–304.

Carlson, J. D., Catanzarite, D. M. and Clair, K. A. 1996. "Commercial Magneto-Rheological Fluid Devices," *International Journal of Modern Physics B*, 10:2857–2865.

Chandra, R. and Chopra, I. 1997. "Actuation of Trailing Edge Flap in Wing Model," *In Proceedings of the 38st AIAA/ASME/ASCE/AHS/ASC Structures, Structural Dynamics and Materials Conference*, 2:1438–1448, Kissimmee, FL, USA.

Chaudhuri, A., Yoo, J.-H., Nersessian, N. and Wereley, N. M. 2006a. "Scaling-Up Issues with a Magnetostrictive Hydraulic Pump," *Proceedings of IMECE, 2006 ASME International Mechanical Engineering Congress and R&D Exposition*, IMECE2006-15695, Chicago, IL, USA.

Chaudhuri, A., Yoo, J.-H. and Wereley, N. M. 2006b. "Dynamic Modeling of a Magnetostrictive Hydraulic Pump," *In Proceedings of the IMECE, 2006 ASME International Mechanical Engineering Congress and R&D Exposition*, 25(210):1906–1913, Chicago, IL, USA.

Chen, P. C. and Chopra, I. 1996. "Induced Strain Actuation of Composite Beams and Rotor Blades with Embedded Piezoceramic Elements," *Smart Materials and Structures*, 5(1):35–48.

Chen, P. C. and Chopra, I. 1997. "Wind Tunnel Test of a Smart Rotor Model With Individual Blade Twist Control," *Journal of Intelligent Material Systems and Structures*, 8(5):414–425.

Choi, S.-B. and Choi, W.-Y. 2000. "Position Control of a Cylinder Using a Hydraulic Bridge Circuit With ER Valves," *ASME Journal of Dynamic Systems, Measurement and Control*, 122(1):202–209.

Choi, S.-B., Sung, K.-G. and Lee, J.-W. 2002. "The Neural Network Position Control of a Moving Platform Using Electrorheological Valves," *ASME Journal of Dynamic Systems, Measurement and Control*, 124(3):435–442.

Choi, Y. T., Wereley, N. M. and Jeon, Y.-K. 2005. "Semi-active Isolators Using Electrorheological/Magnetorheological Fluids," *AIAA Journal of Aircraft*, 42(5):1244–1251.

Chopra, I. 2000. "Status of Application of Smart Structures Technology to Rotorcraft Systems," *Journal of American Helicopter Society*, 45(4):228–252.

Chopra, I. 2002. "Review of State of the Art of Smart Structures and Integrated Systems," *AIAA Journal,*, 40(11):2145–2187.

Culp, G. W. and Nuys, V. 1993. "Apparatus and Method for Piezoelectric Pump," *US Patent Specification 5,192,197*, US Patent Office, Washington, DC.

Damjanovic, D. and Newnham, R. E. 1992. "Electrostrictive and Piezoelectric Materials for Actuator Applications," *Journal of Intelligent Material Systems and Structures*, 3(2):190–208.

Duong, J. and Garcia, E. 1996. "Design and Performance of a Rotary Motor Driven by Piezoelectric Stack Actuators," *Japanese Journal of Applied Physics, Part 1*, 35(12A):6334–6341.

Ellis, C. W. and Jones, R. 1963. "Application of an Absorber to Reduce Helicopter Vibration Levels," *Journal of the American Helicopter Society*, 8(3):30–38.

Ellison, J. 2004. *Investigation of Active Materials As Driving Elements In A Hydraulic-Hybrid Actuator*, Master's thesis, Department of Aerospace Engineering, University of Maryland, College Park.

Facey, W., Rosenfeld, N. C., Choi, Y. T., Wereley, N. M., Choi, S. B. and Chen, P. 2005. "Design and Characterization of a Compact Impact Damper for High Impulsive Loads," *International Journal of Modern Physics B*, 19(7-9):1549–1555.

Facey, W., Rosenfeld, N. C. and Wereley, N. M. 2003. "Design and Characterization of a Compact Impact Damper for High Impulsive Loads," *44th AIAA/ASME/ASCE/AHS Structures, Structural Dynamics, and Materials Conference*, AIAA2003-1645.

Falls, J., Datta, A. and Chopra, I. 2006. "Integrated Trailing-Edge Flaps and Servotabs for Helicopter Primary Control," *In Proceedings of the 62nd Annual Forum of the American Helicopter Society*, 2:1011–1021.

Fenn, R. C., Downer, J. R., Bushko, D. A., Gondhalekar, V. and Ham, N. D. 1996. "Terfenol-D Driven Flaps for Helicopter Vibration Reduction," *Smart Materials and Structures*, 5(1):49–57.

Fiore, G., Redaelli, A., Guadagni, G., Inzoli, F. and Fumero, R. 2002. "Development of a New Disposable Pulsatile Pump for Cardiopulmonary Bypass: Computational Fluid-Dynamic Design and In Vitro Tests," *American Society for Artificial Internal Organs Journal*, 48(3):260–267.

Fox, W. and McDonald, A. 1992. *Introduction to Fluid Mechanics*, New York : J. Wiley.

Frank, J. E., Mockensturm, E. M., Koopmann, G. H., Lesieutre, G. A., Chen, W. and Loverich, J. Y. 2003. "Modeling and Design Optimization of a Bimorph-Driven Rotary Motor," *Journal of Intelligent Material Systems and Structures*, 14(4-5):217–227.

Fulton, M. V. and Ormiston, R. A. 2001. "Hover Testing of a Small-Scale Rotor with On-Blade Elevons," *Journal of the American Helicopter Society*, 46(2):96–106.

Galante, T., Frank, J. E., Bernard, J., Chen, W., Lesieutre, G. A. . and Koopmann, G. H. 2000. "Design, Modeling, and Performance of a High Force Piezoelectric Inchworm Motor," *Journal of Intelligent Material Systems and Structures*, 10(12):962–972.

Gavin, H. P., Hanson, R. D. and Filisko, F. E. 1996a. "Electrorheological Dampers, Part I: Analysis and Design," *ASME Journal of Applied Mechanics*, 63:669–675.

Gavin, H. P., Hanson, R. D. and Filisko, F. E. 1996b. "Electrorheological Dampers, Part II: Analysis and Design," *ASME Journal of Applied Mechanics*, 63:676–682.

Gerver, M. J., Goldie, J. H., Swenbeck, J. R., Shea, R., Jones, P., Ilmonen, R. T., Dozor, D. M., Armstrong, S., Roderick, R., Nimblett, F. E. and Iovanni, R. 1998. "Magnetostrictive Water Pump," *Proceedings of SPIE, Smart Structures and Materials 1998 - Smart Structures and Integrated Systems*, 3329:694–705.

Goto, A., Nohmi, M., Sakurai, T. and Sogawa, Y. 2002. "Hydrodynamic Design System for Pumps Based on 3-D CAD, CFD, and Inverse Design Method," *ASME Journal of Fluids Engineering*, 124(2):329–335.

Goto, A. and Zangeneh, M. 2002. "Hydrodynamic Design of Pump Diffuser Using Inverse Design Method and CFD," *ASME Journal of Fluids Engineering*, 124(2):319–328.

Guinn, K. F. 1982. "Individual Blade Control Independant of a Swashplate," *Journal of the American Helicopter Society*, 27(3):25–31.

Hall, S., Tzianetopoulou, T., Straub, F. and Ngo, H. 2000. "Design and Testing of a Double X-frame Piezoelectric Actuator," *In Proceedings of the SPIE-Smart Structures and Materials 2000: Smart Structures and Integrated Systems*, 3985:26–37.

Hall, S. R. and Prechtl, E. F. 1996. "Development of a Piezoelectric Servoflap for Helicopter Rotor Control," *Smart Materials and Structures*, 5(1):26–34.

Ham, N. D. 1987. "Helicopter Individual-Blade Control Research at MIT 1977-1985," *Vertica*, 11(1/2):109–122.

Hamkins, C. and Bross, S. 2002. "Use of Surface Flow Visualization Methods in Centrifugal Pump Design," *ASME Journal of Fluids Engineering*, 124(2):314–318.

Hemsel, T. and Wallaschek, J. 2000. "Survey of the Present State of the Art of Piezoelectric Linear Motors," *Ultrasonics*, 38(1-8):37–40.

Hiemenz, G., Choi, Y. T. and Wereley, N. M. 2003. "Seismic Control of Civil Structures Utilizing Semi-Active MR Braces," *Journal of Computer-Aided Civil and Infrastructure Engineering*, 18(1):31–44.

Hirsch, C. 1990. *Numerical Computation of Internal and External Flows*, John Wiley and Sons.

Hong, S. R., Choi, S. B., Choi, Y. T. and Wereley, N. M. 2003. "Non-dimensional Analysis for Effective Design of Semi-Active Electrorheological Damping Control System," *In Proceedings of the Institution of Mechanical Engineers, Part D: Journal of Automobile Engineering*, 217(D12):1095–1106.

Hong, S.-R., Choi, S. B., Choi, Y. T. and Wereley, N. M. 2005a. "Non-dimensional Analysis and Design of a Magnetorheological Damper," *Journal of Sound and Vibration*, 288(4-5):847–863.

Hong, S. R., Choi, S. B. and Han, M. S. 2002. "Vibration Control of a Frame Strcuture Using Electro-Rheological Fluid Mounts," *International Journal of Mechanical Sciences*, 44(10):2027–2045.

Hong, S.-R., John, S. and Wereley, N. M. 2005b. "Quasi-Steady Herschel-Bulkley Analysis of Magnetorheological Dampers with Preyield Viscosity," *Proceedings of the ASME Aerospace Division*, 70AD:381–390.

Janocha, H., Schaefer, J., J., D. and Jendritza. 1994. "Piezoelectric and Magnetostrictive Materials for Use in Smart Actuators," *Proceedings of the Joint Hungarian - British International Mechatronics Conference*, 397–404.

John, S. and Cadou, C. 2005. "Unsteady Fluid Flow in Smart Material Actuated Fluid Pumps," *Proceedings of SPIE-Smart Structures and Materials 2005:Smart Structures and Integrated Systems*, 5764:At press.

John, S., Cadou, C. and Wereley, N. M. 2006. "Application of CFD in the Design and Analysis of a Piezoelectric Hydraulic Pump," *Journal of Intelligent Material Systems and Structures*, 17(11):967–979.

John, S., Sirohi, J., Wang, G. and Wereley, N. M. 2007. "Comparison of Piezoelectric, Magnetostrictive and Electrostrictive Hybrid Hydraulic Actuators," *Journal of Intelligent Material Systems and Structures*, at press.

Jolly, M. R. and Carlson, J. D. 1996. "Controllable Squeeze Film Damping Using Magnetorheological Fluid," *Actuator 90, 5th International Conferences on New Actuators*, 333–336.

Kamath, G. and Wereley, N. M. 1997. "Nonlinear viscoelastic-plastic mechanisms-based model of an electrorheological damper," *AIAA Journal of Guidance, Control, and Dynamics*, 20(6):1125–1132.

Kamath, G., Wereley, N. M. and Jolly, M. R. 1999. "Characterization of Magnetorheological Helicopter Lag Dampers," *Journal of the American Helicopter Society*, 44(3):234–248.

Kamath, G. M., Hurt, M. K. and Wereley, N. M. 1996. "Analysis and Testing of Bingham Plastic Behavior in Semi-Active Electrorheological Fluid Dampers," *Smart Materials and Structures*, 5(5):576–590.

Karakas, E. S., Gordaninejad, F., Evrensel, C. A., Yeo, M. S., Liu, Y. and Sahin, H. 2004. "Control of a Quarter HMMWV Suspension System Using a Magnetorheological Fluid," *Proceedings of the SPIE, 1996 Symposium on Smart Material Conference on Industrial and Commercial Applications of Smart Structures Technologies*, 5386:204–213.

Kiris, C., Kwak, D., Rogers, S. and Chang, I.-D. 1997. "Computational Approach for Probing the Flow Through Artificial Heart Devices," *ASME Journal of Biomechanical Engineering*, 119(4):452–460.

Konishi, K., Hashimoto, K., Miyamoto, T. and Tamura, T. 1997. "Hydraulic Actuators Driven by Piezoelectric Elements(4th Report, Construction of Mathematical Models for Simulation," *Journal of Japanese Society of Mechanical Engineering(C)*, 63(605):158–165.

Konishi, K., Yoshimura, T., Hashimoto, K., Hamada, T. and TAmura, T. 1993a. "Hydraulic Actuators Driven by Piezoelectric Elements (2^{nd} Report, Enlargement of Piezoelectric Pumps Output Power Using Hydraulic Resonance)," *Journal of Japanese Society of Mechanical Engineering (C)*, 60(571):228–235.

Konishi, K., Yoshimura, T., Hashimoto, K. and Yamamoto, N. 1993b. "Hydraulic Actuators Driven by Piezoelectric Elements (1^{st} Report, Trial Piezoelectric Pump and its Maximum Power)," *Journal of Japanese Society of Mechanical Engineering (C)*, 59(564):213–220.

Koratkar, N. and Chopra, I. 1997. "Analysis and Testing of a Froude Scaled Helicopter Rotor with Piezoelectric Bender Actuated Trailing Edge Flaps," *Journal of Intelligent Material Systems and Structures*, 8(7):555–570.

Kordonski, W. and Golini, D. 1999. "Magnetorheological Suspension-based High Precision Finishing Technology (MRF)," *Journal of Intelligent Material Systems and Structures*, 9(8):650–654.

Kordonski, W. I., Gorodkin, S. R. and Novikova, Z. 1998. "The Influence of Ferroparticle Concentration and Size on MR Fluid Properties," in *In Proceedings of the 6^{th} International Conference on Electrorheological Fluids, Magnetorheological Suspensions, and their Applications*, 535–542, World Scientific.

Lam, A. H.-F. and Liao, W.-H. 2003. "Semi-active Control of Automotive Suspension Systems with Magneto-rheological Dampers," *International Journal of Vehicle Design*, 33(1-3):50–75.

Leconte, P. and Geoffroy, P. 1994. "Dynamic Optimization of a Rotor Blade," *Aeromechanics Specialists Conference on Aerodynamics, Acoustics and Dynamics, San Francisco, CA*, 5.2–1 to 5.2–9.

Lee, D. G., Or, S. W. and Carmen, G. P. 2004. "Design of a Piezoelectric-Hydraulic Pump with Active Valves," *Journal of Intelligent Material Systems and Structures*, 15(2):107–116.

Lee, D. Y. and Wereley, N. 2000. "Quasi-Steady Herschel-Bulkley Analysis of Electro and Magnetorheological Dampers," *Journal of Intelligent Material Systems and Structures*, 10(10):761–769.

Lee, H. S. and Choi, S. B. 2000. "Control and Response Characteristics of a MagnetoRheological Fluid Damper for Passenger Vehicles," *Journal of Intelligent Material Systems and Structures*, 11:80–87.

Lee, T. 1999. "High Displacement Piezoelectric Trailing-Edge Flap Mechanism for Helicopter Rotors," *Doctor of Philosophy*, Department of Aerospace Engineering, University of Maryland, College Park.

Lee, T. and Chopra, I. 1990. "Development and Validation of a Refined Piezostack-Actuated Trailing Edge Flap Actuator for a Helicopter Rotor," *Proceedings of the 1999 Smart Structures and Materials - Smart Structures and Integrated Systems*, 3668(1):22–36.

Lee, T. and Chopra, I. 1999. "Design and Spin Testing of an Active Trailing Edge Flap Actuated Piezostacks," *Proceedings of the 40^{th} AIAA/ASME/ASCE/AHS/ASC Structures, Structural Dynamics and Materials Conference*, 4:2403–2413.

Lee, U., Kim, D., Hur, N. and Jeon, D. 2000. "Design Analysis and Experimental Evaluation of an MR Fluid Clutch," *Journal of Intelligent Material Systems and Structures*, 10(9):701–707.

Liao, W. H. and Wang, D. H. 2003. "Semi-Active Vibration Control of Train Suspension Systems via Magnetorheological Dampers," *Journal of Intelligent Material Systems and Structures*, 14(3):161–172.

Lim, J. W. 1988. "Aeroelastic Optimization of a Helicopter Rotor," *Doctor of Philosophy*, Deparment of Aerospace Engineering, University of Maryland, College Park.

Lindler, J. and Wereley, N. M. 2000. "Analysis and Testing of Electrorheological Bypass Dampers," *Journal of Intelligent Material Systems and Structures*, 10(5):363–376.

Lindler, J. E., Choi, Y.-T. and Wereley, N. M. 2003. "Double Adjustable Shock Absorbers Utilizing Electrorheological and Magnetorheological Fluids," *International Journal of Vehicle Design*, 33(1-3):189–206.

Lorber, P., Park, C., Polak, D., O'Neill, J. and Welsh, W. A. 2001. "Active Rotor Experiments at Mach Scale using Root Pitch IBC," *In Proceedings of the 57^{th} Annual Forum of the American Helicopter Society*, 2:1100–1112.

Marathe, S., Gandhi, F. and Wang, K. W. 1998. "Helicopter Blade Response and Aeromechanical Stability with a Magnetorheological Fluid based Lag Damper," *Journal of the Intelligent Material Systems and Structures*, 9(4):272–282.

Mauck, L., Oates, W. and Lynch, C. 2001. "Piezoelectric Hydraulic Pump Performance," *In Proceedings of the 2001 SPIE- Symposium on Smart Structures and Materials, Conference on Industrial and Commercial Applications of Smart Structures Technologies*, 4332:246–253.

Mauck, L. D. and Lynch, C. S. 2000. "Piezoelectric Hydraulic Pump Development," *Journal of Intelligent Material Systems and Structures*, 11(10):758–764.

Miao, W., Kottapali, S. B. R. and Frye, H. M. 1986. "Flight Demonstration of Higher Harmonic Control on the S-76," *In Proceedings of the 42^{nd} Annual Forum of the American Helicopter Society*, 2:777–791.

Milgram, J., Chopra, I. and Straub, F. K. 1998. "Rotors with Trailing Edge Flaps: Analysis and Comparison with Experimental Data," *Journal of the American Helicopter Society*, 43(4):319–332.

Munson, B., Young, D. and Okiishi, T. 1990. *Fundamentals of Fluid Mechanics*, John Wiley and Sons.

Nasser, K. and Leo, D. 2000. "Efficiency of Frequency-Rectified Piezohydraulic and Piezopneumatic Actuation," *Journal of Intelligent Material Systems and Structures*, 11(10):798–810.

Nasser, K., Leo, D. J. and Cudney, H. H. 2000. "Compact Piezohydraulic Actuation System," *Proceedings of the 7th SPIE Conference on Smart Structures and Integrated Systems*, 3991:312–322.

Nasser, K. M. 2000. "Development and Analysis of the Lumped Parameter Model of a Piezo-Hydraulic Actuator," *Doctor of Philosophy*, Department of Mechanical Engineering, Virginia Polytechnic Institute and State University.

Newmark, N. 1959. "A Method of Computation for Structural Dynamics," *ASCE Journal of the Engineering Mechanics Division*, 85(Part 1):67–94.

Oates, W. and Lynch, C. 2001. "Piezoelectric Hydraulic Pump System Dynamic Model," *Journal of Intelligent Material Systems and Structures*, 12(11):737–744.

Oates, W., Mauck, L. and Lynch, C. 2002. "System Dynamic Model of a Piezoelectric Hydraulic Pump," *In Proceedings of SPIE, the 2002 Symposium on Smart Structures and Materials: Modeling, Signal Processing and Control*, 4693:598–606.

Ogawa, K., Yoshida, Y., Nishizawa, M., Kamehara, N., Yano, A., Miyaki, A., Ono, M., Numata, Y., Kurihara, K. and Watanabe, K. 1999. "Piezoelectric Pumps," *US Patent Specification 5,798,600*, US Patent Office, Washington, DC.

Ormiston, R. A. 2001. "Aeroelastic Considerations for Rotorcraft Primary Control with On-Blade Elevons," *In Proceedings of the 57th Annual Forum of the American Helicopter Society*, 2:1033–1049.

Paine, J. S. and Chaudhry, Z. 1996. "Effect of amplification on efficiency and energy density of induced strain actuators," *Proceedings of the ASME Aerospace Division*, AD-52:511–516.

Pan, M.-J., Rehrig, P. W., Kucera, J. P., Park, S.-E. and Hackenberger, W. S. 2000. "Comparison of Actuator Properties for Piezoelectric and Electrostrictive Materials," *In Proceedings of SPIE, 2000 symposium on Smart Structures and Materials - Conference on Active Materials: Behavior and Mechanics*, 3992:80–90.

Peel, D. J. Stanway, R. and Bullough, W. A. 1996. "Dynamic Modeling of an Electro-Rheological Vibration Damper for Vehicle Suspension Applicaions," *Smart Materials and Structures*, 5(5):591–606.

Phillips, R. W. 1969. *Engineering Application of Fluids with Variable Yield Stress*, Ph.D. thesis, Department of Mechanical Engineering, University of California at Berkeley.

Phule, P. P. and Ginder, J. M. 1998. "The Materials Science of Field Responsive Fluids," *MRS Bulletin*, 23(8):19–22.

Pomirleanu, R. and Giurgiutiu, V. 2004. "High-Field Characterization of Piezoelectric and Magnetostrictive Actuators," *Journal of Intelligent Material Systems and Structures*, 15(3):161–180.

Prager, W. 1961. *Introduction to Mechanics of Continua*, Ginn and Company, New York.

Prechtl, E. and Hall, S. 1999. "Design of a High Efficiency, Large Stroke, Electromechanical Actuator," *Smart Materials and Structures*, 8(1):13–30.

Regelbrugge, M., Lindler, J. and Anderson, E. 2003. "Design Model for Piezo-Hydraulic Actuators," *44th AIAA/ASME/ASCE/AHS/ASC Structures, Structural Dynamics and Materials Conference*, 3:2163–2171.

Ribakov, Y. and Gluck, J. 2002. "Selective Controlled Base Isolation System with Magnetorheological Dampers." *Earthquake Engineering and Structural Dynamics*, 31(6):1301–1324.

Rodgers, J. P., Hagood, N. W. and Weems, D. B. 1997. "Design and Manufacture of an Integral Twist-Actuated Rotor Blade," *In Proceedings of the 38th AIAA/ASME/ASCE/AHS/ASC Structures, Structural Dynamics and Materials Conference on Adaptive Structures*.

Roget, B. and Chopra, I. 2002. "Robust Individual Blade Control Algorithm for a Dissimilar Rotor," *Journal of Guidance, Control and Dynamics*, 25(5):915–923.

Rosenfeld, N., Wereley, N. M., Radhakrishnan, R. and Sudarshan, T. S. 2002. "Behavior of Magnetorheological Fluids Utilizing Nanometer Iron," *International Journal of Modern Physics B*, 16(17-18):2392–2398.

Sager, F. E. and Matice, C. J. 1998. "Piezoelectric Pumps," *US Patent Specification 5,798,600*, US Patent Office, Washington, DC.

Samak, D. K. and Chopra, I. 1996. "Design of High Force, High Displacement Actuators for Helicopter Rotors," *Smart Materials and Structures*, 5(1):58–67.

Sano, T., Yoshida, Y., Tsujimoto, Y., Nakamura, Y. and Matsushima, T. 2002. "Numerical Study of Rotating Stall in a Pump Vaned Diffuser," *ASME Journal of Fluids Engineering*, 124(2):363–370.

Sashida, T. and Kenjo, T. 1993. *An Introduction to Ultrasonic Motors*, Oxford University Press.

Schuett, E. P. 1969. "Application of Passive Helicopter Rotor Isolation for Alleviation of Rotor Induced Vibration," *Journal of the American Helicopter Society*, 14(2):34–48.

Shen, J. and Chopra, I. 2004. "Swashplateless Helicopter Rotor with Trailing-Edge Flaps," *AIAA Journal of Aircraft*, 41(6):1465–1472.

Shen, J., Yang, M. and Chopra, I. 2004. "Swashplateless Helicopter Rotor with Trailing-edge Flaps for Flight and Vibration Control," *AIAA Journal of Aircraft*, 43(2):346–352.

Shoji, S. and Esashi, M. 1994. "Microflow Devices and Systems," *Journal of Micromechanics and Microengineering*, 4(4):157–171.

Simon, T. M., Ito, K., Banksa, H. T., Reitich, F. and Jolly, M. 2000. "Estimation of the Effective Permeability in Magnetorheological Fluids," *Journal of Intelligent Material Systems and Structures*, 10(11):872–879.

Sims, N. D. and Stanway, R. 2003. "Semi-Active Vehicle Suspension Using Smart Fluid Dampers: A Modeling and Control Study," *International Journal of Vehicle Design*, 33(1-3):76–102.

Sims, N. D., Stanway, R., Johnson, A. R. and Mellor, P. 2001. "Design, Testing, and Model Validation of an MR Squeeze-Flow Vibration Damper," *In Proceedings of SPIE - Symposium on Smart Structures and Materials 2001 - Smart Structures and Integrated Systems*, 4331:111–120.

Sirohi, J. 2002. "Piezoelectric Hydraulic Hybrid Actuator for a Potential Smart Rotor Application," *Doctor of Philosophy*, Department of Aerospace Engineering, University of Maryland, College Park.

Sirohi, J., Cadou, C. and Chopra, I. 2003. "Frequency Domain Modeling of Piezo-Hydraulic Actuator," *44th AIAA/ASME/ASCE/AHS/ASC Structures, Structural Dynamics, and Materials Conference*, 3:2172–2184.

Sirohi, J., Cadou, C. and Chopra, I. 2005. "Investigation of the Dynamic Characteristics of a Piezohydraulic Actuator," *Journal of Intelligent Material Systems and Structures*, 16(6):481–492.

Sirohi, J. and Chopra, I. 2003. "Design and Development of a High Frequency Piezoelectric-Hydraulic Hybrid Actuator," *Journal of Intelligent Material Systems and Structures*, 14(3):135–147.

Skelland, A. H. P. 1967. *Non-Newtonian Flow and Heat Transfer*, John Wiley and Sons, Inc.

Smith, B. L., Mortensen, K. V. and Wendel, S. 2005. "Oscillating Flow in Adverse Pressure Gradients," *Proceedings of FEDSM2005:2005 ASME Fluids Engineering Summer Conference, Houston, USA*, 2:199–206.

Sneed, R., Smith, R., Cash, M., Bales, G. and Anderson, E. 2006. "Development of Smart Material Hydraulic Pumps and Actuators," *ASME International Mechanical Engineering Congress and Exposition, Chicago, Illinois*, IMECE2006-15896, Chicago, IL, USA.

Sodeyama, H., Sunakoda, K., Suzuki, K., Carlson, J. D. and Spencer, B. F. 2001. "Development of Large Capacity Semi-active Vibration Control Device using Magneto-rheological Fluid," *American Society of Mechanical Engineers, Pressure Vessels and Piping Division (Publication) PVP*, 428(2):109–114.

Spangler, R. L. and Hall, S. R. 1990. "Piezoelectric Actuators for Helicopter Rotor Control," *In Proceedings of the 31st AIAA/ASME/ASCE/AHS/ASC Structures, Structural Dynamics and Materials Conference, Long Beach, CA*, 1589.

Spencer, B. and Chopra, I. 1995. "Design and Testing of a Helicopter Trailing Edge Flap with Piezoelectric Stack Actuators," *In Proceedings of the SPIE - Conference on Smart Structures and Materials 1996: Smart Structures and Integrated Systems*, 2717:120–131.

Stanway, R., Sproston, J. L. and El-Wahed, A. K. 1996. "Application of Electro-Rheological Fluids in Vibration Control: A Survey," *Smart Materials and Structures*, 5(4):464–482.

Staple, A. E. 1990. "An Evaluation of Active Control of Structural Response as a MEans of Reducing Helicopter Vibration," *In Proceedings of the* 46^{th} *Annual Forum the Americal Helicopter Society*, 1:3–17.

Staple, A. E. and Wells, D. M. 1990. "Development and Testing of an Active Control of Structural Response System for the EH101 Helicotper," 16^{th} *European Rotorcraft Forum, Glasgow, Scotland*.

Straub, F. K., Ngo, H. T., Anand, V. and Domzalski, D. B. 2001. "Development of a Piezoelectric Actuator for Trailing Edge Flap Control of Full Scale Rotor Blades," *Smart Materials and Structures*, 10(1):25–34.

Takesue, N., Furusho, J. and Kiyota, Y. 2004. "Fast Response MR-Fluid Actuator," *JSME International Journal Series C*, 47(3):783–791.

Takesue, N., Furusho, J. and Sakaguchi, M. 2001. "Improvement of Response Properties of MR Fluid Actuator by Torque Feedback Control," *Proceedings - IEEE International Conference on Robotics and Automation*, 4:3825–3830.

Tan, H., Hurst, W. and Leo, D. 2005. "Performance Modeling of a Piezohydraulic Actuation System with Active Valves," *Smart Materials and Structures*, 14(1):91–110.

Taylor, R. B. 1982. "Helicopter Vibration Reduction by Rotor Blade Modal Shaping," *American Helicopter Society,* 38^{th} *Annual Forum, Anaheim, CA*, 90–101.

Thurston, G. B., Hargrove, L. E. and Cook, B. D. 1957. "Nonlinear Properties of Circular Orifices," *Journal of Acoustical Society of America*, 29(9):992–1001.

Thurston, G. B. and Martin, C. E. 1953. "Periodic Fluid Flow through Circular Orifices," *Journal of Acoustical Society of America*, 25(1):26–31.

Uchino, K. 1997. *Piezoelectric Actuators and Ultrasonic Motors*, Kluwer Academic Publishers, Boston.

Vinokur, M. 1983. “On One-Dimensional Stretching Functions for Finite-Difference Calculations,” *Journal of Computational Physics*, 50(2):214–234.

Wang, X. and Gordaninejad, F. 2000. “Flow Analysis of Field-Controllable, Electro- and Magneto-Rheological Fluids Using Herschel-Bulkley Model,” *Journal of Intelligent Material Systems and Structures*, 10(8):601–608.

Washio, S., Konishi, T., Nishii, K. and Tanaka, A. 1982a. “Research on Wave Phenomena in Hydraulic Lines(10th Report, Experimental Discussion on Unsteady Nonlinearity of Orifice Flows,” *Bulletin of the Japan Society of Mechanical Engineers*, 25(210):1914–1920.

Washio, S., Konishi, T., Nishii, K. and Tanaka, A. 1982b. “Research on Wave Phenomena in Hydraulic Lines(9th Report, Experimental Investigation of Oscillatory Orifice Flows,” *Bulletin of the Japan Society of Mechanical Engineers*, 25(210):1906–1913.

Watton, J. 1989. *Fluid Power Systems*, Prentice Hall, Reading, MA.

Welsh, W. A., von Hardenberg, P. C., von Hardenberg, P. W. and Staple, A. E. 1990. “Test and Evaluation of Fuselage Vibration Utilizing Active Control of Structural Response(ACSR) Optimized to ADS-27,” *In Proceedings of the*46th *Annual Forum of the American Helicopter Society*, 1:21–37.

Welsh, W. A. and Millott, T. 1999. “Helicopter Active Noise and Vibration Reduction,” 25th *European Rotorcraft Forum, Rome, Italy*, 21–37.

Wereley, N. M. 2003. “Nondimensional Analysis of Electrorheological and Magnetorheological Dampers Using a Herschel-Bulkley Constitutive Model,” *In Proceedings of the 44th ASME/JSME Joint Fluids Engineering Conference*, 1(PartC):1587–1594.

Wereley, N. M., Lindler, J., Rosenfeld, N. C. and Choi, Y. 2004. “Biviscous Damping Behavior in Electrorheological Shock Absorbers,” *Smart Materials and Structures*, 13(4):743–752.

Wereley, N. M. and Pang, L. 1998. "Nondimensional Analysis of Semi-Active Electrorheological and Magnetorheological Dampers Using Approximate Parallel Plate Models," *Smart Materials and Structures*, 7(5):732–743.

Wereley, N. M., Pang, L. and Kamath, G. 1999. "Idealized Hysteresis Modeling of Electrorheological and Magnetorheological Dampers," *Journal of Intelligent Material Systems and Structures*, 9(8):642–649.

White, F. M. 1991. *Viscous Fluid Flow*, McGraw-Hill series in mechanical engineering.

Williams, E. W., Rigby, S. G., Sproston, J. L. and Stanway, R. 1993. "Electrorheological Fluid Applied to an Automotive Engine Mount," *Journal of Non-Newtonian Fluid Mechanics*, 47:221–238.

Wolf-Jesse, C. and Fees, G. 1998. "Examination of Flow Behavior of Electrorheological Fluids in the Flow Mode," *Proceedings of the Institution of Mechanical Engineers, Part I: Journal of Systems and Control Engineering*, 212(3):159–173.

Wood, E. R., Powers, R. W., Cline, C. H. and Hammond, C. E. 1985. "On Developing and Flight Testing a Higher Harmonic Control System," *Journal of the American Helicopter Society*, 30(1):3–20.

Wylie, E. B., Streeter, V. L. and Suo, L. 1993. *Fluid Transients in Systems*, Prentice Hall, Englewood Cliffs, NJ.

Yang, G., Spencer, B. F., Carlson, J. D. and Sain, M. K. 2002. "Large-Scale MR Fluid Dampers: Modeling and Dynamic Performance Considerations," *Engineering Structures*, 24(3):309–323.

Yi, F., Dyke, S. J., Caicedo, J. M. and Carlson, J. D. 2001. "Experimental Verification of Multi-Seismic Control Strategies for Smart Dampers," *ASCE Journal of Engineering Mechanics*, 127:1152–1164.

Yoo, J.-H., Sirohi, J., John, S., Chaudhuri, A., Cadou, C. and Wereley, N. M. 2004. “Bidirectional Control of a Magnetorheological Piezo-Hydraulic Actuator,” *In Proceedings of SPIE - Symposium on Smart Structures and Materials 2004 - Smart Structures and Integrated Systems*, 5390:116–126.

Yoo, J.-H., Sirohi, J. and Wereley, N. M. 2005. “A Magnetorheological Piezohydraulic Actuator,” *Journal of Intelligent Material Systems and Structures*, 16(11-12):945–953.

Yoo, J. H. and Wereley, N. M. 2002. “Design of a High-Efficiency Magnetorheological Valve,” *Journal of Intelligent Material Systems and Structures*, 13(10):679–687.

Yoo, J. H. and Wereley, N. M. 2004. “Performance of a Magnetorheological Hydraulic Power Actuation System,” *Journal of Intelligent Material Systems and Structures*, 15(11):847–858.

Yu, T.-Y., Soni, B. K. and Shih, M.-H. 1995. “Geometry modeling and grid generation using 3D NURBS control volume,” *In Proceedings of the NASA Workshop on Surface Modeling, Grid Generation, and Related Issues in Computational Fluid Dynamic (CFD) Solutions*, (3291):491.

Zhao, J. and Zhang, Q. M. 1996. “Effect of Mechanical Stress on the Electromechanical Performance of PZT and PMN-PT Ceramics,” *In Proceedings of the 1996 10th IEEE International Symposium on Applications of Ferroelectrics, ISAF’96. Part 2 (of 2)*, 2:971–974.